Dipl.-Ing. Nika Mahne, BSc

Singlet Oxygen in Non-Aqueous Battery Chemistries

DISSERTATION

zur Erlangung des akademischen Grades

Doktorin der technischen Wissenschaften

eingereicht an der

Technischen Universität Graz

Betreuer

Assoc.Prof. Sergey M. Borisov
Institut für Analytische Chemie und Lebensmittelchemie

Betreuer und Projektleiter

Dipl.-Ing. Dr.sc.ETH Stefan A. Freunberger
Institut für Chemische Technologie von Materialien

Graz, April 2018

EIDESSTATTLICHE ERKLÄRUNG

Ich erkläre an Eides statt, dass ich die vorliegende Arbeit selbstständig verfasst, andere als die angegebenen Quellen/Hilfsmittel nicht benutzt, und die den benutzten Quellen wörtlich und inhaltlich entnommenen Stellen als solche kenntlich gemacht habe. Das in TUGRAZonline hochgeladene Textdokument ist mit der vorliegenden Dissertation identisch.

_____   _____
          Datum   Unterschrift

Meine Dissertation mit dem Titel *Singulett-Sauerstoff in nicht-wässrigen Batterien* habe ich am Institut für Chemische Technologie von Materialien erarbeitet, verfasst und an der Technischen Universität Graz eingereicht, um den akademischen Grad Doktorin der technischen Wissenschaften zu erlangen. Es war mir eine große Freude, so einzigartige und unterschiedliche Persönlichkeiten kennen zu lernen, mit ihnen zu arbeiten und von ihnen zu lernen! Auf diesem Weg möchte ich mich bei all jenen herzlich bedanken, die mir in den letzten drei Jahren auf unterschiedliche Weise zur Seite gestanden sind.

Mein größter Dank gebührt meinem Betreuer und Projektleiter Stefan A. Freunberger, der meine unerschöpfbare Ressource an Motivation über die Jahre hinweg war. Durch ihn hatte ich nicht nur die Möglichkeit an diesem spannenden und interdisziplinären Thema zu arbeiten, sondern konnte auch von seinem Wissen lernen.

Ein großes Dankeschön möchte ich auch meinem Doktorvater und Betreuer Sergey M. Borisov aussprechen. Trotz der Tatsache, dass ich einen Großteil meiner Arbeit am ACFC im Dunkelraum verbracht habe, hat unsere Zusammenarbeit an diesem angeregten Molekül immer wieder 'Licht ins Dunkel' meiner wissenschaftlichen Ergebnisse gebracht.

Die institutsübergreifende Zusammenarbeit war ein wesentlicher Punkt im Verlauf meiner Dissertation. Durch sie wurde mir eine sehr flexible Arbeitsweise ermöglicht. Bedanken möchte ich mich bei meinen Kooperationspartnern bzw. Mentoren, die mir über die Jahre hinweg mit ihren Ratschlägen und ihrem Wissen zur Seite gestanden sind: C. Slugovc, R. Saf und K. Reichmann vom Institut für Chemische Technologie von Materialien, I. Klimant und T. Mayer vom Institut für Analytische Chemie und Lebensmittelchemie, R. Breinbauer und G.A. Strohmeier vom Institut für Organische Chemie, M. Flock und R. Fischer vom Institut für Anorganische Chemie, und zu guter Letzt S. Landgraf vom Institut für Physikalische und Theoretische Chemie.

Ich möchte mich hiermit auch ganz herzlich bei meiner Arbeitsgruppe den *lila-gelben Kellerasseln* für ein tolles Arbeitsklima bedanken. Die Zusammenarbeit mit Bettina, Christian und Lukas hat in Publikationen gefruchtet. Ausflüge in die steirische Bergwelt, unzählige zelebrierte Kuchenpausen – egal ob nun anlässlich eines Geburtstages, versäumter Glovebox-Verpflichtungen oder Veröffentlichung einer Publikation – Schafzahls'sche kulinarische Abende und andere Arbeitsgruppenaktivitäten haben

Contents

Zusammenfassung

Sauerstoff zählt zu den leichtesten, am häufigsten vorkommenden und versatilsten redox-aktiven Elementen. Jüngst hat die Redoxchemie von Sauerstoff große Aufmerksamkeit an der Spitze der Batterieforschung auf sich gezogen, wie z.B. bei Metall-O_2, Metall-O_2/CO_2 Batterien und Li-reichen Oxiden. Die Bildung von O_2 ist in allen Fällen ein kritisches Phänomen, das bis jetzt nicht vollständig verstanden wurde. Der Betrieb von wiederaufladbaren Metall-O_2 Batterien hängt kritisch von der reversiblen Bildung/Auflösung von Metall(su)peroxiden an der Kathode während des Entlade-/Ladevorgangs ab. Die wohl größte Hürde stellen schwerwiegende parasitäre Reaktionen dar, die bis jetzt Superoxid und Peroxid zugeschrieben wurden. Dennoch können diese beobachteten irreversiblen Prozesse nicht restlos mit deren Reaktivität erklärt werden. Die Möglichkeit der Singulett-Sauerstoff ($^1O_2$) Generierung wurde vermutet, doch diese konnte aufgrund von Detektionsschwierigkeiten nicht nachgewiesen werden. Im Zuge dieser Arbeit wurde ein neuer Methodensatz entwickelt, um $^1O_2$ in nicht-wässriger Elektochemie zu detektieren und dessen Bildung konnte in einer Auswahl an hochaktuellen Batteriechemien gezeigt werden, in denen $^1O_2$ überwiegend zur parasitärer Chemie beiträgt. Erkenntnisse über den sehr reaktiven $^1O_2$ geben einen rationalen Ansatz für zukünftige Forschung in Richtung hoch-reversibler Batteriesysteme: (1) $^1O_2$ bildet sich während des Entladens und von Beginn des Ladens in Li-O_2 Batterien; seine Generierung wird durch Spuren von H_2O verstärkt und kann effektiv durch $^1O_2$ Sonden/Löscher vermindert werden. (2) $^1O_2$ bildet sich in allen Phasen des Zellbetriebes in Na-O_2 Batterien; durch H^+-vermittelte Superoxid Disproportionierung während des Entladens, Lagerns und Ladens $< 3.3\,\mathrm{V}$, und elektrochemisch direkt über $3.3\,\mathrm{V}$ *vs.* Na/Na$^+$. (3) Elektrochemische Oxidation von Li$_2$CO$_3$ bildet $^1O_2$. Bei Spannungen über $3.8\,\mathrm{V}$ *vs.* Li/Li$^+$ zersetzt sich Li$_2$CO$_3$ zu CO_2, wobei keine O_2 Bildung beobachtet wird. Dies wurde zuvor nicht identifizierbaren parasitären Reaktionen zugeschrieben; wir konnten jedoch zeigen, dass $^1O_2$ gebildet wird. Diese Ergebnisse haben signifikante Folgen für die langfristige Zyklisierbarkeit von Batterien und untermauern die Wichtigkeit $^1O_2$ Bildung in Metall-O_2 Batterien zu verhindern. Sie stellen die Möglichkeit einer reversiblen Metall-O_2/CO_2 Batterie in Frage, und tragen zum Verständnis der Grenzflächenreaktivität von Übergangsmetallkathoden mit Li$_2$CO$_3$-Resten bei. $^1O_2$ wurde durch *in/ex-situ* Detektionsmethoden direkt sowie indirekt mittels einer fluoreszierenden Sonde detektiert.

Stichwörter: *Elektrochemie ∗ nicht-wässrige Batterien ∗ reaktive Sauerstoffspezies ∗ Singulett-Sauerstoff ∗ in/ex-situ Methoden ∗ chemische Singulett-Sauerstoff Sonde und Löscher ∗ elektrochemische Oxidation von Lithiumcarbonat*

Abstract

Oxygen redox chemistry is at the heart of energy storage in biological systems. Being one of the lightest, most abundant and most versatile redox active element, the redox chemistry of O_2 moieties has recently come into the focus of the forefront of battery research such as metal-O_2, metal-O_2/CO_2 batteries and Li-rich layered oxides. O_2 evolution is in these chemistries a critical yet not fully understood phenomenon. For example, operation of rechargeable metal-O_2 batteries depends crucially on the reversible formation/decomposition of metal (su)peroxides at the cathode on discharge/charge. The greatest challenge arises from severe parasitic reactions, which so far have been ascribed to the reactivity of superoxide and peroxide. Yet, their reactivity cannot explain the observed irreversible processes. Previously, singlet oxygen ($^1O_2$) has been hypothesized to be generated but could not be verified due to the difficulties with detecting $^1O_2$. Here I developed a set of methods to detect $^1O_2$ in non-aqueous electrochemistries and showed its formation in a number of highly topical battery chemistries in which either case $^1O_2$ accounts for the majority of parasitic chemistry. In these chemistries, awareness of the highly reactive $^1O_2$ gives a rationale for future research towards achieving highly reversible cell operation: (1) $^1O_2$ forms during discharge and from the onset of charge in Li-O_2 batteries, is enhanced by the presence of trace water, and can effectively be reduced by $^1O_2$ traps and quenchers. (2) $^1O_2$ forms in Na-O_2 batteries at all stages of cycling *via* proton-mediated superoxide disproportionation on discharge, rest, and charge below $\sim$3.3 V, and direct electrochemical $^1O_2$ evolution above $\sim$3.3 V *vs.* Na/Na$^+$. (3) Electrochemical oxidation of Li_2CO_3 forms $^1O_2$. When Li_2CO_3 decomposes to CO_2 at potentials above 3.8 V *vs.* Li/Li$^+$, O_2 evolution, as would be expected according to the decomposition reaction $2Li_2CO_3 \rightarrow 4Li^+ + 4e^- + 2CO_2 + O_2$, is not detected. 'Missing O-atoms' were thus previously ascribed to unidentified parasitic reactions: $^1O_2$ was shown to form; therefore, it does not evolve as O_2 in absence of a $^1O_2$ quencher. The substantial implications for the long-term cyclability of batteries are: they further underpin the importance of avoiding $^1O_2$ in metal-O_2 batteries, question the possibility of a reversible metal-O_2/CO_2 battery based on a carbonate discharge product, and help explain the interfacial reactivity of transition-metal cathodes with residual Li_2CO_3. $^1O_2$ was indirectly and directly detected *via in/ex-situ* detection methods: $^1O_2$ was indirectly detected with a selective and sensitive fluorescent $^1O_2$ probe.

Keywords: *electrochemistry* ∗ *non-aqueous batteries* ∗ *reactive oxygen species* ∗ *singlet oxygen* ∗ *in-situ and ex-situ methods* ∗ *singlet oxygen traps, probes and quenchers* ∗ *electrochemical oxidation of lithium carbonate*

Notations

A	absorbance
A_{beam}	area of radiation beam
$A_{634\,nm}$	absorbance of photosensitizer at 634 nm
$[A]_0$	initial concentration of substrate A
c	concentration
d	lightpath of the beam through the sample
DABCO	1,4-diazabicyclo[2.2.2]octane
DEGDME	diethylene glycol dimethyl ether
DMA	9,10-dimethylanthracene
DMA-O_2	9,10-dimethylanthracene endoperoxide
DME	ethylene glycol dimethyl ether
DPA	9,10-diphenylanthracene
DPA-O_2	9,10-diphenylanthracene endoperoxide
DPP	diketo-pyrro-pyrolle
ϵ	extinction coefficient
$f_{abs,\,634\,nm}$	fraction of absorbed light in the sample at 634 nm
F_{hv}	photonflux
f_r^A	fraction of $^1O_2$ quenched by substrate A which reacts
h	Planck constant
I_A	absorbed photonflux
i	current
k_A	rate constant for primary substrate, including k_q and k_r
k_d	first-order decay rate of $^1O_2$ in a solvent
k_r	rate constant for chemical quenching of $^1O_2$
k_Q	rate constant for physical quenching of $^1O_2$
λ	wavelength
$[^1O_2]_{ss}$	steady-state concentration of $^1O_2$
Pd$_4$F	Palladium (II) meso-tetra(4-fluorophenyl)tetrabenzoporphyrin
ϕ_Δ	quantum yield of $^1O_2$ formation
Q	physical quencher
[Q]	concentration of physical quencher
ROS	reactive oxygen species
RROS	reduced reactive oxygen species
r_{ox}	rate of photooxygenation
T	trap
TEGDME	tetraethylene glycol dimethyl ether
U	potential
V	sample volume

Personal Preface

Learning from Nature! Utilizing the air within the earth's atmosphere is an ongoing process implemented by living organisms ever since it reached its equilibrium. The earth's atmosphere consists of a mixture of gases with nitrogen and oxygen as main components, accompanied by argon and trace gases such as carbon dioxide and water. With approximately one fifth of the ambient air, molecular oxygen represents an essential, relatively benign, *quasi* non-depletable, everywhere and anytime accessible renewable feedstock. The utilization of molecular oxygen is necessary for all higher animals, and it is either produced or utilized, or both, by the majority of the living world. It is our fuel for live. For this reason scientists, among them biologists, physicists and chemists, have stressed its fascinating properties by focusing their research on this very molecule.

Better Living Through Chemistry has been my personal maxim over the period of my academic education, and still it is. With continuing education and research in *Technical Chemistry* my interest in the field of *Renewable Resources and Energy Storage* arose. By following this maxim I devoted myself to a scientific study about a topic which combines both, the use of benign and renewable raw materials guided by the principles of *Green Chemistry* and the work on the realization of a future-oriented energy storage technology.

Motivation and Structure of the Thesis

Thoughtless consumption of fossil-based energy has caused an ongoing climate change. Its concomitant adverse effects have set the ball rolling to fundamentally change our energy sources and their use. This has triggered a radical change in perspective, not merely in the population but in fact also politically towards an energy transition based on secure, economical and sustainable energy systems. This energy transition requires electrical energy storage. Lithium-ion batteries (LIB) have revolutionized portable electronics and have gained ground in electro-mobility in recent years. These early estimates were based on extremely simplistic views and do not hold even in theory. Yet realistic estimations of the upper limit of achievable energy density still suggest significantly higher energy storage than Li-ion. However, LIB will be impractical to meet the societal, economical and political needs for long-term applications, and apart from that store electricity from renewable resources with its presently available energy density. Going beyond their limits requires game changing approaches for 'beyond-intercalation' chemistries. In the past decade research on metal-oxygen batteries was vigorously promoted as they are claimed to offer capacities up to 10-fold in comparison to current LIB. However, metal-oxygen batteries such as *e.g.*, Li-O$_2$ cells suffer from parasitic chemistry at the oxygen cathode, which causes poor rechargeability, efficiency and cycle life. These severe reactions are the most persistent hurdle to overcome the practical realization of a long-term rechargeable energy system. It has been assumed that these parasitic reactions are predominantly caused by the reduced reactive oxygen species peroxide/Li$_2$O$_2$ and superoxide/LiO$_2$. Nevertheless, superoxide and peroxide cannot fully explain these side reactions with cell components causing degradation of both the carbon electrode and the electrolyte upon battery cycling. In 2011 singlet oxygen, another reactive oxygen species was theoretically predicted to form at high voltages. Until May 2016, however, experimental evidence was not provided ever since its first reference.

The aim of my work starting in February 2015 was to reveal singlet oxygen as the 'uncovered villain' of so far unidentified parasitic chemistry in non-aqueous metal-oxygen batteries and to investigate its formation mechanism. Consequently, strategies to diminish or even impede its formation should be investigated. The nature of molecular oxygen's reactive species was mainly studied in biological and biochemical media and processes. Singlet oxygen has long been recognised to be the major reactive species that causes aging in living nature. Hence, methods for detecting singlet oxygen were only available for aqueous biological systems. It turned out that operando detection of singlet oxygen in non-aqueous electrochemical systems was not attempted before, and that neither the so far only methods for electrochemical systems from the 1970s nor state-of-the art methods in biochemistry were applicable. So research had to start from scratch: to conduct this task, it was decided to develop a set of new *in-situ* and *ex-situ* methods to proof singlet oxygen formation during discharge and charge in non-aqueous battery systems.

Chapter 1 discusses current intercalation battery systems and game-changing approaches in beyond-intercalation batteries, with contextual focus on non-aqueous Li-air batteries. The subjects of oxygen reduction/evolution reaction, reversibility of cells and parasitic chemistry are elucidated. In *Chapter 2* the nature of 'exciting molecular oxygen' is characterised, physical and chemical properties of ground state and excited molecular oxygen are outlined. In addition, singlet oxygens generation, deactivation *via* quenching and previous state-of-the-art to detect it are discussed. *Chapter 3* explicitly focuses on the development of our new set of *in-situ* and *ex-situ* spectroscopic and analytic methods to directly and indirectly detect singlet oxygen in non-aqueous electrochemical systems. This includes synthesis of new probes and search for suitable singlet oxygen probes and/or traps for these measurements. Reactivity of different suitable probes with singlet oxygen, and their stability towards reactive oxygen species was investigated. In the following *Chapters 4 - 7* publications, of which I am either first author or co-first author, are chronologically incorporated in this cumulative doctoral thesis. *Chapter 4* and *Chapter 6* depict our results on singlet oxygen generation in non-aqueous Li-O_2 and Na-O_2 batteries, which were published in *Nature Energy* and *Angew. Chem. Int. Ed.* in 2017. *Chapter 5* provides a critical perspective on the mechanism and performance on lithium-oxygen batteries, published in *et al. Chemical Science* in 2017. These new insights emphasised in *Chapter 4* and *Chapter 6* paved the way to clarify an observation, which has raised an unanswered question for a long time: what happens to the 'missing third oxygen' in the electrochemical oxidation of lithium carbonate? This question is specifically addressed in *Chapter 7*. The results emerged from a cooperation with B.D. McCloskey from University of California – Berkeley and were published in *Angew. Chem. Int. Ed.* in 2018. Based

on the knowledge obtained, concepts for the synthesis of new singlet oxygen quenchers were developed and characterized in terms of their quenching ability and are described in *Chapter 8*. *Appendix A* covers an extremely vexed subject of elaborate *Experiments with unexpected outcomes* This is the first thesis devoted to singlet oxygen in non-aqueous electrochemistry, it establishes a set of suitable analytical methods and could therewith set first landmarks in the uncharted area of singlet oxygen in non-aqueous battery chemistry. Naturally, within the time frame of the thesis the work could not cover the many important topics that become now accessible. Not least with the work on Li_2CO_3, which is of relevance beyond metal-O_2 batteries, it turned out that singlet oxygen is of relevance for any battery chemistry that involves oxygen redox of some sort. I finalise with overall conclusions and an outlook on both metal-air batteries and the implications of singlet oxygen for battery chemistry more widely. .

Chapter 1

'Beyond-Intercalation' Batteries

In the future, energy storage will be more and more of particular importance than at any time in the past.[1] Its increasing societal demand, for instance for electro-mobility, has therefore become focus of much cutting-edge research.[2,3] State-of-the-art lithium-ion and sodium-ion batteries (LIB and SIB), based on intercalation materials, that store mobile Li^+ or Na^+ ions in stable frameworks of transition metal compounds or carbon, are now approaching their achievable limits.[4,5] With respect to energy, material sustainability and cost reduction, LIB and SIB will not be able to accomplish the demands. Therefore, new generations of batteries with increased energy and power density, improved safety, and lower cost are needed.[6,7] Going beyond the limits of intercalation chemistries requires lighter redox active elements that exchange more electrons and abolishment of non-redox active components. This often goes along with the shift from transition to main group elements. By this, costs can be reduced and better sustainability achieved, which motivates potentially game-changing approaches for 'beyond-intercalation' chemistries (see Figure 1.1).[2,8,9] These approaches rely on fundamentally different reactions to store charge compared to intercalation chemistries.

It is strived for replacing the carbon anode of a LIB or SIB with Si or Sn alloying or even with metallic Li or Na.[10,11,12,13] Intercalation cathodes may be replaced by O_2 or S as cathode.[9,14] 'Beyond-intercalation' chemistries may offer capacities of $1000 - 4000\,mAh{\cdot}g^{-1}$ of the formal charge storage material, compared to $100 - 350\,mAh{\cdot}g^{-1}$ for intercalation chemistries.[13] Particularly, energy storage in alkaline-based batteries is limited by the cathode. This has triggered intense research efforts to increase cathode capacity and/or voltage with candidate chemistries including Li-stoichiometric and Li-rich transition-metal oxide (TMO) intercalation cathodes, featuring higher voltage and capacity than currently used cathodes, or metal-O_2 or metal-O_2/CO_2 cathodes that feature lower voltage but lead to substantially higher theoretical capacity.[8,15]
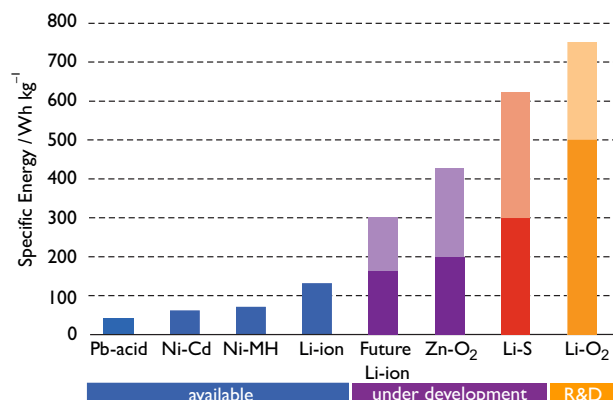
Figure 1.1: Anticipated practical specific energies for future rechargeable batteries *e.g.*, for Li-O_2 batteries in comparison to established systems *e.g.*, Li-ion is given. The Figure was adapted from Bruce *et al.*[16]

Rechargeable non-aqueous metal-O_2 batteries such as Li-O_2, Na-O_2 and K-O_2 cells have attracted considerable interest because of their high theoretical specific energy, with the Li-O_2 cell being the most intensively studied battery chemistry.[13,17,18] In this chemistries charge is stored at the cathode by the reversible formation/decomposition of metal oxides *e.g.*, Li_2O_2 and NaO_2 on discharge/charge.[19,20] Yet, the Li-O_2 and Na-O_2 batteries combine two challenging electrodes: (1) most commonly Li/Na metal is used as an anode, which is, despite decades of research, still associated with poor coulombic efficiencies,[8] and (2) the O_2/M_xO_2 redox couple ($M_x = Li_2$, Na) involves reactive species in the cycling mechanism, which challenge the stability of the aprotic electrolyte and the cathode electrode material, which is in the majority of the cases carbon. However, severe parasitic chemistry at the cathode, concomitant with insufficient cycle life, is the most significant obstacle for metal-oxygen batteries.[21,22] A key measure for parasitic chemistry is the ratio of e^- passed to O_2 consumed/evolved, which is for both cell chemistries deviating from the ideal value, less on discharge than on charge. On discharge typically close to ideal value of $2e^-$ per one O_2 molecule are consumed, despite significant amounts of alkaline-based side products ($M = Li$, Na) such as M-carbonate, - formate and -acetate being formed, whereas on charge, typically the e^-/O_2 ratio deviates significantly from two and more.[23,24,25] There have been many investigations on the origin of parasitic reactions and strategies were proposed to mitigate them. In particular superoxide has been perceived responsible for parasitic chemistry with electrolyte and electrode on discharge due to its strong nucleophilic and alkaline character, since it forms as an intermediate in O_2 reduction.[26,27] Despite superoxides and peroxides reactivity towards cell components, theoretical and experimental work have indicated that it cannot solely account for all parasitic reactions. Only better knowledge of parasitic reactions may allow them to be inhibited, so that progress towards fully reversible cell operation can continue. Besides these scientific and material challenges practical realisation further faces engineering challenges with cell construction and air handling.

1.1 The Non-Aqueous Lithium-Air Battery

The non-aqueous rechargeable lithium-air battery was first reported by Abraham.[28] On discharge, the lithium-metal anode is oxidized releasing Li^+ ions into the electrolyte, and O_2 from the ambient air is reduced in the porous, electrolyte filled electron conducting cathode matrix.[29,30] In a non-aqueous electrolyte O_2 reduction leads to superoxide which binds with Li^+ to LiO_2, which is either further reduced to Li_2O_2 or disproportionates to Li_2O_2. Charging involves Li_2O_2 oxidation to reversibly yield Li^+ and O_2. The overall cathode reaction is $2Li^+ + O_2 + 2e^- \rightleftarrows Li_2O_2$ and corresponds to a theoretical open circuit voltage of $2.96\,V$ vs. Li/Li^+. The realisation of the non-aqueous lithium-air battery from theory to practice presents a number of scientific and technological challenges and requirements regarding the anode, cathode and electrolyte.[31,32,33,34] Perhaps the most significant challenge facing the practical realisation of the non-aqueous Li-O_2 battery arises from severe parasitic reactions during cycling.[16,31,35,36,37] These reactions decompose the electrolyte as well as the porous electrode, which has severe implications causing poor rechargeability, high charging voltages, low efficiency, build up of parasitic reaction products, and early cell death within a few cycles. In addition, concomitant problems regarding the key performance properties as approaching theoretical capacity, reducing voltage gap polarization, improving rate capability and lowering the capacity fading have to be addressed.[16] To operate the cell in ambient air, gases such as H_2O, CO_2 and N_2 have to be removed beforehand, as they must be prevented from reacting with the lithium anode, in order to impede the formation of $LiOH$, Li_2CO_3 and Li_3N in its pores.[9] These side products do not only form a passivation layer on the electrodes, but some among them further cause parasitic side reactions during cycling as described in *Chapter 7*. The non-aqueous lithium-air battery will, therefore, hereafter be referred to as Li-O_2 battery as pure O_2 gas is the fuel.

1.1.1 Reaction mechanism at the Li-O_2 cathode during ORR and OER

The mechanism by which Li_2O_2 is formed and subsequently decomposed during discharge and charge is of crucial importance, as it further directly affects the stability of the cell components and rechargeability *via* the reactivity of the formed intermediates.[38]

Oxygen reduction reaction: Li_2O_2 formation on discharge

The first step of O_2 reduction (oxygen reduction reaction, ORR) in a Li-O_2 battery, in a Li^+ containing electrolyte, results in superoxide (O_2^-) formation, which first associates with Li^+ and, in the second step either undergoes a second $1e^-$ reduction reaction or disproportionates to form Li_2O_2. Two mechanisms have been proposed for how these steps take place during ORR: the first involves a solution process, where O_2^- is solubilized to precipitate Li_2O_2 from the electrolyte solution,[29] the second considers the intermediate as surface bound throughout the process.[39, 40] In aprotic solvents, the solubility of salts is primarily determined by the solvation of the cation, which is correlated with the Gutmann donor number (DN).[41, 42, 43] Typical classes of electrolyte solvents exhibit a broad range of DNs from nitriles and sulfones ($DN = 14 \text{-} 16$) to glymes ($DN = 20 \text{-} 24$), amides ($DN = {\sim}26$) and sulfoxides ($DN = {\sim}30$).[41, 42] Which mechanism prevails has direct implications on the attainable capacity, as illustrated in Figure 1.2. Additives can influence Lewis basicity (DN) or acidity of the electrolyte solution: Solvents and anion donor numbers follow the trend, *e.g.*, nitriles $<$ glymes $<$ amides $<$ sulfoxide and $TFSI^- < FSI^- < Tf^- < NO_3^-$.[44, 45, 46, 47, 48] For example, both high DN solvents and protic additives, that favour the solution mechanism, can enhance unpleasant parasitic reactions.[49, 47, 50, 51] Little mobility for reduced O_2 species is provided
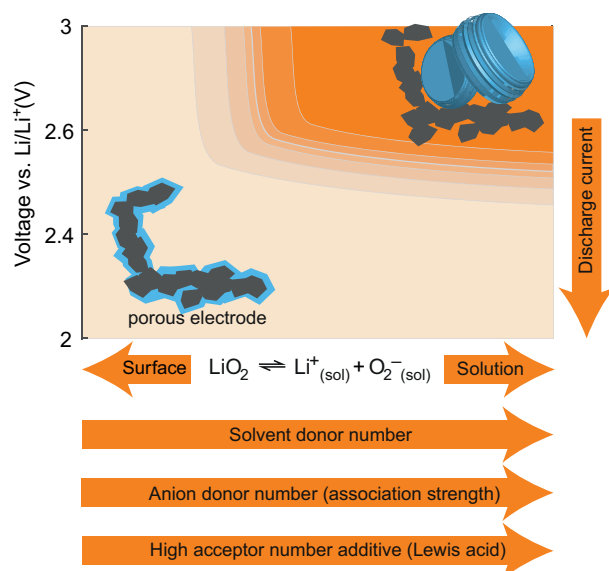
Figure 1.2: Determining parameters for surface and solution growth leading to either conformal coating of the porous electrode or large Li_2O_2 particles in the pores. Increasing current shifts from solution to surface growth. Effective Lewis basicity and acidity of the electrolyte as determined by the solvent, salt anion, and additives governs the position of the equilibrium $LiO_2^* \rightleftarrows Li^+_{(sol)} + O_{2(sol)}^-$, with * denoting a surface species. Additives with high AN are for example H_2O and alcohols. Adapted from Mahne *et al.*[38]

by the surface mechanism, and leads to a conformal coating of the electrode corresponding to low capacities.[40] Notably, discharge ceases after formation of Li_2O_2 of only ${\sim}5 \text{-} 10\,nm$.[52] The solution mechanism, in contrast, keeps electrode area open for longer and always reaches larger capacity by the growth of much larger toroidal particles (μm sized) composed of lamellae, which have the ability

to fill larger pores to a greater extent. *Section 3* in *Chapter 5* elaborates in detail further parameters influencing surface and solution growth. Irrespective of whether the surface or solution pathway prevails, the second electron transfer may, as mentioned before, either proceed *via* a second $1e^-$ reduction or disproportionation as illustrated in Figure 1.3. With a standard potential of 2.96 V for O_2/Li_2O_2 and $\sim$2.65 V for O_2/O_2^-, the standard potential for O_2^-/Li_2O_2 is at $\sim$3.3 V.[42] Hence, the second reduction has at all discharge potentials a strong driving force.

Figure 1.3: Reactions involved in ORR mechanism and its effect on OER. Adapted from Mahne *et al.*[38]
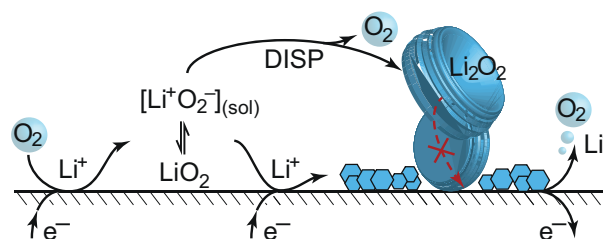
Oxygen Evolution Reaction: Oxidizing Li_2O_2 on charge

Galvanostatic charging of Li-O$_2$ cathodes is typically characterized by an onset of charging (oxygen evolution reaction, OER) slightly above the OCV at $\sim$3 V, followed by steadily increasing voltage as charging proceeds.[13,53] Three underlying phenomena appear to be collectively accountable, yet, details are lively debated: First, electrochemical oxidation of Li_2O_2 is possible with low kinetic barriers at high rates, and second, increasingly impeded electron transfer along recharge contributes a minor fraction of the voltage rise.[38] Third, the rising charging voltage is mostly caused by accumulating parasitic products, which generate a mixed potential. Important for understanding polarization and recharge limitations is at which interface, either at the cathode/Li_2O_2 or the Li_2O_2/electrolyte interface, the oxidation occurs. At the Li_2O_2/electrolyte interface, charge transport through Li_2O_2 will be the limiting factor, whereas at the cathode/Li_2O_2 interface full recharge will be impeded, if Li_2O_2 particles would lose contact. The observed charge potentials rise accounts only partly for the associated rise in impedance. Whereas the majority of the rise is associated with concomitant parasitic chemistry from the start of charge, which increases drastically with growing potential.

1.1.2 Characteristics of reversible cell reactions

True reversibility of the cathode reaction requires[37,38] a set of features (1)-(4) to obey the stoichiometry in compliance with $2Li^+ + O_2 + 2e^- \rightleftarrows Li_2O_2$ and to match each other during discharge and subsequent charge:

(1) One mole of O_2 is consumed/released per two moles of electrons flowing on discharge/charge, in accordance with $e^-/O_2 = 2$.

(2) One mole of O_2 and two moles of e^- produce exactly one mole of Li_2O_2 on discharge. On charge two moles e^- consume one mole of Li_2O_2 and release one mole of O_2. As a result the ratios $e^-/O_2 = e^-/Li_2O_2 = 2$ and $O_2/Li_2O_2 = 1$ result. Notably, $e^-/O_2 = 2$ is not a strict requirement for a rechargeable Li-O_2 battery if Li_2O_2 is not the discharge product as occasionally claimed.[54,55,56]

(3) All electrons involved contribute to the ORR or OER. Thus, no other gas than O_2 evolves during discharge/charge and no soluble or solid product other than Li_2O_2 is formed.

(4) For cycling with equal capacity (Q) on discharge and charge ($Q_{ORR} = Q_{OER}$), the O_2 released on charge correspond the amount consumed, in accordance with $n_{O_2,ORR} = n_{O_2,OER}$.

Concluding about the reversibility of the features 1 - 4 requires numerous *in-situ* and *ex-situ* quantitative analyses.[38] Measuring O_2 consumption/evolution has been described by two quantitative methods: The first is operando online mass spectrometry (OEMS), where the head space of the cell is continuously or periodical purged to a MS.[57,58,59] Using an O_2/Ar mixture allows also quantification of O_2 consumption and of any other gases evolved during discharge. The second method involves measuring the pressure in a hermetically sealed cell head space over discharge and charge.[23] Peroxide or superoxide content of electrodes has been measured *ex-situ* using either iodometric titration or spectrophotometry using the coloured Ti(IV)-peroxide complex.[60,61] This method was combined with equally MS based quantification of Li_2CO_3 and organic products by treatment with acid and Fenton's reagent to separately evolve CO_2 from accumulated inorganic and organic compounds.[62,63] Organic compounds such as acetate and formate may also be quantified by ^{1}H NMR after treating the electrode with D_2O which further allows qualitative analysis of compounds.[64,60] Importantly, all these stated methods capture the integral electrode.[38] Qualitative spectroscopic or microscopic methods such as Raman, FTIR, XRD, XPS or SEM cannot replace the mentioned or similar quantitative integral methods and cannot support solely claims of reversibility by no means.

1.1.3 The fate of oxygen: parasitic chemistry at the Li-O$_2$ cathode

"The partial reduction products of dioxygen, superoxide ion and peroxides, develop naturally in the chemistry of dioxygen. It would be difficult to discuss dioxygen chemistry without first discussing these partial reduction products." Ingraham and Meyer, *Biochemistry of Dioxygen*, Plenum Press **1985**
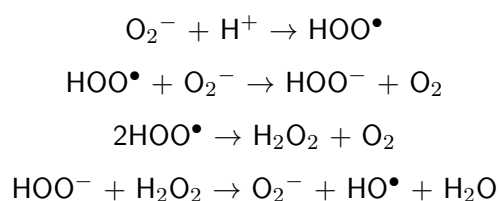
Chemically reactive species containing oxygen are in general referred to as reactive oxygen species (ROS).[65,66] These include radicals, stable molecular oxidants and excited molecules. ROS play a major role in particular in biological cells: they are natural side products in oxygen metabolism, play an important role in cell signalising and high concentrations trigger harmful reactions cumulatively known as oxidative stress.[67] As part of ROS, the reduced reactive oxygen species (RROS) superoxide and peroxide are an integral part of molecular oxygens chemistry.[65] RROS are well known for their reactivity towards a wide range of organic compounds, which has both been used as a reactant and recognized as a source of unwanted reactions.[68,69] The primary species O$_2^-$ and O$_2^{2-}$ are known to form species including HOO$^\bullet$, HOO$^-$ and HO$^\bullet$ in protic environments. Their chemical nature in terms of nucleophilicity, basicity and/or radical character causes reactivity *via* three major routes: nucleophilic substitutions, H$^+$ and H-atom abstraction. Besides that O$_2^-$ can transfer e$^-$. The addition of heteroatoms into aprotic electrolyte solutions changes the polarity, in order to dissolve a Li-salt, which in turn makes adjacent C and H atoms reactive. Due to the incompatibility of carbonate electrolytes for Li-O$_2$ chemistry, owing to O$_2^-$ nucleophilicity, this and other reactivities of RROS and O$_2$ were adduced to explain lesser but significant parasitic chemistry of all so far investigated alternative solvents and cell components.[9,64,70] Bryantsev *et al.* have pioneered this very field in computational chemistry, based on their results for activation and reaction free energies, the probability for the reaction of O$_2^-$ and O$_2$ with organic electrolytes *via* nucleophilic substitution, H$^+$ atom, and H-atom abstraction (Table 1.2 summarizes activation energies).[70,71,72,73] Activation energies for all considered reactions involving the major classes of solvents, excluding not suitable carbonate electrolytes, are too high to expect these reactions to strongly contribute to decomposition. Based on the results gained from experiments, were the stability of various solvents towards KO$_2$ or the reversibility of the O$_2$/O$_2^-$ couple was examined, reactions with activation energies beyond $100\,\text{kJ}\cdot\text{mol}^{-1}$ can be considered not to contribute noticeably, thus they contribute quasi insignificantly.[70] This means that in particular solely esters and lactones are expected to react *via* nucleophilic substitution with O$_2^-$, and possibly ethers *via* H-atom abstraction with Li$_2$O$_2$.[74] With ethers all reactions with O$_2^-$, Li$_2$O$_2$ and O$_2$ require high activation energy, and are of strongly endothermic character.

Table 1.2: Reactions of organic electrolytes with reduced oxygen species and molecular oxygen and their calculated activation energy barrier. ROR' are referred to as organic moieties with polarizing heteroatoms *e.g.*, N or S. The Table was adapted from Mahne *et al.*[38]

ROS	Type of Reaction	Reaction	E_{act} / kJ·mol^{-1}
O_2^-	Nucleophilic subst.	$ROR' + O_2^- \rightarrow RO^- + ROO^\bullet$	121 - 144[a], 105[b], 65 - 95[c]
	H-atom abstraction	$RH + O_2^- \rightarrow R^\bullet + HOO^-$	129 - 180[d], 191[e]
	H$^+$ abstraction	$RH + O_2^- \rightarrow R^- + HOO^\bullet$	pK$_a$ > 30 stable[f]
O_2^{2-}	Nucleophilic subst.	$ROR' + Li_2O_2 \rightarrow RO^-Li^+ + R'OO^-Li^+$	134 - 192[a]
	H-atom abstraction	$RH + Li_2O_2 \rightarrow R^\bullet + [Li_2O_2\text{-}H^\bullet]$	96 - 112[a]
	H$^+$ abstraction	$RH + Li_2O_2 \rightarrow R^-Li^+ + HOO^-Li^+$	116 - 311[a]
O_2	H-atom abstraction	$RH + O_2 \rightarrow R^\bullet + HOO^\bullet$	163 - 183[g], 138 - 161[h]

[a]dimethoxyethane (DME), [b]acetonitrile (MeCN), [c]carbonate and lactones, [d]Free DME, [e]the DME$_2$-Li$^+$ complex, [f]examples for pK$_a$<30: -CH$_2$-CF$_2$-, polyvinylidene difluoride (PVDF), aliphatic dinitriles, alkyl imides. pK$_a$>30: acetonitrile, DMSO, *N*-alkyl amides and lactams, aliphatic ethers. [g]the lower value for free DME, the higher one for the DME$_2$-Li$^+$ complex. [h]lactams and amides.

The presence of proton sources, *e.g.*, water or weak acids, triggers the formation of HOO$^\bullet$, HOO$^-$ and HO$^\bullet$ from O$_2^-$ according to following equations, which are more reactive than the primary RROS:[71, 75]

$$O_2^- + H^+ \rightarrow HOO^\bullet$$
$$HOO^\bullet + O_2^- \rightarrow HOO^- + O_2$$
$$2HOO^\bullet \rightarrow H_2O_2 + O_2$$
$$HOO^- + H_2O_2 \rightarrow O_2^- + HO^\bullet + H_2O$$

HOO$^-$ is a stronger base than O$_2^-$ and forms more readily R$^-$ through H$^+$ abstraction.[65] HO$^\bullet$ could serve as the initiator to form R$^\bullet$, which undergoes fast and thermodynamically favorable onwards chain reactions in the presence of O$_2$.[64, 73] Increasing parasitic chemistry with increasing water content is consistent with the protonated species being more reactive.[49] In conclusion, direct reactivity of O$_2^-$, Li$_2$O$_2$ and O$_2$ with the most important and promising classes of non-aqueous solvents for the Li-O$_2$ cathode is unfavourable. Figure 1.4 (adapted from McCloskey *et al.*[60, 76]) shows the typical pattern of the extend of side reactions, with much higher values during charge than discharge. This perfectly opposed the occurrence of O$_2^-$ and hence additional raises doubts as major cause of parasitic reactions.
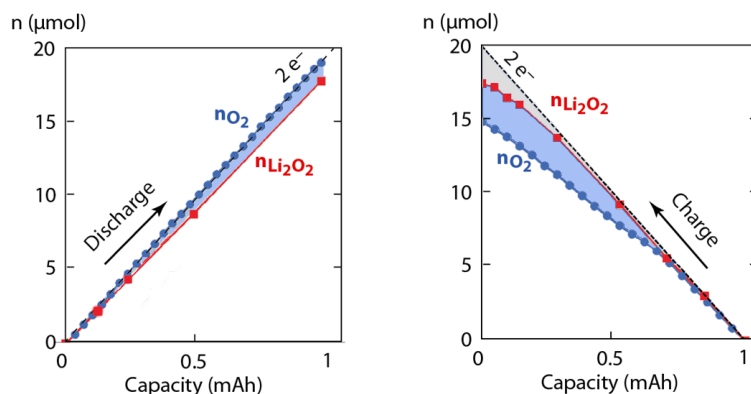
Figure 1.4: Typical deviations from a truly reversible Li-O$_2$ cathode chemistry during discharge and charge. It shows the deviations from a truly reversible Li-O$_2$ cathode chemistry during discharge and charge (left and right): the number of moles of O$_2$ consumed (n_{O_2}, blue) and of Li$_2$O$_2$ formed ($n_{Li_2O_2}$, red) during a 1 mAh Li-O$_2$ discharge are plotted in comparison to the theoretical line for 2e$^-$/O$_2$ consumed, which is indistinguishable from the blue data points. For the 1 mAh Li-O$_2$ recharge, the number of moles of O$_2$ evolved (n_{O_2}, blue) and of Li$_2$O$_2$ formed ($n_{Li_2O_2}$, red) are plotted. The theoretical line for 2e$^-$ consumption reflects the total charging current. The region in blue for discharge and charge, reflects the parasitic contribution that could arise from another so far unidentified reactive oxygen species. Whereby the region in grey on charge is due to parasitic oxidation of species unrelated to Li$_2$O$_2$, and therefore presumably not from an unidentified reactive oxygen species. The Figure was adapted from McCloskey *et al.*[60, 76]

Electrochemical oxidation of Li$_2$O$_2$ was hypothesized by Hassoun *et al.* to be able to generate singlet oxygen (^{1}O$_2$), molecular oxygen's first excited state.[20] This train of thought originated on the basis of knowledge about ^{1}O$_2$ generation upon the chemical oxidation of H$_2$O$_2$ or alkaline peroxides such as Li$_2$O$_2$ and Na$_2$O$_2$.[77,78,79] On account of the reversible potential of Li$_2$O$_2$ formation and the energy difference between ground state oxygen and singlet oxygen of $\sim$1 eV, ^{1}O$_2$ formation has been considered as possible between 3.5 to 3.9 V vs. Li/Li$^+$ in a Li-O$_2$ cell.[20,23] This suggest that the blue region upon discharge and charge could reflect the parasitic contribution that arises from ^{1}O$_2$. This very consideration was addressed by several reports, but could not be verified due to the challenges with detecting ^{1}O$_2$, except for one work. Gasteiger *et al.* identified *via* in-operando EPR spectroscopy small quantities of ^{1}O$_2$ between 3.55 and 3.75 V.[80] They explained ^{1}O$_2$ generation for the charge process according to Li$_2$O$_2 \rightarrow$ O$_2$ + 2Li$^+$ + 2e$^-$, and thus it could contribute explaining parasitic chemistry above 3.55 V. At that time it has been found that from the start of charging below 3.5 V, both a substantial amount of parasitic products is generated and that less than 1 mol O$_2$ evolves per 1 mol Li$_2$O$_2$ consumed. However, both could not be explained by the reactivity of RROS and formation of ^{1}O$_2$ above 3.55 V. We have shown that ^{1}O$_2$ forms also during discharge and from the onset of charge and that it accounts for the majority of parasitic reaction products in Li-O$_2$ batteries, as elaborated in *Chapter 4*.[51] In *Chapter 6* we show that also in Na-O$_2$ batteries ^{1}O$_2$ forms at all stages of cycling and that it is the main driver for parasitic chemistry in Na-O$_2$ batteries.[81]

Chapter 2

Exciting Molecular Oxygen!

Molecular oxygen is a fascinating molecule. The most significant characteristic of ground-state molecular oxygen is that it is a triplet state. This property has a scarcity value since almost all molecules exist as a singlet state in their ground state.[65] In addition, the lowest available orbital to accept an electron is an antibonding orbital. These unusual characteristics contribute to the kinetic barrier in reactions with ground-state molecular oxygen and also influence the type of reactions that do occur.

2.1 Excited Molecular Oxygen: Singlet Oxygen

The unique electronic structure of molecular oxygen and its chemistry can be better understood if we consider the individual orbitals in molecular oxygen occupied by its valence electrons (see Figure 2.1). In ground-state molecular oxygen, two electrons occupy separate antibonding orbitals ($2\pi_x$* and $2\pi_y$*) with unpaired spins as this results in less electron-electron repulsion.[82,83] Hence, its most stable configuration is a triplet state with two unpaired electrons. Ground-state molecular oxygen is usually depicted with the term symbol $^3\Sigma_g^-$, indicating a triplet state with an orbital momentum of zero.[82,79] The two lowest lying excited states of molecular oxygen are singlet states: the lower excited state lies 95 kJ and the higher excited state lies 158 kJ above the triplet ground state.[79,84,65] The electronic configurations of these states differ only by the structure of the antibonding orbitals. The lower excited state has both electrons in one of the antibonding 2π* orbitals, whereas the higher excited state has identical electronical configuration to ground state oxygen, except that the two electrons have antiparallel spin. The two excited states are designated with the term symbol $^1\Delta_g$ with an orbital momentum of two, and $^1\Sigma_g^+$ with a orbital momentum of zero. Both excited states are short lived compared to the stable triplet ground state. The transition from the $^1\Delta_g$ state to the
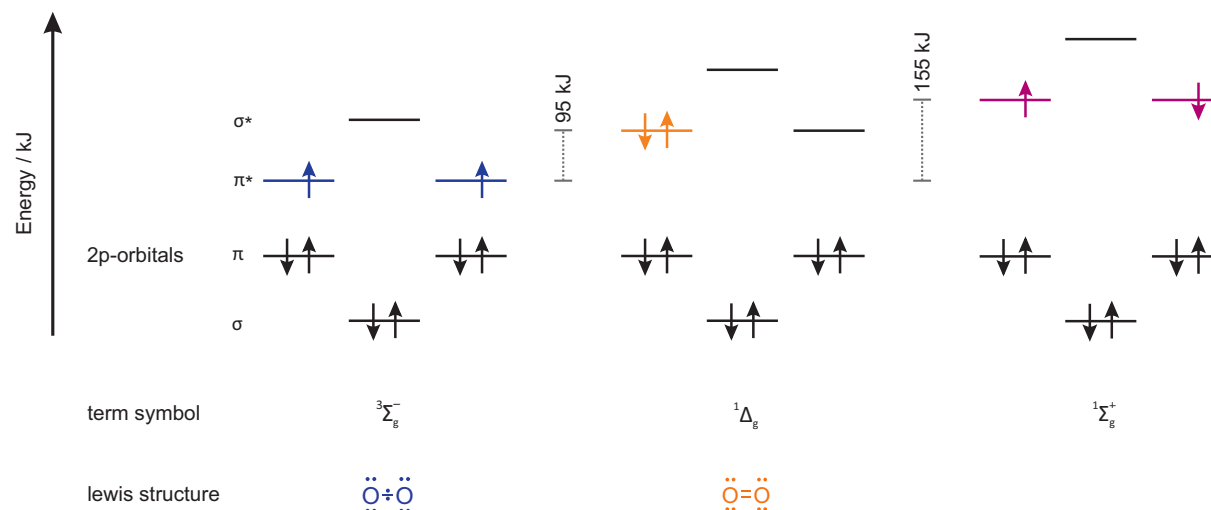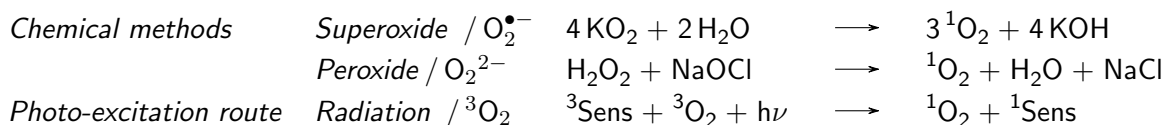
Figure 2.1: Electronic structures, term symbols and Lewis structures of molecular oxygen ($^3\Sigma_g{}^-$, triplet state) and its two lowest excited states ($^1\Delta_g$ and $^1\Sigma_g{}^+$, singlet states). Figure adapted from Holleman *et al.*[82]

$^3\Sigma_g{}^-$ state is spin forbidden, thus the $^1\Sigma_g{}^+$ species is a relatively long-lived species. The transition from $^1\Sigma_g{}^+$ to the $^1\Delta_g$ is short-lived due to the a spin-allowed transition.[84] The different stabilities of these two excited states is exemplified by their radiative lifetime of $^1\Delta_g$ and $^1\Sigma_g{}^+$, which are 45 min and 7 - 12 s in the gas phase respectively, and 10^{-6} - 10^{-3} s and 10^{-11} - 10^{-9} s in solution.[84] In addition, the lifetime of singlet oxygen is highly solvent-dependent and increases significantly in deuterated solvents compared to their protonated analogoues.[65, 85, 79, 86] As a result of this short lifetime, singlet oxygen ($^1\Sigma_g{}^+$) contributes only little to the chemistry of molecular oxygen except by virtue of its ability to decay to $^1\Delta_g$ (spin-allowed singlet-singlet transition).[65] The relatively low excitation energy and sufficiently long lifetime allow $^1\Delta_g$ to contribute to the overall chemistry of molecular oxygen. Hereafter $^1\Delta_g$ will be referred to as singlet oxygen and depicted as $^1O_2$.

2.1.1 Generation of singlet oxygen

Singlet oxygens generation is implementable *via* various different routes based either on chemical reactions involving superoxide and peroxide or photo-chemical reactions involving molecular oxygen, a photo-sensitizer and radiation; some examples are itemized hereafter.[87, 82, 88, 89] Generation of singlet oxygen by electrical discharges is a non suitable method for synthetic chemistry.[90]

Chemical methods	*Superoxide* / $O_2^{\bullet-}$	$4\,KO_2 + 2\,H_2O$	$\longrightarrow$	$3\,^1O_2 + 4\,KOH$
	Peroxide / O_2^{2-}	$H_2O_2 + NaOCl$	$\longrightarrow$	$^1O_2 + H_2O + NaCl$
Photo-excitation route	*Radiation* / $^3O_2$	$^3Sens + {}^3O_2 + h\nu$	$\longrightarrow$	$^1O_2 + {}^1Sens$

It should be highlighted that singlet oxygen cannot be generated directly from its triplet state.[65] The unpaired electrons tend either to stay unpaired or to pair with an electron of the other reactant to form a new bond. If the other reactant does not possess an unpaired electron, the product will also be a triplet.[86] To maintain spin conversion during the reaction, molecular oxygen must either react with another molecule with unpaired electrons or produce a triplet-state compound.[79] The triplet character of ground state molecular oxygen also reduces its rate of reaction. Therefore, there is a need to activate ground state molecular oxygen for reaction, as transitions between different multiplicities are forbidden, in this specific case triplet-singlet transitions. Triplet oxygen does not react like a normal double bond, it exhibits pronounced diradical character. This is another important factor in the low reactivity of molecular oxygen which is extremely beneficial to life.

Photo-sensitized singlet oxygen generation

Photo-sensitized generation of singlet oxygen is a simple, controllable and efficient method requiring only ground state triplet oxygen, radiation and a photo-sensitizer.[91] In general photo-sensitization is the process of transferring the energy of absorbed radiation from a photo-sensitizer to a substrate.[89] The photo-sensitization process of a photo-sensitizer and $^3O_2$ as substrate is illustrated in a simplified *Jablonski* diagram in Figure 2.2.[84]
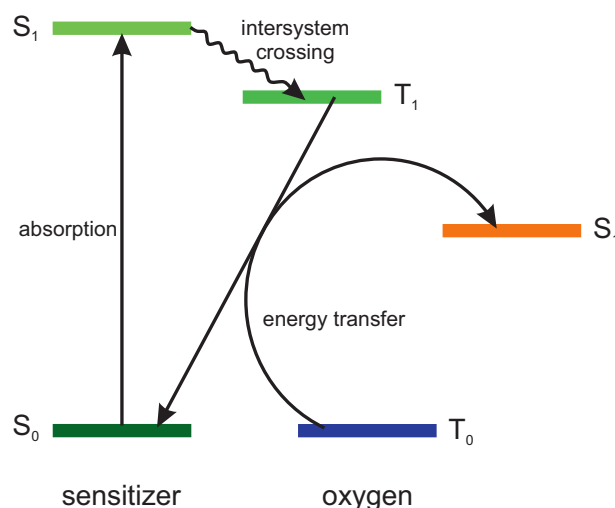
Figure 2.2: Energy chart of a photo-sensitization process using a photo-sensitizer and $^3O_2$ as substrate. The Figure was adapted from Crutchley *et al.*[84]

The process is initiated by the excitation of the photo-sensitizer from its ground state S_0, in general *via* a one-photon transition ($h\nu$), to its singlet excited state S_n. Non-radiative relaxation of S_n yields the lowest excited singlet state of the photo-sensitizer S_1.[84] Intersystem crossing (ISC) from S_1 generates the photo-sensitizers triplet state T_1. The photo-sensitizers T_1 state reacts further *via*

an energy transfer process during collision of the excited photo-sensitizer with the triplet state of molecular oxygen T_0, to generate singlet oxygen S_1. There is a wide scope of molecules that have the ability to generate singlet oxygen *via* UV-Vis light absorbtion. Common photo-sensitizers are organic dyes like *Rose Bengal*, *Eosin Blue*, *Methylene Blue* and macrocyclic compounds as porphyrins and phthalocyanines (see Figure 2.3).[91, 84]
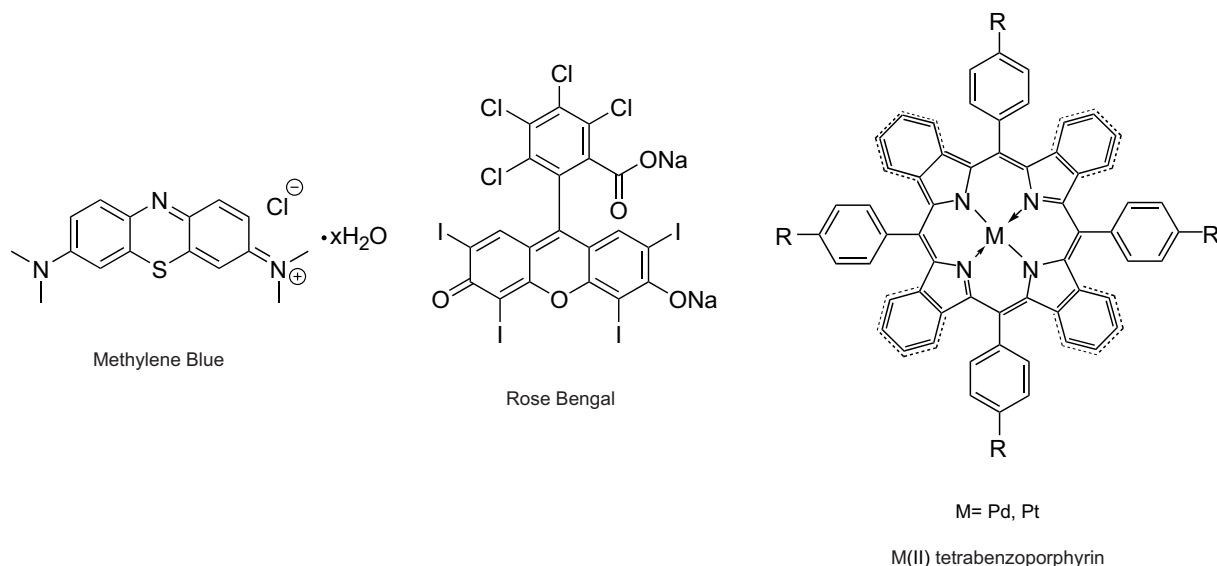
Figure 2.3: Common organic photo-sensitizers: *Methylene Blue* (3,7-bis(dimethylamino)phenazathionium chloride) exhibits strong absorbance in the range of 550 - 700 nm (left), and *Rose Bengal* (4,5,6,7-tetrachloro-2,4,5,7-tetraiodofluorescein disodium salt) exhibits strong absorbance in the range of 480 - 550 nm (right). M(II) tetrabenzoporphyrin derivatives are amongst others excellent photo-sensitizers. The dashed line represents the structural variety of tetrabenzoporphyrins.

A theoretically optimal photo-sensitizer should posses the following features: (1) high absorption coefficient in the spectral region of the excitation light (ϵ), (2) a triplet state of appropriate energy ($E_T \geq 95\,$kJ$\cdot$mol^{-1}) to allow for efficient energy transfer to ground state oxygen, (3) high quantum yield of the triplet state ($\Phi_T > 0.4$), (4) long triplet state lifetimes ($\tau > 1\,$s) and (5) high photo-stability.[84] The efficiency of a photo-sensitizer is significantly dependent on the photo-physical properties of its lowest excited triplet state.

2.1.2 Quenching of singlet oxygen

Once molecular oxygen is in its excited singlet state, it can be deactivated by other species to return to its ground state. This process, referred to as quenching of singlet oxygen, can take place *via* physical quenching or chemical quenching according to the reactions summarized below.[86] Deactivation *via*

physical quenching leads only to deactivation of singlet oxygen *via* the interaction of a so called quencher (Q): no oxygen consumption or product formation occurs. Whereby *chemical quenching* with a trap (T) leads to the formation of a product (T-O$_2$).[79, 85]

$$\textit{Physical Quenching} \quad {}^1O_2 + Q \quad \longrightarrow \quad {}^3O_2 + Q$$
$$\textit{Chemical Quenching} \quad {}^1O_2 + T \quad \longrightarrow \quad \text{T-O}_2$$
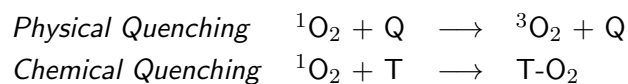
Physical singlet oxygen quenchers

There are many substances that have the ability to quench singlet oxygen *e.g.*, aromatic hydrocarbons, carotenoides, metal-organic compounds, azides, and amines.[92, 93, 94, 95, 96, 97] The tertiary amine 1,4–diazabicyclo[2.2.2]octane (DABCO) is one of the most studied quenchers.[98] Quenching is supposed to occur *via* the formation of an exciplex [${}^1O_2\cdots$Q]‡ followed by competing reactions involving energy transfer (ET), charge transfer (CT) or a chemical reaction.[98]

Chemical quenching and organic reactions of singlet oxygen

In comparison with ground state oxygen, which commonly reacts in chain reactions, reactions of singlet oxygen tend to terminate after oxidation of a reactant, a so-called singlet oxygen trap.[65, 84] Usually it forms products that contain both atoms of oxygen as T-O$_2$. The highly reactive singlet oxygen can react with unsaturated substrates in [4+2]-, [2+2]- or ene-mode.[91] The most common reactions with olefins are endoperoxide forming and allylic-hydroperoxide reactions illustrated in Figure 2.4.
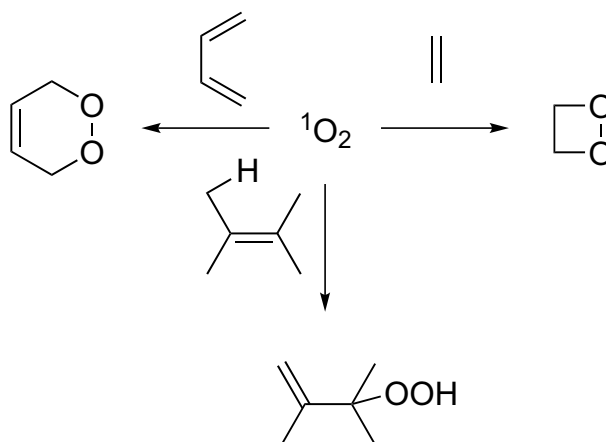

Figure 2.4: Reactions of singlet oxygen with unsaturated substrates in [4+2]-, [2+2]- or ene-mode. The Figure was adapted from Iesce *et al.*[91]

2.1.3   Detection of singlet oxygen

As a result of its chemical and physical properties singlet oxygen can be directly and indirectly detected by various methods involving (I) the detection of the $^1\Delta_g \rightarrow {}^3\Sigma_g^-$ phosphorescence in a time resolved and steady state experiments, (II) use of luminescent probes specific for singlet oxygen, and (III) adding molecules known to specifically quench singlet oxygen.[79]

Direct detection of singlet oxygen's transition into its ground state is the most definitive proof of the presence of singlet oxygen.[79] This transition of one mole singlet oxygen referred to as monomol-emission is accompanied by phosphorescence of a distinct and narrow band at $\sim$1270 nm.[99, 78, 100] The biggest drawback of this method is that it suffers from weak phosphorescence signals. Although this NIR-phosphorescence is very weak, spectral interference from other species in a multicomponent system can be excluded as they usually occur at wavelengths shorter than $\sim$1000 nm.[79] In addition, the quantitative detection of very small amounts of singlet oxygen is currently not possible in any medium.[86] There is an approach which is capable to compensate this. It relies on the introduction of fluorescent probes, which are either non-fluorescent molecules that become fluorescent after reaction with singlet oxygen ('off-on'-system) or fluorescent molecules that exhibit a change *e.g.,* a strong decrease in their fluorescence intensity ('on-off'-system) after reaction with singlet oxygen.[101] Thus the method is ideal for quantitative investigations in aqueous and biological media. Another indirect method to detect singlet oxygen is implemented by adding singlet oxygen quenchers to a given system.[102] The lifetime of singlet oxygen is then shortened in comparison to the system without a quencher. The effect can subsequently be monitored using an independent probe, *e.g.,* cell death. A set of appropriate control experiments has to be performed as the quencher may also trigger side reactions, influence other reaction intermediates, be toxic or penetrate through the cell membrane. In *Chapter 2* we describe our efforts to detect $^1O_2$ in non-aqueous battery chemistries. First, novel fluorescent probes are described in *Section 3.1* followed by the use of substituted anthracenes in *Section 3.2*.

Chapter 3

Singlet Oxygen Sensing

Fluorescent probes for singlet oxygen detection have been shown to be excellent tools in biological media due to their high sensitivity and simplicity in data collection.[79, 101] Nagano *et al.* synthesized 9-[2-(3-carboxy-9,10-diphenyl)anthryl]-6-hydroxy-3H-xanthen-3-ones (DPAX), the first chemical $^1O_2$ trap that allowed fluorescence detection, illustrated in Figure 3.1.[103] DPAX is based on the successful two-component paradigm in which a $^1O_2$ trapping moiety (a substituted anthracene) is coupled to a light-emitting chromophore (a fluorescein derivative). The specific reaction of $^1O_2$ with the scarcely fluorescent DPAX is relatively fast, highly selective and leads to a stable and strongly fluorescent endoperoxide adduct (DPAX-O_2). Before the reaction with $^1O_2$, emission from the chromophore is quenched by photo-induced electron transfer (PET, fluorescence quenching mechanism) by the trapping moiety; the pristine probe is in its "off" position.[104, 105] Upon reaction with $^1O_2$ to DPAX-O_2, the anthracene moiety is no longer an efficient intramolecular electron donor leading to light emission from the fluorescein moiety; a fluorescent switch occurs modifying the probe into its "on" modus. Incorporation of electron-withdrawing groups (*e.g.*, $X = Cl, F$) at position 2 and 7 of the xanthene chromophore stabilizes the DPAX's fluorescence intensity, as it is known to be decreased under acidic conditions in fluorescein derivatives, as this modification lowers the pK_a value of the phenolic oxygen atom of the xanthene chromophore. With the aim to improve the already existing fluorescent probe DPAX, in terms of sensibility and reaction rate, the anthracene scaffold was tuned at position 9 and 10 by incorporation of methyl groups instead of bulky phenyl groups, yielding in 9-[2-(3-carboxy-9,10-dimethyl)anthryl]-6-hydroxy-3H-xanthen-3-ones (DMAX).[106] Figure 3.1 shows the reaction of *quasi* non-fluorescent 9-[2-(3-carboxy-9,10-dimethyl)anthryl]-6-hydroxy-3H-xanthen-3-ones (DMAX) with $^1O_2$ to produce highly fluorescent DMAX-O_2. DMAX reacts with $^1O_2$ more rapidly and its sensitivity is around 53-fold higher than DPAX's.[104] Experiments towards DPAX and DMAX cross-reactivity
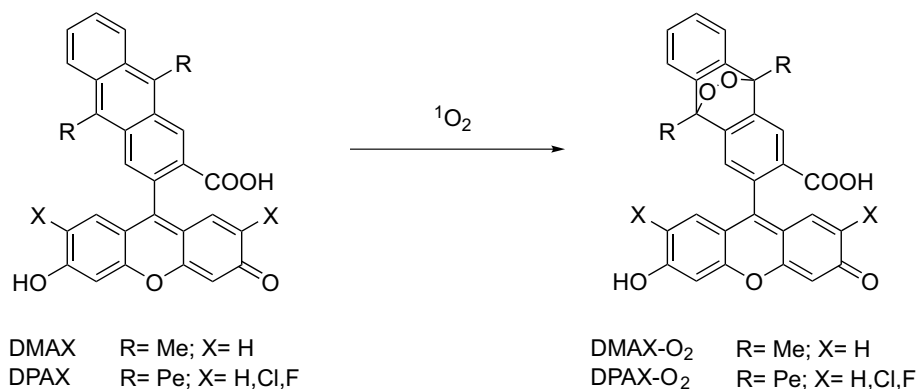
DMAX   R= Me; X= H   DMAX-O$_2$ R= Me; X= H
DPAX   R= Pe; X= H,Cl,F   DPAX-O$_2$ R= Pe; X= H,Cl,F

Figure 3.1: The specific reaction of ^{1}O$_2$ with the scarcely fluorescent DPAX leads to strongly fluorescent DPAX-O$_2$. PET takes place from the fluorescein moiety to the disubstituted anthracene moiety, which causes fluorescence quenching of the latter. When the conjugated π-system of the anthracene moiety is interrupted by an endoperoxide bridge, electron transfer is hindered and a very large enhancement of fluorescence is observed. Upon excitation of the fluorophore, an electron of the highest occupied molecular orbital (HOMO) is promoted to the lowest unoccupied molecular orbital (LUMO), which enables PET from the HOMO of the donor (anthracene moiety) to that of the fluorophore, causing fluorescence quenching of the latter. Upon formation of an endoperoxide, the potential of the donor is raised so that the relevant HOMO becomes lower in energy than that of the fluorphore. Consequently PET is not longer possible and fluorescence quenching is suppressed.[104, 105] The Figure was adapted from Nagano *et al.*[103, 106]

with other reactive oxygen species like superoxide did not lead to any change in fluorescence intensity, which corroborates the specificity of this probes for ^{1}O$_2$.[101] As another highly selective and sensitive probe for singlet oxygen, 4,5-Dimethylthio-4-[2-(9-anthryloxy)ethylthio]tetrathiafulvalene (fulvalene*) has been reported by Zhu *et al.* illustrated in Figure 3.2, where the electron-rich tetrathiafulvalene unit is incorporated into a reactive fluorophore of anthracene.[107] Strong luminescence has been observed of the fulvalene probe upon reaction with ^{1}O$_2$. The presence of other ROS like superoxide did not yield in a reaction. 9,10-dimethylanthracene (DMA) and 9,10-diphenylanthracene (DPA) are
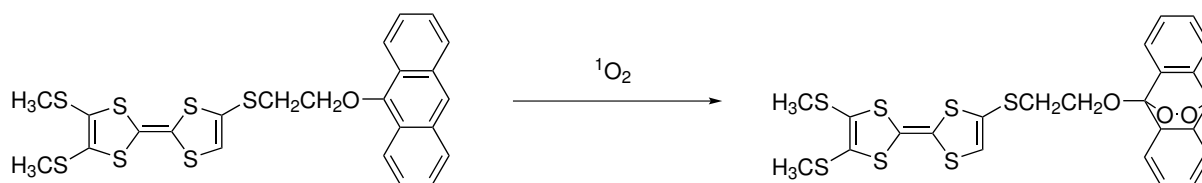
Figure 3.2: Reaction of 4,5-Dimethylthio-4-[2-(9-anthryloxy)ethylthio]tetrathiafulvalene with singlet oxygen forming its endoperoxide. The Figure was adapted from Zhu *et al.*[107]

the most widely used chemical ^{1}O$_2$ traps.[108, 109, 110, 111] They are fluorescent compounds that react specifically with ^{1}O$_2$ to form non-fluorescent endoperoxides DMA-O$_2$ or DPA-O$_2$. The decrease of fluorescence and absorbance of DMA and DPA by the generation of a non-fluorescent endoperoxide can be monitored. *Table* 3.1 summarizes depicted fluorescent ^{1}O$_2$ probes, their photo-physical properties such as excitation/emission wavelengths and the observed ^{1}O$_2$ induced fluorescence changes.

Table 3.1: Photophysical properties and fluorescence change of various fluorescent probes used for indirect $^1O_2$ detection. The Table was adapted from Lima *et al.*[101]

Probe	$\lambda_{exc}/\lambda_{em}[nm]$	$^1O_2$ Induced Fluorescence Changes
DMA	375/436	Fluorescence decrease by generation of non-fluorescent endoperoxide
DMAX	495/515	Production of a fluorescent endoperoxide
DPAX	495/515	Production of a fluorescent endoperoxide
Fulvalene*	370/420	Production of a fluorescent endoperoxide

3.1 New Optical Singlet Oxygen Probes

To incorporate an optical singlet oxygen probe into an electrolyte to detect singlet oxygen during cycling of a Li-O$_2$ battery, the following conditions have to be fulfilled: (1) chemical reaction with singlet oxygen should result in formation of a stable endoperoxide, (2) the probe should be electrochemically stable in the crucial potential range between 2 - 4.5 V *vs.* Li/Li$^+$, (3) the probe should be chemically stable towards superoxide and peroxide, and (4) should be highly soluble in the used electrolytes. Synthesis of optical singlet oxygen probes according to Nagano *et al.* would be a laborious and time consuming procedure as it involves up to 8 synthesis steps. In that sense as a key requirement, electrochemical stability of fluorescent probes has to be investigated first and foremost. Whether probes like DMAX or DPAX would be suitable as an additive in an electrolyte for *in-situ*, indirect detection of singlet oxygen during cycling of a Li-O$_2$ battery, can be estimated by breaking the structure of DMAX and DPAX down to its individual moieties. We compiled a set of fluorescent moieties, suitable for synthesis of a probe consisting of a fluorophore and a singlet oxygen trapping unit (like DMA or DPA) and thus suitable for a fluorescent switch. Cyclic voltammetry measurements were performed under anoxic conditions with several common fluorescent backbones, among them Rhodamin 6G, 2,7-dichlorofluorescein and a modified diketo-pyrollo-pyrolle dye (mDPP) in an electrolyte containing 50 mM TBA$^+$ClO$_4$$^-$ in DCM or MeCN using a Au-pseudo electrode at a scan rate of 100 mV·s^{-1}. The cyclic voltammograms of the fluorescent backbones and their chemical structures are plotted in Figure 3.3, 3.4 and 3.5. All backbones are redox active, to some extent for reduction and/or oxidation in the studied potential range. The electrochemical stability window of mDPP corresponds best with the relevant potential range of 2.5 - 4.2 V *vs.* Li/Li$^+$ and this chromophore was thus used further for the synthesis of new optical singlet oxygen probes.
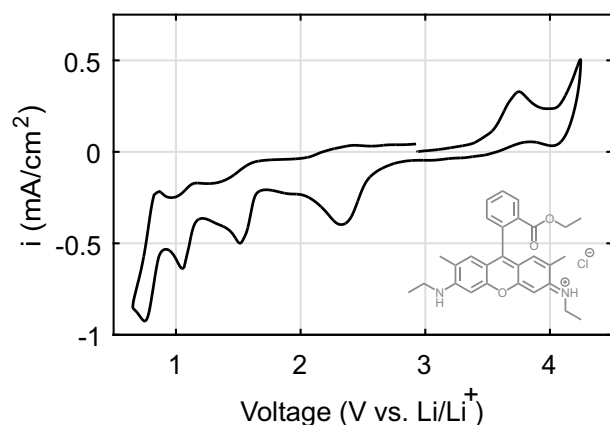
Figure 3.3: Chemical structure and cyclic voltammogram of $2\,\text{mM}$ Rhodamin 6G in $50\,\text{mM}$ $\text{TBA}^+\text{ClO}_4^-$ in MeCN, in Ar-atmosphere at a $3\,\text{mm}$ Au pseudo disc electrode recorded with a scan rate of $100\,\text{mV}\cdot\text{s}^{-1}$.
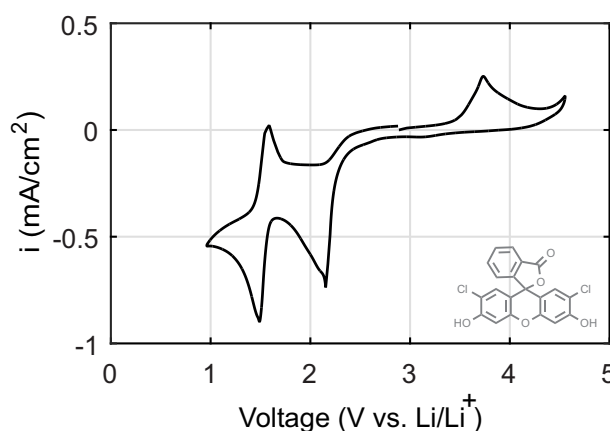
Figure 3.4: Chemical structure and cyclic voltammogram of $2\,\text{mM}$ 2,7-dichlorofluorescein in $50\,\text{mM}$ $\text{TBA}^+\text{ClO}_4^-$ in CHCl_3, in Ar-atmosphere at a $3\,\text{mm}$ Au pseudo disc electrode recorded with a scan rate of $100\,\text{mV}\cdot\text{s}^{-1}$.
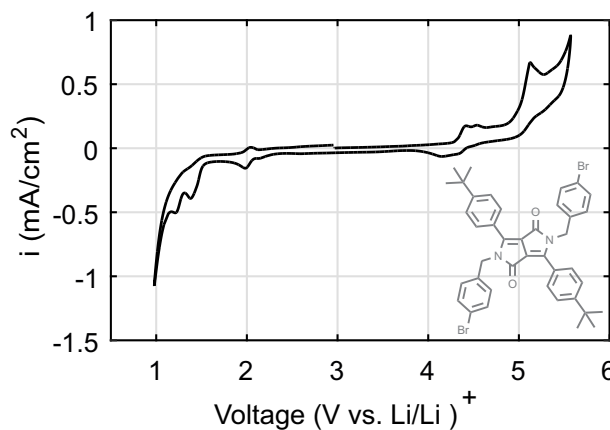
Figure 3.5: Chemical structure and cyclic voltammogram of $2\,\text{mM}$ of an alkylated diketo-pyrrolo-pyrolle dye in $50\,\text{mM}$ $\text{TBA}^+\text{ClO}_4^-$ in CHCl_3, in Ar-atmosphere at a $3\,\text{mm}$ Au pseudo disc electrode recorded with a scan rate of $100\,\text{mV}\cdot\text{s}^{-1}$.

3.1.1   Synthesis of new optical singlet oxygen probes

In the following subsection three design strategies for new optical singlet oxygen probes are elucidated. Attempts to synthesize new optical singlet oxygen probes were conveniently prepared in an one step alkylation reaction and cross-coupling reactions originating from different fluorescent backbones and different singlet oxygen trapping moieties based on anthracene derivatives.

2,5-bis(anthracen-9-ylmethyl)-3,6-bis(4-(tert-butyl)phenyl)-2,5-dihydropyrrolo[3,4-c]pyrrole-1,4-dione

496 μmol potassium *tert*-butoxide and 184 μmol of modified pigment orange 73 were dissolved in 6 mL anhydrous DMF at 60 °C. 500 μmol 9-(chloromethyl)anthracene was added dropwise and the mixture was stirred for 3 h at 80 °C. The product was precipitated in MeOH:H_2O (5:1, v:v) and centrifuged. The obtained precipitate was washed, centrifuged and dried under reduced pressure at 60 °C. The product was dissolved in 5 mL DCM and washed with 10 mL deionized water three times. The organic phase was dried over anhydrous sodium sulfate, filtered and concentrated under reduced pressure. The crude product was purified *via* column chromatography on silica gel using CH:DCM (1:1, v:v) and DCM:THF (98:2, v:v). The products were washed with 3M™ NOVOTEC™ 7200 and dried under reduced pressure. See reaction scheme in Figure 3.6.

Figure 3.6: Alkylation reaction of 2-(anthracen-9-ylmethyl)-3,6-bis(4-(tert-butyl)phenyl)-2,5-dihydropyrrolo[3,4-c]pyrrole-1,4-dione (mono-alkylated, R = H) and 2,5-bis(anthracen-9-ylmethyl)-3,6-bis(4-(tert-butyl)phenyl)-2,5-dihydropyrrolo[3,4-c]pyrrole-1,4-dione (di-alkylated, R = anthracene moiety).

3,6-bis(4-(tert-butyl)phenyl)-2,5-bis(4-(10-phenylanthracen-9-yl)benzyl)-2,5-dihydropyrrolo[3,4-c]pyrrole-1,4-dione

22 μmol 2,5-bis(4-bromobenzyl)-3,6-bis(4-(*tert*-butyl)phenyl)-2,5-dihydropyrrolo[3,4-c]pyrrole-1,4-di one and 88 μmol 10-phenyl-9-anthraceneboronic acid were dissolved in 5 mL toluene at 40 °C. 228 μmol K_2CO_3 dissolved in 1.3 mL deionized H_2O and 4.1 μmol 1,1'-bis(diphenylphosphino)ferrocenedichlorpalladium (II) were added to the mixture and stirred for 12 h at 90 °C. The mixture was dried over anhydrous sodium sulfate. The crude product was purified *via* column chromatography on silica gel using CH:DCM (1:1, v:v) and DCM:THF (98:2, v:v). The products were washed with 3M™ NOVOTEC™ 7200 and dried under reduced pressure. See reaction scheme in Figure 3.7.
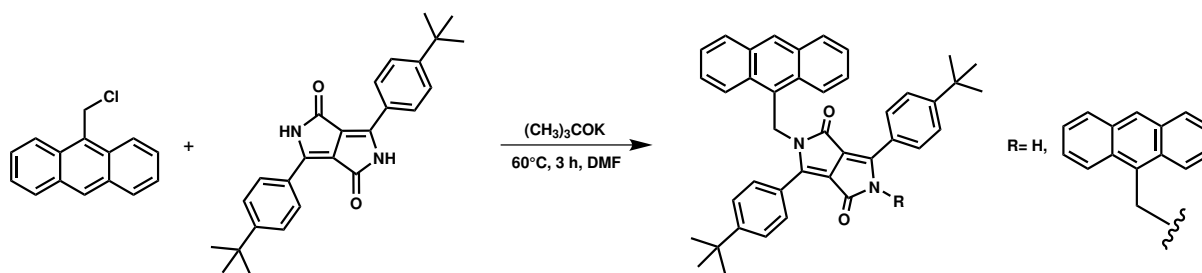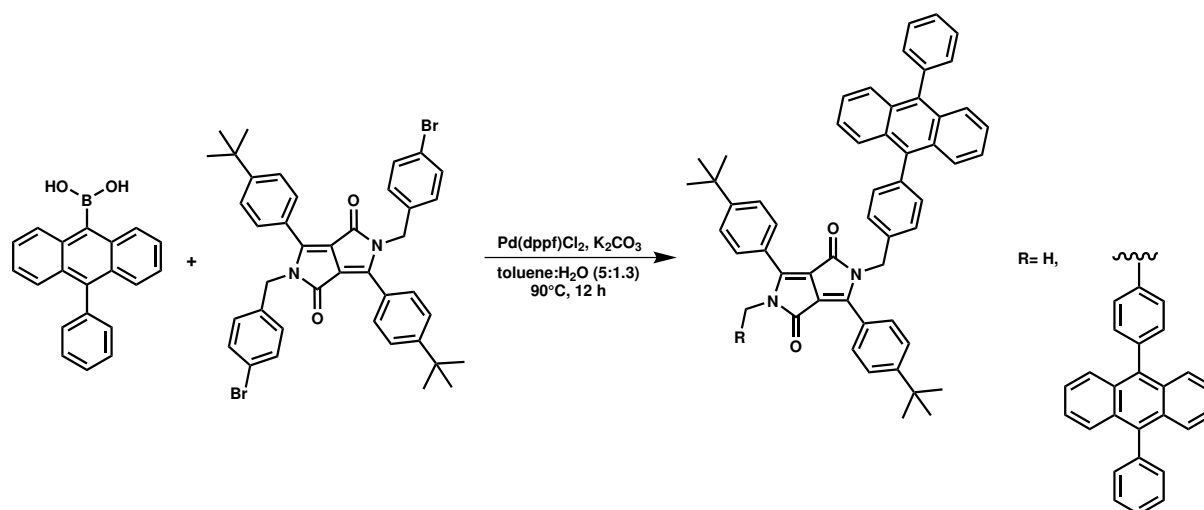
Figure 3.7: Suzuki cross-coupling reaction of 3,6-bis(4-(tert-butyl)phenyl)-2-methyl-5-(4-(10-phenylanthracen-9-yl)benzyl)-2,5-dihydropyrrolo[3,4-c]pyrrole-1,4-dione (mono-alkylated product, R = H) and 3,6-bis(4-(tert-butyl)phenyl)-2,5-bis(4-(10-phenylanthracen-9-yl)benzyl)-2,5-dihydropyrrolo[3,4-c]pyrrole-1,4-dione (di-alkylated product, R = anthracene moiety).

4,7-bis-(4-(10-phenylanthracen-9-yl)phenyl)benzo[c][1,2,5]thiadiazole

80 μmol 9-4-Bromophenyl-10-phenylanthracene, 40 μmol 2,1,3-benzothiadiazole-4,7-bis-boronic-acid-pinacol-ester and 200 μmol K_2CO_3 were dissolved in 2.5 mL toluene at 45 °C. 1.7 μmol tetrakis(triphenylphosphine)palladium (0) was added and the mixture was stirred for 12 h at 90 °C. The mixture was dried over anhydrous sodium sulfate. The crude product was purified *via* column chromatography on silica gel using a gradient from toluene to toluene:DCM (1:1, v:v) and washed with cyclohexane. The products were washed with 3M™ NOVOTEC™ 7200 and dried under reduced pressure. See reaction sceme in Figure 3.8. ^{1}H NMR and MALDI-MS indicate that the isolated fraction contained small quantities of the mono-substituted product, which were however insufficient quantities to obtain pure spectra.

3.1.2 Reactivity of new optical probes towards singlet oxygen

The ability of probes to trap singlet oxygen was studied *via* absorption and fluorescence spectroscopy, and by analyzing the formed product. Therefore, singlet oxygen was *in-situ* generated in the presence of the synthesized traps. First attempts were made *via* chemical generation of singlet oxygen directly from peroxide and superoxide oxidation as elucidated in *Chapter 1*. Chemical routes comprise educts with moderate oxidizing hazard: hydrogen peroxide, sodium hypochloride and potassium superoxide are potent oxidizers. Therefore, scrupulous handling with these educts and side products is required.
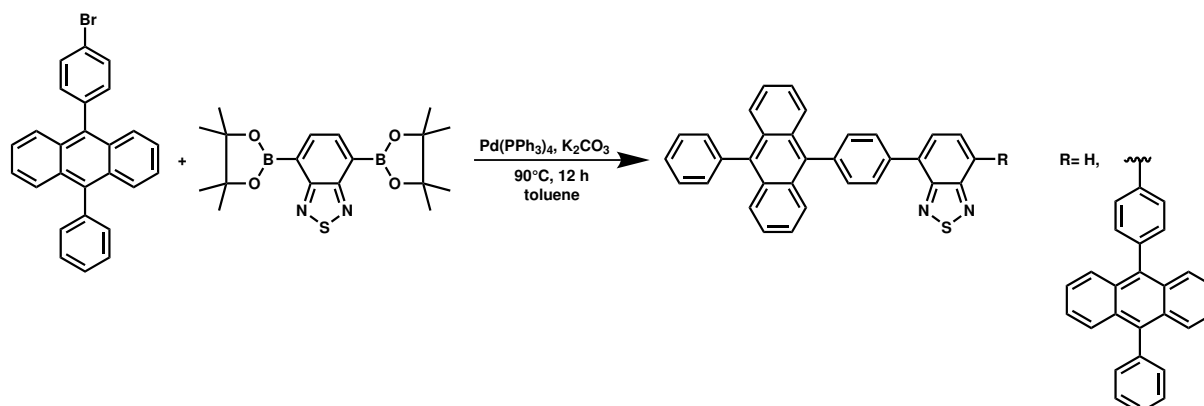
Figure 3.8: Suzuki cross-coupling of 4-(4-(10-phenylanthracen-9-yl)phenyl)benzo[c][1,2,5]thiadiazole (mono-alkylated product, R = H) and 4,7-bis(4-(10-phenylanthracen-9-yl)phenyl)benzo[c][1,2,5]thiadiazole (di-alkylated product, R = anthracene moiety).

In addition, hydrogen peroxide is thermodynamically unstable and may decompose in a side reaction to form water and triplet oxygen. For safety reasons, side product formation and adequate conversion rates, experiments involving singlet oxygen formation were performed *via* photo-sensitization which is a simple, controllable and efficient method. Combining singlet oxygen generation and trapping in 'one-pot' can be done *via* a so-called photooxygenation reaction. In general, a photooxygenation reaction is referred to as a process which combines a substrate, radiation and molecular oxygen in presence of a photo-sensitizer.[112] Once excited a photo-sensitizer can follow two different deactivation pathways: the electronically excited photo-sensitizer can activate the substrate by energy or hydrogen transfer which in turn reacts with molecular oxygen (type I) or activates the molecular oxygen to its excited singlet state, which then reacts with the substrate (type II).[91] Type II reactions are promoted in presence of dyes, with radiation of the sun's spectrum (UV, VIS and IR), in halogenated or deuterated solvents and at low temperatures. In presence of unsaturated substrates, such as anthracene derivates singlet oxygen can react in a [4+2] cycloaddition Diels-Alder type reaction as illustrated in Figure 2.4. A fluorinated palladium (II) tetrabenzoporphyrin complex, palladium (II) meso-tetra(4-fluorophenyl)tetrabenzoporphyrin (following abbreaviated as Pd_4F), was used as a photo-sensitizer as it comprises excellent properties in terms of its chemical-, thermal- and photo-stability.[113, 114] Figure 3.9 shows the absorption spectrum of Pd_4F exhibiting a narrow absorption band in the red part of the spectrum at 629 nm.

Photooxygenation experiments were performed in a continously stirred oxygen saturated solution containing the new optical singlet oxygen traps in the μM range and 1 nmol Pd_4F in a hermetically sealed cuvette with 10 mm lightpath. The photo-sensitizer was irradiated with a red LED light source
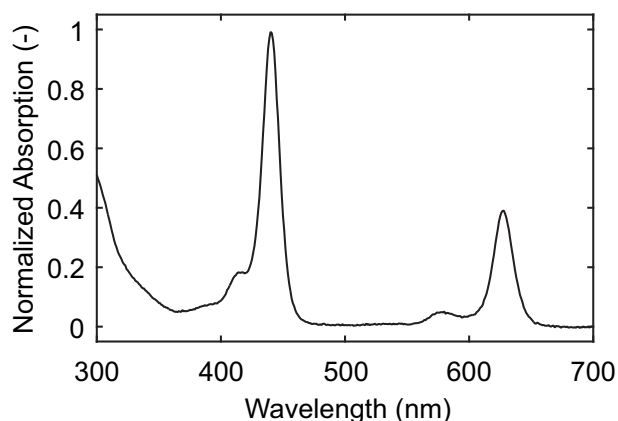
Figure 3.9: Absorption spectrum of the photo-sensitizer palladium (II) meso-tetra(4-fluorophenyl)tetrabenzoporphyrin, Pd_4F in toluene. Pd_4F features characteristic absorption with a very intense Soret-band at $\lambda_{abs,\,max,\,S}$ at 443 nm ($\epsilon = 268000\,M^{-1}\,cm^{-1}$) and Q-band at $\lambda_{abs,\,max,\,Q}$ at 629 nm ($\epsilon = 115000\,M^{-1}\,cm^{-1}$) due to the porphyrin macrocycle. The absorbance is dimensionless, thus there is no unit.[113, 114]

(OSRAM Oslon SSL 80, 634 nm, 7 W) and the reaction process was controlled *via* absorption and fluorescence spectroscopy over time. This method was also used to synthesise reference substances of the product of singlet oxygen with the trap ($T\text{-}O_2$). Over the course of photooxygenation reactions consumption of the photo-sensitizer *via* photobleaching was not observed due to its excellent photo-stability.[113]

2,5-bis(anthracen-9-ylmethyl)-3,6-bis(4-(tert-butyl)phenyl)-2,5-dihydropyrrolo[3,4-c]pyrrole-1,4-dione: Two products, mono- and di-alkyalted probe (in the following referred to as *mono-Probe-I* and *di-Probe-I*), have been isolated and identified from the alkylation reaction (see Figure 3.6). Figure 3.10 and 3.11 show the spectral properties of the isolated products over the course of the photooxygenation reaction in a timeframe of 10 min. The absorption maxima at 443 nm and 629 nm stem from the used photo-sensitizer Pd_4F (see and compare Figure 3.9). Characteristic absorption bands between 350 nm and 420 nm attribute to the anthracene moiety, linked to the fluorophore.[115] The pyrrolo-pyrrole backbone absorbs from 470 nm to 550 nm (broad shoulder) which is more pronounced in di-Probe-I. The fluorescence emission spectra are illustrated in Figure 3.11: *mono-Probe-I* exhibits twice the fluorescence intensity ($\lambda_{max} = 525$ nm and a pronounced shoulder at 560 nm) as *di-Probe-I* ($\lambda_{max} = 529$ nm and a pronounced shoulder at 570 nm). The photooxygenation reaction of $^1O_2$ with the probes lead neither to a decrease in absorption at the anthracene maxima, nor to an increase in fluorescence intensity; only a non significant decrease was observed. Despite the fact that the synthesis led to the proposed products, the probes did not possess the ability to trap singlet oxygen. Therefore, non of the products was further used as a fluorescent singlet oxygen probe.
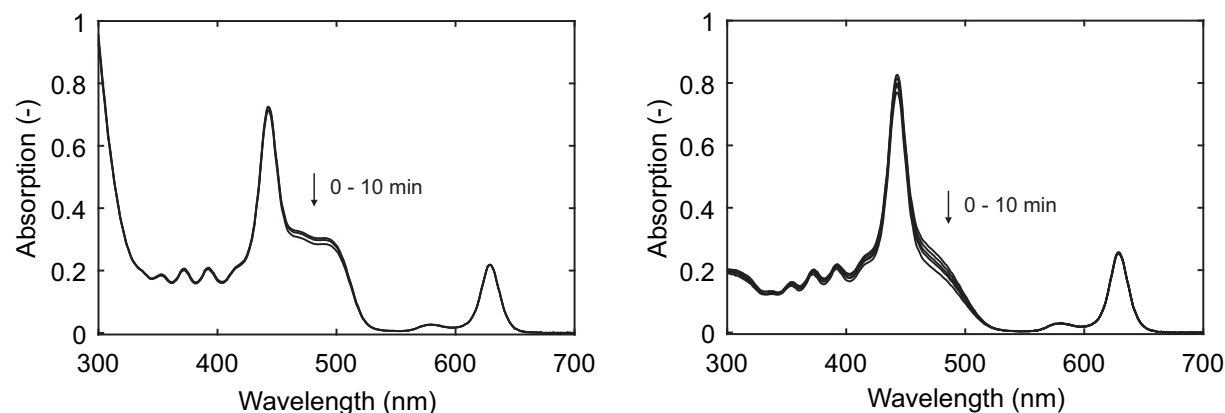
Figure 3.10: Absorption spectra of 2-(anthracen-9-ylmethyl)-3,6-bis(4-(tert-butyl)phenyl)-2,5-dihydropyrrolo[3,4-c]pyrrole-1,4-dione (mono-Probe-I, left) and 2,5-bis(anthracen-9-ylmethyl)-3,6-bis(4-(tert-butyl)phenyl)-2,5-dihydropyrrolo[3,4-c]pyrrole-1,4-dione (di-Probe-I, right) over the course of the photooxygenation reactions of 10 min.
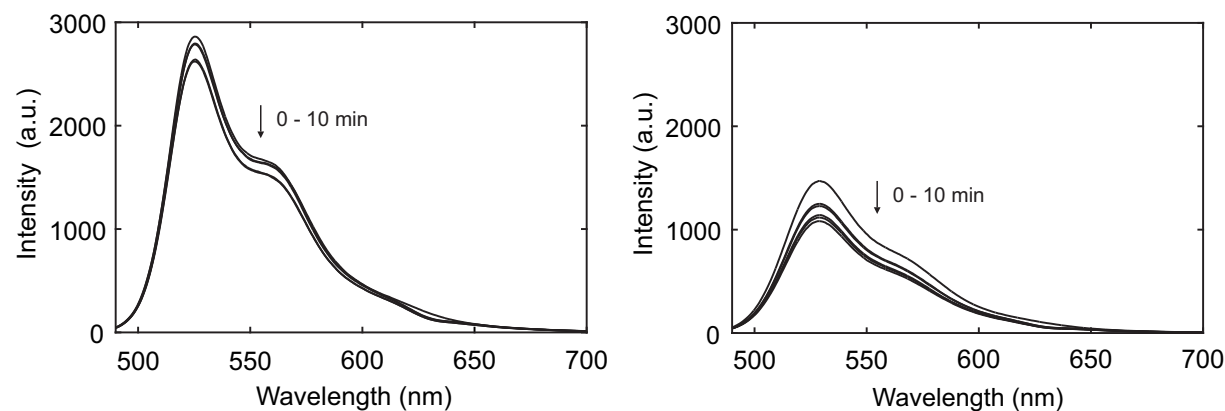
Figure 3.11: Fluorescence emission spectra of 2-(anthracen-9-ylmethyl)-3,6-bis(4-(tert-butyl)phenyl)-2,5-dihydropyrrolo[3,4-c]pyrrole-1,4-dione (mono-Probe-I, left) and 2,5-bis(anthracen-9-ylmethyl)-3,6-bis(4-(tert-butyl)phenyl)-2,5-dihydropyrrolo[3,4-c]pyrrole-1,4-dione (di-Probe-I, right) over the course of the photooxygenation reactions of 10 min.

3,6-bis(4-(tert-butyl)phenyl)-2,5-bis(4-(10-phenylanthracen-9-yl)benzyl)-2,5-dihydropyrrolo[3,4-c]pyrrole-1,4-dione: The previous approach to design a capable probe failed due to the low reactivity of the anthracene moiety in *mono-Probe-I* and *di-Probe-I* as both probes did not trap singlet oxygen. Owing to the lack of stereochemical features in the singlet oxygen molecule, the stereoselectivity is directed by the substrate: to overcome this obstacle the incoporation of a 9,10-diphenylanthracene moiety *via* a *Suzuki* cross-coupling reaction was performed to have a directing effect of the introduced phenyl groups to improve the probes selectivity to react with singlet oxygen, like in DPAX (see Figure 3.7).[112] The absorption spectra of the isolated dialkylated product (di-Probe-II) are illustrated in Figure 3.12, left. The initial spectrum do not differ significantly from the *mono-Probe-I* and *di-Probe-I* from the previous approach containing

anthracene as trapping unit, only the shoulder from 470 nm to 550 nm is more weakly pronounced. Over the course of the photooxygenation reaction the absorption spectra of the di-Probe-II changes, due to the formation of an endoperoxide expressed in the decrease of absorption of the specific maxima of the anthracene moiety. Unfortunately, hardly any change in the fluorescence intensity was observed (see Figure 3.12, right). Even though a decrease in absorption was observed, no significant change *e.g.*, increase, decrease, shift or shoulder in the fluorescence intensity and fluorescence spectra was observed. Therefore, it was not used as a fluorescent singlet oxygen probe for further experiments.
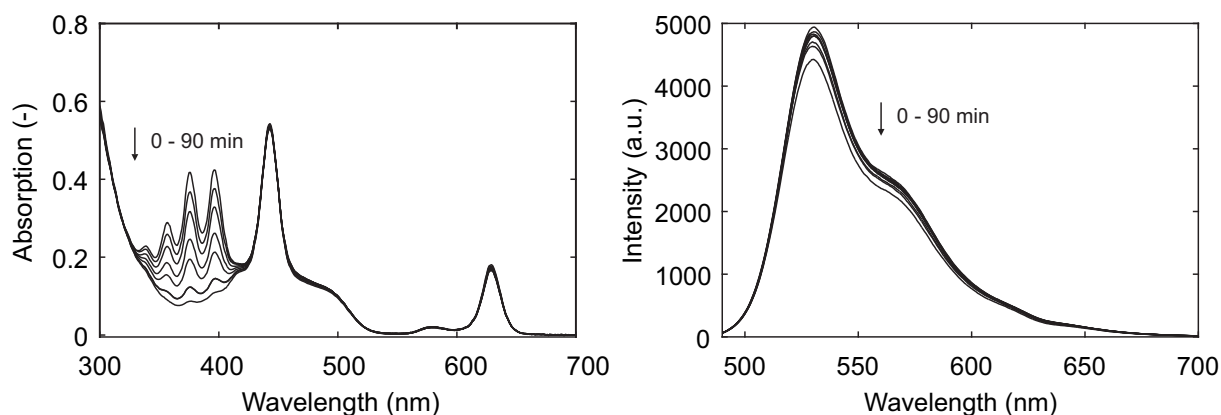
Figure 3.12: Absorption and fluorescence emission spectra of 3,6-bis(4-(tert-butyl)phenyl)-2-methyl-5-(4-(10-phenylanthracen-9-yl)benzyl)-2,5-dihydropyrrolo[3,4-c]pyrrole-1,4-dione (left and right) over the course of the photooxygenation reactions.

4,7-bis(4-(10-phenylanthracen-9-yl)phenyl)benzo[c][1,2,5]thiadiazole: A new approach to synthesise a novel fluorescent singlet oxygen probe *via* a *Suzuki*-cross coupling reaction (see Figure 3.8) was performed to obtain a probe with singlet oxygen trapping ability and at the same time being exhibiting a fluorescence switch. A 9,10-diphenylanthracene moiety was again used as a singlet oxygen trapping moiety which was linked to another fluorescent backbone, a thiadiazole derivative. Figure 3.13 shows the absorption spectra of the photooxygenation reactions of the *mono-Probe-III*: The pronounced absorbance maxima of 9,10-diphenylanthracenes in the region of 320 nm to 410 nm are dimiminshing over the course of photooxygenation. The absorption of the thiadiazole backbone remains constant in the region of 290 nm to 400 nm, which is overlapping with the anthracene absorbance. Concomitant with the decrease in absorbance due to the formation of a *mono-Probe-III* endoperoxide, a decrease of the fluorescence intensity at 490 nm occurred and a new shoulder appeared at 415 nm indicating a fluorescence switch system. The synthesis led to the proposed product,

as confirmed by ^{1}H NMR and MALDI. Reaction of *mono-Probe-III* with singlet oxygen led to a specific decrease in fluorescence intensity indicated by the decrease of the maximum of *mono-Probe-III* at 495 nm and a new shoulder at 415 nm caused by the formation of a fluorescent endoperoxide, *via* PET mechanism. An emission inner filter effect, so-called self-absorption, is observed in the emission spectra of *mono-Probe-III* which reduces the fluorescence intensity in our sample due to high concentration of *mono-Probe-III*.[104] Excitation and emission spectra of *mono-Probe-III* and its corresponding endoperoxide after complete conversion of the probe are illustrated in Figure 3.14. The excitation spectrum of *mono-Probe-III* exhibits strong absorbance bands between 350 nm and 400 nm, which disappear after formation of an endoperoxide, as exhibited in the excitation spectrum of the product. The emission maximum of the product of *mono-Probe-III* with singlet oxygen shiftet 50 nm to lower wavelengths compared to the pristine *mono-Probe-III*.
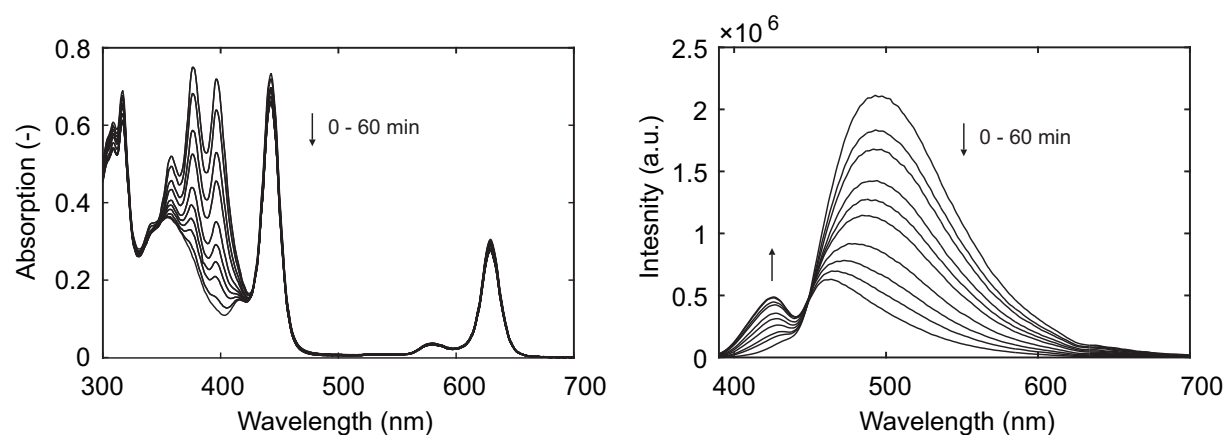
Figure 3.13: Absorption and Fluorescence spectra of 4-(4-(10-phenylanthracen-9-yl)phenyl)benzo[c][1,2,5]thiadiazole (mono-alkylated product, R = H) (left and right).

Figure 3.14: Excitation and emission spectrum of probe 4-(4-(10-phenylanthracen-9-yl)phenyl)benzo[c][1,2,5]thiadiazole (mono-alkylated product, R = H) in toluene (black traces, — trace, λ_{max}= 475 nm and - - - trace, λ_{max}= 495 nm). The excitation spectrum was recorded from 280 nm - 500 nm with λ_{ex} at 520 nm; emission was recorded from 380 - 700 nm with λ_{em} at 370 nm. Excitation and emission spectra of *mono-Probe-III* endoperoxide (grey traces, — trace, λ_{max}= 416 nm and - - - trace, λ_{max}= 445 nm). The excitation spectrum was recorded from 280 nm - 425 nm with λ_{ex} at 430 nm. The emission was recorded from 370 - 700 nm with λ_{em} at 355 nm.
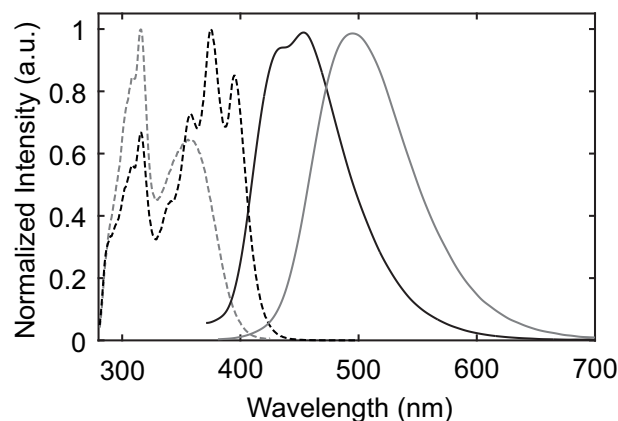
The synthesis led to the proposed product *mono-Probe-III*, and it featured two characteristics for a suitable optical singlet oxygen trap, namely the capability to trap singlet oxygen and the fluorescent

switch upon reaction with singlet oxygen. Therefore, *mono-Probe-III* was subject to further analysis in terms of its electrochemical stability. The electrochemical stability of 4-(4-(10-phenylanthracen-9-yl)phenyl)benzo[c][1,2,5]thiadiazole was investigated *via* cyclic voltammetry. The cyclic voltam-mogramm of the novel optical singlet oxygen probe *mono-Probe-III* is illustrated in Figure 3.15. *mono-Probe-III* does not show sufficient electrochemical stability in the potential range of 2 - 4.5 V as it exhibit an oxidation onset at 4 V and a reduction onset at 2.8 V.
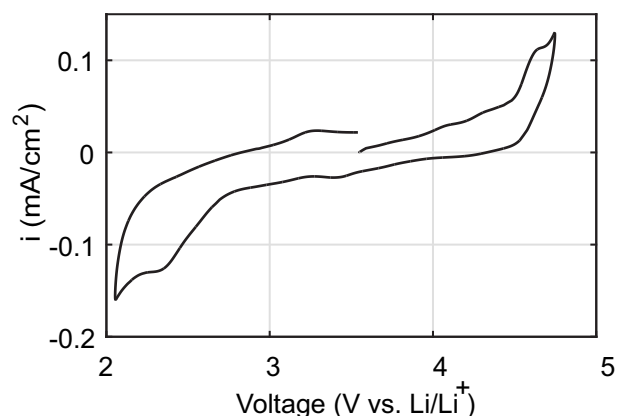
Figure 3.15: Cyclic voltammo-gram of 4-(4-(10-phenylanthracen-9-yl)phenyl)benzo[c][1,2,5]thiadiazole, mono-Probe-III in 0.1 M LiClO$_4$ in TEGDME with a scan rate of 100 mV·s^{-1}.

In consequence of the small electrochemical stability window, *mono-Probe-III* can, with restrictions in the electrochemical window, be used as a novel optical singlet oxygen probe as an electrolyte additive in Li-O$_2$ batteries. In other systems than electrochemical cells it can be used as a optical singlet oxygen probe. Further investigations in terms of pH, temperature dependency and kinetics have to be performed; though tis experiments are beyond the scope of this thesis.

3.2   Disubstituted Anthracenes as Singlet Oxygen Probes

Given the fact that our attempts to synthesize a fluorescence probe with sufficient electrochemical stability did not lead to the desired outcome, we had to strike a new path in order to detect ^{1}O$_2$ during cell operation. Disubstituted anthracene derivatives have been shown to be efficient trapping units in optical singlet oxygen probes as described in *Chapter 2* and Chapter 3.[103,106] Their structural derivatives 9,10-dimethylantracene (DMA) and 9,10-diphenylanthracene (DPA) have been shown to react with singlet oxygen forming stable endoperoxides accompanied by a decrease in absorbance and fluorescence intensity.[88,109,108] Therefore, DMA and DPA were subjected for further analysis as possible fluorescent 'on-off' probes in terms of their reactivity (kinetics) towards ^{1}O$_2$ and electrochemical and chemical stability towards RROS.

3.2.1   Reactivity of DMA and DPA towards $^1O_2$

In general, Diels-Alder reactions occur between a conjugated diene and an alkene, a so-called dienophile.[116] Figure 3.16 shows the frontier orbital description of a [4+2]-cycloaddition where two new bonds are formed simultaneously between an electron-rich diene, such as an anthracene derivative and the electron-poor dienophile such as singlet oxygen. The electron-deficient dienophile has a low-
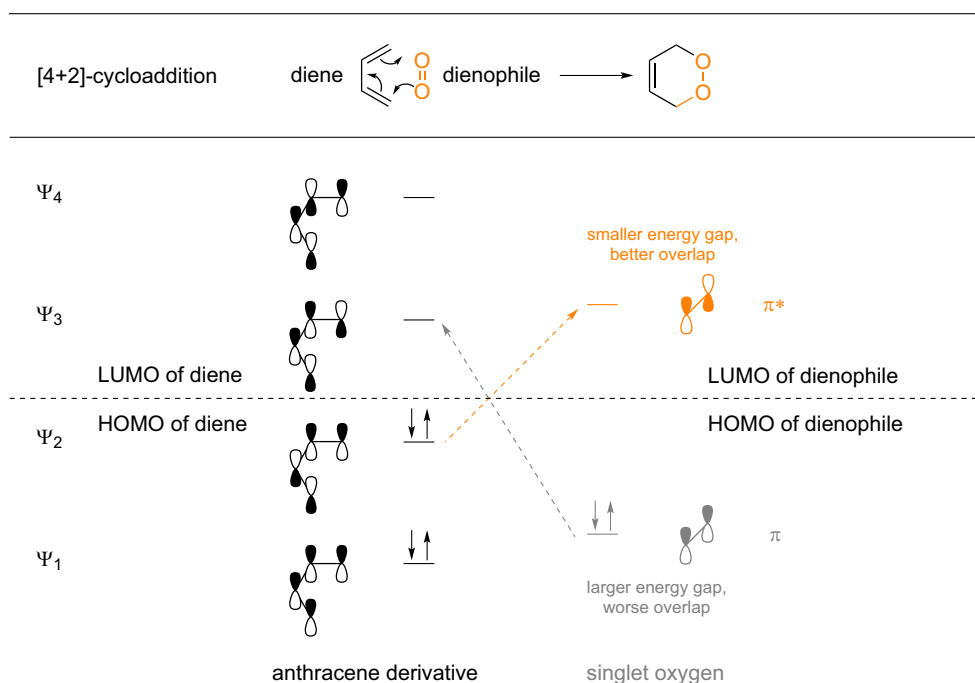
Figure 3.16: Frontier orbital description of [4+2]-cycloaddition where two new bonds are formed between an electron-rich diene and the electron-poor dienophile singlet oxygen. Figure adapted from *Clayden et al. Organic Chemistry.*[116]

energy LUMO and the electron-rich diene has a high-energy HOMO, so that this combination gives a favourable overlap in the transition state.[116] The reaction of the aromatic ring of the anthracene core with singlet oxygen into its endoperoxide *via* [4+2]-cycloaddition is accompanied by a decrease in absorbance of the aromatic compound, which can be monitored as described previously in *Chapter 2* and *Chapter 3*.[117, 101, 110] As there are inconclusive reports in the literature about the kinetics of the reaction of DMA and DPA with singlet oxygen, we studied the kinetics of these reactions.[88, 101, 118] UV-Vis absorption spectra of DMA and DPA in toluene differ to a small extent from each other as they only differ structurally at position 9 and 10 of the anthracene moiety.[115] Figure 3.17 shows the result of the photooxygenation reactions: under the same conditions, $^1O_2$ shows two orders of magnitude faster reaction with DMA than with DPA. An explanation for this might be the steric hindrance

of the phenyl group ($-C_6H_5$) attached to the anthracene core, as it is rather large compared to the smaller methyl group ($-CH_3$). With respect to the orbitals involved in the reaction, the energy of
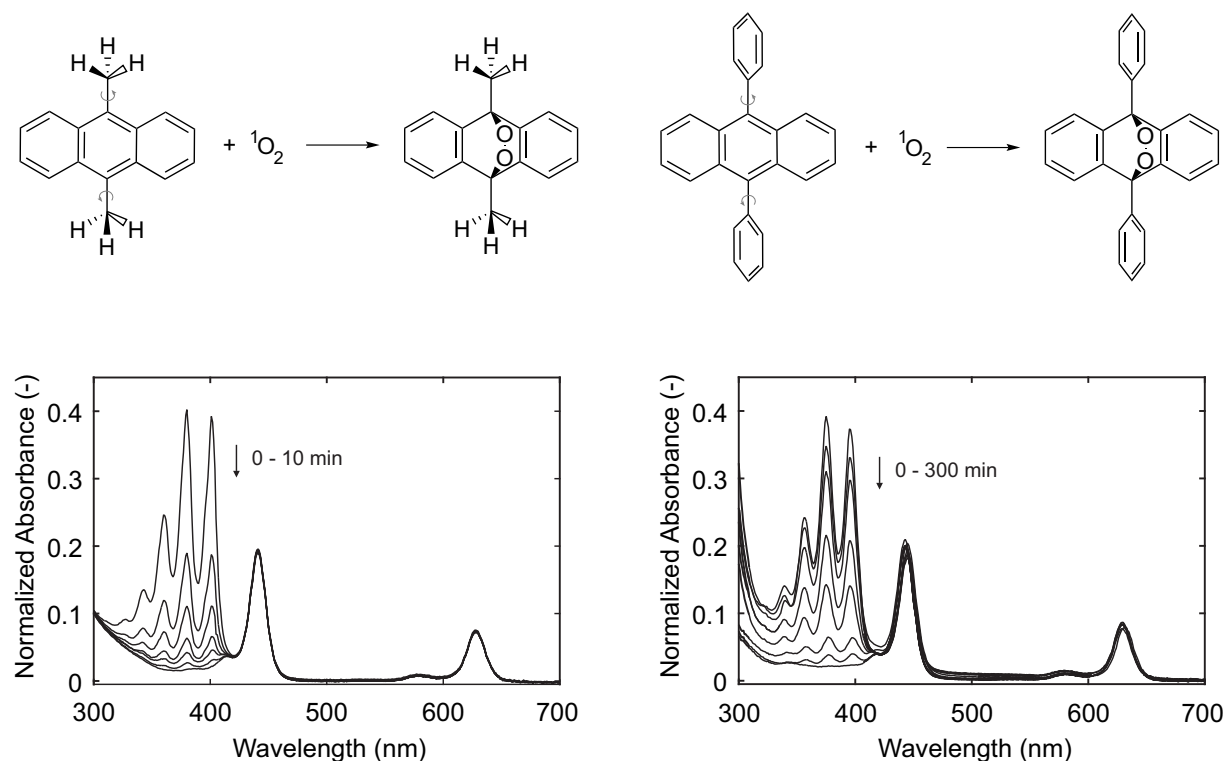
Figure 3.17: UV-Vis absorption spectra of 9,10-dimethylanthracene (DMA) and 9,10-diphenylanthracene (DPA) over the course of photooxygenation. The introduction of phenyl groups at position 9 and 10 causes very little change in the anthracene moiety spectrum, whereas the introduction of a methyl group causes a batochromic shift of ∼ 5 nm. The significant maxima in the absorption spectrum of 9,10-disubstituted anthracene in the region between 300 - 410 nm can be ascribed to vibrational sublevels (−C–H bending) of the conjugated system of the anthracene moiety. The reaction of $^1O_2$ with DMA is two orders of magnitude faster than that with DPA.

the orbitals between the HOMO of the diene and LUMO of the dienophile might be smaller in DMA than in DPA. To prove this statement, density functional theory (DFT) calculations were performed by D. Kramer from Engineering Sciences at the University of Southampton, using Gaussian Software based on the assumption that the whole system of O_2 with DMA and DPA is a singlet. Figure 3.18 illustrates the computed results: The values for the reaction free energy of the pristine DMA and DPA are shown with respect to the energies of the reactants plus $^3O_2$. In addition, the transition states of the formed endoperoxides of DMA and DPA with $^1O_2$ DMA-O_2 and DPA-O_2 are illustrated. For DMA the reaction is both more exothermic and has much lower activation energy than for DPA. These results are in accordance with the previously mentioned theory of Diels-Alder reactions and our experimental observations.
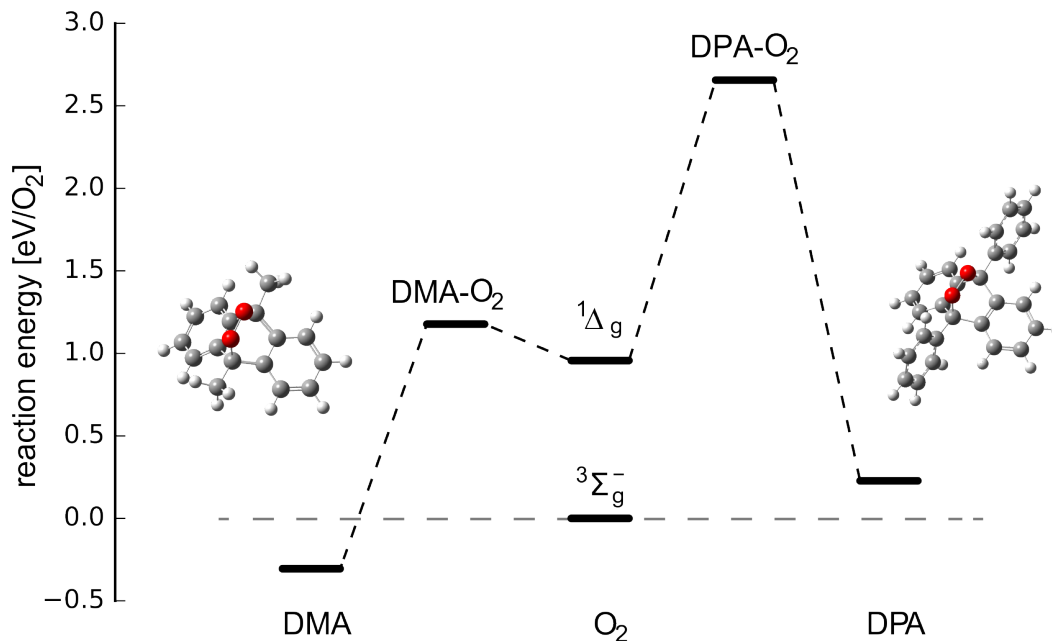
Figure 3.18: Reaction free energies of the pristine anthracenes DMA (left), molecular oxygen (ground, $^3O_2$ and first excited singlet state $^1O_2$, mid) and DPA (right). In addition, the transition states of the corresponding endoperoxides of DMA and DPA with $^1O_2$, DMA-O_2 and DPA-O_2 are illustrated. The reaction free energy of DMA-O_2 with $1.2\,eV/O_2$ is lower compared to DPA-O_2 with $2.7\,eV/O_2$, and therefore, DMA shows faster kinetics with $^1O_2$.

3.2.2   Electrochemical and chemical stability of DMA and DPA

Figure 3.19 and Figure 3.20 shows the cyclic voltammograms of DMA, DMA-O_2, DPA and DPA-O_2. DMA and DPA were photooxygenized to obtain their endoperoxides DMA-O_2 and DPA-O_2. First 2 mM DMA and 0.1 M LiClO$_4$ in DIDME were measured under Ar atmosphere. $^1O_2$ was then generated photo-chemically with the photo-sensitizer Pd$_4$F (1 nmol) under O_2-atmosphere and the formed DMA-O_2 was subsequently measured under Ar atmosphere. DMA and DMA-O_2 are stable in the potential range of 2 - 4.2 V whereas DPA and DPA-O_2 are stable in the potential range of 1.8 - 4.1 V.

3.2.3   Stability of DMA towards ROS

In general, uncertainties derive not from the reaction of the probe with singlet oxygen, but from reactions of the probe with reactive oxygen species other than singlet oxygen, *e.g.*, superoxide which is an intermediate during cell discharge and peroxide as the main discharge product.[101] Due to lithium superoxide's instability it cannot be directly used as reactant, and therefore a substitute has to be used. Potassium superoxide is a stable salt of K$^+$ and $O_2^{\bullet-}$ and is known to be solubilized by crown

Figure 3.19: Electrochemical stability of 9,10-dimethylanthracene (DMA) and 9,10-dimethylanthracene endoperoxide (DMA-O_2). Cyclic voltammetry was performed at a 3 mm glassy carbon disc electrode at a sweep rate of $50\,mV \cdot s^{-1}$. First 2 mM DMA and 0.1 M LiClO$_4$ in DIDME were measured under Ar atmosphere. $^1O_2$ was then generated photo-chemically with 1 nmol photo-sensitizer Pd$_4$F under O$_2$-atmosphere and the formed DMA-O_2 was subsequently measured under Ar atmosphere.

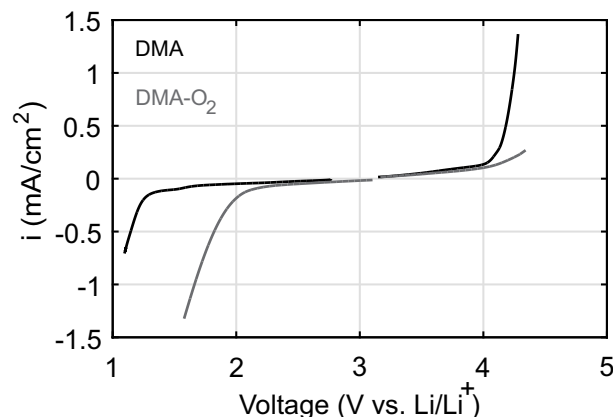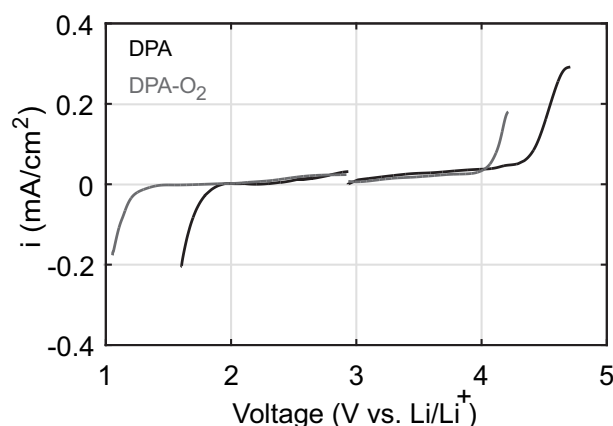**Figure 3.20:** Electrochemical stability of 9,10-diphenylanthracene (DPA) and 9,10-diphenylanthracene endoperoxide (DPA-O_2). Cyclic voltammetry was performed at a 3 mm glassy carbon disc electrode at a sweep rate of $50\,mV \cdot s^{-1}$. First, 10 mM DPA and 0.1 M LiClO$_4$ in TEGDME were measured under Ar atmosphere. $^1O_2$ was then generated photo-chemically with 1 nmol photo-sensitizer Pd$_4$F under O$_2$-atmosphere and the formed DPA-O_2 was subsequently measured under Ar atmosphere.

ethers like 1,4,7,10,13,16-hexaoxacyclooctadecane (18-Crown-6) to form a free superoxide anion.[82,66] To obtain free superoxide one equivalent of 18-crown-6 ether was added to KO$_2$ in 0.1 M LiTFSI in d-DMSO and was stirred for a given time frame. The test solutions exposed to lithium peroxide and free superoxide were filtered and further analyzed using ^{1}H NMR, UV-Vis spectroscopy and HPLC. DMA is stable towards attack of free superoxide and peroxide as shown in the results which have been published in *Nature Energy* **2017** (see *Chapter 4* Page 47-49), *Angew. Chem. Int. Ed.* **2017** (see *Chapter 6* Page 83) and *Angew. Chem. Int. Ed.* **2018** (see *Chapter 7* Page 96).

3.2.4 Stability of DMA towards photo-sensitizer under anoxic conditions

To test whether the excited photo-sensitizer is able to react with DMA under anoxic conditions a test set-up was used, similar to all previous photooxygenation experiments. An electrolyte containing 3 mM DMA and 3 μM photo-sensitizer (Pd$_4$F) in 0.3 M LiTFSI TEGDME was deoxygenated with pure Ar for 25 min. The photo-sensitizer was excited with a beam of a powerful laser diode (focused with aperture and lens, λ_{max} at 634 nm). Once the photo-sensitizer is excited, theoretically three processes can occur: the photo-sensitizer (in its first excited state, S$_1$) will undergo inter system crossing (ISC)

into its triplet state (T_1) and then (1) decay into its ground state (S_0) *via* phosphorescence, or (2) decay into its ground state (S_0) *via* non-radiative decay, or (3) transfer its energy to the emitter (DMA, in this studied system) in a triplet-triplet energy transfer, resulting in so-called triplet-triplet-annihilation (TTA) induced up-conversion.[84, 104, 105] This is unlikely since the photo-sensitizers triplet state should be above the acceptor's triplet state, and the concentration of the photo-sensitizer under experimental conditions should be rather high (which was not the case due to low light intensities used) or if TTA induced upconversion would be possible it would only result in emission of fluorescence from the anthracene.[119] No TTA induced up-conversion was observed, which would be accompanied by the emission of blue light.[120, 121, 122, 123] The experiment was repeated with a significantly higher photo-sensitizer concentration, where also no TTA-induced up-conversion was observed. This complies with the calculated results for the triplet-state energy of DPA of ~ 1.77 eV (needed photon energy) which corresponds to a wavelength of 700 nm.[120, 124] As the π-system of DMA is smaller than DPA, the triplet energy is even higher and therefore TTA-induced up-conversion is not possible or unlikely to happen with a Pd-benzoporphyrin such as Pd_4F.[121] An electrolyte containing 3 mM DMA and 3 μM photo-sensitizer (Pd_4F) in 0.3 M LiTFSI TEGDME was deoxygenated with pure Ar for 25 min. The photo-sensitizer was excited with a red LED for 5, 10, 30, 60 and 120 min. The samples taken after each excitation period where further analysed using UV and HPLC analysis, were however, no indication of product formation was observed. In conclusion, DMA and DPA are both commercially available and can easily be purified *via* recrystallisation, they react with singlet oxygen to form stable endoperoxides, are chemically stable towards superoxide and peroxide, and are sufficiently electrochemically stable. As 9,10-dimethylanthracene offers fast reactivity with $^1O_2$ and complies reasonably with the requirements for a suitable probe for indirect singlet oxygen detection, it was further used for a set of *in-situ* and *ex-situ* measurements.

Chapter 4

Singlet Oxygen in the Li-O$_2$ Battery

Non-aqueous metal-oxygen batteries depend critically on the reversible formation/decomposition of metal oxides on cycling. Irreversible parasitic reactions cause poor rechargeability, efficiency, and cycle life. They have predominantly been ascribed to the reactivity of reduced oxygen species with cell components. These species, however, cannot fully explain the side reactions. Singlet oxygen, the most important remaining reactive oxygen species, was mostly overlooked in the context of non-aqueous battery chemistries. In 2011 Hassoun *et al.* conjectured that it could form above ∼3.9 V based on the reversible potential of Li$_2$O$_2$ oxidation and the energy difference of ∼1 eV between triplet and singlet oxygen.[20] This was picked up subsequently in scattered references, yet without giving any proof because of the difficulty to detect ^{1}O$_2$. Our group started working on ^{1}O$_2$ detection in the challenging environment of metal-O$_2$ cells in 2014 with the clear requirement of developing a method that is capable of detecting ^{1}O$_2$ during both discharge and charge > 4 V. Close to completion, Gasteiger et al. published first detection of ^{1}O$_2$ in the Li-O$_2$ cell above 3.5 V in small quantities.[80] However, their method was incompatible with discharge and failed above 3.75 V. As depicted in *Chapter 2* it is crucial for indirect ^{1}O$_2$ detection to use a fully suitable fluorescent probe. Due to the dilemma with the stability of literature-known fluorescent ^{1}O$_2$ probes and our novel fluorescent probes as described in *Chapter 3*, we decided to perform ^{1}O$_2$ detection with the commercially available ^{1}O$_2$ trap DMA. In our comprehensive work we demonstrate *via* a set of developed *in-situ* and *ex-situ* methods that singlet oxygen forms at the cathode of a Li-O$_2$ cell during discharge and from the onset of charge. Its amount increases during discharge, early stages of charge as well as charging at higher voltages and accounts for the majority of parasitic reaction products. In addition ^{1}O$_2$ generation is enhanced by the presence of trace water. Superoxide and peroxide appear to be involved in ^{1}O$_2$ generation. We have studied the effect of ^{1}O$_2$ quenchers on side product formation and have shown

that ^{1}O$_2$ traps and quenchers effectively reduce parasitic reactions, so that the chemical measure of reversibility, the ratio of evolved O$_2$ to consumed O$_2$, increased significantly.

N. Mahne, B. Schafzahl, C. Leypold, M. Leypold, S. Grumm, A. Leitgeb, G.A. Strohmeier, M. Wilkening, O. Fontaine, D. Kramer, C. Slugovc, S.M. Borisov and S.A. Freunberger
Singlet oxygen generation as a major cause for parasitic reactions during cycling of aprotic lithium-oxygen batteries, *Nature Energy* **2017**, 2, 17036

These new findings challenged the longstanding view that parasitic reactions stem from the reactivity of RROS and underpin the importance to set a new path in the prevention of parasitic reactions in Li-O$_2$ batteries, triggered not only by superoxide and peroxide, but rather by ^{1}O$_2$. Prevention of ^{1}O$_2$ generation in Li-O$_2$ batteries has highest priority. Physical deactivation of ^{1}O$_2$ during cycling, in particular at high voltages, is unfortunately not possible due to the narrow electrochemical stability-window of known quenchers such as DABCO. In *Chapter 8* a new strategy is described to design novel singlet oxygen quenchers which are electrochemically stable over the entire potential range of the Li-O$_2$ battery. On the basis of these new insights a need for similar research in other metall-O$_2$ battery systems arouse, such as Na-O$_2$ cells which as well suffer from low cyclic stability from still not entirely clarified origin. These findings suggest that the issue of ^{1}O$_2$ formation may equally be relevant for the other non-aqueous battery chemistries involving oxygen redox. These are for example Na-O$_2$ and K-O$_2$ cells, the chemistry of alkali metal carbonates and of intercalation materials with O-redox. Work regarding Na-O$_2$ cells is presented in *Chapter 6* and on Li$_2$CO$_3$ in *Chapter 7*.

Singlet oxygen generation as a major cause for parasitic reactions during cycling of aprotic lithium–oxygen batteries

Nika Mahne[1], Bettina Schafzahl[1], Christian Leypold[1], Mario Leypold[2], Sandra Grumm[1], Anita Leitgeb[1], Gernot A. Strohmeier[2,3], Martin Wilkening[1], Olivier Fontaine[4,5], Denis Kramer[6], Christian Slugovc[1], Sergey M. Borisov[7] and Stefan A. Freunberger[1]*

Non-aqueous metal–oxygen batteries depend critically on the reversible formation/decomposition of metal oxides on cycling. Irreversible parasitic reactions cause poor rechargeability, efficiency, and cycle life, and have predominantly been ascribed to the reactivity of reduced oxygen species with cell components. These species, however, cannot fully explain the side reactions. Here we show that singlet oxygen forms at the cathode of a lithium–oxygen cell during discharge and from the onset of charge, and accounts for the majority of parasitic reaction products. The amount increases during discharge, early stages of charge, and charging at higher voltages, and is enhanced by the presence of trace water. Superoxide and peroxide appear to be involved in singlet oxygen generation. Singlet oxygen traps and quenchers can reduce parasitic reactions effectively. Awareness of the highly reactive singlet oxygen in non-aqueous metal–oxygen batteries gives a rationale for future research towards achieving highly reversible cell operation.

Rechargeable non-aqueous metal–O_2 (air) batteries have attracted immense interest because of their high theoretical specific energy and potentially better sustainability and cost in comparison to current lithium-ion batteries[1–5]. Cell chemistries include Li–O_2, Na–O_2 and K–O_2, with the Li–O_2 cell being most intensely studied[6–9]. Charge is stored at the cathode by the reversible formation/decomposition of metal oxides on discharge/charge[10,11]. In the Li–O_2 cell this is typically Li_2O_2. Practical realization, however, still faces many challenges[5,8,12–14]. Perhaps the most significant obstacle arises from severe parasitic reactions during cycling[3–5,7,8,10,11,13–26]. These reactions decompose the electrolyte as well as the porous electrode (typically carbon with binder), and cause poor rechargeability, high charging voltages, low efficiency, build-up of parasitic reaction products, and early cell death within a few cycles.

Many researchers have investigated the origin of parasitic reactions and proposed strategies to mitigate them[7,8,10,16–19]. Superoxide has been most widely mentioned in causing side reactions on discharge since it forms as an intermediate in O_2 reduction and is a strong nucleophile and base[3,11,14,20,21,27]. Also, Li_2O_2 was found to react with the electrolyte and carbon on discharge[3,21–24]. These reactivities were used to explain the observation that on discharge typically close to the ideal value of two electrons per one O_2 molecule are consumed despite significant amounts of side products such as Li_2CO_3, Li formate and Li acetate being formed[17,24]. On charge, typically the e^-/O_2 ratio deviates significantly from two, and more of the side products form[5,7,15,24,25]. These parasitic reactions occur at charging potentials well within the stability window (oxidative stability) of carbon and electrolyte in the absence of Li_2O_2 (refs 21,23,25). It was therefore suggested that some sort of reactive intermediates of Li_2O_2 oxidation cause electrolyte and carbon decomposition on charge[11,23,25,28].

Chemical oxidation of alkaline peroxides in non-aqueous media is known to generate singlet oxygen ($^1\Delta_g$ or $^1O_2$), the first excited state of triplet ground state dioxygen ($^3\Sigma_g^-$)[29–32]. Based on the reversible potential of Li_2O_2 formation and the energy difference between triplet and singlet oxygen, the formation of $^1O_2$ in the Li–O_2 cell has been hypothesized to be possible at charging potentials exceeding 3.5 to 3.9 V versus Li/Li$^+$ (refs 11,23). Only recently $^1O_2$ was reported to form in small quantities between 3.55 and 3.75 V (ref. 28). Overall, the hitherto known processes cannot consistently explain the observed irreversibilities. Only better knowledge of parasitic reactions may allow them to be inhibited so that progress towards fully reversible cell operation can continue.

Here we show that $^1O_2$ forms in the Li–O_2 cathode during discharge and from the onset charge, and that it is responsible for a major fraction of the side products in the investigated system with ether electrolyte. The lower abundance on discharge and higher abundance on charge can consistently explain the typically observed deviations of the e^-/O_2 ratio from the ideal value of two. The origin of the $^1O_2$ on charge appears to be superoxide and peroxide. The presence of trace water enhances the formation during both

[1]Institute for Chemistry and Technology of Materials, Graz University of Technology, Stremayrgasse 9, 8010 Graz, Austria. [2]Institute of Organic Chemistry, Graz University of Technology, Stremayrgasse 9, 8010 Graz, Austria. [3]Austrian Centre of Industrial Biotechnology (acib) GmbH, Petersgasse 14, 8010 Graz, Austria. [4]Institut Charles Gerhardt Montpellier, UMR 5253, CC 1701, Université Montpellier, Place Eugène Bataillon, 34095 Montpellier Cedex 5, France. [5]Réseau sur le Stockage Électrochimique de l'Énergie (RS2E), CNRS FR3459, 33 rue Saint Leu, 80039 Amiens Cedex, France. [6]Engineering Sciences, University Road, University of Southampton, Southampton SO17 1BJ, UK. [7]Institute for Analytical Chemistry and Food Chemistry, Graz University of Technology, Stremayrgasse 9, 8010 Graz, Austria. *e-mail: freunberger@tugraz.at

discharge and charge. We also show that $^1O_2$ traps and quenchers as electrolyte additives can significantly reduce the amount of side products associated with $^1O_2$.

Reactivity of the electrolyte with singlet oxygen

The discharge product formed at the Li–O_2 cathode in relatively stable electrolytes, such as the widely used glyme (oligo-ethylene glycol dimethyl ether) based ones, consists predominantly of Li_2O_2 accompanied by a typical pattern of side products, including Li_2CO_3, Li acetate and Li formate[12,15,21,23,24,26,33]. The same side products form upon oxidation of Li_2O_2 (charging), and eventually release CO_2 and other fragments at sufficiently oxidizing potentials[21,25]. A large body of work has identified the reduced O_2 species superoxide and peroxide or their lithium compounds to trigger the formation of these products[3,11,14,15,20,21,34]. To investigate whether $^1O_2$ would lead to the same products, we generated it inside a typical electrolyte, 0.1 M lithium perchlorate ($LiClO_4$) in ethylene glycol dimethyl ether (DME), and analysed the formed products (Fig. 1). $^1O_2$ was generated photochemically by illuminating the O_2-saturated electrolyte containing a small concentration of a photosensitizer inside a closed vessel (for experimental details see Methods). The head space was then purged to a mass spectrometer (MS) for analysis to detect readily evolved gases, and, after addition of acid, to detect whether Li_2CO_3 had formed (Fig. 1a). MS analysis does not show any detectable direct CO_2 evolution, but CO_2 evolving from Li_2CO_3. A second portion of equally treated electrolyte was dissolved in D_2O and subjected to ^1H-NMR spectroscopy (Fig. 1b). The ^1H-NMR spectrum confirms the presence of Li formate and Li acetate via the peaks for HCOOD and CH_3COOD that form upon contact with D_2O. The literature on the reactivity of $^1O_2$ with organic substrates most commonly states peroxides as an initial product[32]. Going along this line, we assume that $^1O_2$ produces ROOH, $R^\bullet$, and $ROO^\bullet$ as the first reactive intermediates of electrolyte degradation more efficiently than the reduced oxygen species, which were proposed to initiate electrolyte degradation via the same intermediates, albeit high activation energies have been noted[33,35,36]. Taken together, these results show that the typical pattern of parasitic reaction products formed during discharge and charge of Li–O_2 cells could to some extent originate from the presence of $^1O_2$.

Operando detection of singlet oxygen in the Li–O_2 cathode

Probing whether $^1O_2$ is involved in the cell reaction requires sensitive methods that are compatible with the cell environment. So far, described methods for detection of $^1O_2$ are based either on direct detection of characteristic light emissions upon decay into the ground state, or on the selective reactivity with probe molecules that are themselves interrogated by spectroscopic means[32]. The short lifetime of $^1O_2$ in liquid media, various competing decay routes, and low sensitivity of near-infrared (NIR) detectors make the detection of the specific emission of $^1O_2$ at 1,270 nm challenging and insensitive[31,32,37]. Therefore, the absence of a detectable signal would provide no definite proof for the absence of $^1O_2$. Nevertheless, we could detect this emission for a case with high $^1O_2$ abundance, as discussed later.

To detect $^1O_2$ at quantities which would be responsible even for small amounts of parasitic products, we devised a sensitive and selective method with a chemical probe compatible with the cell environment at any stage of cycling. Previously, highly sensitive probes for aqueous media have been described, which contain a quencher group attached to a chromophore and show fluorescence 'switch on' upon reaction of the quenching group with singlet oxygen[32,38]. However, the chromophores used so far are not electrochemically inert in the relevant potential range of ~2 to 4 V versus Li/Li$^+$. Typically used chromophores include fluorescein and rhodamine, which all undergo electrochemical reactions in this range (Supplementary Fig. 1). The quencher group for $^1O_2$ is typically a substituted
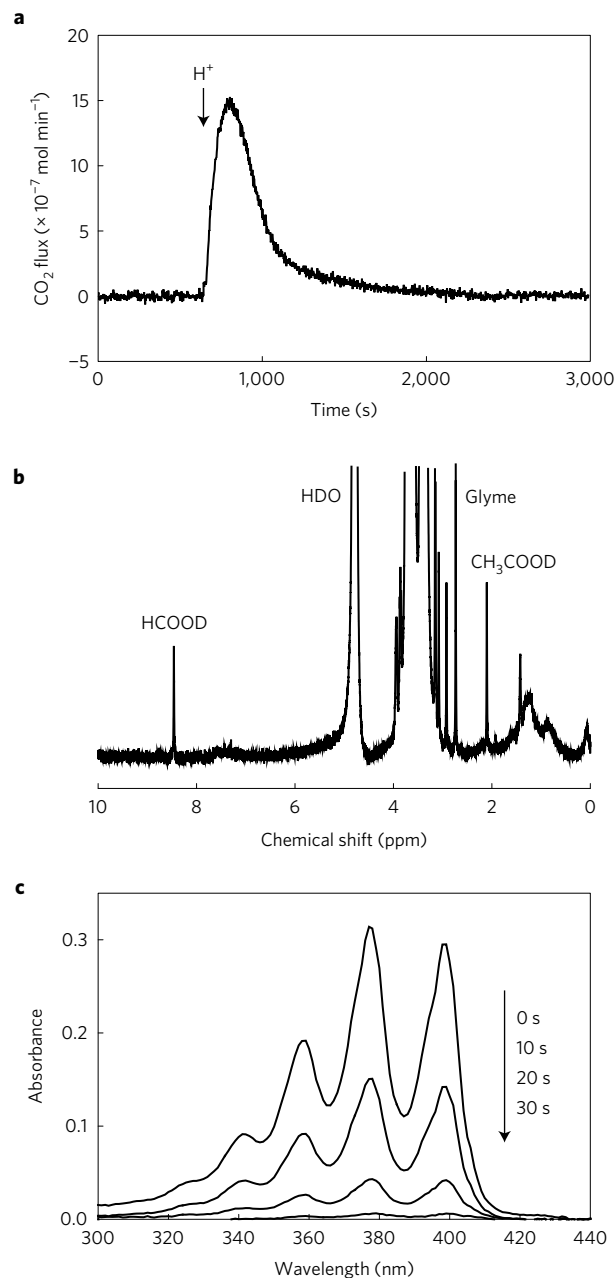
Figure 1 | Reactivity of the electrolyte with singlet oxygen. a, CO_2 evolution measured by mass spectrometry above O_2-saturated 0.1 M $LiClO_4$ in DME electrolyte that has been exposed for 30 min to $^1O_2$. The latter has been produced *in situ* by photogeneration with the sensitizer palladium(II) *meso*-tetra(4-fluorophenyl)tetrabenzoporphyrin with the head space closed. After illumination the head space was purged to the mass spectrometer and H_3PO_4 added at the time indicated to evolve CO_2 from Li_2CO_3. **b**, ^1H-NMR spectrum of the equally treated electrolyte when dissolved in D_2O. **c**, UV–Vis absorption spectra as a function of illumination time of the same electrolyte that additionally contained 2.6×10^{-5} M 9,10-dimethylanthracene. The absorbance in the ordinate of **c** is dimensionless, thus there is no unit.

anthracene derivative such as 9,10-dimethylanthracene (DMA) or 9,10-diphenylanthracene (DPA), which form the corresponding endoperoxide. DPA itself has been used directly as an $^1O_2$ probe based on the decrease of absorbance as a sign for the presence of $^1O_2$ (ref. 39). We have added 2.6×10^{-5} M DMA to 0.1 M $LiClO_4$ in DME and exposed the solution to *in situ* photogenerated $^1O_2$; all DMA was consumed within less than a minute, which indicates

a rapid reaction with $^1O_2$ to its endoperoxide (DMA–O_2) in this environment (Fig. 1c). DPA reacted in the same experiment approximately two orders of magnitude slower (Supplementary Fig. 2). Cyclic voltammograms with 2 mM DMA and 0.1 M LiClO$_4$ in DME under Ar show electrochemical stability between 1.8 and 4.5 V (Supplementary Fig. 3). The DMA was then transformed to its endoperoxide (DMA–O_2) by means of *in situ* photogenerated $^1O_2$. Cyclic voltammograms taken thereafter show likewise stability of the DMA–O_2 between 2.5 and >4.5 V. Inertness against superoxide (O_2^-), and hence selectivity for $^1O_2$, was confirmed by stirring DMA with an excess of KO_2 in DME containing 0.1 M LiClO$_4$ and taking ^{1}H-NMR spectra and ultraviolet–visible (UV-Vis) spectra at time intervals up to 22 h. The results do not show any detectable decomposition products of the DMA (Supplementary Figs 4 to 7). Taken together, the above experiments confirm DMA to be a sensitive and selective probe for $^1O_2$ in the cell environment. We use DMA in the following first as a fluorescent probe for operando detection of $^1O_2$. Operando fluorescence requires a relatively low DMA concentration in the μM range, which slightly restricts the detection limit. Later we use DMA in the mM range to detect $^1O_2$ with maximum sensitivity and to remove it, which requires measuring the conversion of DMA to DMA–O_2 by *ex situ* high-performance liquid chromatography (HPLC).

An operando fluorescence set-up as detailed in the Methods was constructed. Briefly, the cell consisted of a porous carbon working electrode in an O_2-saturated electrolyte containing 1.6×10^{-5} M DMA and 0.1 M LiClO$_4$ in tetraethylene glycol dimethyl ether (TEGDME). As the counter electrode we used Li$_{1-x}$FePO$_4$ to exclude reactivity of the DMA with a Li metal anode. The cell was assembled inside a gas-tight quartz cuvette with a slightly pressurized O_2 head space. Excitation and emission wavelengths were chosen according to the respective maxima in these spectra of DMA (Supplementary Fig. 8). The electrolyte was stirred to ensure constant O_2 concentration irrespective of consumption or evolution during cycling. This is important, since O_2 is a fluorescence quencher, and changes in intensity could otherwise stem from changing O_2 concentration, as shown in Supplementary Fig. 9.

Results for charging a cathode, containing chemically produced Li$_2O_2$ with 0.1 M LiClO$_4$ in TEGDME as the electrolyte, by applying voltage steps are shown in Fig. 2a. At voltages up to 3.5 V the fluorescence intensity, reflecting DMA concentration, remains unchanged within the measurement accuracy. Above this voltage, the signal drops with increasing rate. The cumulatively consumed DMA corresponds to ~2% of the theoretically evolved O_2 (based on charge) being $^1O_2$. This value is the lower boundary of the actual abundance since at the low DMA concentration (~0.5% of the O_2 concentration) competing sinks for $^1O_2$ other than reaction with DMA can be expected to dominate.

To probe whether $^1O_2$ is also formed during discharge, we cycled electrodes in the fluorescence set-up. Results for galvanostatic cycling of a porous carbon cathode in dry 0.1 M LiClO$_4$ in TEGDME are shown in Fig. 2b. Upon discharge the DMA concentration remains nearly unchanged within the measurement accuracy. However, immediately after switching to charging, starting from ~3 V, the signal drops with increasing slope as charging progresses and the voltage climbs towards 4.3 V, where full recharge is reached. The cumulatively consumed DMA corresponds to ~4% of the expected O_2 being $^1O_2$. The results demonstrate that $^1O_2$ was formed from the very beginning of charge at a significant rate. However, this experiment could not tell with certainty whether $^1O_2$ was formed on discharge. A possible source of $^1O_2$ on discharge is the reaction of the superoxide intermediate, the first step of O_2 reduction, with trace water, which has been shown to result in $^1O_2$ (ref. 37). Therefore, we have run an analogous experiment with 1,000 ppm H_2O in the electrolyte (Fig. 2c). DMA consumption was seen throughout discharge at an approximately constant rate. Again,
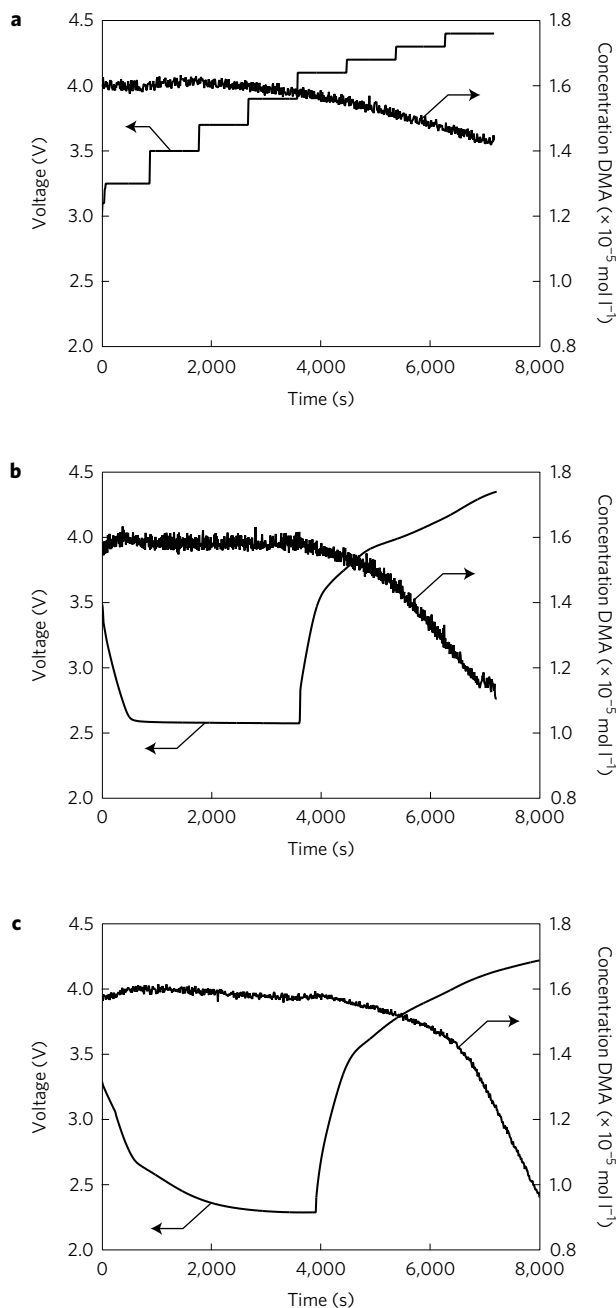

Figure 2 | Operando fluorescence spectroscopy during Li–O_2 cell operation with electrolytes containing 9,10-dimethylanthracene (DMA) as singlet oxygen trap. a, Potentiostatic oxidation of a carbon black electrode containing chemically produced Li$_2O_2$ in O_2-saturated 0.1 M LiClO$_4$ in TEGDME. Voltage steps and DMA concentration. **b**, Galvanostatic discharge and charge of a carbon black electrode at 25 μA cm^{-2} in dry O_2-saturated 0.1 M LiClO$_4$ in TEGDME. Voltage profile and DMA concentration. **c**, Galvanostatic discharge and charge of a carbon black electrode at 25 μA cm^{-2} in O_2-saturated 0.1 M LiClO$_4$ in TEGDME containing 1,000 ppm water. Voltage profile and DMA concentration. All electrolytes had an initial DMA concentration of 1.6×10^{-5} M.

the rate of DMA consumption increased substantially immediately after the cell was switched to charging, and increased as charge progressed to higher voltages. The consumption during charging is increased in comparison to the dry electrolyte, and reaches a value of ~6% of the expected O_2 being $^1O_2$. This suggests that trace water contributes to the formation of $^1O_2$ on discharge and charge. Since the required DMA concentration for operando fluorescence
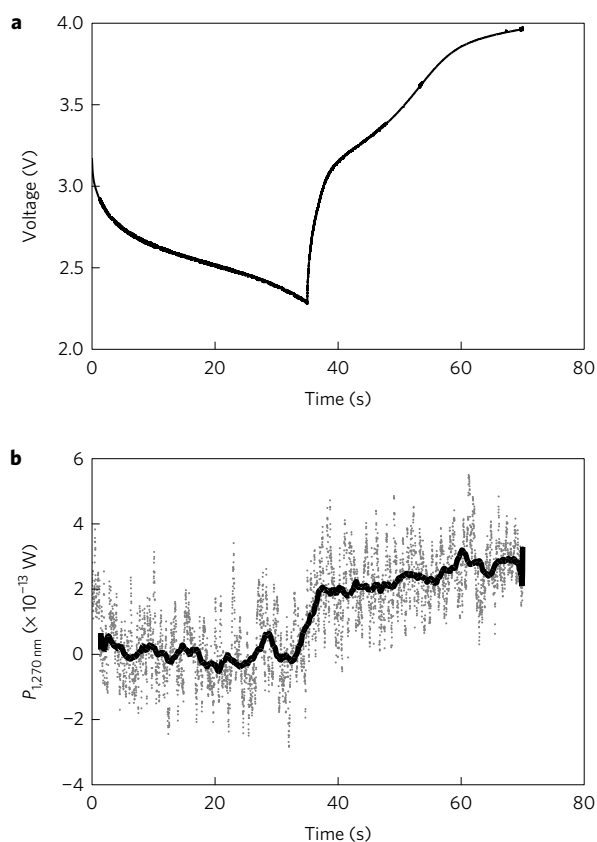
Figure 3 | Operando NIR emission measurement during cycling of a Li–O₂ cathode. a, Voltage profile during galvanostatic reduction and oxidation of an Au-grid electrode at 0.12 mA cm^{-2} in O_2-saturated 0.1 M $LiClO_4$ in deuterated acetonitrile containing 1,000 ppm D_2O. **b**, The power of the optical emission at 1,270 nm. The grey trace represents the sensor signal and the black trace the moving average to guide the eye.

is low, the abundance of $^1O_2$ on discharge appears to be close to the detection limit. Clear evidence for $^1O_2$ on discharge comes from *ex situ* measurements with ~2,000 times the DMA concentration, as discussed later.

We have shown above that DMA is very reactive with $^1O_2$ and reactive to a negligible extent with superoxide in the cell environment. To unambiguously show that there is indeed $^1O_2$ formation and that the DMA consumption does not originate from possible other reactive oxygen species, we measured the specific emission of $^1O_2$ at 1,270 nm (for experimental details see the Methods). This radiative decay to the ground state gives a very weak signal, which is further attenuated by competing sinks for $^1O_2$. One such is deactivation with the solvent with a strongly solvent-dependent lifetime[31]. Attempts to detect radiative decay in the ether electrolyte proved fruitless, which is explicable by the short lifetime in this solvent. Therefore, we have chosen deuterated acetonitrile, where the $^1O_2$ lifetime is higher than in ethers and also higher than in the non-deuterated solvents[32]. We also added 1,000 ppm D_2O, since the above experiments have shown higher $^1O_2$ generation when trace water was present, besides that the lifetime is longer in D_2O than in H_2O. Results for galvanostatic cycling are shown in Fig. 3. The signal/noise ratio does not permit a clear statement about the abundance of $^1O_2$ during discharge, which is to be expected given the low generation rate detected with operando fluorescence in Fig. 2. In accord with above results there is, however, unambiguous proof of $^1O_2$ generation from the start of charging, and increasing rate as charging progresses to higher voltages.

Trapping and quenching singlet oxygen

The above results show that $^1O_2$ forms in significant quantities from the start of charging, and suggest a smaller abundance during discharge. To estimate the fraction of the parasitic products during discharge and charge that originates from $^1O_2$ and to investigate whether removing the $^1O_2$ before it can react with cell components would effectively reduce these parasitic reactions, we examined the effect of $^1O_2$ trapping and quenching. The former removes $^1O_2$ in a chemical reaction and the latter deactivates it by physical quenching, for example, via a temporary charge transfer complex[40]. Trapping is, however, irreversible and physical quenching is therefore preferred because neither quencher nor O_2 is consumed. The literature suggests a variety of quenchers, including aliphatic amines and quinones[41]. We have chosen DMA as $^1O_2$ trap since it is effective in the cell environment, and 1,4-diazabicyclo[2.2.2]octane (DABCO) as quencher since it has been reported to be effective in a non-aqueous environment[41]. DABCO also allows access to a relevant potential range between ~2.0 and 3.6 V, and is stable with superoxide (Supplementary Figs 10 and 11).

Li–O₂ cells with porous carbon black electrodes were constructed as described in the Methods. Three electrolytes were used: 0.1 M $LiClO_4$ in TEGDME that either contained no additive, 30 mM DMA, or 10 mM DABCO. Cycling was carried out at constant current in an O_2 atmosphere. Cells were cycled to various discharge and charge capacities, then stopped and subjected to further analysis. A typical load curve is shown in Fig. 4a. As DABCO is oxidized at ~3.6 V, cells containing this additive were recharged only to 3.5 V, and then held there until the first recharge capacity was reached.

To quantify the amount of carbonaceous side products (Li_2CO_3 and Li carboxylates) formed at each stage of discharge and charge, the electrodes were analysed with a previously established procedure[25]. It involves treating the washed electrodes with acid to decompose the Li_2CO_3 present, followed by treatment with Fenton's reagent to oxidize the Li carboxylates. The evolved CO_2 was quantified by mass spectrometry, and the results are presented in Fig. 4b. DMA as a $^1O_2$ trap is consumed and forms the corresponding endoperoxide DMA–O_2. We take advantage of this feature for quantifying the $^1O_2$ present in the cell by measuring the conversion of DMA to DMA–O_2 by means of HPLC (Fig. 4c and Supplementary Fig. 12). Here we use 30 mM DMA in the electrolyte, which is close to saturation and ~2,000 times the concentration used in the fluorescence experiments. It can therefore be expected that a large fraction of any $^1O_2$ present, albeit not necessarily all, will react with the DMA instead of other cell components. At the same time, DMA becomes a significantly more sensitive probe for $^1O_2$ than as used for fluorescence.

Considering the cell without additive, there is continuous growth of the amount of side products with increasing discharge capacity. The amount further increases to the sampling point at one-third recharge, and then vanishes nearly completely towards full recharge. This is in accord with previous investigations on the build-up and removal of the side products during cycling[15,24,25]. It was shown that, on discharge, side products originate predominantly from the electrolyte. At early stages of charge, the electrolyte further decomposes to solid products, accompanied by Li_2CO_3 from the carbon electrode[24,25]. As charge continues to higher voltages, carbon decomposition becomes more significant, and carbon and electrolyte decomposition go along with CO_2 evolution from already present parasitic products. So far it was reasoned that side products during discharge stem from the reactivity of cell components with the superoxide intermediate or Li_2O_2 (refs 3,11,14,20–24,27). It is worth noting that carbon is considered stable on oxidation well beyond 4 V in the absence of Li_2O_2, and so is the ethereal electrolyte[15,21,25]. Carbon corrosion and electrolyte decomposition at lower charging voltages were therefore tentatively associated with
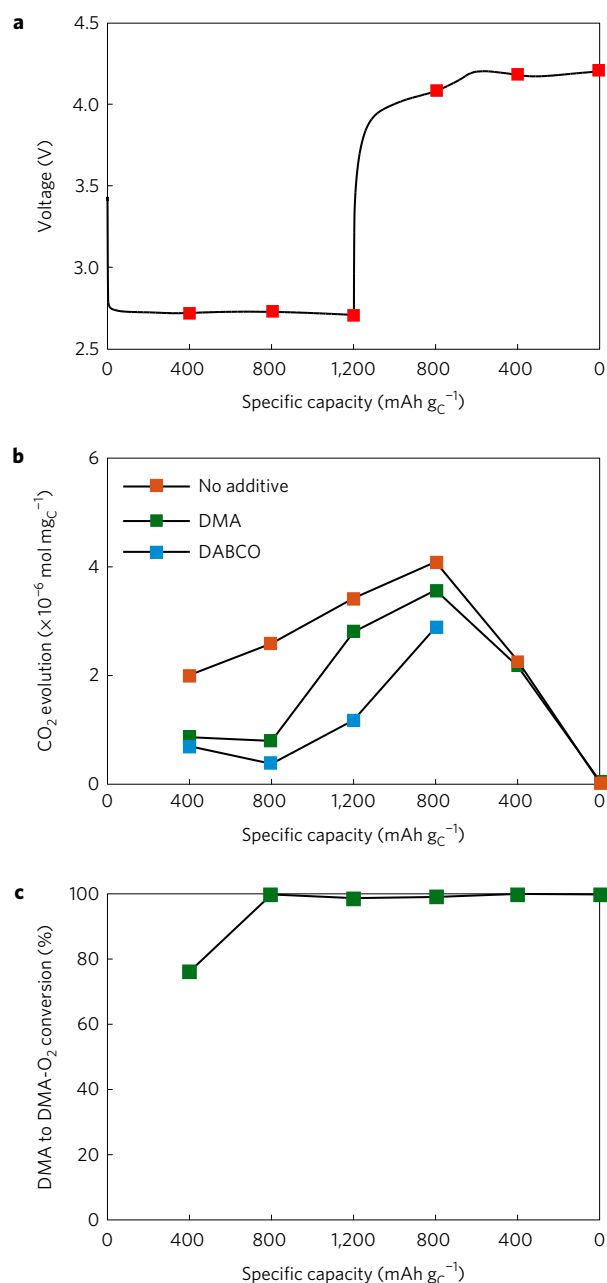
Figure 4 | *Ex situ* analysis of Li–O_2 cathodes run with electrolytes without or with $^1O_2$ trap DMA or quencher DABCO. a, Representative voltage profile during galvanostatic discharge and charge of a porous carbon black electrode at 70 mA g_C^{-1} in O_2-saturated 0.1 M $LiClO_4$ in TEGDME containing either no additive, 30 mM DMA, or 10 mM DABCO. Cells were stopped and analysed at the capacities indicated by the red squares. **b**, Amount of carbonaceous side reaction products per mg carbon. **c**, Fraction of the initial DMA that has reacted to DMA–O_2 via the reaction with $^1O_2$ in the cells that contained DMA as additive.

intermediates of Li_2O_2 oxidation[23,25]. Our operando fluorescence results show that recharging the cell forms $^1O_2$ from the very start of charging, and that it is responsible for at least part of the carbon and electrolyte decomposition from the start of charge.

Turning to the cells with $^1O_2$ trap or quencher, a significant reduction of side products during discharge is evident for both additives (Fig. 4b). Considering first the cell with DMA, the side products amount to between a half and a third of those without additive up to the second sampling point. Thereafter, the side products grow close to the level without the DMA. This can be

explained considering the conversion of DMA to DMA–O_2 (Fig. 4c). At the first sampling point, 76% of the initially present DMA was consumed, and it was fully consumed at the second point. Thereafter, no effect on side product formation can be expected, as is seen in the carbonate/carboxylate data (Fig. 4b). By considering the charge passed at the first sampling point and the DMA conversion, a ratio of ∼1 mol DMA consumed per 10 mol of O_2 reduced can be determined.

Turning to the cells with DABCO as quencher, side products amount to consistently less than in the case of DMA additive and to 10 to 30% of the additive-free case on discharge (Fig. 4b). From these values, we can estimate the fraction of parasitic products on discharge originating from $^1O_2$ to be at least 70%. DABCO is also effective upon charging, and significantly reduces the side products at the first sampling point on charge. We assume the reason for the lower efficiency on charging to be the much higher $^1O_2$ generation on charge than on discharge, as we have shown above with operando fluorescence. With DABCO we could, however, not recharge the cell fully due to the electrochemical stability limit of 3.5 V (Supplementary Fig. 10). Quenchers need to be efficient in the cell environment, electrochemically stable and inert in contact with superoxide and Li_2O_2. These conditions are also the ones distinguishing quenchers required for the Li–O_2 cell from previous uses of quenchers[32].

To prove the effective $^1O_2$ removal by the trap over an entire cycle and to estimate the fraction of the parasitic products during charge that originates from $^1O_2$, we performed operando electrochemical mass spectrometry (OEMS) experiments with cells containing either no additive or 30 mM DMA. Figure 4c has shown that at a discharge capacity of 400 mA g_C^{-1} ∼75% of the DMA had been converted to DMA–O_2. Therefore the mass spectrometry cells were discharged to only 200 mAh g_C^{-1} to ensure that most of the DMA was still present at the end of discharge and could act on charge. The results for charge are shown in Fig. 5 and the full data in Supplementary Figs 13 and 14. During discharge the e^-/O_2 ratio is close to the theoretical value of two, with the ratio being closer with DMA (2.01 e^-/O_2) than without (2.11 e^-/O_2).

With the DMA additive the recharge voltage is lower throughout than without DMA. With DMA the O_2 evolution reaches ∼93% of the theoretical value at the beginning, and fades to ∼2/3 towards the end of charge. Without DMA the O_2 evolution is significantly lower throughout charging, and reaches a maximum of 2/3 of the theoretical value. An even stronger difference is seen in the CO_2 evolution. Significant CO_2 evolution without DMA is contrasted by a 30-fold reduced CO_2 amount with DMA (based on the integral peak area in Supplementary Fig. 14b,f). The strong reduction of the CO_2 amount in combination with the observed O_2 evolution suggests that the majority of the parasitic products that form during charge at voltages below the oxidative stability limit of electrolyte and carbon are due to the occurrence of $^1O_2$. A more detailed discussion for this assignment is given in the Supplementary Discussion in the Supplementary Information. Taken together, the trap and quencher experiments contribute more evidence that $^1O_2$ is responsible for the majority of side products upon discharge and charge, and that suitable additives can effectively reduce side reactions. The required oxidation stability of such additives can be reduced by using redox mediators that greatly reduce the charging voltage[8,42,43].

Pathways to singlet oxygen
The results are consistent with $^1O_2$ being to a large part responsible for commonly reported observations about the O_2 balance and side products. First, on discharge the e^-/O_2 ratio is typically found within several per cent of the ideal value of two despite significant amounts of side products such as Li_2CO_3, Li formate and Li acetate with Li_2O_2 yields reported below 90% (refs 24–26). Second, on charge the
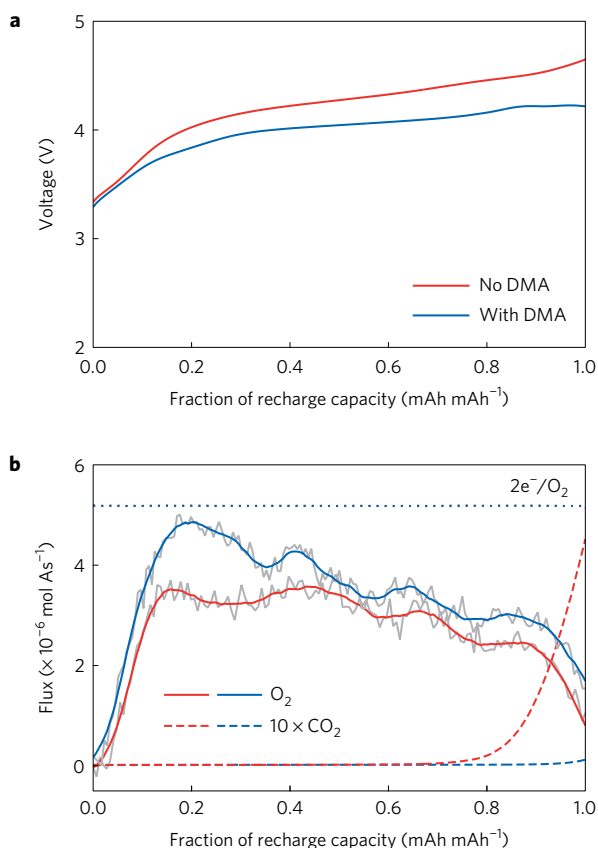
Figure 5 | Operando electrochemical mass spectrometry of Li–O$_2$ cathodes run with electrolytes containing either no additive or the $^1O_2$ trap DMA. a,b, Voltage profiles (**a**) and fluxes of O$_2$, e$^-$ and CO$_2$ (**b**) during galvanostatic charge after the cells have been discharged to 200 mAh g$_C^{-1}$. The porous carbon black electrodes were run at 100 mA g$_C^{-1}$ in 0.1 M LiClO$_4$ in TEGDME containing either no additive or 30 mM DMA. The grey traces in **b** represent the measurements and the blue and red traces the moving average to guide the eye.

e$^-$/O$_2$ ratio typically deviates significantly by more than 10% from the ideal value of two from the start, with the deviation increasing as charging progresses[24]. This deviation goes along with the formation of more of the mentioned solid side products until the charging voltage is sufficiently high to oxidize them to release CO$_2$ and other fragments[15,25,26]. So far the formation of these products could not be consistently explained by the reactivity of the known reactive species superoxide and peroxide alone[14,23–25]. The previous hypothesis that $^1O_2$ can form by charging Li$_2$O$_2$ via Li$_2$O$_2$ → O$_2$ + 2Li$^+$ + 2e$^-$ at voltages exceeding 3.5 to 3.9 V has only recently been verified, with small quantities forming between 3.55 and 3.75 V (refs 11,23,28). The formation of $^1O_2$ on discharge and on charge below 3.5 V was, however, neither suggested on theoretical grounds nor shown experimentally before.

On discharge one possible source of $^1O_2$ is the disproportionation of LiO$_2$ according to

$$2LiO_2 \rightarrow (LiO_2)_2 \rightarrow Li_2O_2 + {}^1O_2 \tag{1}$$
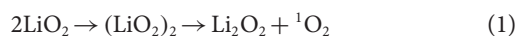
This pathway via a (LiO$_2$)$_2$ dimer appears plausible when the structures and energies of some of these dimers as calculated by Bryantsev *et al.* are considered[44]. They found low lying isomers in both the triplet and singlet state. They have given reaction-free energies for the disproportionation reaction via the lowest triplet dimer to yield $^3O_2$, and it is reasonable to assume that the reaction proceeding via a singlet dimer will yield $^1O_2$. When H$_2$O or other

proton sources are available the superoxide will be protonated to form HOO$^\bullet$, which has been reported to either undergo reduction by superoxide or disproportionate and to be able to release in either case $^1O_2$ in the overall reaction, which is more detailed in the Supplementary Discussion[37,45]:

$$2O_2^- + 2H^+ \rightarrow H_2O_2 + {}^1O_2 \tag{2}$$
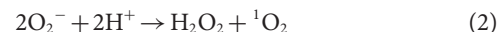
Overall we propose the disproportionation of superoxide in the presence of either Li$^+$ or H$^+$ as the $^1O_2$ source on discharge. On charge we suggest three possible pathways. First, we suggest an analogous path to the one on discharge involving disproportionation of superoxide in the presence of either Li$^+$ or H$^+$. It has been suggested that the first step of charging Li$_2$O$_2$ involves a deintercalation at the surface to form LiO$_2$-like surface species (Li$_2$O$_2$ → LiO$_2$ + Li$^+$ + e$^-$) that further disproportionate to evolve O$_2$ in an overall 2e$^-$/O$_2$ process[46–48]. Here $^1O_2$ may form analogously to equation (1). Similarly, $^1O_2$ may form from proton sources (such as H$_2$O) reacting with the LiO$_2$-like surfaces according to equation (2). This pathway for $^1O_2$ formation can be active from the onset of charge as soon as Li$^+$ and e$^-$ are extracted. Second, a further 1e$^-$ oxidation of the surface LiO$_2$ species (LiO$_2$ → O$_2$ + Li$^+$ + e$^-$) could give $^1O_2$ in an overall 2e$^-$/O$_2$ process. Thermodynamically, $^1O_2$ formation from electrochemical oxidation of superoxide is possible above $E^0_{O_2/LiO_2} + E({}^1\Delta_g \leftarrow {}^3\Sigma_g^-)$. The thermodynamic equilibrium potential $E^0_{O_2/LiO_2}$ was estimated to be between 2.29 and 2.46 V (refs 9,47,49). With an energy difference of ~1 eV between $^1O_2$ and $^3O_2$, a thermodynamic voltage for $^1O_2$ evolution of 3.26 to 3.43 V can be estimated. Finally, above ~3.55 V the known pathway sets in, as suggested before by Scrosati *et al.* and shown by Gasteiger *et al.*, with $^1O_2$ evolving from electrochemical oxidation of Li$_2$O$_2$ in a 2e$^-$/O$_2$ process (Li$_2$O$_2$ → O$_2$ + 2Li$^+$ + 2e$^-$). Note that superoxide is both a proficient source and efficient quencher of $^1O_2$ via equation (3)[50]:

$$O_2^- + {}^1O_2 \rightarrow {}^3O_2 + O_2^- \tag{3}$$
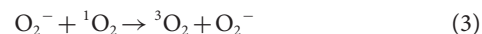
We therefore believe that our observation of less $^1O_2$ on discharge and more on charge in the ether electrolyte results at least in part from the differing abundance of superoxide that can reduce the $^1O_2$ lifetime by quenching, which counteracts equally superoxide-concentration-driven formation. More precisely, net formation of $^1O_2$ will depend on the relative kinetics of all superoxide sources and sinks (with $^1O_2$ being involved in both) and not solely on the superoxide concentration. These sources and sinks are both electrochemical and chemical, and change with discharge and charge, electrolyte, current and potential. We thus further suggest that the current density and electrolyte properties will influence $^1O_2$ formation in much the same way it governs the occurrence of superoxide on discharge and charge below 3.5 V (refs 5,33). Further, charge current will drive $^1O_2$ production if it causes charging voltages above 3.5 V.

Conclusions

By combining complementary methods we could give evidence that $^1O_2$ forms in the Li–O$_2$ battery during discharge and from the onset of charge, and that it can account for a major fraction of the side products formed. Hence, $^1O_2$ arises as perhaps the biggest obstacle for cycling of the Li–O$_2$ cell by reversible formation/decomposition of Li$_2$O$_2$. Presence of trace water, which was already known to increase side reactions, acts at least in part by raising the amount of $^1O_2$ generated. We show that $^1O_2$ traps and quenchers can effectively reduce the side reactions on discharge and charge. The level of $^1O_2$ abundance makes traps less likely to be effective for long-term cycling since they will be consumed rapidly. Physical quenchers are preferred since they are not consumed. Future work

should therefore focus on finding quenchers that are entirely compatible with the cell environment, with the electrochemical potential window, compatibility, and stability against superoxide and peroxide being the most prominent requirements. Equally it needs to be compatible with anodes such as possibly protected Li metal. Alkaline superoxides in the cycling mechanism suggest that the Na–O$_2$ and K–O$_2$ systems would merit investigating whether $^1O_2$ is involved.

Methods

Materials. Ethylene glycol dimethyl ether (DME, >99.0%), 9,10-dimethylanthracene (DMA, >98.0%) and 9,10-diphenylanthracene (DPA, >98.0%) were purchased from TCI Europe. Tetraethylene glycol dimethyl ether (TEGDME, ≥99%), d$_3$-acetonitrile (≥99.8 at.%), LiClO$_4$ (battery grade, dry, 99.9%), 1,4-diazabicyclo[2.2.2]octane (DABCO, ≥99%) and H$_2$O (HPLC grade) were purchased from Sigma-Aldrich. APCI/APPI tuning mix was purchased from Agilent Technologies. Formic acid was bought from Fluka Analytical (puriss. p.a. ∼98%). Acetonitrile (HiPerSolv Prolabo) was purchased from VWR Chemicals. High-purity oxygen (O$_2$ 3.5, >99.95 vol%), high-purity Ar (Ar 5.0, >99.999 vol%) and a mixture of Ar 6.0 and O$_2$ 5.5 (Ar ∼5 vol%) were purchased from Messer Austria. Moisture content of the solvents and electrolytes was measured by Karl Fischer titration using a TitroLine KF trace (Schott). Solvents were purified by distillation and further dried over activated molecular sieves. LiClO$_4$ was dried under vacuum for 24 h at 160 °C. All chemicals were used without any further purification, except for DABCO, which was purified by recrystallization from absolute diethyl ether. The sensitizer palladium(II) *meso*-tetra(4-fluorophenyl)tetrabenzoporphyrin was synthesized according a previously reported procedure[51]. Li$_2$O$_2$ was synthesized according to a previously reported procedure[25].

Operando and *ex situ* electrochemical methods and analysis. Carbon cathodes were fabricated by first making a slurry of Super P carbon (TIMCAL) with polytetrafluoroethylene (PTFE) binder in the ratio 9:1 (m/m) using isopropanol. The slurry was then coated onto a stainless steel mesh current collector. The electrodes were vacuum dried at 200 °C for 24 h and then transferred to an Ar-filled glove box without exposure to air. The glass fibre separators were washed with ethanol and dried overnight at 200 °C under vacuum prior to use. The LiFePO$_4$ counter electrodes were made by mixing partially delithiated active material with Super P and PTFE in the ratio 8:1:1(m/m/m). The electrodes were vacuum dried at 200 °C for 24 h. The counter electrodes had three times the expected capacity of the positive electrode. The electrochemical cells used to investigate cycling were based on a Swagelok design. Typical working electrodes had a carbon mass loading of 1 mg and the cells were assembled with 70 μl electrolyte.

Electrochemical tests were run on either a SP-300 (BioLogic) or BT-2000 (Arbin Instruments) potentiostat/galvanostat. Cyclic voltammograms were recorded in a three-electrode arrangement with a glassy carbon disc working electrode (BAS), a Ag wire pseudo-reference and a Pt wire counter electrode inside a glass cell with a PTFE lid. The cells were run inside an Ar-filled glovebox and purged with high-purity Ar or O$_2$. The redox system Fc/Fc$^+$ was used to reference the measured data versus the Li/Li$^+$ scale.

UV–Vis absorption spectra were recorded on a UV–Vis spectrophotometer Cary 50 (Varian). The molar absorption coefficient of DMA was determined as an average of three independent measurements. Photochemical generation of $^1O_2$ was done by *in situ* photogeneration with the sensitizer palladium(II) *meso*-tetra(4-fluorophenyl)tetrabenzoporphyrin[51]. The sensitizer in the O$_2$-saturated solution was irradiated with a red light-emitting diode light source (643 nm, 7 W).

Fluorescence measurements were recorded on a Fluorolog 3 fluorescence spectrometer (Horiba) equipped with a NIR-sensitive photomultiplier R2658 (300–1,050 nm) from Hamamatsu. The operando fluorescence measurements were performed in the front face mode in kinetic acquisition mode with 0.1 s excitation every 10 s to minimize photobleaching of the DMA. The fluorophore concentration was adjusted to attain an absorbance of ∼0.2 to avoid inner filter effects and to achieve good correlation between the observed fluorescence intensity (proportional to the amount of the absorbed light) and absorbance (proportional to the concentration) of the $^1O_2$ trap. DMA was excited at 378 nm and the emission was detected at 425 nm. The cell for operando fluorescence was a 1 cm absorption high-precision quartz cell (Hellma Analytics) with a purpose-made gas-tight PTFE lid. The working electrode was composed of a Super P/PTFE mixture that was pasted onto a Ti grid. The electrode pre-filled with chemically synthesized Li$_2$O$_2$ was made by mixing the dried electrode material with Li$_2$O$_2$ and pressing the mixture onto the Ti grid. The reference and counter electrodes were partly delithiated LiFePO$_4$ pasted onto Al grids. The assembling was performed in an Ar-filled glovebox. The cell contained a

magnetic stirrer bar, was filled with electrolyte, streamed with O$_2$, further connected with a pure O$_2$ reservoir and hermetically sealed before placing it into the spectrometer. During the measurement the electrolyte was stirred to ensure O$_2$ saturation and uniform DMA concentration. The DMA concentration of 1.6×10^{-5} M for the operando fluorescence was chosen to optimize the sensitivity of the method. At an absorbance of $A = 0.2$ (measurement conditions), 37% of the excitation light is absorbed by the chromophore ($=1–10^{-A}$). In a hypothetical example, reaction of 10% of DMA with $^1O_2$ will decrease absorbance by 10%—that is, from 0.2 to 0.18. Thus, after the reaction 34% of the excitation light will be absorbed by the chromophore. Since the fluorescence intensity is proportional to the amount of the absorbed light, the decrease of fluorescence intensity will be $(37 - 34)/37 \times 100 = 8\%$. Analogous calculation with ten times the DMA concentration ($A = 2$) results in 99% of excitation light absorbed before bleaching and 98.4% of the excitation light absorbed after bleaching. Thus, the decrease of fluorescence intensity would be $(99 - 98.4)/99 \times 100 = 0.6\%$, which is much lower than for the comparably low concentration of the trap. Therefore, a relatively low concentration of DMA is essential for the best sensitivity of operando fluorescence.

Operando NIR spectroscopy to detect the emission of singlet oxygen was performed using a germanium detector (model 261, UDT Instruments, Gamma Scientific Company). It was cooled to −30 °C using a Peltier cooling unit. A longpass-filter with a cut-on wavelength of 1,200 nm and a shortpass-filter with a cutoff wavelength of 1,350 nm (Edmund Optics) were placed directly in front of the sensor. The cell for operando NIR spectroscopy was a 1 mm absorption high precision quartz cell (Hellma Analytics) with a purpose-made gas-tight PTFE lid. The working electrode was an Au-grid electrode (ALS). The reference and counter electrodes were partly delithiated LiFePO$_4$ attached to an Al grid. The cell was placed directly in front of the filters followed by an Au mirror. The optical set-up containing the measurement cell was located in a blackbox to avoid ingress of stray light. The detector signal was amplified by a photodiode amplifier PDA-750 (Terahertz Technologies) and the signal recorded on the potentiostat which controlled the cell.

The operando electrochemical mass spectrometry set-up was built in-house and is similar to the one described previously[52,53]. It consisted of a commercial quadrupole mass spectrometer (Balzers) with a turbomolecular pump (Pfeiffer) that is backed by a membrane pump and leak inlet which samples from the purge gas stream. The electrochemical cell was based on a three-electrode Swagelok design. The set-up was calibrated for different gases (Ar, O$_2$, CO$_2$, H$_2$, N$_2$ and H$_2$O) using calibration mixtures in steps over the anticipated concentration ranges to capture nonlinearity and cross-sensitivity. During measurements either a gas mixture consisting of 95% O$_2$ and 5% Ar or pure Ar was used. All calibrations and quantifications were performed using in-house software. The purge gas system consisted of a digital mass flow controller (Bronkhorst) and stainless steel tubing. The procedure for the carbonate/carboxylate analysis was as described earlier[25].

High-performance liquid chromatography coupled with mass spectrometry (HPLC–MS) was used for determining the degree of the DMA to DMA–O$_2$ conversion. The sample handling was performed inside an Ar-filled glovebox. The electrolyte was extracted from the cell using DME that was then removed by evaporation at room temperature. The residue was dissolved in 50 μl DME and a volume of 1 μl was injected into the HPLC. The HPLC instrument was a 1200 Series (Agilent Technology) with a multiple wavelength UV–Vis detector (Agilent Technology G1365C MWD SL) coupled to a mass spectrometer using atmospheric pressure chemical ionization (APCI) as the ionization method (Agilent Technologies 6120 Quadrupole LC/MS). The samples were analysed by a reversed-phase Poroshell column (120 EC-C8, 3.0 mm × 100 mm, Ø 2.7 μm, Agilent Technology) using a gradient system of acetonitrile (solvent B) and water containing 0.01% formic acid (solvent A). A pre-column (UHPLC 3PK, Poroshell 120 EC-C8 3.0 × 5 mm 2.7 μm, Agilent Technology) was connected before the reversed-phase column. The elution started with 50% solvent B and was then increased to 100% solvent B within 5 min at a flow rate of 0.7 ml min^{-1}. The column was held at 15 °C throughout the measurements. The eluent was monitored via an UV–Vis detector at the wavelengths of 258 nm and 374 nm. The MS signal was recorded starting after 2 min in a mass range of 100–450 m/z using the APCI in the positive ion mode. The MS signal was used to identify the retention times for DMA and DMA–O$_2$. The extent of the transformation of 9,10-dimethylanthracene (DMA) to 9,10-dimethylanthracene-endoperoxide (DMA–O$_2$) was determined from the absorbance at 258 nm and the molar absorption coefficients $\varepsilon_{DMA, 258\,nm}$ and $\varepsilon_{DMA-O_2, 258\,nm}$. The latter was determined from DMA–O$_2$, which was obtained by conversion of DMA with photogenerated $^1O_2$.

References

1. Larcher, D. & Tarascon, J.-M. Towards greener and more sustainable batteries for electrical energy storage. *Nat. Chem.* **7**, 19–29 (2014).
2. Choi, J. W. & Aurbach, D. Promise and reality of post-lithium-ion batteries with high energy densities. *Nat. Rev. Mater.* **1**, 16013 (2016).
3. Luntz, A. C. & McCloskey, B. D. Nonaqueous Li–air batteries: a status report. *Chem. Rev.* **114**, 11721–11750 (2014).
4. Choi, N.-S. *et al.* Challenges facing lithium batteries and electrical double-layer capacitors. *Angew. Chem. Int. Ed.* **51**, 9994–10024 (2012).
5. Lu, Y.-C. *et al.* Lithium-oxygen batteries: bridging mechanistic understanding and battery performance. *Energy Environ. Sci.* **6**, 750–768 (2013).
6. Ren, X. & Wu, Y. A low-overpotential potassium–oxygen battery based on potassium superoxide. *J. Am. Chem. Soc.* **135**, 2923–2926 (2013).
7. Walker, W. *et al.* A rechargeable Li–O$_2$ battery using a lithium nitrate/N,N-dimethylacetamide electrolyte. *J. Am. Chem. Soc.* **135**, 2076–2079 (2013).
8. Lim, H.-D. *et al.* Rational design of redox mediators for advanced Li–O$_2$ batteries. *Nat. Energy* **1**, 16066 (2016).
9. Bender, C. L., Hartmann, P., Vračar, M., Adelhelm, P. & Janek, J. On the thermodynamics, the role of the carbon cathode, and the cycle life of the sodium superoxide (NaO$_2$) battery. *Adv. Energy Mater.* **4**, 1301863 (2014).
10. Laoire, C. O., Mukerjee, S., Plichta, E. J., Hendrickson, M. A. & Abraham, K. M. Rechargeable lithium/TEGDME-LiPF$_6$/O$_2$ battery. *J. Electrochem. Soc.* **158**, A302–A308 (2011).
11. Hassoun, J., Croce, F., Armand, M. & Scrosati, B. Investigation of the O$_2$ electrochemistry in a polymer electrolyte solid-state cell. *Angew. Chem. Int. Ed.* **50**, 2999–3002 (2011).
12. Younesi, R. *et al.* Ether based electrolyte, LiB(CN)$_4$ salt and binder degradation in the Li–O$_2$ battery studied by hard X-ray photoelectron spectroscopy (haxpes). *J. Phys. Chem. C* **116**, 18597–18604 (2012).
13. Amanchukwu, C. V., Harding, J. R., Shao-Horn, Y. & Hammond, P. T. Understanding the chemical stability of polymers for lithium-air batteries. *Chem. Mater.* **27**, 550–561 (2015).
14. Bryantsev, V. S. *et al.* The identification of stable solvents for nonaqueous rechargeable Li–air batteries. *J. Electrochem. Soc.* **160**, A160–A171 (2013).
15. Xu, W. *et al.* The stability of organic solvents and carbon electrode in nonaqueous Li–O$_2$ batteries. *J. Power Sources* **215**, 240–247 (2012).
16. Ottakam Thotiyl, M. M. *et al.* A stable cathode for the aprotic Li–O$_2$ battery. *Nat. Mater.* **12**, 1050–1056 (2013).
17. Adams, B. D. *et al.* Towards a stable organic electrolyte for the lithium oxygen battery. *Adv. Energy Mater.* **5**, 1400867 (2015).
18. Khetan, A., Luntz, A. & Viswanathan, V. Trade-offs in capacity and rechargeability in nonaqueous Li–O$_2$ batteries: solution-driven growth versus nucleophilic stability. *J. Phys. Chem. Lett.* **6**, 1254–1259 (2015).
19. Aetukuri, N. B. *et al.* Solvating additives drive solution-mediated electrochemistry and enhance toroid growth in non-aqueous Li–O$_2$ batteries. *Nat. Chem.* **7**, 50–56 (2015).
20. Black, R. *et al.* Screening for superoxide reactivity in Li–O$_2$ batteries: effect on Li$_2$O$_2$/LiOH crystallization. *J. Am. Chem. Soc.* **134**, 2902–2905 (2012).
21. McCloskey, B. D. *et al.* Twin problems of interfacial carbonate formation in nonaqueous Li–O$_2$ batteries. *J. Phys. Chem. Lett.* **3**, 997–1001 (2012).
22. Younesi, R., Hahlin, M., Björefors, F., Johansson, P. & Edström, K. Li–O$_2$ battery degradation by lithium peroxide (Li$_2$O$_2$): a model study. *Chem. Mater.* **25**, 77–84 (2012).
23. McCloskey, B. D. *et al.* Limitations in rechargeability of Li–O$_2$ batteries and possible origins. *J. Phys. Chem. Lett.* **3**, 3043–3047 (2012).
24. McCloskey, B. D. *et al.* Combining accurate O$_2$ and Li$_2$O$_2$ assays to separate discharge and charge stability limitations in nonaqueous Li–O$_2$ batteries. *J. Phys. Chem. Lett.* **4**, 2989–2993 (2013).
25. Ottakam Thotiyl, M. M., Freunberger, S. A., Peng, Z. & Bruce, P. G. The carbon electrode in nonaqueous Li–O$_2$ cells. *J. Am. Chem. Soc.* **135**, 494–500 (2013).
26. Freunberger, S. A. *et al.* The lithium–oxygen battery with ether-based electrolytes. *Angew. Chem. Int. Ed.* **50**, 8609–8613 (2011).
27. Carboni, M., Marrani, A. G., Spezia, R. & Brutti, S. 1,2-dimethoxyethane degradation thermodynamics in Li–O$_2$ redox environments. *Chem. Eur. J.* **22**, 17188–17203 (2016).
28. Wandt, J., Jakes, P., Granwehr, J., Gasteiger, H. A. & Eichel, R.-A. Singlet oxygen formation during the charging process of an aprotic lithium–oxygen battery. *Angew. Chem. Int. Ed.* **55**, 6892–6895 (2016).
29. Alfano, A. J. & Christe, K. O. Singlet delta oxygen production from a gas–solid reaction. *Angew. Chem. Int. Ed.* **41**, 3252–3254 (2002).
30. Li, Q. *et al.* A spectroscopic study on singlet oxygen production from different reaction paths using solid inorganic peroxides as starting materials. *Bull. Korean Chem. Soc.* **28**, 1656–1660 (2007).
31. Schweitzer, C. & Schmidt, R. Physical mechanisms of generation and deactivation of singlet oxygen. *Chem. Rev.* **103**, 1685–1758 (2003).
32. Ogilby, P. R. Singlet oxygen: there is indeed something new under the sun. *Chem. Soc. Rev.* **39**, 3181–3209 (2010).
33. Aurbach, D., McCloskey, B. D., Nazar, L. F. & Bruce, P. G. Advances in understanding mechanisms underpinning lithium–air batteries. *Nat. Energy* **1**, 16128 (2016).
34. Bryantsev, V. S. *et al.* Predicting solvent stability in aprotic electrolyte Li–air batteries: nucleophilic substitution by the superoxide anion radical (O$_2$$^{•-}$). *J. Phys. Chem. A* **115**, 12399–12409 (2011).
35. Bryantsev, V. S. & Blanco, M. Computational study of the mechanisms of superoxide-induced decomposition of organic carbonate-based electrolytes. *J. Phys. Chem. Lett.* **2**, 379–383 (2011).
36. Bryantsev, V. S. & Faglioni, F. Predicting autoxidation stability of ether- and amide-based electrolyte solvents for Li–air batteries. *J. Phys. Chem. A* **116**, 7128–7138 (2012).
37. Khan, A. U. Direct spectral evidence of the generation of singlet molecular oxygen (1.Delta.g) in the reaction of potassium superoxide with water. *J. Am. Chem. Soc.* **103**, 6516–6517 (1981).
38. Umezawa, N. *et al.* Novel fluorescent probes for singlet oxygen. *Angew. Chem. Int. Ed.* **38**, 2899–2901 (1999).
39. Miyamoto, S., Martinez, G. R., Medeiros, M. H. G. & Di Mascio, P. Singlet molecular oxygen generated from lipid hydroperoxides by the russell mechanism: studies using ^{18}O-labeled linoleic acid hydroperoxide and monomol light emission measurements. *J. Am. Chem. Soc.* **125**, 6172–6179 (2003).
40. Young, R. H. & Brewer, D. R. in *Singlet Oxygen. Reactions with Organic Compounds Polymers* (eds Ranby, B. & Rabek, J. F.) (Wiley, 1978).
41. Enko, B. *et al.* Singlet oxygen-induced photodegradation of the polymers and dyes in optical sensing materials and the effect of stabilizers on these processes. *J. Phys. Chem. A* **117**, 8873–8882 (2013).
42. Chase, G. V. *et al.* Soluble oxygen evolving catalysts for rechargeable metal-air batteries. US patent 13/093,759 (2011).
43. Chen, Y., Freunberger, S. A., Peng, Z., Fontaine, O. & Bruce, P. G. Charging a Li–O$_2$ battery using a redox mediator. *Nat. Chem.* **5**, 489–494 (2013).
44. Bryantsev, V. S., Blanco, M. & Faglioni, F. Stability of lithium superoxide LiO$_2$ in the gas phase: computational study of dimerization and disproportionation reactions. *J. Phys. Chem. A* **114**, 8165–8169 (2010).
45. Koppenol, W. H. Reactions involving singlet oxygen and the superoxide anion. *Nature* **262**, 420–421 (1976).
46. Hummelshoj, J. S., Luntz, A. C. & Norskov, J. K. Theoretical evidence for low kinetic overpotentials in Li–O$_2$ electrochemistry. *J. Chem. Phys.* **138**, 034703 (2013).
47. Kang, S., Mo, Y., Ong, S. P. & Ceder, G. A facile mechanism for recharging Li$_2$O$_2$ in Li–O$_2$ batteries. *Chem. Mater.* **25**, 3328–3336 (2013).
48. Mo, Y., Ong, S. P. & Ceder, G. First-principles study of the oxygen evolution reaction of lithium peroxide in the lithium-air battery. *Phys. Rev. B* **84**, 205446 (2011).
49. Snow, R. H. *Thermodynamic Evaluation of the Possibility of Lithium Superoxide Production* (Aerospace Medical Research Laboratories, 1965).
50. Khan, A. U. Activated oxygen: singlet molecular oxygen and superoxide anion. *Photochem. Photobiol.* **28**, 615–626 (1978).
51. Borisov, S. M. *et al.* New NIR-emitting complexes of platinum(II) and palladium(II) with fluorinated benzoporphyrins. *J. Photochem. Photobiol. A* **201**, 128–135 (2009).
52. Chen, Y., Freunberger, S. A., Peng, Z., Bardé, F. & Bruce, P. G. Li–O$_2$ battery with a dimethylformamide electrolyte. *J. Am. Chem. Soc.* **134**, 7952–7957 (2012).
53. Peng, Z., Freunberger, S. A., Chen, Y. & Bruce, P. G. A reversible and higher-rate Li–O$_2$ battery. *Science* **337**, 563–566 (2012).

Author contributions

N.M. performed the main part of the experiments and analysed the results. B.S., S.G. and C.L. performed cell cycling, MS and NMR experiments. G.A.S. did HPLC analysis. S.A.F., D.K., C.S., O.F. and M.L. discussed the reaction mechanisms. S.M.B. supervised the optical experiments. S.A.F. conceived and directed the research, set up and performed experiments, analysed the results and wrote the manuscript with help of the other authors. All authors contributed to the discussion and interpretation of the results.

Additional information

Supplementary information is available for this paper.

Reprints and permissions information is available at www.nature.com/reprints.

Correspondence and requests for materials should be addressed to S.A.F.

How to cite this article: Mahne, N. *et al.* Singlet oxygen generation as a major cause for parasitic reactions during cycling of aprotic lithium–oxygen batteries. *Nat. Energy* **2**, 17036 (2017).

Publisher's note: Springer Nature remains neutral with regard to jurisdictional claims in published maps and institutional affiliations.

Competing interests

The authors declare no competing financial interests.

Supporting Information: The Role of Singlet Oxygen during Cycling of the Aprotic Lithium-Oxygen Battery

Nika Mahne[1], Bettina Schafzahl[1], Christian Leypold[1], Mario Leypold[3], Sandra Grumm[1], Anita Leitgeb[1], Gernot A. Strohmeier[3,4], Martin Wilkening[1], Denis Kramer[5], Christian Slugovc[1], Sergey M. Borisov[2] and Stefan A. Freunberger[1]*

[1] Institute for Chemistry and Technology of Materials, Graz University of Technology, Stremayrgasse 9, 8010 Graz, Austria
[2] Institute for Analytical Chemistry and Food Chemistry, Graz University of Technology, Stremayrgasse 9, 8010 Graz, Austria
[3] Institute of Organic Chemistry, Graz University of Technology, Stremayrgasse 9, 8010 Graz, Austria
[4] acib - Austrian Centre of Industrial Biotechnology GmbH, Petersgasse 14, 8010 Graz, Austria
[5] Engineering Sciences, University of Southampton, SO17 1BJ, Southampton, UK

Supplementary References

[1] Andrieux, C. P., Hapiot, P. & Saveant, J. M. Mechanism of superoxide ion disproportionation in aprotic solvents. J. Am. Chem. Soc. 109, 3768‑3775, (1987)

[2] Chin, D. H., Chiericato, G., Nanni, E. J. & Sawyer, D. T. Proton-induced disproportionation of superoxide ion in aprotic media. J. Am. Chem. Soc. 104, 1296‑1299, (1982)

[3] Che, Y. et al. Water-induced disproportionation of superoxide ion in aprotic solvents. J. Phys. Chem. 100, 20134‑20137, (1996)

[4] Corey, E. J., Mehrotra, M. M. & Khan, A. U. Water induced dismutation of superoxide anion generates singlet molecular oxygen. Biochemical and Biophysical Research Communications 145, 842‑846, (1987)

[5] Khan, A. U. Direct spectral evidence of the generation of singlet molecular oxygen (1.Delta.G) in the reaction of potassium superoxide with water. J. Am. Chem. Soc. 103, 6516‑6517, (1981)

[6] Koppenol, W. H. Reactions involving singlet oxygen and the superoxide anion. Nature 262, 420‑421, (1976)

[7] Mayeda, E. A. & Bard, A. J. Singlet oxygen. Suppresion of its production in dismutation of superoxide ion by superoxide dismutase. J. Am. Chem. Soc. 96, 4023‑4024, (1974)

[8] Stanley, J. P. Reactions of superoxide with peroxides. J. Org. Chem. 45, 1413‑1418, (1980)
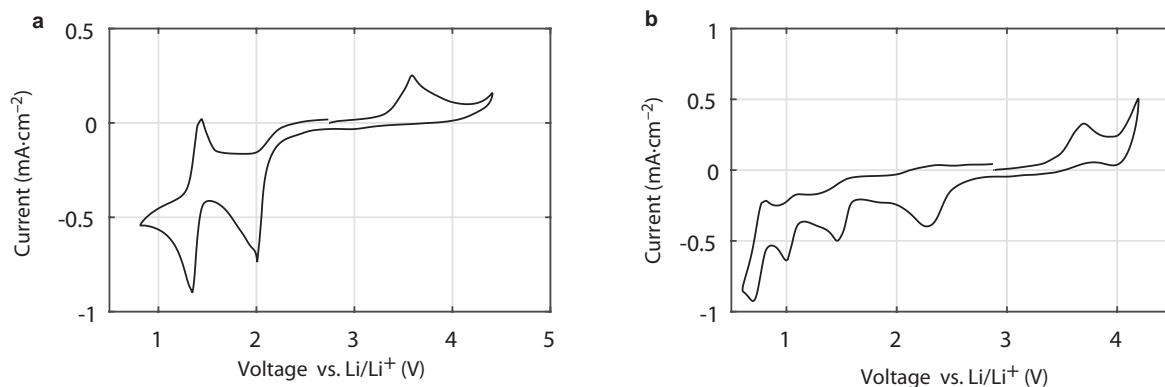
Supplementary Figures

Figure 4.1: Supplementary Figure S1 | Electrochemistry of typical chromophores used in fluorescent $^1O_2$ probes. a, fluorescein, b, rhodamine 6G.

Figure 4.2: Supplementary Figure S2 | Reaction of 9,10-diphenylanthracene with singlet oxygen to 9,10-diphenylanthracene endoperoxide. UV-Vis absorption spectra of a 3.0×10^{-5} M solution of 9,10-diphenylanthracene, in TEGDME containing palladium (II) meso-tetra(4-fluorophenyl)tetrabenzoporphyrin upon illumination for the times indicated.
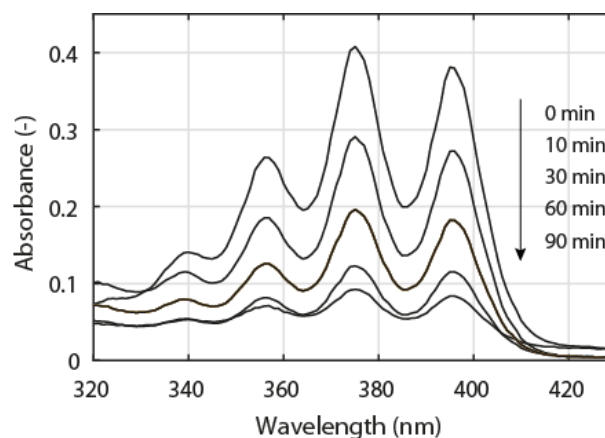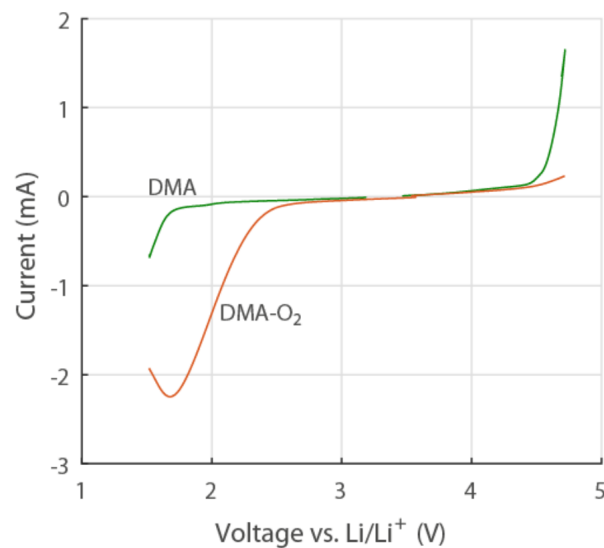

Figure 4.3: Supplementary Figure S3 | Electrochemical stability of 9,10-dimethylanthracene (DMA) and 9,10-dimethylanthracene-endoperoxide (DMA-O₂). Cyclic voltammetry was performed at a 3 mm glassy carbon disc electrode at a sweep rate of $100\,mV\cdot s^{-1}$. First 2 mM DMA and 0.1 M LiClO₄ in TEGDME were measured under Ar-atmosphere, $^1O_2$ was then generated photochemically with the sensitizer palladium (II) meso-tetra(4-fluorophenyl)tetrabenzoporphyrin under O₂-atmosphere and then the formed DMA-O₂ was measured under Ar-atmosphere.
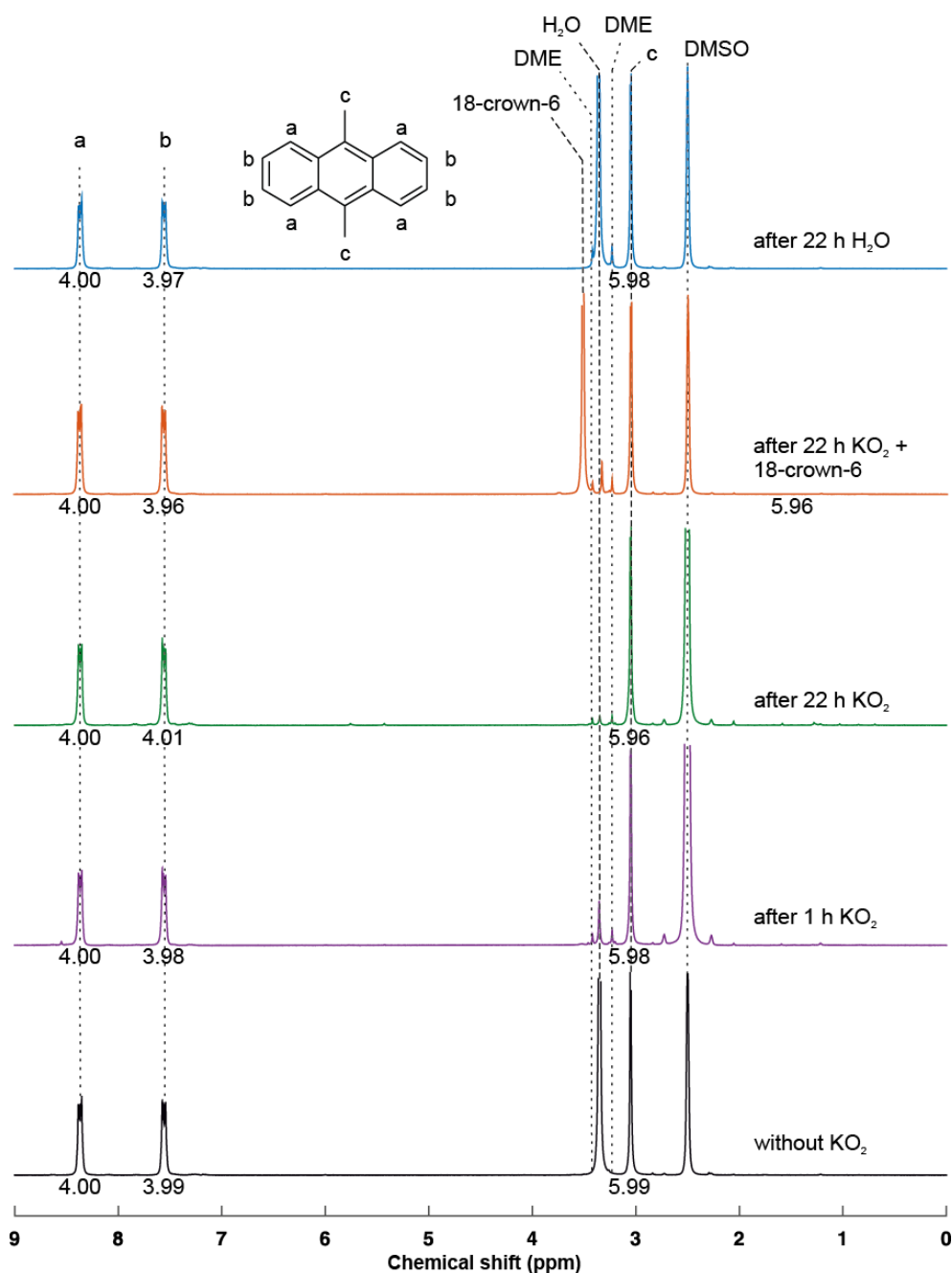
Figure 4.4: Supplementary Figure S4 | Stability of DMA in contact with KO$_2$ and H$_2$O, respectively, in 0.1 M LiClO$_4$ in DME. A solution of $4{\times}10^{-4}$ M DMA in dry DME containing 0.1 M LiClO$_4$ was stirred with an excess of KO$_2$ and ^{1}H-NMR samples taken after the times indicated. The electrolyte solvent was evaporated and the remainder dissolved in d$_6$-DMSO. Analogously for the top-most spectrum 1000 ppm H$_2$O were added to a solution of $4{\times}10^{-2}$ M DMA in DME containing 0.1 M LiClO$_4$ and a ^{1}H-NMR sample taken after the time indicated. The letters a, b, c denote the peaks of the DMA and the numbers underneath the integrals, where the integrals for the proton a is normalized to 4. Peaks associated with DMA, H$_2$O and DMSO are indicated. The small peaks symmetric to the DMSO peak are satellites.

Figure 4.5: Supplementary Figure S5 | UV-Vis absorption spectra of 9,10-dimethylanthracene in contact with KO_2 in DME. A solution of 2.5×10^{-5} M DMA in DME was stirred with an excess of KO_2. UV-Vis absorption spectra were recorded at the times indicated.
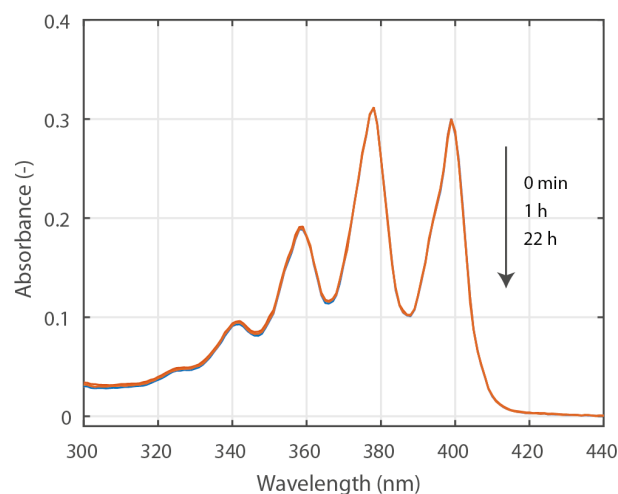
Figure 4.6: Supplementary Figure S6 | Stability of 9,10-dimethylanthracene in presence of 1000 ppm H_2O in 0.1 M $LiClO_4$ in DME. A solution of 3.0×10^{-5} M DMA in DME was stirred in presence of 1000 ppm H_2O. UV-Vis absorption spectra were recorded at the times indicated.
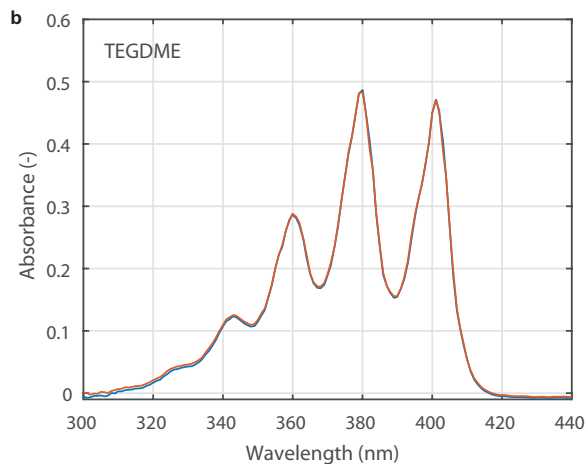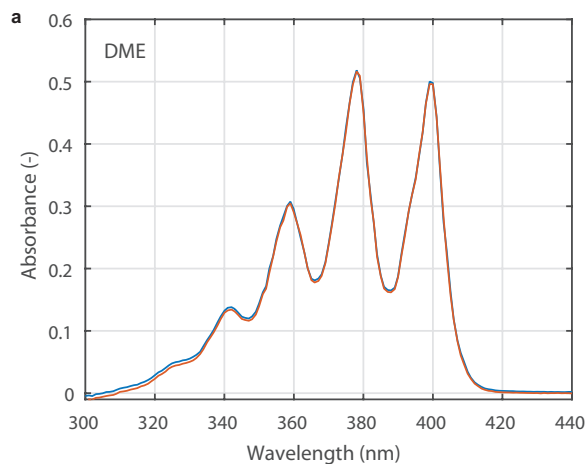

Figure 4.7: Supplementary Figure S7 | Stability of DMA in contact with KO_2 in DME and TEGDME containing 18-crown-6. A solution of 4×10^{-2} M DMA in dry DME or TEGDME containing 0.1 M $LiClO_4$ was mixed with both an excess of KO_2 and the crown ether 18-crown-6 and UV-Vis samples were taken before KO_2 addition and after 22 h. The samples were diluted 1:600 in the respective solvent to yield a measurable absorbance. The absorbance is dimensionless, thus there is no unit.

Figure 4.8: Supplementary Figure S8 | Excitation spectrum (blue trace, $\lambda_{em} = 425$ nm) and the emission spectrum (orange trace, $\lambda_{ex} = 378$ nm) of dimethylanthracene in 0.1 M LiClO$_4$ in TEGDME. The excitation was recorded from 280 nm 420 nm with $\lambda_{em} = 425$ nm. The emission was recorded from 380 nm - 700 nm with $\lambda_{ex} = 378$ nm. An emission spectrum is the wavelength distribution of an emission, measured at a single constant excitation wavelength (λ_{ex}, here 378 nm), which is in general the maximum of emission. Conversely, an excitation spectrum is the dependence of emission intensity, measured at a single emission wavelength (λ_{em}, here 425 nm), upon scanning the excitation wavelength.

Figure 4.9: Supplementary Figure S9 | Quenching of DMA fluorescence by varying O$_2$ concentrations. Emission spectrum of 1.6×10^{-5} M DMA in 0.1 M LiClO$_4$ in TEGDME that is either purged with Ar, dry air or pure O$_2$. The excitation wavelength was $\lambda_{ex = 378\,nm}$.

Figure 4.10: Supplementary Figure S10 | Electrochemical stability of DABCO. Cyclic voltammogram of 2 mM DABCO and 100 mM LiClO$_4$ in TEGDME at an Au-disc electrode with a scan rate of 100 mV·s^{-1}.
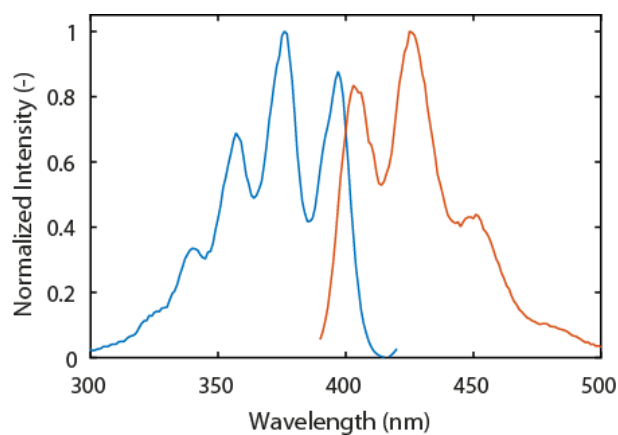
Figure 4.11: Supplementary Figure 11 | Stability of DABCO in contact with KO_2 in $0.1\,M$ $LiClO_4$ in DME. A solution of $9\times10^{-2}\,M$ DABCO in DME containing $0.1\,M$ $LiClO_4$ was stirred with an excess of KO_2 and ^{1}H-NMR samples taken after the times indicated. The electrolyte solvent was evaporated and the remainder dissolved in $CDCl_3$. The peak at $7.26\,ppm$ is the $CHCl_3$ peak.

Figure 4.12: Supplementary Figure 13 | Operando electrochemical mass spectrometry during discharge of Li-O$_2$ cathodes to $200\,\mathrm{mAh \cdot g_C}^{-1}$ with electrolytes containing either no additive or DMA. a to d, without DMA. Voltage profiles (a), fluxes of O$_2$, e$^-$, and CO$_2$ (b), e$^-$/O$_2$ ratio (c), cumulative fluxes of O$_2$ and e$^-$ (d). e to h, with DMA. Voltage profiles (a), fluxes of O$_2$, e$^-$, and CO$_2$ (b), e$^-$/O$_2$ ratio (c), cumulative fluxes of O$_2$ and e$^-$ (d). Cells were run at $70\,\mathrm{mA \cdot g_C}^{-1}$ in $0.1\,\mathrm{M}$ LiClO$_4$ in TEGDME containing either no additive or $30\,\mathrm{mM}$ DMA.

Figure 4.13: Supplementary Figure 14 | Operando electrochemical mass spectrometry during charge of Li-O$_2$ cathodes after discharge to $200\,\text{mAh}\cdot\text{g}_\text{C}{}^{-1}$ with electrolytes containing either no additive or DMA. a to d, without DMA. Voltage profiles (a), fluxes of O$_2$, e$^-$, and CO$_2$ (b), e$^-$/O$_2$ ratio (c), cumulative fluxes of O$_2$ and e$^-$ (d). e to h, with DMA. Voltage profiles (a), fluxes of e$^-$, and CO$_2$ (b), O$_2$, e$^-$/ O$_2$ ratio (c), cumulative fluxes of O$_2$ and e$^-$ (d). Cells were run at $70\,\text{mA}\cdot\text{g}_\text{C}{}^{-1}$ in $0.1\,\text{M}$ LiClO$_4$ in TEGDME containing either no additive or $30\,\text{mM}$ DMA.

Figure 4.14: Supplementary Figure 15 | DMA consumption rate in relation to the theoretical O$_2$ evolution rate as derived from Fig. 2b. a, Voltage profile and DMA concentration as a function of charge time. a, Ratio of DMA consumption rate (dnDMA/dt) and theoretical O$_2$ evolution rate (dnO$_2$/dt, based on current).

Figure 4.15: Supplementary Figure 12 | HPLC-MS analysis of DMA containing electrolyte after operation in an Li-O$_2$ cell for the quantification of DMA and DMA-O$_2$. A typical HPLC chromatogram of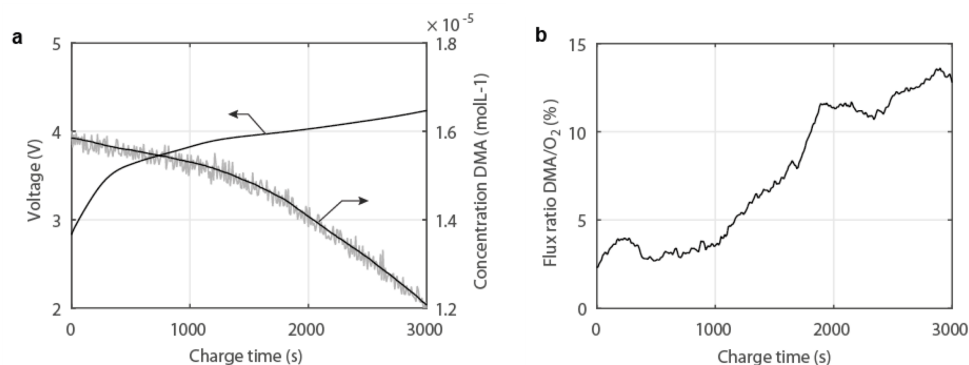 the electrolyte extracted from a Li-O$_2$ cell after galvanostatic cycling. The MS signal was used to identify the retention times for DMA and DMA-O$_2$ which were found to be 4.7 min and 3.1 min. The DMA signal showed up in the mass spectrum at [M+H]$^+$ 207 m/z (calcd 207.1 m/z), whereas the DMA-O$_2$ signal showed up at [M+H]$^+$ 239 m/z (calcd 239.1 m/z).

Supplementary Table

Supplementary Table 1 | Amount of side products as a function of discharge capacity as shown in Fig. 4b.

	No additive		DMA		DABCO
Capacity$_{dis}$ mAh·g$_C^{-1}$	mol CO$_2$/mg$_C^{-1}$ ×10^{-6}	mol CO$_2$/mg$_C^{-1}$ ×10^{-6}	Fraction vs. no additive	mmol CO$_2$/mg$_C^{-1}$ ×10^{-6}	Fraction vs. no additive
400	2.00	0.86	43%	0.67	34%
800	2.60	0.79	32%	0.36	14%
1200	3.43	2.81	82%	1.13	33%
			37 $^+$/$_-$ 6 % average[1]		27 $^+$/$_-$ 10 % average

1) For averaging the sample at 1200 mAh·g$_C^{-1}$ with DMA was ignored since no DMA was present any more from the second sample point onwards, see Fig. 4c.

Supplementary Discussion

Fraction of parasitic reactions due to singlet oxygen

Supplementary Figure S11 investigates the stability of DABCO versus superoxide. DABCO was dissolved in 0.1 M $LiClO_4$ and was stirred with an excess of KO_2 and ^{1}H-NMR samples taken after the times indicated. Even after one week there is no change in the spectra visible. Note that the nitrogen coordinates to the cation and shifts the CH_2 peak in comparison to DABCO alone in the NMR solvent. That the shift after KO_2 addition originates from this is demonstrated by analogously bringing DABCO in contact with K_2CO_3, which affords the same shift as seen in the red trace.

Estimating the fraction of parasitic reactions due to $^1O_2$ is easier on discharge and the value can be estimated from Fig. 4b. As mentioned in the text neither DMA nor DABCO will necessarily divert all formed $^1O_2$ from building side products. Therefore the observed amount of side reaction products is not the same for DMA and DABCO and can be considered as still partially stemming from $^1O_2$. The values are summarized in Supplementary Table 1. DABCO appears to be the more effective agent. In average DMA reduces the amount of side products to ∼37%, DABCO to ∼27%. From the value with DABCO we deduce that some ∼70% of the side products are related to $^1O_2$ on discharge. This supports our interpretation that the majority of parasitic products on discharge is due to $^1O_2$.

Estimating the fraction of the parasitic products due to $^1O_2$ on charge is more difficult than on discharge. This is because of two reasons: First, the discharge product will not be 100% Li_2O_2 and oxidation current therefore not 100% related to Li_2O_2 oxidation. Second, DMA will gradually be consumed on charge and at a much higher rate than on discharge as seen in Fig. 2. Nevertheless, conditions at the start of charge, when most of the DMA is still present will give a good indication.

The O_2 evolution rate missing to the theoretical rate can be considered an approximate measure for the rate at which $^1O_2$ is formed and diverted into building parasitic products. In the case shown in Fig. 5 without DMA (orange curve) roughly one third of the theoretical O_2 evolution rate is missing at the start of charge and more than half missing towards the end of charge. As mentioned a significant part of the current will not be related to Li_2O_2 oxidation and an estimation of the fraction of the parasitic products due to $^1O_2$ on charge will be unreliable.

For the case with DMA (green curve) the discharge product can be regarded as much purer Li_2O_2 than without DMA and the O_2 evolution rate reaches ∼93% of the theoretical value. This value can be understood when considering the rate at which DMA is consumed on charge during the operando

fluorescence measurement in Fig. 2b. It must be kept in mind that in the fluorescence experiments the DMA concentration was only 16 μM which is why the DMA consumption rate will present a lower boundary of the ^{1}O$_2$ formation rate. Supplementary Fig. 15 shows the DMA consumption rate in relation to the theoretical O$_2$ evolution rate (based on current) as derived from Fig. 2b. DMA is consumed (as ^{1}O$_2$ is formed) at a rate of $\sim$4-5% of the O$_2$ evolution rate at the onset of charge, which is in reasonable agreement with the $\sim$93% O$_2$ evolution rate in onli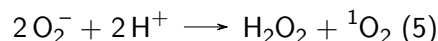ne MS, Fig. 5. Therefore the underevolution of O$_2$ can be interpreted as being linked to ^{1}O$_2$ generation. Further support for this interpretation comes from the comparison of CO$_2$ evolution with and without DMA, Fig. 5b. The dramatic decrease of CO$_2$ with DMA suggests that the species responsible for parasitic products on charge (^{1}O$_2$) has overwhelmingly been eliminated by the DMA (the ^{1}O$_2$ trap). Taken together, these results suggest that the majority of the parasitic products that form during charge are due to the occurrence of ^{1}O$_2$.

Proton assisted singlet oxygen formation

A more in depth discussion of possible ^{1}O$_2$ formation mechanisms is given in the following. When H$_2$O or other proton sources is available the superoxide will be protonated to form HOO$^\bullet$ (Eq. 2) that has been reported to either undergo reduction by superoxide (Eq. 3) or disproportionate (Eq. 4)[1-3] and to be able to release in either case ^{1}O$_2$[4-7].

$$O_2^- + H^+ \longrightarrow HOO^\bullet \quad (2)$$
$$HOO^\bullet + O_2^- \longrightarrow HO_4^- \longrightarrow HOO^- + {}^1O_2 \quad (3)$$
$$2HOO^\bullet + H_2O \longrightarrow H_2O_4 \longrightarrow H_2O_2 + H_2O + {}^1O_2 \quad (4)$$

With the overall reaction

$$2\,O_2^- + 2\,H^+ \longrightarrow H_2O_2 + {}^1O_2 \quad (5)$$

H$_2$O$_2$ is believed to further react with HOO$^-$ to form the highly reactive hydroxyl radical

$$H_2O_2 + HOO^- \longrightarrow H_2O + HO^\bullet + {}^1O_2 \quad (7)$$

whereas the reaction H$_2$O$_2$ + O$_2^-$ $\longrightarrow$ OH$^-$+HO$^\bullet$+^{1}O$_2$ was shown to be unfavourable[8].

Chapter 5

Perspective on Mechanism and Performance of Li-O$_2$ batteries

In this work we review recent progress in understanding the chemistry at the Li-O$_2$ cathode and provide a perspective on major research needs. The potentially significantly higher energy storage of Li-O$_2$ compared to Li-ion motivating this chemistry, however, is very often grossly misunderstood.[125] True performance metrics and their reporting as well as identification of reversibility and quantitative measures to do so are discussed. Li-O$_2$ batteries are special in that the positive electrode does not contain the redox material O$_2$ in the as-built (charged) state that could be taken as a reference for capacity. It has thus become a habit to report capacity with respect to substrate and to cycle at often severely restricted capacity which masks true performance with respect to full electrode weigth and irreversible reactions. There has been major progress with understanding Li$_2$O$_2$ formation and decomposition, and the involved parasitic chemistry. We could recently identify singlet oxygen formation as the predominant cause for parasitic chemistry as opposed to reduced oxygen species as previously thought. We discuss the far reaching implications of this finding on electrolyte and cathode stability, electrocatalysis, and future research needs. These include better understanding of the singlet oxygen formation mechanism, alternatives to commonly used porous cathode design to avoid carbon degradation and formation of parasitic products such as Li$_2$CO$_3$ (which has further consequences, see *Chapter 7*). Additionally, we scrutinize the use of heterogeneous electrocatalysts and solution based cell chemistry by the use of redox mediators to reversibly form and decompose large amounts of the highly insulating Li$_2$O$_2$ and thus to achieve high reversible capacities.

Real progress has been achieved with mechanistic understanding in the last years, which now puts us in a better position than ever to state that the disillusioned view of Li-O$_2$ never leaving the state of a cell with low capacity, rate, energy efficiency and cycle life is too pessimistic. Yet it is unclear whether it can eventually lead to a technology. The many challenges can only be overcome by fundamental understanding of the processes taking place. Only understanding the science may then form the foundation for tackling the engineering challenges.

PERSPECTIVE

Check for updates

Mechanism and performance of lithium–oxygen batteries – a perspective

Nika Mahne,[a] Olivier Fontaine,[bc] Musthafa Ottakam Thotiyl,[d] Martin Wilkening [ID][a] and Stefan A. Freunberger [ID] *[a]

Rechargeable Li–O$_2$ batteries have amongst the highest formal energy and could store significantly more energy than other rechargeable batteries in practice if at least a large part of their promise could be realized. Realization, however, still faces many challenges than can only be overcome by fundamental understanding of the processes taking place. Here, we review recent advances in understanding the chemistry of the Li–O$_2$ cathode and provide a perspective on dominant research needs. We put particular emphasis on issues that are often grossly misunderstood: realistic performance metrics and their reporting as well as identifying reversibility and quantitative measures to do so. Parasitic reactions are the prime obstacle for reversible cell operation and have recently been identified to be predominantly caused by singlet oxygen and not by reduced oxygen species as thought before. We discuss the far reaching implications of this finding on electrolyte and cathode stability, electrocatalysis, and future research needs.

1. Introduction

Raising energy storage beyond the limits of current battery technology has become a societal demand and focus of much Frontier research. The achievable limits of Li-ion batteries with

[a]*Institute for Chemistry and Technology of Materials, Graz University of Technology, Stremayrgasse 9, 8010 Graz, Austria. E-mail: freunberger@tugraz.at*

[b]*Institut Charles Gerhardt Montpellier, UMR 5253, CC 1701, Université Montpellier, Place Eugène Bataillon, 34095 Montpellier Cedex 5, France*

[c]*Réseau sur le Stockage Electrochimique de l'énergie (RS2E), FR CNRS, France*

[d]*Department of Chemistry, Indian Institute of Science Education and Research (IISER), Dr Homi Bhabha Road, Pashan, Pune, 411008, India*

respect to energy, material sustainability and cost will likely not satisfy the needs. This motivates ambitious approaches with 'beyond-intercalation chemistries'.[1–3] They store charge instead of intercalation by fundamentally different reactions. These include replacing the graphite anode by Li metal and intercalation cathodes by the O$_2$ cathode to form the Li–O$_2$ (air) battery, which is considered the battery with the highest specific energy. The O$_2$ cathode comprises a porous, electrolyte filled electron conducting matrix, wherein O$_2$ from the ambiance is reduced on discharge to form Li$_2$O$_2$ and the reverse process on charge.

There is lots of ambiguity of what energy a Li–O$_2$ cell could store, despite it being the motivation for the research. The problem arises from confusing formal capacity (1168 mA h g^{-1},

Nika Mahne obtained her M.Sc. in Chemistry from Graz University of Technology, Austria, and is now Ph.D. student with Stefan Freunberger. Her research is focused on new materials for metal–O$_2$ batteries and in situ and ex situ spectroscopic and analytical methods to elucidate reaction mechanisms, particularly also parasitic chemistry with singlet oxygen.

Olivier Fontaine obtained M.Sc. and Ph.D. in Electrochemistry of ionic liquids from the University Diderot, Paris. After post docs at the Collége de France, Paris and the University of St. Andrews, UK, on Li–O$_2$ reaction mechanism he took up his current position as a lecturer at the Institut Charles Gerhardt, University of Montpellier. He specializes at the interface of analytical electro-chemistry, the chemistry of nanomaterials and functional ionic liquids with both fundamental aspects and applications to energy storage.

2500 mA h cm^{-3} Li$_2$O$_2$) with theoretical capacity (Li$_2$O$_2$ including the minimum electron and ion conductor to allow the storage process O$_2$ + 2e$^-$ + 2Li$^+$ ↔ Li$_2$O$_2$ to take place) and achieved true capacity (Li$_2$O$_2$ including the used electron and ion conductor).[4] We thus shall first discuss realistic performance metrics.

The Li–O$_2$ battery combines two challenging electrodes. In most cases a Li metal anode is used, which is, despite decades of research, still associated with poor coulombic efficiencies.[3] Other high capacity anodes such as Si may also be considered but likely require in either case protection against O$_2$ ingress from the cathode. Until a couple of years ago there was hardly any knowledge on the O$_2$/Li$_2$O$_2$ redox couple in aprotic media. Reactive species involved in the cycling mechanism, which challenge the stability of electrolyte and electrode material, turned out to be another critical research direction. Next to these scientific and materials challenges practical realization further faces engineering challenges with cell construction and air handling. Only understanding the science may thus form the foundation for tackling the engineering.

In this perspective we focus on the science underpinning the O$_2$ cathode. After dealing with performance we discuss the current understanding of Li$_2$O$_2$ formation and decomposition on cycling, followed by measures of reversibility, mechanisms that degrade electrolyte and electrode components and porous cathode design. Potentially transformative ideas start with much enthusiasm and hyped expectations. Thereafter, illusions of low hanging fruit fall and only going the extra mile for true understanding can allow progress to continue. The field of Li–O$_2$ batteries is now in the latter stage. Real progress has been achieved with mechanistic understanding in the last years, which now puts us in a better position than ever to state that the disillusioned view of Li–O$_2$ never leaving the state of a cell with low capacity, rate, energy efficiency and cycle life is too pessimistic. Yet it is unclear whether it can eventually lead to a technology.
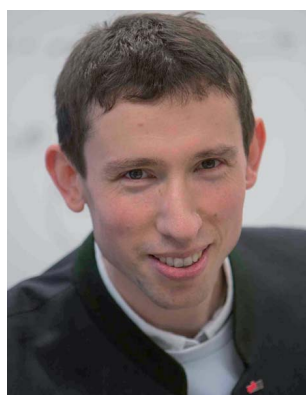
Muhammed Musthafa obtained his PhD in fuel cells from the Indian Institute of Science, Bangalore in collaboration with the Université Joseph Fourier, Grenoble, France. As a research associate at the University of St Andrews he investigated the fundamental (electro)chemistry of the aprotic Li–O$_2$ battery. Since 2014 he is assistant professor at the Indian Institute of Science Education and Research, Pune, India. His research interests include energy storage and conversion and semiconductor electrochemistry with special emphasis on solar fuel production.

2. True performance metrics – myths, reality, and reporting standards

When performance is the argument for research work then data need to stand up to it. An alleged 5 to 10 fold theoretical higher specific energy in comparison to current LIBs is often found as justification when papers on the topic are introduced. However, these numbers stem from very simplistic views and are not realistic even in theory.[4,5]

Departing from the intercalation concept of LIBs does generally not allow for a stable framework in the active material. In the Li–O$_2$ cathode this means that the full volume of Li$_2$O$_2$ forms/disappears during discharge/charge. The basic charge storage process at the cathode is linking the redox moiety O$_2$ to electron and ion transport according to O$_2$ + 2e$^-$ + 2Li$^+$ ↔ Li$_2$O$_2$. However, Li$_2$O$_2$ can, akin to most storage materials, not be cycled anywhere near to the bulk substance. Ion and electron

Martin Wilkening studied Chemistry at the Leibniz University Hannover and obtained his Ph.D. in 2005 with a dissertation on 'Ultraslow Li Motions in Solids', which was awarded the Starck-Promotionspreis of the German Chemical Society (GDCh) and the Wissenschaftspreis Hannover. In 2009 he received the ADUC annual award of the GDCh for his contributions to spin-alignment echo NMR. Since 2011 he has been a Full Professor at the Graz University of Technology. In his workgroup, ion dynamics in solids are studied by NMR and impedance spectroscopy with a focus on nanostructured and amorphous energy materials.

Stefan Freunberger obtained his PhD in Chemistry from ETH Zürich and was post doc at the University of St Andrews, working on many aspects of Li–O$_2$ chemistry. He is now PI at Graz University of Technology, Austria, with research interests embracing energy-storage materials, including alkaline-ion and metal–O$_2$ batteries, electrolytes, and in situ techniques. His research has been recognized by the Srinivasan Young Investigator Award of The Electrochemical Society, the invited visiting professorship la Chaire Total de la Fondation Balard, elected membership of the Austrian Academy of Sciences, and an ERC Starting Grant.

transport are too poor to allow for practical bulk material electrodes. To provide simultaneous contact with ionic pathways to the electrolyte and electronic pathways to the current collector an electrolyte filled porous cathode is used. The capacity at a given initial porosity is determined by the degree of pore filling. Thus, beyond the scale of the single Li_2O_2 particle, the electrode including electrolyte becomes the actual Li^+ host structure, which is required to fulfil the charge storage processes of linking formal ion host particles (Li_2O_2) to electron and ion transport. This introduces a 'super-host structure' that becomes an indispensable and integral part of the cell chemistry in a given electrode architecture and needs to be accounted for when reporting performance.

What capacity could the Li–O_2 cathode with a reasonable super-host structure at best achieve and how does it compare to intercalation chemistries? One can assume that the Li_2O_2 particles could at best be packed with 74% volume occupation into a face centred cubic (fcc) structure, the theoretically limiting case. When charged the porous electrode is filled by electrolyte, which is displaced upon Li_2O_2 growth. Fig. 1 illustrates the relationship between formal host material and the super-host structure, and the maximum true specific capacity, which reaches $\sim$700 mA h g_{total}^{-1}, which is higher than intercalation electrodes.

Metal–O_2 batteries are special in that the positive electrode does not contain the redox material in the charged state that could be taken as a reference for capacity. Thus, it is convenient to report capacities per weight of porous electron conductor. Often, up to several 10 000 mA h g_{carbon}^{-1} are reached as first discharge capacities, which compare superficially favourably with some 100 mA h g^{-1} for intercalation materials.[3,6,7] As a result of difficulties to cycle at full capacity it has become a habit to report cycling at, e.g., 1000 mA h g_{carbon}^{-1}, which may still seem a lot in comparison to LIBs. Formal capacities are, however, easily misjudged since true capacities strongly depend on initial porosity and thus the substrate/electrolyte ratio as indicated by the vertical dotted line in Fig. 1a; true capacity at 1000 mA h g_{carbon}^{-1} grows with decreasing initial porosity due to the growing electrolyte/Li_2O_2 ratio at shallow discharge, Fig. 1b and c.

Limited-capacity cycling often allows simulating a large possible cycle number even if the same cell at full discharge would not reach more than a few cycles and cumulative capacity equating to only a few full cycles. Clearly, overly capacity-limited cycling is not suitable to demonstrate large reversible capacities for many cycles. Yet, it is a common feature of beyond-intercalation chemistries that reasonably capacity-limited cycling can be enabling for cyclability and at the same time yield significant improvement over intercalation if the capacity on a total weight basis is kept in mind as shown in Fig. 1a.[4]

For higher true capacities than intercalation electrodes it is crucial to achieve an as high as possible packing density of Li_2O_2 and to minimize inactive mass and volume. Low packing density and overly restricted depth-of-cycling likely result in no advantage over intercalation electrodes as demonstrated in Fig. 1. Reporting capacity with respect to the porous substrate mass does not reveal whether the electrode performs better
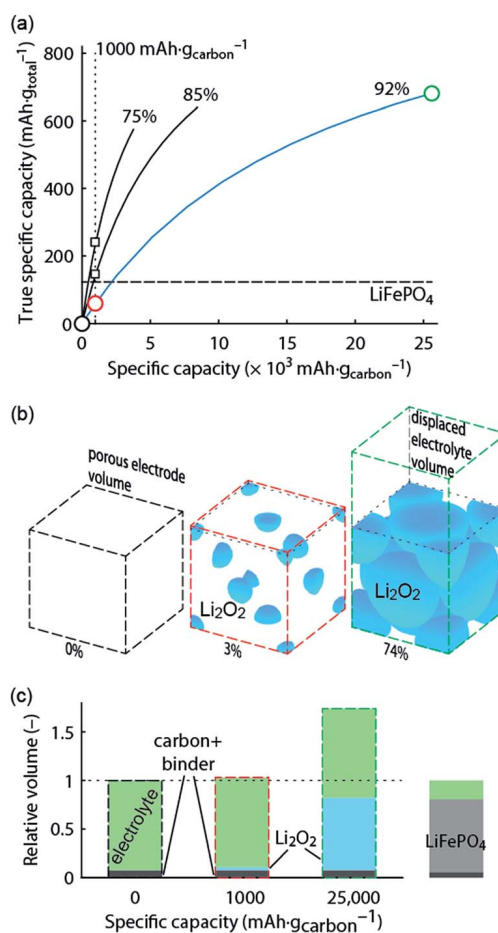

Fig. 1 True electrode capacity with limited capacity cycling. (a) True capacity of a Li–O_2 cathode as a function cycling capacity per mass of carbon substrate for three cases of initial porosity (percentages above the curves). 4% volume are accounted for the binder, and the carbon volume fraction is adapted to yield the initial porosity. At an initial porosity of 92% a Li_2O_2 volume occupation of 74% (fcc packing) corresponds to 80% filling of the available pore space. The same 80% filling of the available pore space is assumed for the other initial porosities. The analogous value for the intercalation material LiFePO$_4$ is shown for comparison. (b) Space filling of spherical Li_2O_2 inside the porous electrode volume with fixed sphere centres and the displaced electrolyte volume (together the super-host structure) at 0, 1000, and 25 000 mA h g_{carbon}^{-1}, respectively (indicated by the circles in a). Sphere sizes are to scale and the numbers indicate their volume occupation in the porous electrode volume. (c) Volumes of the electrode components at these capacities normalized to the full electrode volume in the delithiated state. Values for a LiFePO$_4$ cathode are shown for comparison and demonstrate a very different electrolyte/active material ratio. The figure is adapted from ref. 4 with permission of NPG.

than an intercalation electrode. A fair assessment requires therefore giving capacity per total electrode mass and volume. Unfortunately, many studies do not report the required measures to work out full electrode performance metrics. The following parameters are required to do so with electrode thickness and electrolyte loading being the only parameters beyond typically reported ones.

(1) The thickness of the porous electrode.

(2) The mass fractions of all components (carbon, binder, and electrolyte) as obtained from the mass fractions of all solids, their loading and the loading of electrolyte per unit electrode area.

(3) The volume fractions of all electrode components are then obtained from the mass fractions and the densities.

(4) With these measures it is straightforward to convert the capacity with respect to substrate into true capacity per mass and volume of total electrode including electrolyte.
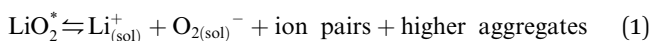
These parameters are easily obtained and journal editors and referees are urged to insist on them being provided for papers. There is no theoretical barrier for the Li–O$_2$ cathode to achieve higher true capacity than intercalation cathodes also in practice; key is high active material packing density and a small inactive/active material ratio.

3. Reaction mechanism at the Li–O$_2$ cathode

With true energy depending crucially on filling of the available pore space, the mechanism by which Li$_2$O$_2$ is forming/decomposing attains paramount importance. It further directly impacts the stability of the cell components and rechargeability *via* the reactivity of the intermediates.

3.1. Li$_2$O$_2$ formation on discharge

The first step of O$_2$ reduction in aprotic Li$^+$-electrolytes results in superoxide (O$_2^-$), which associates with Li$^+$ and in the second step either undergoes a second 1e$^-$ reduction or disproportionates to form Li$_2$O$_2$. Two mechanisms have been proposed for how these steps proceed. The first involves a solution process, where O$_2^-$ is solubilized to precipitate Li$_2$O$_2$ from the electrolyte solution,[8] and the second considers the intermediate as surface bound throughout the process.[9,10] Recently, a unified mechanism was described, where the solution and surface mechanism, respectively, are limiting cases.[11] It describes the partition between these cases by the solubilisation of LiO$_2$ in the equilibrium

$$LiO_2^* \leftrightharpoons Li_{(sol)}^+ + O_{2(sol)}^- + \text{ion pairs} + \text{higher aggregates} \quad (1)$$

where * denotes surface species. In aprotic solvents the solubility of salts is primarily determined by the solvation of the cation, which is correlated with the Gutmann donor number (DN).[8,11,13,14] O$_2^-$ solvation, correlated with the solvent acceptor number (AN), is usually weaker.[13] The typical classes of electrolyte solvents span a wide range of DN from nitriles and sulfones (DN = 14–16), *via* glymes (DN = 20–24), amides (DN ∼ 26), sulfoxide (DN ∼ 30).[11,14] Fig. 2a summarizes these and further parameters influencing surface or solution growth.

Lewis basicity (DN) or acidity (AN) of the electrolyte solution can be influenced by additives. Strongly Li$^+$-coordinating salt anions can shift above equilibrium to the right to a similar extent as the solvent DN by competing association with the Li$^+$ ion between salt anion and O$_2^-$.[15–18] Similarly, Lewis acidic additives enhance O$_2^-$ solvation as shown with water, alcohols, and onium cations.[12,19–22] Unfortunately, both high DN solvents
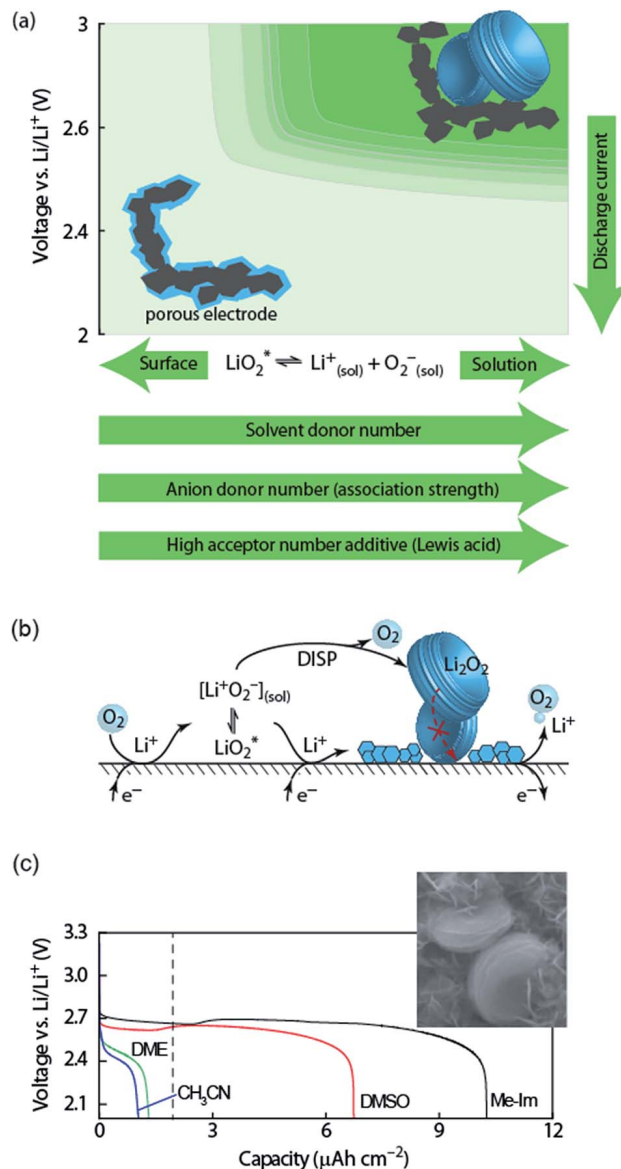

Fig. 2 (a) Parameters determining surface and solution growth. These lead to Li$_2$O$_2$ as either conformal coating of the porous electrode or large particles in the pores. Effective Lewis basicity and acidity of the electrolyte as determined by solvent, salt anion, and additives governs the position of the equilibrium LiO$_2^* \leftrightharpoons Li_{(sol)}^+ + O_{2(sol)}^-$. Solvent and anion donor numbers follow the trend, *e.g.*, nitriles < glymes < amides < sulfoxide and TFSI$^-$ < FSI$^-$ < Tf$^-$ < NO$_3^-$. High AN additives are, for example, H$_2$O and alcohols. Increasing current shifts from solution to surface growth. (b) Reactions involved in the reduction mechanism and effect on charge. (c) Potential *versus* capacity for galvanostatic discharge in various electrolytes containing 0.1 M LiClO$_4$. Me–Im is 1-methylimidazole (DN = 47). The dashed line indicates 7 nm solid layer thickness, which is seen as the limit for e$^-$ tunneling. The insert shows an electron micrograph of toroidal deposits composed of lamellae as obtained from solution growth. (c) is adapted from ref. 11, the insert in (c) is reproduced from ref. 12 with permission from NPG.

and protic additives that favour the solution mechanism can enhance parasitic reactions.[12,20,23,24]

Irrespective of whether the surface or solution pathway prevails, the second electron transfer may either proceed *via* a second 1e$^-$ reduction or disproportionation (Fig. 2b). With

a standard potential of 2.96 V for O_2/Li_2O_2 and $\sim$2.65 V for O_2/O_2^-, the standard potential for O_2^-/Li_2O_2 is at $\sim$3.3 V.[11] The second reduction has therefore at all discharge potentials a strong driving force. However, electrochemical measurements combined with *in situ* Raman have shown that disproportionation dominates at low overpotentials in electrolytes with sufficient solvation strength to support solution growth.[11,25,26] Higher overpotential (higher current) accelerate in the same electrolytes the second reduction at the expense of disproportionation and change the mechanism to surface growth. Recently, it was suggested that not only effective solvation strength controls surface/solution growth based on a correlation between effective solvent polarity (E_τ^N), tuned by additives, and the onset of the second reduction in DMSO.[27] This was explained by an increasing solvent rearrangement energy with polarity and thus, according to Marcus–Hush theory, an increasing activation barrier for the second reduction.

Which mechanism prevails has important consequences for attainable capacity as exemplified in Fig. 2b for variation of solvent DN. The surface mechanism provides little mobility for reduced O_2 species and leads to a conformal coating of the electrode with discharge ceasing after only $\sim$5 to 10 nm, corresponding to low capacity.[10,25] Beyond this thickness the charge transport resistance increases greatly as determined by impedance spectroscopy and does not permit sustaining the current any longer.[10,28] The solution mechanism, in contrast, keeps electrode area open for longer and allows for larger capacity by the growth of large (micrometer sized), toroidal particles composed of lamellae, which can fill larger pores to a bigger extent (insert in Fig. 2c).[25] The electrochemically active surface area does initially not change, followed by gradual surface blocking. The capacity is equally limited by greatly increasing charge transfer resistance R_{CT}.[28] Concurrently, the aspect ratio and average particle size of newly formed Li_2O_2 decreases with progressive discharge.[29] Together, evolution of R_{CT} and particle shape suggest that with shrinking active surface, growing overpotential and local current, the mechanism gradually shifts towards the surface mechanism, which finally causes full passivation.

3.2. Oxidizing Li_2O_2 on charge

Galvanostatic charging of Li–O_2 cathodes is typically characterized by an onset of charging (O_2 evolution) slightly above the OCV at $\sim$3 V and ever increasing voltage as charging progresses. Three underlying phenomena appear to be consolidated although details are still under debate: (1) electrochemical oxidation of Li_2O_2 is possible with low kinetic barriers at high rates; (2) increasingly difficult electron transfer along recharge contributes a minor fraction of the voltage rise; (3) rising voltage is mostly caused by accumulating parasitic products, which cause a mixed potential.

Theoretical studies determined the overpotential at which Li^+, e^-, and O_2 can be removed from Li_2O_2.[30–33] They suggested that Li^+ and e^- can be removed starting below 0.2 V overpotential, leading to either surface LiO_2^* or bulk $Li_{2-x}O_2$ *via* topotactic delithiation.[30–32] Bulk $Li_{2-x}O_2$ appears to comprise

Li_2O_2 and LiO_2 domains.[32] O_2 evolution was initially suggested to have the highest barrier along the whole path.[30,31] Later, a pathway was shown where O_2 evolves facile after progressive delithiation at $\sim$0.3 V overpotential *via* $Li_{2-x}O_2$ to LiO_2, which then decomposes rapidly at $\sim$2.6 V *vs.* Li/Li^+ (Fig. 3a).[32] Low theoretical charge overpotential is in agreement with experiments, albeit experimental overpotential even approaches zero since observed O_2 evolution starts from $\sim$3 V.[9,33,34] Li-deficient $Li_{2-x}O_2$ phases were confirmed by operando X-ray diffraction (Fig. 3b).[35] An open question is whether O_2 release after the initial delithiation proceeds by disproportionation of LiO_2 domains in $Li_{2-x}O_2$ *via* $2LiO_2 \rightarrow Li_2O_2 + Li^+ + O_2$ or *via* further e^- extraction. This is significant as the first pathway would imply that charge could be influenced in much the same way as discharge by the discussed factors governing surface or solution routes, and it could be a key for singlet oxygen formation and thus the major source a parasitic chemistry on charge as discussed in Section 4.3.

An intriguing feature of Li_2O_2 is that the electronic conductivity depends strongly on applied voltage, crystallinity and defects. Increasing potential was postulated to significantly increase conductivity by either reducing the tunnelling barrier or through the formed Li-deficient phases.[36,37] This is consistent with impedance measurements that reveal much higher, capacity limiting, polarization resistance at the end of discharge

Fig. 3 (a) Calculated oxidation potentials for topotactic delithiation of Li_2O_2 to $Li_{2-x}O_2$. The dashed line denotes the O_2/Li_2O_2 standard potential. The inserts show the structures of Li_2O_2 and $Li_{1.75}O_2$.[32] (b) Average Li occupancy during charging of electrochemically formed Li_2O_2 and the associated voltage.[35] (a) and (b) are adapted from ref. 32 and 35, respectively, with permission from the American Chemical Society.

than after switching to charging.[28] Theoretical and experimental work on pure Li_2O_2 have highlighted the importance of defects and grain boundaries on charge transport.[38–40] Orders of magnitude higher conductivity of amorphous *vs.* crystalline Li_2O_2 is consistent with the observed oxidation of amorphous and poorly crystalline Li_2O_2 at lower voltage followed by the crystalline Li_2O_2.[35,38,41]

Important for understanding polarization and limitations of recharge is whether oxidation occurs at the cathode/Li_2O_2 or the Li_2O_2/electrolyte interface. While charge transport through Li_2O_2 will be limiting in the latter case, in the former case the question arises whether Li_2O_2 particles would lose contact, which would impede full recharge. Recent work including with isotope labelled O_2 suggested that e^- transport is limiting during discharge and charge.[9,42] Thus, Li_2O_2 can deposit at the cathode/Li_2O_2 interface beneath previously formed product if Li^+ and O_2 can reach the surface *via* cracks in the Li_2O_2 and this later deposit is oxidized first, eventually leading to a gap between cathode and Li_2O_2 and contributing to increasingly difficult oxidation.[42] Note that the associated rise in impedance accounts only partly for the observed rise in charge potential. The majority of the rise is associated with concomitant parasitic chemistry from the start of charge, which is accelerated with growing potential and predominantly caused by singlet oxygen as discussed in Section 4.3.[24,43–45] Current understanding of solid catalysts for the OER will be discussed in Section 5.2 and redox mediators as charge transfer agents for O_2 reduction and evolution in Section 6.

4. Parasitic chemistry

Typically close to two electrons per one O_2 are consumed on discharge despite significant amounts of a typical pattern of side products being formed including Li_2CO_3, Li formate and Li acetate.[46–49] On charge, the e^-/O_2 ratio typically deviates significantly from two and more of the side products form. Parasitic chemistry is the prime obstacle for reversible Li–O_2 cell cycling and understanding the mechanisms to counteract them is thus the most pressing research need in the field.

4.1. Characteristics of reversible cell reactions

True reversibility of the cathode reaction, $2Li^+ + O_2 + 2e^- \leftrightarrow Li_2O_2$, requires a set of quantities to obey the stoichiometry and to match each other during discharge and subsequent charge. These are:

(A) One mole of O_2 is consumed/released per two moles of electrons flowing on discharge/charge. Thus $e^-/O_2 = 2$.

(B) One mole of O_2 and two moles e^- produce exactly one mole of Li_2O_2 on discharge. On charge two moles e^- consume one mole of Li_2O_2 and release one mole of O_2. Thus:

$$e^-/O_2 = e^-/Li_2O_2 = 2 \text{ and } O_2/Li_2O_2 = 1 \quad (2)$$

The ratio $e^-/O_2 = 2$ is not a strict requirement for a rechargeable Li–O_2 battery if Li_2O_2 is not the discharge product as occasionally claimed.[6,7,50] For example, if Li_2O_2 with a certain fraction of 'LiO_2-like' species or even pure LiO_2 is the

product e^-/O_2 may be lower than 2. However, in any case $e^-/O_2 = e^-/Li_xO_2$ must be identical on discharge and charge. These conditions further imply:

(C) All electrons involved contribute to the oxygen reduction reaction (ORR) or oxygen evolution reaction (OER). Thus, no other gas than O_2 evolves during discharge and charge and no soluble or solid product other than Li_2O_2 (or H_2O_2) is produced.

(D) For cycling with equal capacity on discharge and charge ($Q_{ORR} = Q_{OER}$) the O_2 released on charge matches the amount consumed, thus $n_{O_2,ORR} = n_{O_2,OER}$.

Importantly, none of these measures can be taken for granted to be mutually met even if, for example, $e^-/O_2 \approx 2$ on discharge is fulfilled. Before discussing the current understanding of reactions leading to deviating measures in the next two subsections, we first consider the basic interpretation of the load curves and quantitative analyses to determine the measures (A) to (D).

As discussed in Section 2 on performance metrics, it has become a habit to cycle cells at fixed discharge/charge capacities of, *e.g.*, 1000 mA h $g_{substrate}^{-1}$, thus forcing $Q_{charge} = Q_{discharge}$. Truncating discharge reasonably to avoid full electrode blockage may enable cyclability and appears justified as long as the true capacity based on the total weight is obeyed (see Fig. 1a). Capacity controlled recharge with $Q_{charge} = Q_{discharge}$ is, however, prone to mask parasitic chemistry as illustrated in Fig. 4. The full and dashed blue curves at the bottom show discharge with voltage or capacity limitation, respectively. Basic thermodynamics requires for the charge reaction to be the reverse of the preceding discharge that (a) the voltage remains within the stability of electrolyte and electrode without Li_2O_2 (black dashed line); and (b) that as the capacity approaches full recharge the depletion of the Li_2O_2 must cause the voltage to rise ever steeper before it transits into a plateau at the electrolyte oxidation potential, blue curve in Fig. 4a. Concurrently,
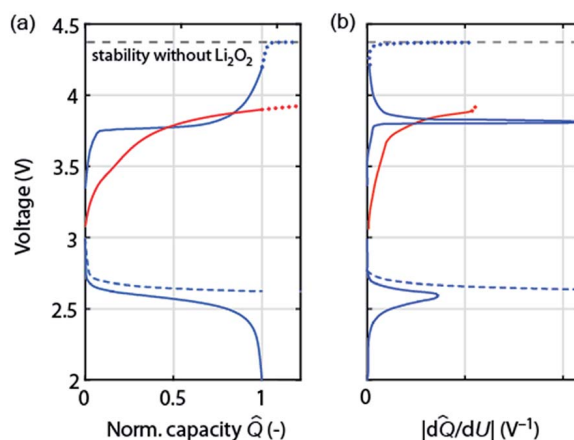

Fig. 4 (a) Schematic of load curves that are either possibly commensurate with cycling according to $Li_2O_2 \rightarrow O_2 + 2Li^+ + 2e^-$ (blue) or with certainty indicating a major fraction of parasitic chemistry (red). The left graph shows the voltage *versus* normalized capacity $\hat{Q}$ (capacity divided by final discharge capacity). Full and dashed curves correspond to voltage or capacity controlled discharge, respectively. Dotted curves on charge extrapolate to overcharge. (b) The corresponding differential capacity curves $|d\hat{Q}/dU|$.

differential capacity $d\hat{Q}/dU$ must approach zero at full recharge irrespective of whether the preceding discharge was limited by voltage or capacity, Fig. 4b (blue curve).

Frequently observed load curves of the type as shown in the red curve in Fig. 4 are, in contrast, with certainty indicating major parasitic chemistry. They are characterized of approaching full recharge flat with $d\hat{Q}/dU$ remaining high, Fig. 4a and b. Flat and high relate here to the rest of the charge curve. Whatever reaction takes place can thus not have finished, can thus not be predominantly Li_2O_2 oxidation, and would continue with a continuing flat plateau if such a cell were over charged (extrapolation by the red dotted curve). An exception is cells with oxidation mediators with large electrolyte-to-Li_2O_2 ratio. Notably, remaining within the oxidative stability window (without Li_2O_2) does not ensure absence of oxidative electrolyte decomposition nor does a lower recharge plateau *per se* (*e.g.*, as a result of electrocatalysts) indicate less parasitic chemistry.[47,51]

Concluding about reversibility by the measures (A) to (D) requires multiple quantitative analyses. Measuring O_2 consumption/evolution has been described by two methods: (A) quantitative operando online mass spectrometry (MS), where the cell head space is continuously or intermittently purged to a MS.[34,48,52] Using an O_2/Ar mix allows also quantification of O_2 consumption and of any other gases evolved on discharge.[19,24,34,53] (B) Measuring the pressure in a closed cell head space.[54] Peroxide or superoxide content of electrodes has been measured *ex situ* using either iodometric titration[49] or spectrophotometry using the coloured $[Ti(O_2^{2-})]^{2+}$ complex.[55] This method was combined with equally MS based quantification of Li_2CO_3 and organic products by treatment with acid and Fenton's reagent to separately evolve CO_2 from inorganic and organic compounds.[44] The latter may also be quantified by ^1H-NMR after immersing the electrode in D_2O which further allows for speciation of the compounds.[47,49] Importantly, all these methods capture the integral electrode. Qualitative spectroscopic or microscopic methods such as Raman, FTIR, XRD, XPS, or SEM cannot replace the mentioned or similar quantitative integral methods and cannot support claims of reversibility.

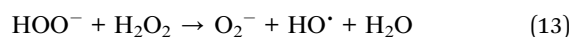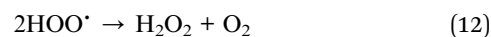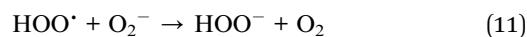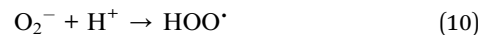## 4.2. Reactions with reduced oxygen species and molecular oxygen

Reduced reactive oxygen species (RROS) are well known for their reactivity with a wide range of organic substrates, which has both been used as a reactant and recognized as a source of unwanted reactions.[56,57] Primary species are O_2^- and O_2^{2-}, which in protic environments form species including $HOO^\bullet$, HOO^-, and $HO^\bullet$. Their nucleophilicity, basicity, and/or radical nature cause reactivity *via* three major routes: nucleophilic substitutions, H^+ and H-atom abstraction. The latter may also proceed with dioxygen in auto-oxidation reactions. Additionally, O_2^- can transfer electrons.

Polarity is introduced to aprotic electrolyte solvents *via* heteroatoms to dissolve a Li-salt. The polarity in turn makes adjacent C and H atoms reactive. After the complete failure of carbonate electrolytes for Li–O_2 chemistry was rightly

associated with the nucleophilicity of O_2^-, this and the other reactivities of RROS and O_2 were taken to explain lesser but significant parasitic chemistry of all so far investigated alternative solvents and cell components.[1,47,58] In the era of computational chemistry the likelihood for this assignment can be judged based on activation and reaction free energies. Bryantsev *et al.* have pioneered this field for O_2^- and O_2 reacting with organic electrolytes *via* nucleophilic substitution, H-atom, and H^+ abstraction.[58–61] Their data for activation energies together with those of other researchers are summarized in Table 1.

Strikingly, activation energies for all considered reactions involving the major classes of solvents – except for the very unstable solvents like carbonates – are too high to expect these reactions to strongly contribute to decomposition. Based on solvent stability screening experiments with KO_2 exposure or the reversibility of the O_2/O_2^- couple, reactions with activation energies beyond 100 kJ mol^{-1} can be considered not to contribute noticeably.[58] Hence, only esters and lactones are expected to react *via* nucleophilic substitution with O_2^- and possibly ethers *via* H-abstraction with Li_2O_2.[62] With ethers, for example, all pathways with O_2^-, Li_2O_2 and O_2 require high activation energy and are strongly endothermic. The only exception is one study that found H-abstraction by Li_2O_2 clusters slightly exothermic with $E^{act} < 100$ kJ mol^{-1}.[62] Solvent coordination with Li^+ was reported to further stabilize against H-abstraction by O_2^- and O_2.[61,63]

In presence of proton sources such as water or weak acids O_2^- forms *via* eqn (10)–(13) $HOO^\bullet$, HOO^-, and $HO^\bullet$, which are more reactive than the primary RROS.[59,64]

$$O_2^- + H^+ \rightarrow HOO^\bullet \tag{10}$$

$$HOO^\bullet + O_2^- \rightarrow HOO^- + O_2 \tag{11}$$

$$2HOO^\bullet \rightarrow H_2O_2 + O_2 \tag{12}$$

$$HOO^- + H_2O_2 \rightarrow O_2^- + HO^\bullet + H_2O \tag{13}$$

HOO^- is a stronger base than O_2^- and more readily abstracts protons to form R^-. $HO^\bullet$ could serve as the initiator to form $R^\bullet$, which undergoes fast and thermodynamically favourable onwards chain reactions in the presence of O_2.[47,61] Overall, direct reactivity of O_2^-, Li_2O_2 and O_2 with the most important classes of non-aqueous solvents for the Li–O_2 cathode is unfavourable. Increasing parasitic chemistry with increasing water content is consistent with the protonated species being more reactive.[12] Yet, much higher side reactions on charge than on discharge, which opposes superoxide occurrence, points at RROS not to be the prime cause for parasitic chemistry.

4.3. Singlet oxygen formation and suppression during discharge and charge

Electrochemically oxidizing Li_2O_2 was hypothesised by Hassoun *et al.* to be able to generate singlet oxygen ($^1\Delta_g$ or $^1O_2$), the highly reactive first excited state of triplet ground state dioxygen ($^3\Sigma_g^-$ or $^3O_2$).[69] This view was motivated by the known formation of $^1O_2$ by chemical oxidation of H_2O_2 or alkaline peroxides.[70] Based

Table 1 Reactions of organic electrolytes with reduced oxygen species and molecular oxygen and their calculated activation energy barriers. ROR′ is generically used for organic moieties with polarizing heteroatoms and reactions may accordingly be translated to, *e.g.*, N or S containing ones
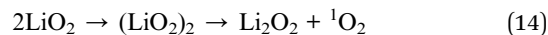
Reactant	Type of reaction	Reaction	E^{act} (kJ mol^{-1})	References
O_2^-	Nucleophilic substitution	$ROR' + O_2^- \rightarrow RO^- + ROO^{\bullet}$ (3)	121–144[a], 105[b], 65–95[c]	58, 61, 65 and 66
	H-atom abstraction	$RH + O_2^- \rightarrow R^{\bullet} + HOO^-$ (4)	129–180[d], 191[e]	61, 63, 65 and 67
	H$^+$ abstraction	$RH + O_2^- \rightarrow R^- + HOO^{\bullet}$ (5)	pK_a > 30 stable[f]	59 and 68
Li_2O_2	Nucleophilic substitution	$ROR' + Li_2O_2 \rightarrow RO^-Li^+ + R'OO^-Li^+$ (6)	134–192[a]	62
	H-atom abstraction	$RH + Li_2O_2 \rightarrow R^{\bullet} + [Li_2O_2\text{-}H^{\bullet}]$ (7)	96–112[a]	62
	H$^+$ abstraction	$RH + Li_2O_2 \rightarrow R^-Li^+ + HOO^-Li^+$ (8)	116–311[a]	62 and 66
O_2	H-atom abstraction	$RH + O_2 \rightarrow R^{\bullet} + HOO^{\bullet}$ (9)	163–183[g], 138–161[h]	61

[a] Dimethoxyethane (DME). [b] Acetonitrile. [c] Carbonate and lactones. [d] Free DME. [e] The DME$_2$–Li$^+$ complex. [f] Examples for pK_a < 30: –CH$_2$–CF$_2$–, polyvinylidene difluoride (PVDF), aliphatic dinitriles, alkyl imides. pK_a > 30: acetonitrile, DMSO, N-alkyl amides and lactams, aliphatic ethers. [g] The lower value for free DME, the higher one for the DME$_2$–Li$^+$ complex. [h] Lactams and amides.
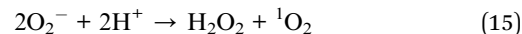
on the reversible potential of Li$_2$O$_2$ formation and the energy difference between triplet and singlet oxygen of ∼1 eV, $^1O_2$ formation in the Li–O$_2$ cell has been considered possible at charging potentials exceeding 3.5 to 3.9 V *vs.* Li/Li$^+$.[54,69,71] The idea was picked up by several reports but could not be verified due to the difficulties with detecting $^1O_2$ except for one work, which identified small quantities of $^1O_2$ between 3.55 and 3.75 V and explained it on thermodynamic grounds for the process Li$_2$O$_2$ → O$_2$ + 2Li$^+$ + 2e$^-$.[18,45,71] It could thus contribute to explaining parasitic chemistry above 3.55 V. Yet it has been found that from the start of charging below 3.5 V both a substantial amount of parasitic products is generated[43,44,49] and that less than 1 mol O$_2$ evolves per 1 mol Li$_2$O$_2$ consumed.[49] Both could not be explained by reactivity of reduced O$_2$ species and formation of $^1O_2$ above 3.55 V.

Recently, Mahne *et al.* have shown that $^1O_2$ forms also during discharge and from the onset of charge and that it accounts for the majority of parasitic reaction products.[24] The amount of $^1O_2$ increases during discharge, early stages of charge, and charging at higher voltages, and is enhanced by the presence of trace water. They used the $^1O_2$ specific conversion of 9,10-dimethylanthracene (DMA) into its endoperoxide (DMA–O$_2$) to probe $^1O_2$ in the cell. Operando fluorescence detection on discharge and charge has shown rather small $^1O_2$ abundance on discharge and significant $^1O_2$ formation immediately after switching to charging, starting from ∼3 V (Fig. 5a). $^1O_2$ on discharge is significant as shown by detecting the degree of DMA to DMA–O$_2$ conversion (Fig. 5c) and the substantially reduced amount of side products with DMA (Fig. 5b). Hence, a suitable $^1O_2$ trap such as DMA can divert $^1O_2$ from reacting with cell components, is, however, quickly consumed at the level of $^1O_2$ abundance. In contrast, a $^1O_2$ quencher physically deactivates singlet into triplet oxygen and is itself not consumed. Using 1,4-diazabicyclo[2.2.2]octane (DABCO) as quencher they have shown even more substantial reduction of side products (Fig. 5b). DABCO has, however, limited electrochemical stability between ∼2.0 and 3.6 V, which allows for only partial recharge. Future work should therefore focus on finding quenchers that meet all requirements including electrochemical potential window, stability with the reduced oxygen species, and high quenching rate.

On discharge one possible source of $^1O_2$ is the disproportionation of LiO$_2$ according to

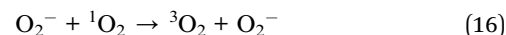$$2LiO_2 \rightarrow (LiO_2)_2 \rightarrow Li_2O_2 + {}^1O_2 \quad (14)$$

This pathway appears plausible when the structures and energies of dimers as calculated by Bryantsev *et al.* are considered.[60] When H$_2$O or other proton sources are available the superoxide will be protonated to form HOO$^{\bullet}$ that has been reported to be able to release $^1O_2$ in the overall reaction.[72,73]

$$2O_2^- + 2H^+ \rightarrow H_2O_2 + {}^1O_2 \quad (15)$$

Overall, the disproportionation of superoxide in the presence of either Li$^+$ or H$^+$ appears to be the $^1O_2$ source on discharge. On charge three possible pathways were suggested. First, an analogous path to the one on discharge involving disproportionation of superoxide in the presence of either Li$^+$ or H$^+$. The LiO$_2$-like surface species could form during the initial charging steps as discussed above[30–32] and $^1O_2$ may form analogously to eqn (14) or (15). This pathway for $^1O_2$ formation can be active from the first onset of charge as soon as Li$^+$ and e$^-$ are extracted. Second, a further 1e$^-$ oxidation of the surface LiO$_2$ species could give $^1O_2$ above $E^0_{O_2/LiO_2} + E(^1\Delta_g \leftarrow {}^3\Sigma_g^-)$. With the thermodynamic equilibrium potential $E^0_{O_2/LiO_2}$ estimated to be between 2.29 and 2.46 V (ref. 32, 74 and 75) and $E(^1\Delta_g \leftarrow {}^3\Sigma_g^-) \sim 1$ eV, a thermodynamic voltage for $^1O_2$ evolution of 3.26 to 3.43 V can be estimated. Finally, above ∼3.55 V the pathway can sets in as suggested by Hassoun *et al.* and shown by Wandt *et al.* with $^1O_2$ evolving by 2e$^-$–oxidation of Li$_2$O$_2$ (Li$_2$O$_2$ → O$_2$ + 2Li$^+$ + 2e$^-$).[69,71]

Superoxide is both a proficient source and efficient quencher of $^1O_2$ *via* eqn (5).[76]

$$O_2^- + {}^1O_2 \rightarrow {}^3O_2 + O_2^- \quad (16)$$

Net formation of $^1O_2$ may depend on the relative kinetics of all superoxide sources and sinks (with $^1O_2$ being involved in both) and not solely on the superoxide concentration. These sources and sinks are both electrochemical and chemical and change with discharge/charge, electrolyte, current, and potential. Current density and electrolyte properties will influence the
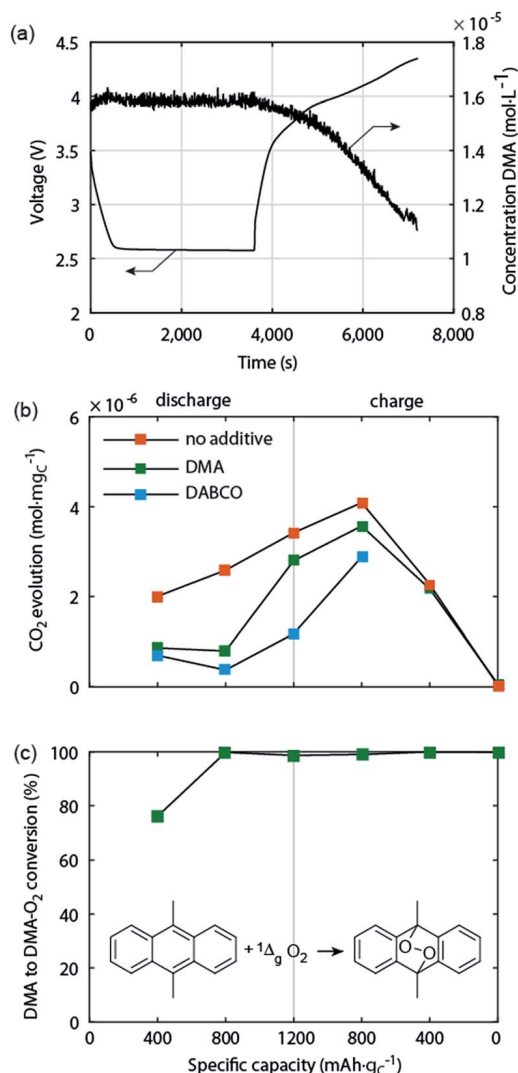
Fig. 5 Singlet oxygen formation and suppression during cycling of the Li–O_2 cathode.[24] (a) Operando fluorescence spectroscopy during galvanostatic discharge and charge of a carbon black electrode in O_2 saturated 0.1 M $LiClO_4$ in tetraglyme containing 1.6×10^{-5} M 9,10-dimethylanthracene (DMA) as singlet oxygen trap. (b) Amount of carbonaceous side reaction products at various sample points during discharge and charge of cells containing no additive, 30 mM trap DMA, or 10 mM quencher DABCO. (c) Fraction of the initial DMA that has reacted to DMA–O_2 in the cells that contained DMA as additive.

$^1O_2$ formation in much the same way as they govern the occurrence of superoxide on discharge and charge below 3.5 V.[77] Charge current will drive $^1O_2$ production if it causes charging voltages above ~3.5 V.

4.4.   Alternative storage media to Li_2O_2

In occasional reports the discharge product was reported to be Li_2O_2 with remaining stable LiO_2 species, resembling the $Li_{2-x}O_2$ intermediate on charge.[50] Based on these findings an Ir–graphene based cathode was reported to cycle in ether electrolyte via crystalline LiO_2.[7] These assignments were mostly based on Raman spectra that can distinguish O–O stretch vibrations in Li_2O_2 and LiO_2. However, it was recently shown

that PVDF binder decomposition can lead to vibrations mimicking those of LiO_2, thus concluding that cycling was not based on LiO_2.[78]

Surprisingly large water contamination up to 1000s of ppm in ether electrolyte has been shown to still lead to Li_2O_2 as the main discharge product rather than LiOH as one could intuitively assume.[12,19] Instead, water promotes discharge via the solution mechanism. Whether Li_2O_2 or LiOH forms was suggested to be governed by the effective pK_a value of water in the electrolyte.[20] A value of 35 in MeCN compared to 47 in DME was used to explain LiOH to form in the former and Li_2O_2 in latter. At water concentrations beyond 1% LiOOH was shown to form together with LiOH.[79] LiOH was also found to form in a $4e^-/O_2$ reduction in presence of LiI.[6,80] Unfortunately, O_2 evolution from LiOH could so far not be shown and apparent cyclability must be accounted for I^- electrochemistry and parasitic chemistry.[80]

Li_2CO_3 not only forms as a result of parasitic reactions, but also when the O_2 supply is CO_2 contaminated.[47,81,82] CO_2 has a high barrier for direct reduction but reacts readily with O_2^- along with the formation of Li_2O_2. If Li_2CO_3 could be decomposed on charge to the educts it would make the cell insensitive to CO_2 in the O_2 supply. While Li_2CO_3 can be decomposed from ~3.8 V, it does not evolve O_2 together with the CO_2, which suggests that reactive intermediate form that decompose the electrolyte.[47,48,82] Apparent cyclability of O_2/CO_2 cells that was shown in some cases was so far not compellingly associated with reversible chemistry. Making Li–O_2 chemistry insensitive to H_2O and CO_2 contamination should thus remain a high priority, which foremost calls for rigorously investigating the associated parasitic chemistry.

5.   Porous cathode design

5.1.   Cathode support

Carbon is the most common porous electron conducting matrix for the O_2–cathode due to low cost, high conductivity, and easily tuneable surface area and pore sizes. Carbon was, however, found to decompose itself on cycling and to promote electrolyte decomposition.[43,44,49,83] Using ^{13}C carbon black and MS analysis of the gaseous and solid products at various stages of cycling, carbon was observed to be relatively stable on discharge despite thermodynamic instability in contact with Li_2O_2; the majority of side products stems from the electrolyte. From the onset of charge, however, carbon decomposes to form Li_2CO_3 with increasing rate as the potential grows.[44,49] Defect rich hydrophilic carbon is both much more vulnerable itself and promotes more strongly electrolyte decomposition during discharge and charge than hydrophobic carbon.[44,83]

As with electrolyte decomposition, the carbon instability was related to O_2^- attack. The perfectly opposing trend of O_2^- abundance – highest on discharge and ever decreasing as charge voltage grows – to decomposition rates makes this interpretation unsatisfactory. Therefore, reactive intermediates on oxidizing Li_2O_2 have been suggested.[44,45] Carbon and electrolyte decomposition rates both follow the trend of $^1O_2$ abundance as shown in Fig. 5a. This is consistent with $^1O_2$ being the

dominant driver of parasitic chemistry; possibly the nearly exclusive one on charge.

Given the instability of carbon, alternative corrosion resistant materials have been sought that at the same time do not promote electrolyte decomposition. They include Ti ceramics and nanoporous Au that allow for more stable cycling.[52,53] For TiC a thin passivating layer of TiO_{2-x} and TiOC has been identified to be critical for stability and conductivity.[53,84] The metallic Magnéli phase Ti_4O_7 was equally shown to form surface TiO_{2-x} and to allow for cyclability similar to Au and TiC.[85] Limited binder stability adds another dimension to cathode design. Standard PVDF binder as used in LIB was found to react with Li_2O_2 and KO_2,[59,78,86,87] but equally $^1O_2$ can be expected to contribute. More stable alternatives include PTFE and Nafion.[86,87]

So far the surface chemistry and electrochemistry of these alternative materials have been investigated with bound nanoparticles forming low porosity electrodes. Achieving high capacity based on the total electrode weight requires, however, filling highly porous electrodes to a large extent with Li_2O_2. High porosity becomes even more important when going from C to much denser metals or ceramics. Fig. 6 shows the relation between initial electrode porosity and maximum achievable true capacity for the examples of C, TiC, and Au. Shaping chemically stable materials into highly porous electrodes, ideally with well beyond 80% porosity, favourable surface area and pore size distribution arises therefore as a major need in the field.

5.2. Heterogeneous electrocatalysis

Typical overpotentials relative to $E^0_{O_2/Li_2O_2} = 2.96$ V are ~0.3 V on discharge and ever rising values on charge from nearly zero to, in some cases, up to 2 V. Inspired by aqueous O_2 electrochemistry, these overpotentials were accounted to sluggish kinetics and evoked substantial efforts in finding efficient electrocatalysts including noble metals, transition metal oxides, and

Fig. 6 Specific capacity of a Li–O$_2$ cathode with respect to total electrode weight including electrolyte as a function initial porosity. The initial porosity is in the fully charged state filled with electrolyte and at full discharge filled to 80% with Li_2O_2; the dotted lines show values for 100% pore filling for comparison. Values are given for cathodes made from C, TiC, or Au respectively. The calculation is analogous to Fig. 1.

doped carbons.[51] Considering the mechanism for Li_2O_2 formation/decomposition, there are, however, three major barriers questioning true effectiveness of solid electrocatalysts. First, ideal Li–O$_2$ chemistry does not involve O–O bond breaking, the step necessitating catalysts in aqueous media. O_2 reduction to superoxide and peroxide, in contrast, has been shown to be facile even on bare glassy carbon.[33] Hence, perceived overpotentials are not due to ORR or OER kinetics. The discharge potential of ~2.7 V is not due to overpotential of the O_2/Li_2O_2 couple but is pinned there by the reversible potential of the O_2/O_2^- couple, the first step on O_2 reduction to Li_2O_2 and can thus not be raised by electrocatalysts.[9,11,88] Li_2O_2 oxidation starts with nearly zero overpotential at ~3 V. Rising charge potentials are, as discussed in Section 3.2, caused partly by increasingly difficult electron transfer in the receding Li_2O_2 and mostly by parasitic chemistry. Second, conventional electrocatalysis would only act on dissolved redox species. On discharge there would thus be no effect beyond monolayers of Li_2O_2 forming with the surface mechanism. Deep discharge with both surface and solution mechanism blocks eventually all electrochemically active surface. Third, charge transport limitations through forming Li_2O_2 (ref. 10 and 36) and mass transport of O_2 through the porous electrode[89] are not addressed by solid catalysts.

Whether solid electrocatalysts can have any effect on charge depends on the processes at the buried cathode/Li_2O_2 interface and how they proceed as charge progresses. Given the insolubility of Li_2O_2, solution transport to open sites can be largely neglected. Proposed pathways for how the substrate could modulate oxidation of adhering Li_2O_2 include *in situ* doping of the deposited Li_2O_2 with slightly soluble transition metal catalysts during discharge, helping charging through enhanced polaron transport or vacancy transport with O_2 evolution at the Li_2O_2/electrolyte interface.[90] Further, supporting metal(oxides) may alter the delithiation kinetics of Li_2O_2 by forming Li-transition metal-oxides.[77] Acting beyond the initial stages of charge requires maintaining the electrode/Li_2O_2 contact, for which the driving force is not clear as the Li_2O_2 closest to the electrode will necessarily be oxidized first. In the case of large Li_2O_2 deposits forming by the solution mechanism, this contact may never be fulfilled for a large fraction of the Li_2O_2. Not least did the habit of extended cycling at a small fraction of a possible single discharge capacity (see Section 2) arise from catalyst studies; with deep discharge the same cells fail typically very quickly, which hints at very limited effectiveness of the catalysts to oxidize large amounts of detached Li_2O_2.

Given the paramount importance of parasitic chemistry, electrocatalysts must not catalyse parasitic reactions with the electrolyte or electrode. Unfortunately, materials identified as electrocatalysts do enhance parasitic reactions.[46,51,91] The exact pathways are not fully clarified but are at least in part associated with the catalyst's ability to dissociate the O–O bond. Concluding about a catalyst's ability to enhance efficiency and cyclability requires quantitative measures of reactant turnover and parasitic products without which any claim is inadequate (see Section 4.1).
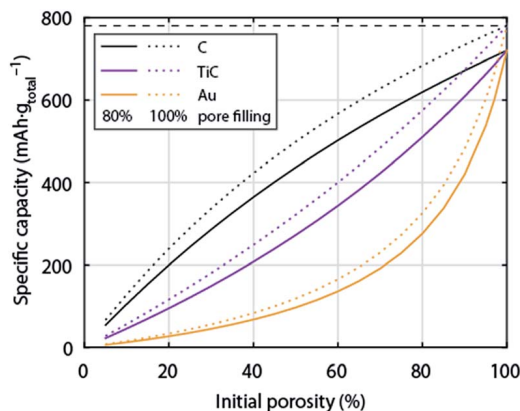
6. Solution based Li–O$_2$ cell chemistry

Lithium peroxide is a good charge storage medium with respect to formal capacity per mass and volume. It is, however, a poor medium with respect to the basic charge storage process of linking the redox moiety O$_2$ to electron and ion transport according to O$_2$ + 2e$^-$ + 2Li$^+$ ↔ Li$_2$O$_2$. However, different to other Li$^+$ storage materials, Li$^+$ and e$^-$ transport into/out of the bulk Li$_2$O$_2$ particle is not even required since growth/dissolution occurs in any case at its surface. This unique feature of Li$_2$O$_2$ can be turned into a major advantage in terms of rate capability. It is the several orders of magnitude slower ion diffusivity compared to liquids that makes batteries slow and the very fast charge transport in liquids that makes supercapacitors high-power devices.[92] Bypassing Li$_2$O$_2$ for ion and electron transport through a phase, where both are facile may thus enable high-power Li–O$_2$ cells. Li$_2$O$_2$ would then only serve as the charge storage medium. While the liquid electrolyte (where the reaction takes place) provides facile ions transport, moving electrons through the liquid is more difficult. Possibilities involve: (a) giving solubility to LiO$_2$ for it to act as an electron mediator during discharge (Fig. 7a, discussed in Section 3); (b) redox mediators that are reduced/oxidized at the e$^-$ conductor, then move through the electrolyte and act in a distant position to reduce O$_2$ or oxidize Li$_2$O$_2$, thereby being regenerated themselves (Fig. 7b).

Two classes of reduction mediators have been put forward. With the first, the reduced mediator M$^-$ reduces O$_2$ in an outer
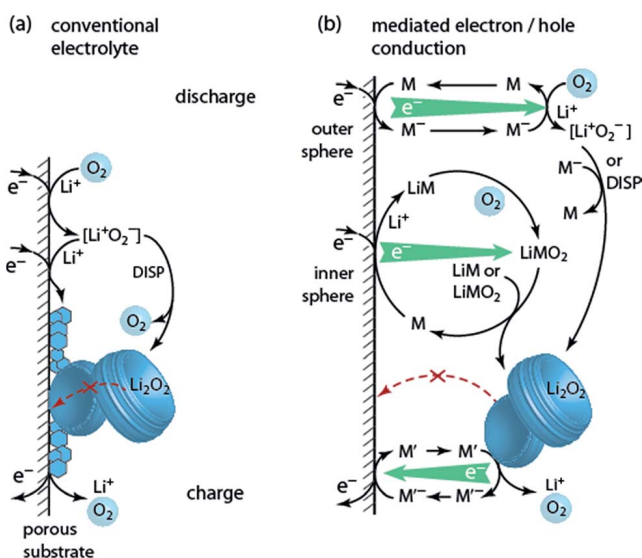
sphere reaction to superoxide, which then can undergo disproportionation or is further reduced by another M$^-$ (Fig. 7b top), with investigated compounds including viologens and *N*-heterocyclic complexes.[93–95] However, improvement of discharge capacity has not clearly been shown. Recently, particular quinones (*e.g.*, 2,5-di-*tert*-butyl-1,4-benzoquinone (DBBQ)) were shown to form Li$_2$O$_2$ in an inner sphere process without the involvement of free superoxide (Fig. 7b centre).[96] Reduction of the quinone in presence of Li$^+$ and O$_2$ leads to a LiM and then LiMO$_2$ complex. The latter is more stable than [Li$^+$O$_2$$^-$] as seen by the higher discharge potential, and disproportionates to form Li$_2$O$_2$ and to reform M. LiMO$_2$ dissolves even in poorly solvating glyme electrolytes, thus mitigating the trade-off between solubilisation and stability and allowing for substantially increased discharge capacity.[23,96] Higher Li$_2$O$_2$ yield with DBBQ than without it was attributed to the absence of free superoxide, albeit it is still unclear whether the quinone suppresses the direct reactivity of the superoxide or ^{1}O$_2$ formation.[24]

Oxidation mediators allow, in principle, charging at nearly zero overpotential and numerous oxidation mediators have been explored for redox potential and O$_2$ evolution efficiency (e$^-$/O$_2$).[18,97–101] Early work has found that some oxidation mediators with suitable redox potentials oxidize Li$_2$O$_2$ with the expected amount of O$_2$ evolution whereas others with similar potential evolve considerably less O$_2$.[98] As mechanistic descriptor for this behaviour, the position of the HOMO level of M$^+$ was put forward, which, when close to the HOMO of the electrolyte, is prone to oxidize the electrolyte.[99]

Two pitfalls have to be considered with mediators: first, oxidation mediators M$^+$ may, instead of oxidizing Li$_2$O$_2$, diffuse out of the cathode to the counter electrode to cause leak-current by shuttling. This may be avoided by using Li$^+$ conducting diffusion barriers such as ceramics or polymers as the separator.[101] Second, mediators, which are mostly organic molecules, are themselves susceptible to decomposition. Both issues make it imperative to quantitatively measure O$_2$ consumption/evolution, Li$_2$O$_2$ formation/oxidation, and parasitic products as discussed in Section 4.1. Any claim about performance improvements is inadequate without these measures.

7. Outlook

The past few years have brought substantial progress with the mechanisms underpinning the operation of the Li–O$_2$ cathode. The two central issues are: (A) discharge/charge mechanisms of Li$_2$O$_2$, and (B) mechanisms of parasitic chemistry.

A central issue was to identify conditions leading to discharge *via* a surface passivating mechanism (giving low capacities) or a solution based process to form large Li$_2$O$_2$ particles (required for high capacities). The deciding factor is the solvation of the superoxide intermediate by tuning the electrolyte interaction with Li$^+$ or O$_2$$^-$ *via* solvent, salt, and additive Lewis basicity/acidity. Oxidation of Li$_2$O$_2$ proceeds at low kinetic overpotentials and can thus, in principle, take place at high rates close to the thermodynamic potential. Rising voltage is predominantly associated with parasitic chemistry.

Fig. 7 (a) Schematic of the reactions taking place in a Li–O$_2$ cathode (O$_2$ + 2Li$^+$ + 2e$^-$ ↔ Li$_2$O$_2$) during discharge and charge in conventional electrolyte. The insoluble and insulating discharge product Li$_2$O$_2$ forms on the surface of the conducting porous substrate and passivates it. Charging is hampered by poor electron transport. (b) Mediated electron/hole transport by mediators M and M′. The reduction mediator M may transfer electrons to O$_2$ either in an outer sphere process or *via* an O$_2$-binding transition state in an inner sphere process.

Nevertheless, when discharge proceeds *via* the solution mechanism charge transport from large Li_2O_2 particles will contribute to overpotentials.

Solution based $Li–O_2$ chemistry appears to be the way forward for high capacity and rate capability and low overpotentials, here, Li_2O_2 only serves as the storage medium and is bypassed for charge transport through the electrolyte by means of redox mediators. With reduction mediators the pathway to form Li_2O_2 may be altered such that there is not free superoxide, which is a source of singlet oxygen and thus parasitic chemistry on discharge. Oxidation mediators allow, in principle, for charging at nearly zero overpotential. The biggest open question with mediators is their own susceptibility to decomposition and their impact on singlet oxygen formation.

The major barrier for reversible cell operation is parasitic chemistry with electrolyte and cell components. The previous view of superoxide and Li_2O_2 being the major cause was only recently overturned by finding that singlet oxygen ($^1O_2$) is formed on discharge and charge; the extent matches the pattern of parasitic reactions with relatively little on discharge and much more on charge. Practical realization of $Li–O_2$ batteries will, in our opinion, stand or fall with mastering $^1O_2$ formation. Open questions centre around: (1) factors influencing $^1O_2$ formation including catalysts, electrolytes, mediators, and protic additives; (2) more detailed insight into formation mechanisms; (3) finding efficient quenchers; (4) finding mechanism to prevent $^1O_2$ formation. Given that so far significant parasitic chemistry is to be expected during both discharge and charge, concluding about the efficacy of any measure to improve capacity, efficiency and cyclability requires quantitative analysis of reactant turnover and parasitic products without which any claim of improvement is inadequate.

There is no theoretical barrier for the $Li–O_2$ cathode to achieve much higher capacity than intercalation cathodes. However, to do so it is crucial to achieve an as high as possible packing density of Li_2O_2 in the cathode and to minimize the inactive mass and volume including the electrolyte. Two habits make tracing progress in the field difficult: first, reporting capacity with respect to porous substrate mass, which represents a minor and widely varying fraction of the total electrode mass; second, reporting cycling at, *e.g.*, 1000 mA h g_{carbon}^{-1}, which may still seem a lot in comparison to intercalation electrodes. The problem is that in most cases true performance is below intercalation electrodes and that it masks irreversible reactions. Therefore, it is important to report performance with respect to the full electrode to allow for a fair assessment of energy, power, and cycle life.

Acknowledgements

Notes and references

1 A. C. Luntz and B. D. McCloskey, *Chem. Rev.*, 2014, **114**, 11721–11750.

2 D. Larcher and J. M. Tarascon, *Nat. Chem.*, 2014, **7**, 19–29.

3 J. W. Choi and D. Aurbach, *Nat. Rev. Mater.*, 2016, **1**, 16013.

4 S. A. Freunberger, *Nat. Energy*, 2017, **2**, 17091 (in press).

5 K. G. Gallagher, S. Goebel, T. Greszler, M. Mathias, W. Oelerich, D. Eroglu and V. Srinivasan, *Energy Environ. Sci.*, 2014, **7**, 1555–1563.

6 T. Liu, M. Leskes, W. Yu, A. J. Moore, L. Zhou, P. M. Bayley, G. Kim and C. P. Grey, *Science*, 2015, **350**, 530–533.

7 J. Lu, Y. Jung Lee, X. Luo, K. Chun Lau, M. Asadi, H.-H. Wang, S. Brombosz, J. Wen, D. Zhai, Z. Chen, D. J. Miller, Y. Sub Jeong, J.-B. Park, Z. Zak Fang, B. Kumar, A. Salehi-Khojin, Y.-K. Sun, L. A. Curtiss and K. Amine, *Nature*, 2016, **529**, 377–382.

8 C. O. Laoire, S. Mukerjee, K. M. Abraham, E. J. Plichta and M. A. Hendrickson, *J. Phys. Chem. C*, 2010, **114**, 9178–9186.

9 B. D. McCloskey, R. Scheffler, A. Speidel, G. Girishkumar and A. C. Luntz, *J. Phys. Chem. C*, 2012, **116**, 23897–23905.

10 V. Viswanathan, K. S. Thygesen, J. S. Hummelshoj, J. K. Norskov, G. Girishkumar, B. D. McCloskey and A. C. Luntz, *J. Chem. Phys.*, 2011, **135**, 214704.

11 L. Johnson, C. Li, Z. Liu, Y. Chen, S. A. Freunberger, J.-M. Tarascon, P. C. Ashok, B. B. Praveen, K. Dholakia and P. G. Bruce, *Nat. Chem.*, 2014, **6**, 1091–1099.

12 N. B. Aetukuri, B. D. McCloskey, J. M. García, L. E. Krupp, V. Viswanathan and A. C. Luntz, *Nat. Chem.*, 2015, **7**, 50–56.

13 D. G. Kwabi, V. S. Bryantsev, T. P. Batcho, D. M. Itkis, C. V. Thompson and Y. Shao-Horn, *Angew. Chem., Int. Ed.*, 2016, **55**, 3129–3134.

14 V. Gutmann, *Coord. Chem. Rev.*, 1976, **18**, 225–255.

15 C. M. Burke, V. Pande, A. Khetan, V. Viswanathan and B. D. McCloskey, *Proc. Natl. Acad. Sci. U. S. A.*, 2015, **112**, 9293–9298.

16 D. Sharon, D. Hirsberg, M. Salama, M. Afri, A. A. Frimer, M. Noked, W. Kwak, Y.-K. Sun and D. Aurbach, *ACS Appl. Mater. Interfaces*, 2016, **8**(8), 5300–5307.

17 I. Gunasekara, S. Mukerjee, E. J. Plichta, M. A. Hendrickson and K. M. Abraham, *J. Electrochem. Soc.*, 2015, **162**, A1055–A1066.

18 D. Sharon, D. Hirsberg, M. Afri, F. Chesneau, R. Lavi, A. A. Frimer, Y.-K. Sun and D. Aurbach, *ACS Appl. Mater. Interfaces*, 2015, **7**, 16590–16600.

19 K. U. Schwenke, M. Metzger, T. Restle, M. Piana and H. A. Gasteiger, *J. Electrochem. Soc.*, 2015, **162**, A573–A584.

20 D. G. Kwabi, T. P. Batcho, S. Feng, L. Giordano, C. V. Thompson and Y. Shao-Horn, *Phys. Chem. Chem. Phys.*, 2016, **18**, 24944–24953.

21 C. Li, O. Fontaine, S. A. Freunberger, L. Johnson, S. Grugeon, S. Laruelle, P. G. Bruce and M. Armand, *J. Phys. Chem. C*, 2014, **118**, 3393–3401.

22 X. Gao, Z. P. Jovanov, Y. Chen, L. R. Johnson and P. G. Bruce, *Angew. Chem., Int. Ed.*, 2017, **56**(23), 6539–6543.

23 A. Khetan, A. Luntz and V. Viswanathan, *J. Phys. Chem. Lett.*, 2015, **6**, 1254–1259.

24 N. Mahne, B. Schafzahl, C. Leypold, M. Leypold, S. Grumm, A. Leitgeb, G. A. Strohmeier, M. Wilkening, O. Fontaine, D. Kramer, C. Slugovc, S. M. Borisov and S. A. Freunberger, *Nat. Energy*, 2017, **2**, 17036.

25 B. D. Adams, C. Radtke, R. Black, M. L. Trudeau, K. Zaghib and L. F. Nazar, *Energy Environ. Sci.*, 2013, **6**, 1772–1778.

26 Y. Zhang, X. Zhang, J. Wang, W. C. McKee, Y. Xu and Z. Peng, *J. Phys. Chem. C*, 2016, **120**, 3690–3698.

27 C. J. Bondue, P. P. Bawol, A. A. Abd-El-Latif, P. Reinsberg and H. Baltruschat, *J. Phys. Chem. C*, 2017, **121**, 8864–8872.

28 K. B. Knudsen, T. Vegge, B. D. McCloskey and J. Hjelm, *J. Electrochem. Soc.*, 2016, **163**, A2065–A2071.

29 Z. Li, S. Ganapathy, Y. Xu, J. R. Heringa, Q. Zhu, W. Chen and M. Wagemaker, *Chem. Mater.*, 2017, **29**, 1577–1586.

30 Y. Mo, S. P. Ong and G. Ceder, *Phys. Rev. B: Condens. Matter Mater. Phys.*, 2011, **84**, 205446.

31 J. S. Hummelshoj, A. C. Luntz and J. K. Norskov, *J. Chem. Phys.*, 2013, **138**, 034703.

32 S. Kang, Y. Mo, S. P. Ong and G. Ceder, *Chem. Mater.*, 2013, **25**, 3328–3336.

33 V. Viswanathan, J. K. Nørskov, A. Speidel, R. Scheffler, S. Gowda and A. C. Luntz, *J. Phys. Chem. Lett.*, 2013, 556–560, DOI: 10.1021/jz400019y.

34 Y. Chen, S. A. Freunberger, Z. Peng, F. Bardé and P. G. Bruce, *J. Am. Chem. Soc.*, 2012, **134**, 7952–7957.

35 S. Ganapathy, B. D. Adams, G. Stenou, M. S. Anastasaki, K. Goubitz, X.-F. Miao, L. F. Nazar and M. Wagemaker, *J. Am. Chem. Soc.*, 2014, **136**, 16335–16344.

36 A. C. Luntz, V. Viswanathan, J. Voss, J. B. Varley, J. K. Norskov, R. Scheffler and A. Speidel, *J. Phys. Chem. Lett.*, 2013, **4**(20), 3494–3499.

37 M. D. Radin and D. J. Siegel, *Energy Environ. Sci.*, 2013, **6**, 2370–2379.

38 Y. Zhang, Q. Cui, X. Zhang, W. C. McKee, Y. Xu, S. Ling, H. Li, G. Zhong, Y. Yang and Z. Peng, *Angew. Chem., Int. Ed.*, 2016, **55**, 10717–10721.

39 A. Dunst, V. Epp, I. Hanzu, S. A. Freunberger and M. Wilkening, *Energy Environ. Sci.*, 2014, **7**, 2739–2752.

40 O. Gerbig, R. Merkle and J. Maier, *Adv. Mater.*, 2013, **25**, 3129–3133.

41 F. Tian, M. D. Radin and D. J. Siegel, *Chem. Mater.*, 2014, **26**, 2952–2959.

42 J. Wang, Y. Zhang, L. Guo, E. Wang and Z. Peng, *Angew. Chem., Int. Ed.*, 2016, **55**(17), 5201–5205.

43 B. D. McCloskey, A. Speidel, R. Scheffler, D. C. Miller, V. Viswanathan, J. S. Hummelshøj, J. K. Nørskov and A. C. Luntz, *J. Phys. Chem. Lett.*, 2012, **3**, 997–1001.

44 M. M. Ottakam Thotiyl, S. A. Freunberger, Z. Peng and P. G. Bruce, *J. Am. Chem. Soc.*, 2013, **135**, 494–500.

45 R. Black, J.-H. Lee, B. Adams, C. A. Mims and L. F. Nazar, *Angew. Chem., Int. Ed.*, 2013, **52**, 392–396.

46 S. A. Freunberger, Y. Chen, N. E. Drewett, L. J. Hardwick, F. Bardé and P. G. Bruce, *Angew. Chem., Int. Ed.*, 2011, **50**, 8609–8613.

47 S. A. Freunberger, Y. Chen, Z. Peng, J. M. Griffin, L. J. Hardwick, F. Bardé, P. Novák and P. G. Bruce, *J. Am. Chem. Soc.*, 2011, **133**, 8040–8047.

48 B. D. McCloskey, D. S. Bethune, R. M. Shelby, G. Girishkumar and A. C. Luntz, *J. Phys. Chem. Lett.*, 2011, **2**, 1161–1166.

49 B. D. McCloskey, A. Valery, A. C. Luntz, S. R. Gowda, G. M. Wallraff, J. M. Garcia, T. Mori and L. E. Krupp, *J. Phys. Chem. Lett.*, 2013, 2989–2993, DOI: 10.1021/jz401659f.

50 J. Yang, D. Zhai, H.-H. Wang, K. C. Lau, J. A. Schlueter, P. Du, D. J. Myers, Y.-K. Sun, L. A. Curtiss and K. Amine, *Phys. Chem. Chem. Phys.*, 2013, **15**, 3764–3771.

51 B. D. McCloskey, R. Scheffler, A. Speidel, D. S. Bethune, R. M. Shelby and A. C. Luntz, *J. Am. Chem. Soc.*, 2011, **133**, 18038–18041.

52 Z. Peng, S. A. Freunberger, Y. Chen and P. G. Bruce, *Science*, 2012, **337**, 563–566.

53 M. M. Ottakam Thotiyl, S. A. Freunberger, Z. Peng, Y. Chen, Z. Liu and P. G. Bruce, *Nat. Mater.*, 2013, **12**, 1050–1056.

54 B. D. McCloskey, D. S. Bethune, R. M. Shelby, T. Mori, R. Scheffler, A. Speidel, M. Sherwood and A. C. Luntz, *J. Phys. Chem. Lett.*, 2012, **3**, 3043–3047.

55 P. Hartmann, C. L. Bender, J. Sann, A. K. Durr, M. Jansen, J. Janek and P. Adelhelm, *Phys. Chem. Chem. Phys.*, 2013, **15**, 11661–11672.

56 D. T. Sawyer and J. S. Valentine, *Acc. Chem. Res.*, 1981, **14**, 393–400.

57 D. Aurbach, M. Daroux, P. Faguy and E. Yeager, *J. Electroanal. Chem.*, 1991, **297**, 225–244.

58 V. S. Bryantsev, V. Giordani, W. Walker, M. Blanco, S. Zecevic, K. Sasaki, J. Uddin, D. Addison and G. V. Chase, *J. Phys. Chem. A*, 2011, **115**, 12399–12409.

59 V. S. Bryantsev, *Chem. Phys. Lett.*, 2013, **558**, 42–47.

60 V. S. Bryantsev, M. Blanco and F. Faglioni, *J. Phys. Chem. A*, 2010, **114**, 8165–8169.

61 V. S. Bryantsev and F. Faglioni, *J. Phys. Chem. A*, 2012, **116**, 7128–7138.

62 R. S. Assary, K. C. Lau, K. Amine, Y.-K. Sun and L. A. Curtiss, *J. Phys. Chem. C*, 2013, **117**, 8041–8049.

63 B. Liu, W. Xu, P. Yan, X. Sun, M. E. Bowden, J. Read, J. Qian, D. Mei, C.-M. Wang and J.-G. Zhang, *Adv. Funct. Mater.*, 2016, **26**, 605–613.

64 C. P. Andrieux, P. Hapiot and J. M. Saveant, *J. Am. Chem. Soc.*, 1987, **109**, 3768–3775.

65 B. Genorio, J. Staszak-Jirkovský, R. S. Assary, J. G. Connell, D. Strmcnik, C. E. Diesendruck, P. P. Lopes, V. R. Stamenkovic, J. S. Moore, L. A. Curtiss and N. M. Markovic, *J. Phys. Chem. C*, 2016, **120**, 15909–15914.

66 Z. Zhang, J. Lu, R. S. Assary, P. Du, H.-H. Wang, Y.-K. Sun, Y. Qin, K. C. Lau, J. Greeley, P. C. Redfern, H. Iddir, L. A. Curtiss and K. Amine, *J. Phys. Chem. C*, 2011, **115**, 25535–25542.

67 M. Carboni, A. G. Marrani, R. Spezia and S. Brutti, *Chem.–Eur. J.*, 2016, **22**, 17188–17203.

68 A. Khetan, H. Pitsch and V. Viswanathan, *J. Phys. Chem. Lett.*, 2014, **5**, 2419–2424.

69 J. Hassoun, F. Croce, M. Armand and B. Scrosati, *Angew. Chem., Int. Ed.*, 2011, **50**, 2999–3002.

70 Q. Li, F. Chen, W. Zhao, M. Xu, B. Fang, Y. Zhang, L. Duo, Y. Jin and F. Sang, *Bull. Korean Chem. Soc.*, 2007, **28**, 1656–1660.

71 J. Wandt, P. Jakes, J. Granwehr, H. A. Gasteiger and R.-A. Eichel, *Angew. Chem., Int. Ed.*, 2016, **55**, 6892–6895.

72 A. U. Khan, *J. Am. Chem. Soc.*, 1981, **103**, 6516–6517.

73 W. H. Koppenol, *Nature*, 1976, **262**, 420–421.

74 C. L. Bender, P. Hartmann, M. Vračar, P. Adelhelm and J. Janek, *Adv. Energy Mater.*, 2014, **4**, 1–10.

75 R. H. Snow, *U. S. Govt. Res. Dev. Rept.*, 1965, 41, pp. 1–34.

76 A. U. Khan, *Photochem. Photobiol.*, 1978, **28**, 615–626.

77 Y.-C. Lu, B. M. Gallant, D. G. Kwabi, J. R. Harding, R. R. Mitchell, M. S. Whittingham and Y. Shao-Horn, *Energy Environ. Sci.*, 2013, **6**, 750–768.

78 J. K. Papp, J. D. Forster, C. M. Burke, H. W. Kim, A. C. Luntz, R. M. Shelby, J. J. Urban and B. D. McCloskey, *J. Phys. Chem. Lett.*, 2017, 1169–1174, DOI: 10.1021/acs.jpclett.7b00040.

79 Y. G. Zhu, Q. Liu, Y. Rong, H. Chen, J. Yang, C. Jia, L.-J. Yu, A. Karton, Y. Ren, X. Xu, S. Adams and Q. Wang, *Nat. Commun.*, 2017, **8**, 14308.

80 C. M. Burke, R. Black, I. R. Kochetkov, V. Giordani, D. Addison, L. F. Nazar and B. D. McCloskey, *ACS Energy Lett.*, 2016, **1**(4), 747–756.

81 W. Yin, A. Grimaud, F. Lepoivre, C. Yang and J.-M. Tarascon, *J. Phys. Chem. Lett.*, 2017, **8**(1), 214–222.

82 S. R. Gowda, A. Brunet, G. M. Wallraff and B. D. McCloskey, *J. Phys. Chem. Lett.*, 2012, **4**, 276–279.

83 D. M. Itkis, D. A. Semenenko, E. Y. Kataev, A. I. Belova, V. S. Neudachina, A. P. Sirotina, M. Hävecker, D. Teschner, A. Knop-Gericke, P. Dudin, A. Barinov, E. A. Goodilin, Y. Shao-Horn and L. V. Yashina, *Nano Lett.*, 2013, **13**, 4697–4701.

84 B. D. Adams, R. Black, C. Radtke, Z. Williams, B. L. Mehdi, N. D. Browning and L. F. Nazar, *ACS Nano*, 2014, **8**, 12483–12493.

85 L. Nazar, D. Kundu, R. Black and E. Jamstorp, *Energy Environ. Sci.*, 2015, **8**, 1292–1298.

86 C. V. Amanchukwu, J. R. Harding, Y. Shao-Horn and P. T. Hammond, *Chem. Mater.*, 2015, **27**(2), 550–561.

87 E. Nasybulin, W. Xu, M. H. Engelhard, Z. Nie, X. S. Li and J.-G. Zhang, *J. Power Sources*, 2013, **243**, 899–907.

88 Z. Peng, S. A. Freunberger, L. J. Hardwick, Y. Chen, V. Giordani, F. Bardé, P. Novák, D. Graham, J.-M. Tarascon and P. G. Bruce, *Angew. Chem., Int. Ed.*, 2011, **50**, 6351–6355.

89 G. Blanquer, Y. Yin, M. A. Quiroga and A. A. Franco, *J. Electrochem. Soc.*, 2016, **163**, A329–A337.

90 M. D. Radin, C. W. Monroe and D. J. Siegel, *Chem. Mater.*, 2015, **27**, 839–847.

91 V. Giordani, S. A. Freunberger, P. G. Bruce, J.-M. Tarascon and D. Larcher, *Electrochem. Solid-State Lett.*, 2010, **13**, A180–A183.

92 E. Mourad, L. Coustan, P. Lannelongue, D. Zigah, A. Mehdi, A. Vioux, S. A. Freunberger, F. Favier and O. Fontaine, *Nat. Mater.*, 2016, **16**, 446–453.

93 M. J. Lacey, J. T. Frith and J. R. Owen, *Electrochem. Commun.*, 2013, **26**, 74–76.

94 L. Yang, J. T. Frith, N. Garcia-Araez and J. R. Owen, *Chem. Commun.*, 2015, **51**, 1705–1708.

95 D. Sun, Y. Shen, W. Zhang, L. Yu, Z. Yi, W. Yin, D. Wang, Y. Huang, J. Wang, D. Wang and J. B. Goodenough, *J. Am. Chem. Soc.*, 2014, **136**, 8941–8946.

96 X. Gao, Y. Chen, L. Johnson and P. G. Bruce, *Nat. Mater.*, 2016, **15**, 882–888.

97 V. Giordani, *presented in part at the Abstract for 16th IMLB*, Jeju, Korea, 2012, pp. S6–S3.

98 Y. Chen, S. A. Freunberger, Z. Peng, O. Fontaine and P. G. Bruce, *Nat. Chem.*, 2013, **5**, 489–494.

99 H.-D. Lim, B. Lee, Y. Zheng, J. Hong, J. Kim, H. Gwon, Y. Ko, M. Lee, K. Cho and K. Kang, *Nat. Energy*, 2016, **1**, 16066.

100 D. Kundu, R. Black, B. Adams and L. F. Nazar, *ACS Cent. Sci.*, 2015, **1**, 510–515.

101 B. G. Kim, J.-S. Kim, J. Min, Y.-H. Lee, J. H. Choi, M. C. Jang, S. A. Freunberger and J. W. Choi, *Adv. Funct. Mater.*, 2016, **26**(11), 1747–1756.

Chapter 6

Singlet Oxygen in the Na-O$_2$ Battery

Over the past decade rechargeable aprotic metal-oxygen batteries have been studied emphatically as promising candidates for 'beyond-intercalation chemistries' as they may result in higher-energy devices than state-of-the-art LIBs. Theoretically the Li-O$_2$ and Na-O$_2$ cathode yield specific capacities of 1168 mAh·g^{-1} and 488 mAh·g^{-1}, respectively.[21] Of these battery chemistries the non-aqueous Na-O$_2$ cell has been reported to have significant advantages over the Li-O$_2$ cell due to its high stability, improved full-cycle efficiency and lower overpotentials on charge.[126] However, insufficient cycle life associated with parasitic chemistry at the O$_2$ cathode is perhaps the most challenging hurdle to its practical implementation. Based on the findings and hence gained knowledge about the generation of ^{1}O$_2$ in aprotic Li-O$_2$ batteries shown in *Chapter 3*, we examined the parasitic chemistry at the Na-O$_2$ cathode. In this work we demonstrate *via* at set of *in/ex-situ* methods, ^{1}O$_2$ formation at the cathode during all stages of cycling, during rest, and that it is accounting for a significant amount of side product formation.

Future work should thus focus on finding ways to either prevent ^{1}O$_2$ formation or to efficiently eliminate it in non-aqueous battery systems. A promising strategy is elaborated in *Chapter 7*. Beyond the previously examined batteries, the reversible K-O$_2$ cell should be inspected towards ^{1}O$_2$ generation during its reversible electrochemical process of $K^+ + O_2 + e^- \rightleftarrows KO_2$ formation and dissolution. Despite, KO$_2$ shows greater thermodynamic and kinetic stability,[127] which prevents it from spontaneous disproportionation to potassium peroxide, electrolyte or oxygen contamination with water has to be thoroughly obviated as the reaction of $4KO_2 + 2H_2O \rightarrow 4KOH + 3O_2$ is known to generate ^{1}O$_2$.[87]

(VIP) **Batteries** *Very Important Paper*

Singlet Oxygen during Cycling of the Aprotic Sodium–O$_2$ Battery

Lukas Schafzahl[+], Nika Mahne[+], Bettina Schafzahl, Martin Wilkening, Christian Slugovc, Sergey M. Borisov, and Stefan A. Freunberger*

Abstract: *Aprotic sodium–O$_2$ batteries require the reversible formation/dissolution of sodium superoxide (NaO$_2$) on cycling. Poor cycle life has been associated with parasitic chemistry caused by the reactivity of electrolyte and electrode with NaO$_2$, a strong nucleophile and base. Its reactivity can, however, not consistently explain the side reactions and irreversibility. Herein we show that singlet oxygen (^{1}O$_2$) forms at all stages of cycling and that it is a main driver for parasitic chemistry. It was detected in- and ex-situ via a ^{1}O$_2$ trap that selectively and rapidly forms a stable adduct with ^{1}O$_2$. The ^{1}O$_2$ formation mechanism involves proton-mediated super-oxide disproportionation on discharge, rest, and charge below ca. 3.3 V, and direct electrochemical ^{1}O$_2$ evolution above ca. 3.3 V. Trace water, which is needed for high capacities also drives parasitic chemistry. Controlling the highly reactive singlet oxygen is thus crucial for achieving highly reversible cell operation.*

$\mathbf{T}$he need to advance batteries beyond the limits of current technology in terms of energy, sustainability, and cost has generated immense interest in rechargeable aprotic metal–O$_2$ batteries.[1] They store charge at the cathode by reversibly forming/decomposing Li$_2$O$_2$ or NaO$_2$ in the Li–O$_2$ or Na–O$_2$ cell, respectively. Despite the lower theoretical specific capacity of 488 mAh g^{-1} of NaO$_2$ and lower voltage of 2.27 V (vs. 1168 mAh g^{-1} at 2.96 V for Li–O$_2$), the Na–O$_2$ cell has been reported to have significant advantages over Li–O$_2$ with respect to rechargeability and energy efficiency.[2] Realizing the Na–O$_2$ cell, however, still faces many challenges in practice, including the Na-metal anode, lower than theoretical cathode capacity, and perhaps most importantly,

insufficient cycle life associated with parasitic chemistry (that is, side reactions) at the cathode.[2,3]

Since the very first papers published on Na–O$_2$ batteries, superoxide has been perceived responsible for parasitic chemistry with electrolyte and electrode.[1c,3,4] A key measure for parasitic chemistry is the ratio of e$^-$ passed to O$_2$ consumed/evolved. During discharge, this ratio is typically at the ideal value of one despite approximately 5% of the expected NaO$_2$ being missing and replaced by side products, such as Na$_2$CO$_3$, Na acetate, and Na formate. During subsequent resting and charge, more of these side products form and typically the e$^-$/O$_2$ ratio deviates by several percent from one.[2a,3c,4b,5] Although less side products form than in the Li–O$_2$ cell, cyclability is similarly poor: restricted capacity can often be maintained for up to hundreds of cycles albeit at the expense of true energy, but at full discharge cells fail within some 10 cycles and capacity fading becomes significantly worse with rising charge cut-off voltage.[1c,2a,c,d,3a,d,6]

Superoxide's potential reactivity towards organic substrates stems from its nucleophilicity, basicity, and radical nature, which may cause nucleophilic substitutions, H$^+$ and H-atom abstraction.[7] Theoretical work, however, has revealed that all these reactions are unlikely with commonly used ether electrolytes owing to the high activation energies and strong endothermicity.[8] Also, the extent of parasitic chemistry at the various stages of cycling does not match the abundance of superoxide. Overall, the reactivity of superoxide cannot consistently explain the observed parasitic chemistry, which thus may only be inhibited with better knowledge about reactive species and their formation mechanism.

Herein we show that singlet oxygen ($^1\Delta_g$ or ^{1}O$_2$), the first excited state of ground state triplet oxygen ($^3\Sigma_g^-$ or ^{3}O$_2$), is the reactive species, which drives parasitic reactions. It is generated at all stages of cycling in relative quantities resembling the occurrence of side reactions: relatively little during discharge, rest, and low charging voltages, and strongly increasing amounts at higher charging voltages.

Methods to sensitively detect ^{1}O$_2$ rely on chemical probes, which selectively react with ^{1}O$_2$. Probes include spin traps and fluorophores, which become EPR active or fluorescing upon reaction with ^{1}O$_2$.[9] However, these probes are not electro-chemically inert in the relevant potential range between approximately 2 and 3.6 V versus Na/Na$^+$ and may react with superoxide. Previously, we have shown that 9,10-dimethylan-thracene (DMA) fulfills all the requirements;[10] it is stable in contact with superoxide, reacts rapidly with ^{1}O$_2$ to its endoperoxide (DMA-O$_2$), and has a sufficiently wide potential window (Figure S1 and Scheme S1 in the Supporting Information). ^{1}O$_2$ can either be monitored by DMA consumption via its absorbance or fluorescence between 300 and

[*] L. Schafzahl,[+] N. Mahne,[+] B. Schafzahl, Prof. M. Wilkening, Prof. C. Slugovc, Dr. S. A. Freunberger
Institute for Chemistry and Technology of Materials
Graz University of Technology
Stremayrgasse 9, 8010 Graz (Austria)
E-mail: freunberger@tugraz.at

Prof. S. M. Borisov
Institute for Analytical Chemistry and Food Chemistry
Graz University of Technology
Stremayrgasse 9, 8010 Graz (Austria)

[+] These authors contributed equally to this work.

Supporting information and the ORCID identification number(s) for the author(s) of this article can be found under:
https://doi.org/10.1002/anie.201709351.

500 nm (Figure S2), or by detecting DMA and DMA-O_2 via HPLC.

To probe whether $^1O_2$ would form during discharge and charge we constructed Na–O_2 cells as detailed in the Methods Section of the Supporting Information with 0.5 M $NaSO_3CF_3$ (NaOTf) in diglyme containing 40 ppm H_2O and 30 mM DMA as the electrolyte. Water was used because it is required as a phase-transfer catalyst to allow large NaO_2 particles to grow.[2c] To specifically probe reactions at the cathode and to exclude unwanted reactions of electrolyte components with a Na-metal anode, we used the Na intercalation material $Na_{3-x}V_2(PO_4)_3$ as the counter electrode. It operates at approximately 3.4 V versus Na/Na$^+$ and is thus well within the stability window of the electrolyte.[11] Cells were run at constant current to various states of discharge or charge, then stopped, and the electrolyte extracted and analyzed using HPLC (Figure 1).
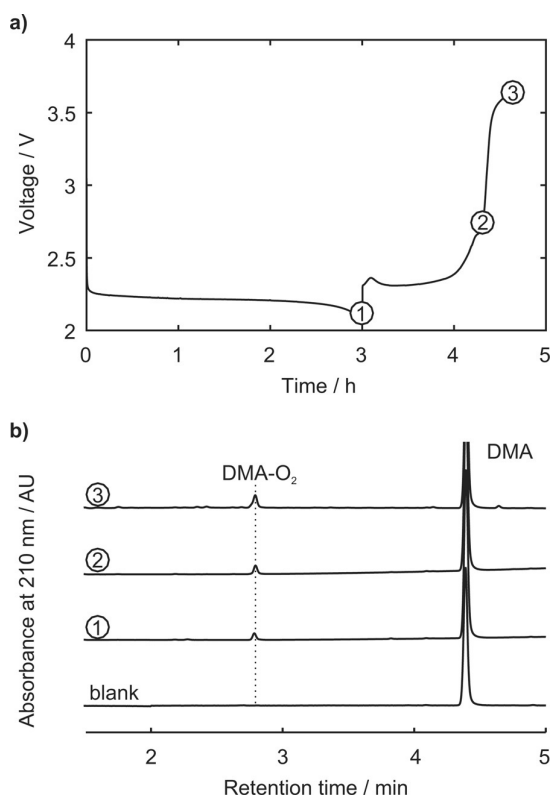
Figure 1. a) Load curve for galvanostatic cycling of a carbon-paper cathode at 90 µA cm^{-2} in 0.5 M NaOTf in diglyme containing 40 ppm H_2O and 30 mM DMA. b) HPLC runs of electrolyte samples taken at the points ①, ②, and ③ in (a), showing $^1O_2$ to have formed as indicated by the conversion of DMA into DMA-O_2. The blank sample was extracted from a cell that rested for 5 h.

The cycle curve shows flat discharge and charge plateaus at approximately 2.2 and 2.3 V, respectively, with a sharp rise in voltage when recharge approaches about 55% (Figure 1 a). X-ray diffraction confirms that the cube-shaped discharge product is NaO_2 (Figure S3, S4) in accord with many previous

reports on similar cells.[1b,c, 2a,b, 3a] After discharge or recharge to 2.8 and 3.65 V, 4.1, 4.3, and 7.2%, respectively, of the DMA at the sample points ①, ②, and ③ was converted into DMA-O_2 (Figure 1 b). The amounts of DMA-O_2 equate to 1.4, 1.3, and 2.1% of the O_2 involved based on the charge at these stages of cycling to have turned into $^1O_2$. $^1O_2$ is thus generated both on discharge and charge, and charging to higher voltage yields significantly more $^1O_2$.

Operando spectroscopy is well suited to probe in detail onset potentials and reaction rates. An operando fluorescence set-up as detailed in the Supporting Information was constructed. Briefly, it consisted of a gas-tight quartz cuvette with a carbon paper working electrode and $Na_{3-x}V_2(PO_4)_3$ as counter and reference electrode and an O_2 filled head space. The O_2-saturated electrolyte was the same as before except for a lower DMA concentration (1.6×10^{-5} M), which best suits fluorescence detection (see the Supporting Information). Excitation and emission wavelengths were chosen according to the maxima in the respective spectra (Figure S2).

While cells as in Figure 1 comprising a porous separator sandwiched between working and counter electrode typically yield NaO_2, cycling the cathode in the operando setup yielded $Na_2O_2 \cdot H_2O$ as can be inferred from the high charging voltage (Figure S5). Rather similar thermodynamics of NaO_2 and Na_2O_2 ($E^0_{O_2/NaO_2} = 2.27$ V, $E^0_{O_2/Na_2O_2} = 2.33$ V) were used to explain that the Na–O_2 cell could yield both as a discharge product.[1b,3b] Proton sources decisively influence the discharge product, yet the precise governing factors are unknown.[1b] The reason for peroxide rather than superoxide as a discharge product in the operando setup may be the large electrolyte-to-electrode volume ratio and the stirred electrolyte, both of which are essential for the method. The electrolyte after discharge in the operando setup also contains DMA-O_2, revealing that discharge to Na_2O_2 also forms $^1O_2$ (Figure S6).

To investigate charging of NaO_2, we first discharged a cathode in the standard cell and then placed it in the operando cell. Figure 2 shows the DMA concentration and consumption rate for stepwise potentiostatic charging up to 3.7 V. As soon as the cell was polarized to charging potentials, DMA was consumed at an initially moderate rate, which sharply increased beyond a voltage of about 3.3 V. Thermodynamically, $^1O_2$ can be expected to form upon electrochemically oxidizing NaO_2 above $E^0_{O_2/NaO_2} + E(^1\Delta_g \leftarrow {}^3\Sigma_g^-)$. With 0.97 eV energy difference between $^1O_2$ and $^3O_2$ the thermodynamic threshold to evolve $^1O_2$ can be estimated to be 3.24 V. $^1O_2$ forming at high rate above approximately 3.3 V can thus be explained by the reaction $NaO_2 \rightarrow Na^+ + e^- + {}^1O_2$ beyond the thermodynamic threshold of 3.24 V. Up to 3.3 V the $^1O_2$ fraction is around 0.75 to 1.1% of the expected O_2 (Figure S7). Beyond 3.3 V this fraction increases steadily to around 4%.

Previously it was reported that most parasitic chemistry occurs during discharge and less on charge.[2a,3a] Charging above around 3.5 V caused the number of O_2 per e$^-$ evolved to deviate more significantly from one than at lower voltages. Correlating these findings with the results in Figure 1, Figure 2, and Figure S7 suggests that parasitic chemistry in the Na–O_2 cathode is closely related to $^1O_2$ formation since
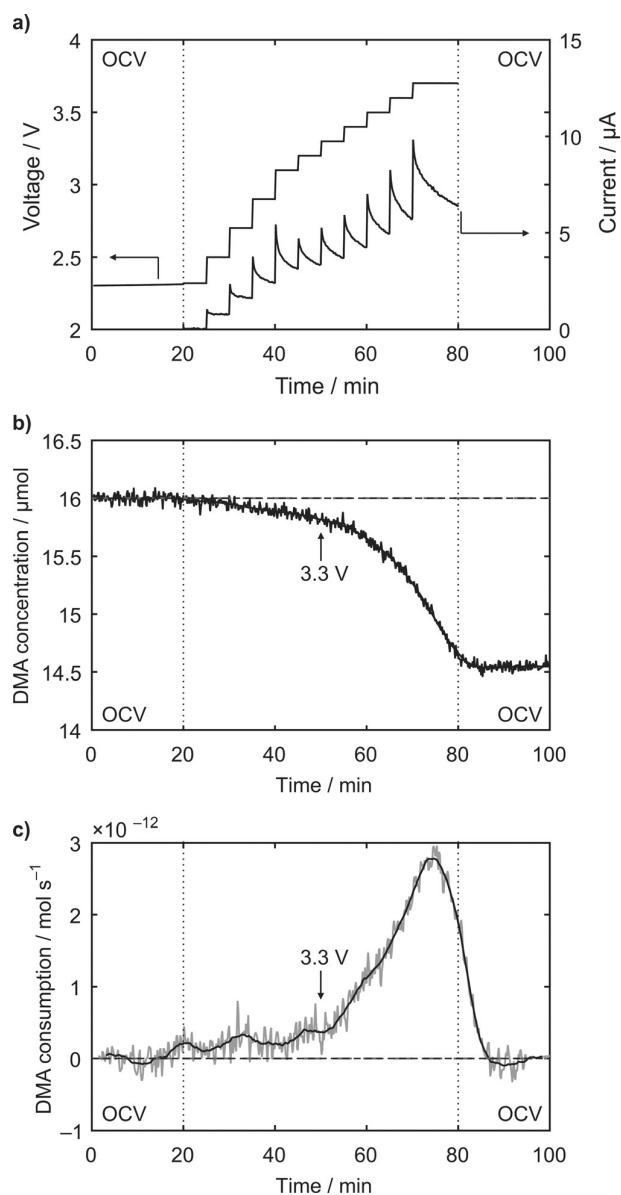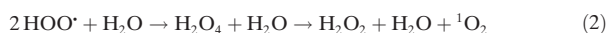
a)

b)

c)

Figure 2. Operando fluorescence detection of $^1O_2$ during potentiostatic charging of a Na–O_2 cathode. The carbon-paper cathode was first discharged in a Swagelok type cell to 75 mAh cm^{-2} in 0.5 M NaOTf in diglyme containing 40 ppm H_2O and then introduced into the operando setup containing the same electrolyte and additionally 1.6×10^{-5} M DMA. a) Voltage and current profile. b) DMA concentration. c) DMA consumption rate.

the extent of side reactions follows the occurrence of $^1O_2$: $^1O_2$ is formed at a higher rate during discharge than at charging below 3.3 V and at much higher rate above 3.3 V. In quantitative terms the 1.4% $^1O_2$ during discharge and an approximately 95% yield of NaO$_2$ suggests a significant fraction of the side products stem from $^1O_2$. Measured $^1O_2$ amounts represents a lower bound since at the low DMA concentration not necessarily all $^1O_2$ will react with DMA and may undergo other decay routes, such as reactions with cell components.

While thermodynamics directly explains how $^1O_2$ forms when NaO$_2$ is oxidized above 3.3 V, its formation during discharge and recharge below 3.3 V is more surprising. With the Li–O_2 cell, disproportionation of the LiO$_2$ intermediate to Li$_2$O$_2$ was suggested as a major $^1O_2$ source during discharge and low charging voltages.[10] This pathway is inactive in the Na–O_2 cell since discharge stops at NaO$_2$. When, however, water or other proton sources are present, oxygen reduction will lead to HOO·.[12] This soluble species enables proton-assisted phase-transfer catalysis, which allows the typical micron-sized NaO$_2$ cubes to grow on discharge and to be oxidized on charge; HOO· is soluble and mobile in the electrolyte and precipitates NaO$_2$ via the metathesis reaction HOO· + Na$^+$ $\rightleftharpoons$ NaO$_2$ + H$^+$.[2c,13] HOO·, however, can be reduced by superoxide or disproportionate according to Equation (1) and (2),[12] which both have been shown to release $^1O_2$.[14]

$$HOO^\bullet + O_2^- \rightarrow HO_4^- \rightarrow HOO^- + {}^1O_2 \tag{1}$$

$$2\,HOO^\bullet + H_2O \rightarrow H_2O_4 + H_2O \rightarrow H_2O_2 + H_2O + {}^1O_2 \tag{2}$$

That water is driving these reactions is supported by significantly less $^1O_2$ being formed with dry electrolyte as compared to wet electrolyte (Figure S8).

These reactions may not only take place during discharge, where new superoxide is generated, but also at rest since the metathesis reaction is an equilibrium and allows NaO$_2$ to redissolve into HOO·. A number of studies have shown instability of NaO$_2$ upon prolonged rest.[3c,4,5] Although details vary, they generally report gradual conversion of NaO$_2$ into Na$_2$O$_2$·H$_2$O accompanied by electrolyte degradation to form NaOH, Na$_2$CO$_3$, and organic compounds including Na formate and acetate. Explanations included nucleophilic attack, H$^+$ and H-atom abstraction by superoxide. To probe how $^1O_2$ is involved in forming the parasitic products we first discharged electrodes in DMA-free electrolyte and then placed them for various times in electrolyte containing 30 mM DMA. X-ray diffraction after storage shows decreased NaO$_2$ and side products to have formed in accord with previous studies (Figure S9). The electrolyte was then analyzed for DMA-O_2 and the electrodes were analyzed for Na$_2$CO$_3$ content by immersing them in 0.1M H$_2$SO$_4$ and monitoring the CO_2 evolved by mass spectrometry (Figure 3). $^1O_2$ as indicated by the presence of DMA-O_2 continuously increases with resting time as does the Na$_2$CO$_3$ content, which serves as an indication for the extent of parasitic products.

DMA-O_2 and Na$_2$CO$_3$ roughly increase proportional to the square root of the resting time, which means that the formation rate decreases with time. The formed parasitic products thus partly passivate the NaO$_2$ surface and slow down further decomposition. A larger amount of DMA-O_2 than additional Na$_2$CO$_3$ formed, which can be explained by two phenomena. First, $^1O_2$ trapped by DMA does not react with cell components and would thus have led to even more parasitic products without DMA. Second, other compounds than Na$_2$CO$_3$ will form which are not expelled by acid. Overall, Figure 3 shows that the previously reported electro-
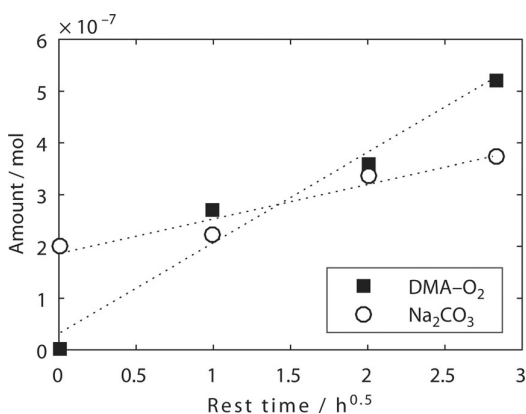
Figure 3. $^1O_2$ generation and parasitic chemistry during prolonged contact of the discharge product NaO_2 with the electrolyte. Cells were first discharged in DMA-free electrolyte (0.5 M NaOTf in diglyme containing 40 ppm H_2O), then the cathodes washed and immersed in the same electrolyte containing additionally 30 mM DMA. After the times indicated the electrolyte was analyzed for DMA-O_2 and the electrodes for Na_2CO_3. The dotted lines are linear fits versus the square root of rest time.
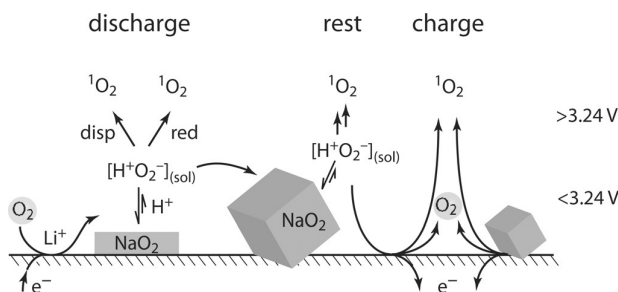
Scheme 1. Pathways leading to $^1O_2$ during discharge, rest, and charge. "Disp" = disproportionation and "red" = reduction.

lyte degradation upon resting is significantly driven by $^1O_2$ formation.

Pathways to $^1O_2$ during discharge, rest, and charge are summarized in Scheme 1. We suggest proton mediated superoxide disproportionation or reduction to interfere with the metathesis equilibrium $HOO^{\bullet} + Na^+ \rightleftharpoons NaO_2 + H^+$ as a universal path to $^1O_2$ during all stages of cycling. Upon charge at voltages exceeding the thermodynamic threshold of 3.24 V $^1O_2$ evolves by direct electrochemical oxidation according to $NaO_2 \rightarrow Na^+ + e^- + {}^1O_2$.

In conclusion we demonstrate that singlet oxygen forms at the cathode of the Na–O_2 cell during all stages of cycling and during rest, and accounts for a significant fraction of the side-products formed. $^1O_2$ is thus a major hurdle in cycling the Na–O_2 cell via the reversible formation/decomposition of NaO_2. Water takes up an ambivalent role by being required for high capacity via solution-mediated growth and dissolution of large NaO_2 deposits, and at the same time appearing to be the main driver for $^1O_2$ formation during discharge and at low charging voltages. Future work should thus focus on finding ways to either prevent $^1O_2$ formation or to efficiently eliminate it.

Conflict of interest

The authors declare no conflict of interest.

[1] a) D. Aurbach, B. D. McCloskey, L. F. Nazar, P. G. Bruce, *Nat. Energy* **2016**, *1*, 16128; b) C. L. Bender, D. Schröder, R. Pinedo, P. Adelhelm, J. Janek, *Angew. Chem. Int. Ed.* **2016**, *55*, 4640–4649; *Angew. Chem.* **2016**, *128*, 4716–4726; c) P. Hartmann, C. L. Bender, M. Vračar, A. K. Dürr, A. Garsuch, J. Janek, P. Adelhelm, *Nat. Mater.* **2012**, *12*, 228–232.

[2] a) B. D. McCloskey, J. M. Garcia, A. C. Luntz, *J. Phys. Chem. Lett.* **2014**, *5*, 1230–1235; b) R. Morasch, D. G. Kwabi, M. Tulodziecki, M. Risch, S. Zhang, Y. Shao-Horn, *ACS Appl. Mater. Interfaces* **2017**, *9*, 4374–4381; c) C. Xia, R. Black, R. Fernandes, B. Adams, L. F. Nazar, *Nat. Chem.* **2015**, *7*, 496–501; d) I. Landa-Medrano, C. Li, N. Ortiz-Vitoriano, I. Ruiz de Larramendi, J. Carrasco, T. Rojo, *J. Phys. Chem. Lett.* **2016**, *7*, 1161–1166.

[3] a) P. Hartmann, C. L. Bender, J. Sann, A. K. Durr, M. Jansen, J. Janek, P. Adelhelm, *Phys. Chem. Chem. Phys.* **2013**, *15*, 11661–11672; b) C. L. Bender, P. Hartmann, M. Vračar, P. Adelhelm, J. Janek, *Adv. Energy Mater.* **2014**, *4*, 1301863; c) S. Y. Sayed, K. P. C. Yao, D. G. Kwabi, T. P. Batcho, C. V. Amanchukwu, S. Feng, C. V. Thompson, Y. Shao-Horn, *Chem. Commun.* **2016**, *52*, 9691–9694; d) M. He, K. C. Lau, X. Ren, N. Xiao, W. D. McCulloch, L. A. Curtiss, Y. Wu, *Angew. Chem. Int. Ed.* **2016**, *55*, 15310–15314; *Angew. Chem.* **2016**, *128*, 15536–15540.

[4] a) J. Kim, H. Park, B. Lee, W. M. Seong, H.-D. Lim, Y. Bae, H. Kim, W. K. Kim, K. H. Ryu, K. Kang, *Nat. Commun.* **2016**, *7*, 10670; b) T. Liu, G. Kim, M. T. L. Casford, C. P. Grey, *J. Phys. Chem. Lett.* **2016**, *7*, 4841–4846.

[5] I. Landa-Medrano, R. Pinedo, X. Bi, I. Ruiz de Larramendi, L. Lezama, J. Janek, K. Amine, J. Lu, T. Rojo, *ACS Appl. Mater. Interfaces* **2016**, *8*, 20120–20127.

[6] S. A. Freunberger, *Nat. Energy* **2017**, *2*, 17091.

[7] a) D. T. Sawyer, J. S. Valentine, *Acc. Chem. Res.* **1981**, *14*, 393–400; b) D. Aurbach, M. L. Daroux, P. W. Faguy, E. Yeager, *J. Electrochem. Soc.* **1988**, *135*, 1863–1871.

[8] a) V. S. Bryantsev, F. Faglioni, *J. Phys. Chem. A* **2012**, *116*, 7128–7138; b) V. S. Bryantsev, V. Giordani, W. Walker, M. Blanco, S. Zecevic, K. Sasaki, J. Uddin, D. Addison, G. V. Chase, *J. Phys. Chem. A* **2011**, *115*, 12399–12409; c) M. Carboni, A. G. Marrani, R. Spezia, S. Brutti, *Chem. Eur. J.* **2016**, *22*, 17188–17203; d) A. Khetan, H. Pitsch, V. Viswanathan, *J. Phys. Chem. Lett.* **2014**, *5*, 2419–2424; e) N. Mahne, O. Fontaine, M. O. Thotiyl, M. Wilkening, S. A. Freunberger, *Chem. Sci.* **2017**, *8*, 6716–6729.

[9] a) P. R. Ogilby, *Chem. Soc. Rev.* **2010**, *39*, 3181–3209; b) J. Wandt, P. Jakes, J. Granwehr, H. A. Gasteiger, R.-A. Eichel, *Angew. Chem. Int. Ed.* **2016**, *55*, 6892–6895; *Angew. Chem.* **2016**, *128*, 7006–7009.

[10] N. Mahne, B. Schafzahl, C. Leypold, M. Leypold, S. Grumm, A. Leitgeb, G. A. Strohmeier, M. Wilkening, O. Fontaine, D. Kramer, C. Slugovc, S. M. Borisov, S. A. Freunberger, *Nat. Energy* **2017**, *2*, 17036.

[11] Y. Zhang, L. Ma, L. Zhang, Z. Peng, *J. Electrochem. Soc.* **2016**, *163*, A1270–A1274.

[12] a) D. H. Chin, G. Chiericato, E. J. Nanni, D. T. Sawyer, *J. Am. Chem. Soc.* **1982**, *104*, 1296–1299; b) C. P. Andrieux, P. Hapiot, J. M. Saveant, *J. Am. Chem. Soc.* **1987**, *109*, 3768–3775; c) Y. Che, M. Tsushima, F. Matsumoto, T. Okajima, K. Tokuda, T. Ohsaka, *J. Phys. Chem.* **1996**, *100*, 20134–20137.

[13] X. Gao, Z. P. Jovanov, Y. Chen, L. R. Johnson, P. G. Bruce, *Angew. Chem. Int. Ed.* **2017**, *56*, 6539–6543; *Angew. Chem.* **2017**, *129*, 6639–6643.

[14] a) E. J. Corey, M. M. Mehrotra, A. U. Khan, *Biochem. Biophys. Res. Commun.* **1987**, *145*, 842–846; b) A. U. Khan, *J. Am. Chem. Soc.* **1981**, *103*, 6516–6517; c) W. H. Koppenol, *Nature* **1976**, *262*, 420–421; d) E. A. Mayeda, A. J. Bard, *J. Am. Chem. Soc.* **1974**, *96*, 4023–4024.

Supporting Information: Singlet Oxygen during Cycling of the Aprotic Sodium–O$_2$ Battery

Lukas Schafzahl[†,1], Nika Mahne[†,1], Bettina Schafzahl[1], Martin Wilkening[1], Christian Slugovc[1], Sergey M. Borisov[2], and Stefan A. Freunberger[1,*]

1   Institute for Chemistry and Technology of Materials, Graz University of Technology, Stremayr-
    gasse 9, 8010 Graz, Austria
2   Institute for Analytical Chemistry and Food Chemistry, Graz University of Technology,
    Stremayrgasse 9, 8010 Graz, Austria

Author Contributions

L.S. Data curation: Equal[†]; Software: Supporting; Visualization: Supporting, N.M. Data curation: Equal[†]; Methodology: Lead; Visualization: Supporting, B.S. Data curation: Supporting; Methodology: Supporting, M.W. Funding acquisition: Supporting; Resources: Supporting; Writing review & editing: Supporting, C.S. Conceptualization: Supporting; Funding acquisition: Supporting; Project administration: Supporting; Resources: Supporting; Supervision: Supporting; Writing review & editing: Supporting, S.B. Methodology: Equal; Resources: Supporting; Supervision: Supporting; Writing review & editing: Supporting.

Materials and Methods

Chemicals

Diethylene glycol dimethyl ether (DEGDME, >99.0%), 9,10-dimethylanthracene (DMA, >98.0%) and sodium trifluoromethanesulfonate (NaOTf, >98%) were purchased from TCI EUROPE. Tetraethylene glycol dimethyl ether (TEGDME, >99%), and H$_2$O (CHROMASOLV for HPLC) were purchased from Sigma-Aldrich®. Acetonitrile (HiPerSolv CHROMANORM Prolabo) was purchased from VWR Chemicals. High purity oxygen (O$_2$ 3.5, >99.95% vol) was purchased from Messer Austria GmbH. Moisture determination of all used solvents and electrolytes according to Karl Fischer titration was performed on a TitroLine KF trace (Schott Instruments). Solvents were purified by distillation and further dried over activated molecular sieves. The other chemicals were used without further purification. The sensitizer palladium (II) meso-tetra(4-fluorophenyl)tetrabenzoporphyrin was synthesized according a previously reported procedure[1].

Electrode Fabrication and Cell Design

Binder-free carbon fiber gas diffusion layer (GDL) cathodes (Freudenberg 2315, Quintech) were heated at 900 °C under H$_2$/Ar (5/95 vol/vol) atmosphere. Na$_3$V$_2$(PO$_4$)$_3$ (NVP) was synthesized according to a previously published procedure[2] and coated with a conductive poly(3,4-ethylendioxythiophene) layer.[3] Self-standing NVP counter electrodes were prepared by mixing active material with Super P (TIMCAL) and PTFE in the ratio 8:1:1 (m/m/m). The electrodes were subsequently dried overnight under vacuum at 120 °C and then transferred to an Ar filled glove box without exposure to air. Their capacity was at least 0.750 mAh and thus exceeded the cathode ∼3-fold. The glass fibre separators (Whatman GF-F) were washed with ethanol and dried overnight under vacuum at 200°C. The electrochemical cells used to investigate cycling were based on a Swagelok design and the cells were assembled with 140 µL electrolyte.

Electrochemical Methods

Electrochemical tests were run on either a SP-300 (BioLogic SA, France) or BT-2000 (Arbin Instruments) potentiostat/galvanostat. Cyclic voltammograms were recorded in a three-electrode arrangement with glassy carbon disc working electrode (BAS Inc.), a Pt wire counter electrode and partially desodiated NVP as reference electrode inside a glass cell with PTFE lid. The cells were run inside an Ar filled glovebox and purged with high-purity Ar.

UV-Vis Spectroscopy

Absorption spectra were recorded on a UV-Vis spectrophotometer (Varian Cary 50). The molar absorption coefficient of DMA was determined as an average of three independent measurements.

Operando Fluorescence Measurements

Excitation and emission spectra were recorded on a Fluorolog 3 fluorescence spectrometer (Horiba) equipped with a NIR-sensitive photomultiplier R2658 (300 - 1050 nm) from Hamamatsu. The *in-situ* fluorescence measurements were performed in front face mode. The measurements were performed in kinetic acquisition modus with 0.1 s excitation every 10 s to minimize photobleaching of the DMA. The fluorophore concentration was adjusted to attain an absorbance of 0.2 to avoid inner filter effects and to achieve better correlation between the observed fluorescence intensity (proportional to the amount of the absorbed light) and absorption (proportional to the concentration) of the ^{1}O$_2$ trap. DMA was excited at 378 nm and the emission was detected at 425 nm. The cell for operando fluorescence was a 1 cm absorption high precision quartz cell (Hellma Analytics) with a purpose made gas-tight PTFE-lid. The working electrode was a carbon fibre GDL (see above) mounted on a stain-

less steel wire that had been predischarged to 1 mAh in a swagelok cell. The reference and counter electrodes were partially desodiated NVP on an stainless steel or Al-foil current collector, respectively. The assembling was performed in an Ar filled glovebox. The cell contained a magnetic stirrer bar, was filled with electrolyte, streamed with O_2, further connected with a pure O_2 reservoir and hermetically sealed before being placed it in the spectrometer. During the measurement the electrolyte was stirred to ensure O_2 saturation and uniform DMA concentration. The DMA concentration of 1.6×10^{-5} M for the operando fluorescence was chosen to optimize the sensitivity of the method. At an absorbance of A = 0.2 (measurement conditions), 37% of the excitation light is absorbed by the chromophore ($= 1 - 10^{-A}$). In a hypothetical example, reaction of 10% of DMA with $^1O_2$ will decrease absorbance by 10%, i.e. from 0.2 to 0.18. Thus, after the reaction 34% of the excitation light will be absorbed by the chromophore. Since the fluorescence intensity is proportional to the amount of the absorbed light, the decrease of fluorescence intensity will be (37-34)/37×100 = 8%. Analogous calculation with 10 times the DMA concentration (A = 2) results in 99% of excitation light absorbed before bleaching and 98.4% of the excitation light absorbed after $^1O_2$ bleaching. Thus, the decrease of fluorescence intensity would be (99-98.4)/99×100 = 0.6% which is much lower than for the comparably low concentration of the trap. Therefore, a relatively low concentration of DMA is essential for the best sensitivity of operando fluorescence.

Carbonate/Carboxylate and NaO$_2$ Quantification

The procedure was performed as described earlier[4]. The purge gas flow was typically 5 mL/min. The NaO$_2$ content was measured using $TiOSO_4$ according to a previously described procedure[5].

Photo-chemical Generation of $^1O_2$

To perform experiments with a known generation of $^1O_2$ we used in situ photogeneration with the sensitizer palladium (II) meso-tetra(4-fluorophenyl)tetrabenzoporphyrin[1]. The sensitizer was irradiated with a red LED light source (643 nm, 7 W).

HPLC-MS Measurements

HPLC-MS (high-performance liquid chromatography coupled with mass spectrometry) was used for determining the degree of conversion from DMA to DMA-O$_2$. The sample handling was performed inside an Ar filled glovebox. The electrolyte was extracted from the cell using DME that was then removed by evaporation at room temperature. 10 μL of the residue were diluted with 90 μL of TEGDME and a volume of 1 μL was injected into the HPLC. The HPLC instrument was an Agilent Technologies 1200 Series (Agilent Technology, USA) with a multiple wavelength UV-Vis detector

(Agilent Technology G1365C MWD SL). The samples were separated by a reversed-phase Poroshell column (120 EC-C8, 3.0 mm × 100 mm, Ø 2.7 μm, Agilent Technology, USA) using a gradient system of acetonitrile (solvent B) and water containing 0.01% formic acid (solvent A). A pre-column (UHPLC 3PK, Poroshell 120 EC-C8 3.0 × 5 mm 2.7 μm, Agilent Technology, USA) was connected before the reversed phase column. The elution started with isocratic solvent B of 50% over the course of 1 min and was then increased to 100% of B within 5 min at a flow rate of 0.7 mL/min. The column was held at 20°C throughout the measurements. The eluent was monitored *via* an UV-Vis detector at the wavelengths of 210 nm and 254 nm. The extent of the transformation of 9,10-dimetylanthracene (DMA) to 9,10-dimethylanthracene endoperoxide (DMA-O$_2$) was determined from the absorbance at 210 nm and the molar absorption coefficients $\epsilon_{\text{DMA, 210 nm}}$ and $\epsilon_{\text{DMA-O}_2\text{, 210 nm}}$. The latter was determined from DMA-O$_2$, which was obtained by conversion of DMA with photogenerated ^{1}O$_2$.

Supplementary References

[1]   S. M. Borisov, G. Nuss, W. Haas, R. Saf, M. Schmuck, I. Klimant, J. Photochem. Photobiol. A 2009, 201, 128 - 135.

[2]   Y. Zhang, L. Ma, L. Zhang, Z. Peng, J. Electrochem. Soc. 2016, 163, A1270 - A1274.

[3]   D. Lepage, C. Michot, G. Liang, M. Gauthier, S. B. Schougaard, Angew. Chem. Int. Ed. 2011, 50, 6884 - 6887.

[4]   M. M. Ottakam Thotiyl, S. A. Freunberger, Z. Peng, P. G. Bruce, J. Am. Chem. Soc. 2013, 135, 494 - 500.

[5]   P. Hartmann, C. L. Bender, J. Sann, A. K. Durr, M. Jansen, J. Janek, P. Adelhelm, Phys. Chem. Chem. Phys. 2013, 15, 11661 - 11672.

[6]   N. Mahne, B. Schafzahl, C. Leypold, M. Leypold, S. Grumm, A. Leitgeb, G. A. Strohmeier, M. Wilkening, O. Fontaine, D. Kramer, C. Slugovc, S. M. Borisov, S. A. Freunberger, Nat. Energy 2017, 2, 17036.

[7]   C. L. Bender, D. Schrder, R. Pinedo, P. Adelhelm, J. Janek, Angew. Chem. Int. Ed. 2016, 4640 4649.

Supplementary Figures

Figure 6.1: Figure S1. Electrochemical stability of 9,10-dimethylanthracene (DMA) and 9,10-dimethylanthracene endoperoxide (DMA-O_2). Cyclic voltammetry was performed at a 3 mm glassy carbon disc electrode at a sweep rate of 50 mV·s^{-1}. First 2 mM DMA and 0.1 M NaOTf in diglyme were measured under Ar atmosphere. $^1O_2$ was then generated photochemically with the sensitizer palladium(II) meso-tetra(4-fluorophenyl)tetrabenzoporphyrin under O_2-atmosphere and then the formed DMA-O_2 was measured under Ar-atmosphere.
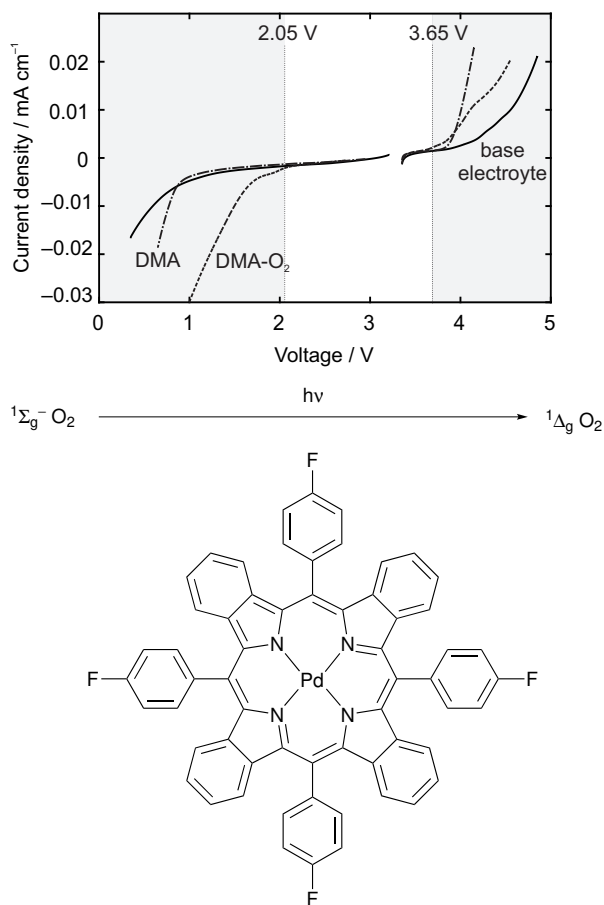
Figure 6.2: Scheme S1. Photogeneration of $^1O_2$ from $^3O_2$ using the sensitizer palladium(II) meso-tetra(4-fluorophenyl)tetrabenzoporphyrin (top). Reaction of 9,10-dimethylanthracene with singlet oxygen to 9,10-dimethylanthracene-endoperoxide (bottom).
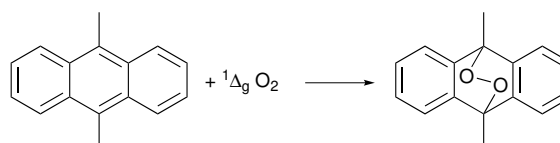
Figure 6.3: Figure S2. Excitation spectrum (blue trace, $\lambda_{em} = 425$ nm) and the emission spectrum (orange trace, $\lambda_{ex} = 378$ nm) of dimethylanthracene.[6] The excitation was recorded from 300 nm - 420 nm with $\lambda_{em} = 425$ nm. The emission was recorded from 380 nm - 500 nm with $\lambda_{ex} = 378$ nm.
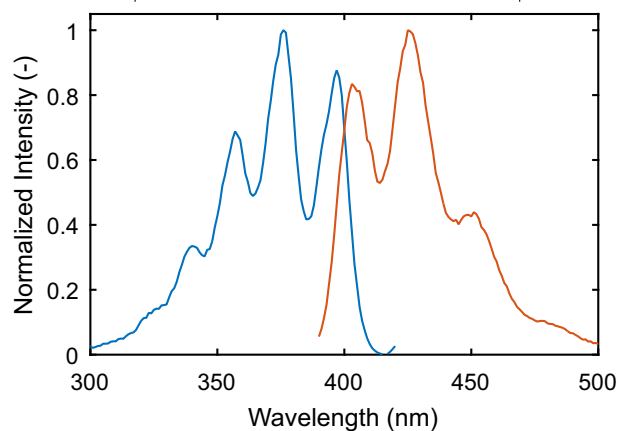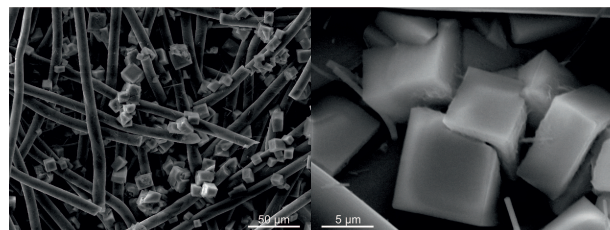
Figure 6.4: Figure S3. SEM images of a discharged Na-O$_2$ cathode corresponding to Figure 1a.
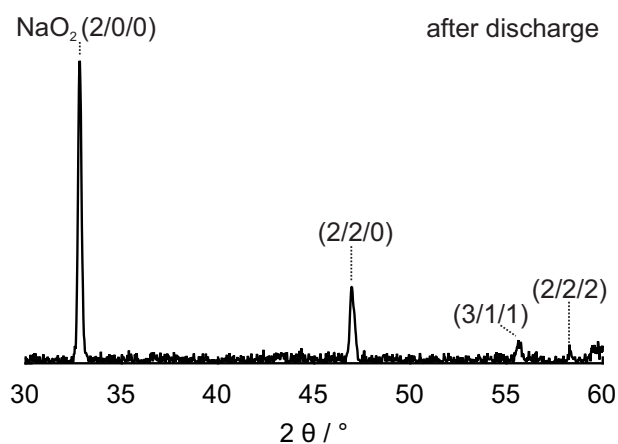

Figure 6.5: Figure S4. Powder XRD pattern of a discharged Na-O$_2$ cathode corresponding to Figure 1a.
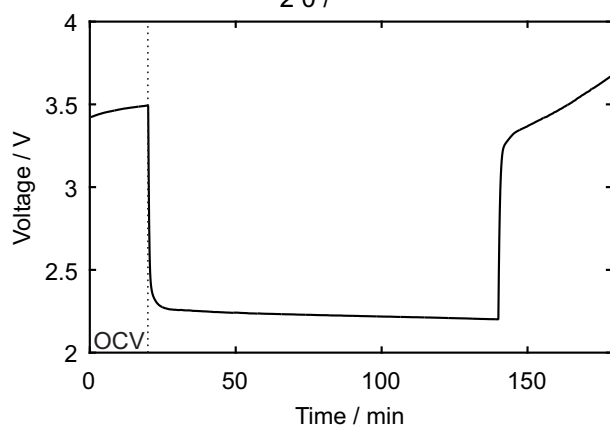

Figure 6.6: Figure S5. Load curve for galvanostatic cycling of a carbon paper cathode in the operando fluorescence setup in 0.5 M NaOTf in diglyme containing 40 ppm H$_2$O and 1.6×10^{-5} M DMA. The high charging voltage suggests Na$_2$O$_2 \cdot$H$_2$O as the discharge product in accord with previous reports.[7] Due to the small capacity achieved in the operando setup the formed phase could not be determined by XRD.
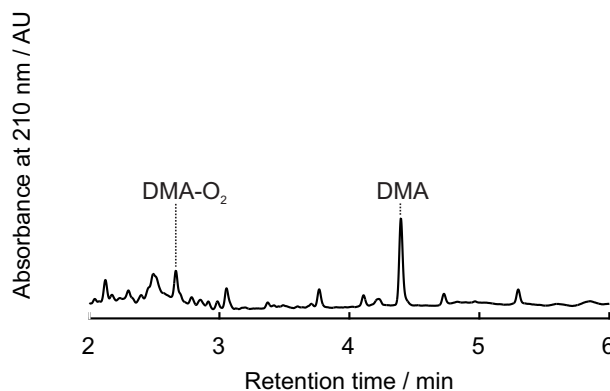

Figure 6.7: Figure S6. HPLC run of the electrolyte taken from the operando fluorescence setup after a single galvanostatic discharge showing ^{1}O$_2$ to form as indicated by the conversion of DMA to DMA-O$_2$. The electrolyte was in 0.5 M NaOTf in diglyme containing 40 ppm H$_2$O and 1.6×10^{-5} M DMA.

Figure 6.8: Figure S7. Fraction of the oxidized NaO_2 (based on charge) liberating $^1O_2$ as determined by operando fluorescence (Fig. 2).
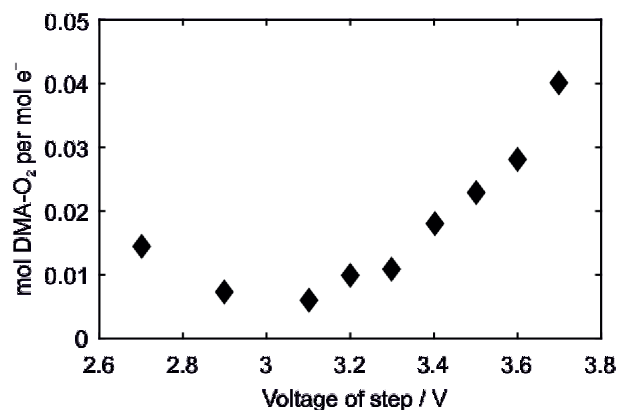
Figure 6.9: Figure S8. a) Load curve for galvanostatic cycling of a carbon paper electrode at $90\,\mu A\cdot cm^{-2}$ in 0.5 M NaOTf in diglyme containing 40 ppm of water or no additional water (6 ppm). b) HPLC data after discharge in nominally dry electrolyte and electrolyte containing 40 ppm water. Figure S8. compares the voltage profiles with nominally dry electrolyte (6 ppm H_2O) and electrolyte containing 40 ppm H_2O. With the dry electrolyte, discharge capacity is reduced to a third and recharge voltage climbs immediately above 3 V in accord with Nazar *et al.* (Nat. Chem. 2015, 7, 496-501), who explained this behaviour by proton-induced phase transfer catalysis. HPLC analysis of the electrolyte shows ∼10% as much DMA-O_2 to have formed as with the wet electrolyte. The amount of $^1O_2$ per unit of charge was therefore significantly lower in the dry electrolyte as compared to the wet electrolyte, which supports the conclusion that proton sources drive $^1O_2$ formation

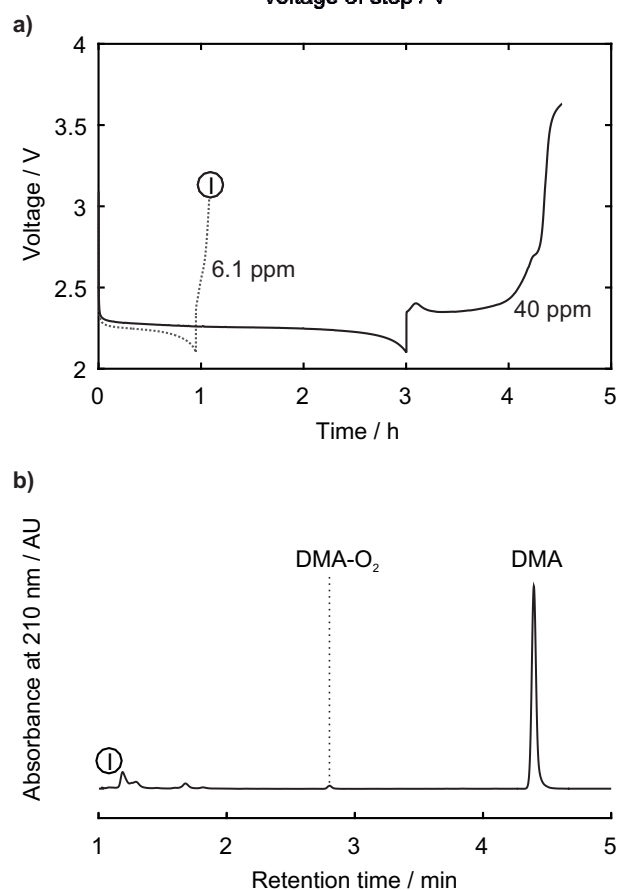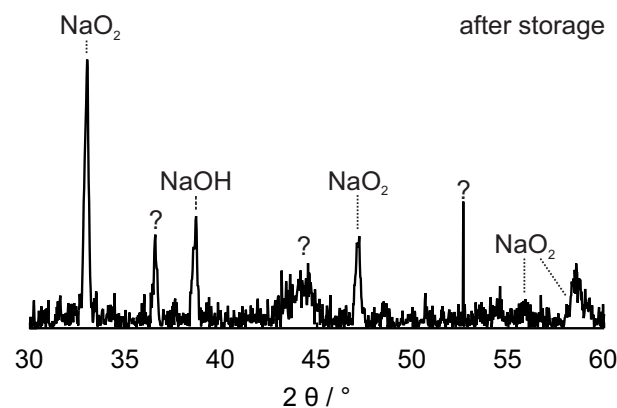**Figure 6.10:** Figure S9. Powder XRD pattern of discharged Na-O_2 cathode after prolonged contact with the electrolyte. The cathode was first discharged in DMA-free electrolyte (0.5 M NaOTf in diglyme containing 40 ppm H_2O), then washed and immersed in the same electrolyte additionally containing 30 mM DMA.

Chapter 7

Singlet Oxygen Generation during Electrochemical Oxidation of Li$_2$CO$_3$

Li$_2$CO$_3$ is a universal passivation layer component of intercalation battery materials and a common parasitic product in Li-O$_2$ batteries. It is believed to form/decompose reversibly in Li-O$_2$/CO$_2$ cells; theoretically according to $2\,\text{Li}_2\text{CO}_3 \longrightarrow 4\,\text{Li}^+ + 4\,\text{e}^- + 2\,\text{CO}_2 + \text{O}_2$. In these cathodes Li$_2CO_3$ decomposes to CO$_2$ when exposed to potentials above 3.8 V $vs.$ Li/Li$^+$. However, O$_2$ evolution has so far not been detected. This indicates that the evolved third 'missing O-atom' reacts in some other uncontrolled fashion, which was so far ascribed to unidentified parasitic reactions. Here, we show that highly reactive singlet oxygen forms upon Li$_2$CO$_3$ oxidation in an aprotic electrolyte and therefore does not evolve as O$_2$. We oxidized Li$_2$CO$_3$ packed electrodes in an electrolyte containing a ^{1}O$_2$ trap and subsequently identified its selective product with the trap starting from 3.8 V via HPLC and ^{1}H NMR. In addition, ^{3}O$_2$ evolution was detected through deactivation of ^{1}O$_2$ in presence of a quencher via OEMS.

N. Mahne, S.E. Renfrew, B.D. McCloskey and S.A. Freunberger

These results have substantial implications for the long-term cyclability of battery chemistries such as Li-ion, Li-O$_2$/CO$_2$ and underpin the importance of avoiding ^{1}O$_2$ in metal-O$_2$ batteries. They also question the possibility of a reversible metal-CO$_2$ battery based on a carbonate discharge product and help explaining the interfacial reactivity of transition-metal cathodes with residual Li$_2$CO$_3$. In battery chemistries where electrodes operate beyond 3.8 V $vs.$ Li/Li$^+$ the presence of Li$_2$CO$_3$, whether at impurity level or as a main component, or through electrolyte or electrode degradation, will affect

their stability. Strategies have to be conceived to reduce $^1O_2$ generation and avoid the presence of Li_2CO_3 during battery operation.[129]

Further attempts to quantify $^3O_2$ using an optical trace sensor during electrochemical oxidation of Li_2CO_3 in presence of several quenchers such as DABCO and azides *e.g.*, LiN_3 and NaN_3 are described in Appendix A.2 Page 124). Initially, we tried to synthesize Li_2CO_3 and carbonaceous products *via* combined electrochemical and chemical routes *i.e.*, discharge of a O_2 cathode in $1\,M$ LiTFSI PC:DME (v:v; 1:1) to form Li_2O_2 and subsequent exposure to CO_2 in order to convert Li_2O_2 according to $2Li_2O_2 + 2CO_2 \rightarrow 2Li_2CO_3 + O_2$. Oxidation of these prepared electrodes resulted in O_2 and CO_2 evolution derived from Li_2O_2 oxidation as no full conversion to Li_2CO_3 was accomplished, which was confirmed by acid titration as negligible traces of CO_2 were evolved. Therefore, selective synthesis of Li_2CO_3 *via* electrochemical and/or chemical route is inefficient and electrodes made in this manner were not used for further analysis.

# Electrochemical Oxidation of Lithium Carbonate Generates Singlet Oxygen

Nika Mahne, Sara E. Renfrew, Bryan D. McCloskey, and Stefan A. Freunberger*

Abstract: *Solid alkali metal carbonates are universal passivation layer components of intercalation battery materials and common side products in metal-O_2 batteries, and are believed to form and decompose reversibly in metal-O_2/CO_2 cells. In these cathodes, Li_2CO_3 decomposes to CO_2 when exposed to potentials above 3.8 V vs. Li/Li$^+$. However, O_2 evolution, as would be expected according to the decomposition reaction $2 Li_2CO_3 \rightarrow 4 Li^+ + 4 e^- + 2 CO_2 + O_2$, is not detected. O atoms are thus unaccounted for, which was previously ascribed to unidentified parasitic reactions. Here, we show that highly reactive singlet oxygen ($^1O_2$) forms upon oxidizing Li_2CO_3 in an aprotic electrolyte and therefore does not evolve as O_2. These results have substantial implications for the long-term cyclability of batteries: they underpin the importance of avoiding $^1O_2$ in metal-O_2 batteries, question the possibility of a reversible metal-O_2/CO_2 battery based on a carbonate discharge product, and help explain the interfacial reactivity of transition-metal cathodes with residual Li_2CO_3.*

Energy storage in Li-based batteries is limited by the cathode, which has triggered intense research efforts to increase cathode capacity and/or voltage.[1] Candidate approaches include Li-stoichiometric[2] and Li-rich[3] transition-metal oxide (TMO) intercalation cathodes, which have higher voltage and capacity than currently used cathodes, and metal-O_2 or metal-O_2/CO_2 cathodes,[1,4] which have lower voltage but substantially higher theoretical capacity. Making high-voltage TMOs viable requires increasing the reversible potential window through understanding the high-voltage instabilities of intercalation materials and electrolytes.[1] Much recent work has revealed an intimate interdependence

of electrolyte decomposition, surface species formation/decomposition, and TMO bulk and surface reconstruction.[2d,3d,5] In particular, it was recently found that the outgassing of CO_2 during the first cycle in Li-ion batteries is mostly governed by residual Li_2CO_3, which in turn affects O_2 evolution from the TMO lattice.[5b] With respect to Li-O_2 batteries, Li_2CO_3 is an unwanted parasitic product, which hampers rechargeability, accumulates on cycling, and hence causes poor energy efficiency and cycle life.[1,4a–f] The burden of Li_2CO_3 formation was seemingly made use of in rechargeable metal-O_2/CO_2 batteries based on the observation that Li_2CO_3 can be electrochemically decomposed.[4f–j,6]

Thus Li_2CO_3, be it a trace or main component, plays a central role in considerations of cyclability and stability for a large fraction of future Li battery systems, and understanding its electrochemical oxidation is paramount for further development. While it is clear that Li_2CO_3 decomposition evolves CO_2, the fate of the third O atom in CO_3^{2-} has been an enduring open question since no O_2 evolves, although this would be expected from the formal oxidation reaction:[3e,4c,f–h,j,5b]

$$2 Li_2CO_3 \rightarrow 4 Li^+ + 4 e^- + 2 CO_2 + O_2 \quad E° = 3.82 \text{ V vs. Li/Li}^+ \quad (1)$$
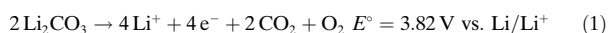
Previous explanations have proposed the formation of superoxide or "nascent oxygen", which could react with cell components in a reaction path involving carbon,[4f,6] without, however, definite proof for these mechanisms. Herein, we provide compelling evidence that the electrochemical oxidation of Li_2CO_3 forms highly reactive $^1O_2$, which, through a parasitic reaction of $^1O_2$ with battery components, explains the absence of O_2 evolution. Given its exceptional reactivity, the formation of $^1O_2$ has far-reaching implications for TMO surface reactivity and coupled parasitic reactions upon recharging metal-O_2 and metal-O_2/CO_2 batteries.

$^1O_2$ may be detected using chemical probes, which react specifically with $^1O_2$ and can be detected spectroscopically by measuring the disappearance of the probe and/or the appearance of the adduct. Reported probes include fluorophores or spin traps, which may be detected by fluorescence "switch on/off" or by EPR spectroscopy.[7] However, these probes are typically electrochemically unstable above 3.5–3.7 V vs. Li/Li$^+$ and do not allow access to the relevant Li_2CO_3 oxidation potential range above 3.8 V. Previously, we have shown that 9,10-dimethylanthracene (DMA) fulfills these requirements: it rapidly forms the endoperoxide (DMA-O_2) in the presence of $^1O_2$; both DMA and DMA-O_2 are electrochemically stable beyond 4 V (Figure S1); and DMA is also stable against superoxide, another possible reactive oxygen species. In other words, exposing DMA to superoxide

[*] N. Mahne, Dr. S. A. Freunberger
Institute for Chemistry and Technology of Materials
Graz University of Technology, Stremayrgasse 9, 8010 Graz (Austria)
E-mail: freunberger@tugraz.at
S. E. Renfrew, Prof. B. D. McCloskey
Energy Storage and Distributed Resources Division
Lawrence Berkeley National Laboratory
and
Department of Chemical and Biomolecular Engineering
University of California – Berkeley, Berkeley, CA 94720 (USA)

Supporting information and the ORCID identification number(s) for the author(s) of this article can be found under:
https://doi.org/10.1002/anie.201802277.

does not form DMA-O$_2$, which otherwise would be falsely assigned to the presence of $^1O_2$.[8] To further confirm that DMA-O$_2$ forms only with $^1O_2$ but not with other possibly reactive O-containing species, we exposed the electrolyte with DMA separately to Li$_2$CO$_3$, O$_2$, CO$_2$, and Li$_2$O$_2$ and did not observe DMA-O$_2$ (Figure S2). The same holds true for DMA exposed to Li$_2$O$_2$ with CO$_2$, which forms a peroxodicarbonate, a possible intermediate of Li$_2$CO$_3$ oxidation.[9] Together, these results confirm that DMA→DMA-O$_2$ conversion is a sensitive and selective method to detect $^1O_2$ in the cell environment.

To probe whether $^1O_2$ forms upon oxidizing Li$_2$CO$_3$, we constructed electrochemical cells with Li$_2$CO$_3$-packed working electrodes as detailed in the Methods section in the Supporting Information. Li$_2$CO$_3$ was ball-milled with carbon black to ensure intimate contact between the two and the resulting powder was used to form composite electrodes using PTFE binder. To specifically probe reactions at the working electrode and to exclude unwanted reactions of the electrolyte with a Li metal anode, we used Li$_{1-x}$FePO$_4$ ($E° = 3.45$ V vs. Li/Li$^+$) as the counter and reference electrode. First, we established the onset potential of Li$_2$CO$_3$ oxidation using a potential sweep measurement in an online electrochemical mass spectrometry (OEMS) setup to follow the gases evolved. Figure 1 shows CO$_2$, O$_2$, CO, and H$_2$ evolution in comparison
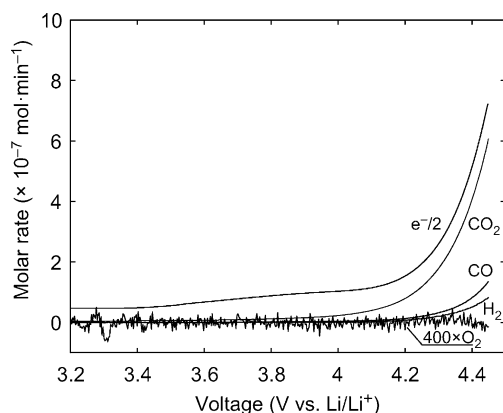

Figure 1. CO$_2$, O$_2$, CO, and H$_2$ evolution from carbon black/Li$_2$CO$_3$/PTFE (9:1:1, m:m) composite electrodes during a linear potential scan at 0.14 mV s^{-1} in 0.1 M LiTFSI in TEGDME under an Ar atmosphere.

to the electron consumption rate. CO$_2$ evolution commences at around 3.8 V, with a ratio of approximately $2e^-/CO_2$ observed at higher voltages. Note that capacitive current accounts for the initial electron consumption rate above open circuit and causes the electron consumption rate to remain slightly higher than the CO$_2$ evolution rate. The onset of CO$_2$ evolution at 3.8 V is in accordance with the equilibrium potential of Reaction 1 ($E° = 3.82$ V vs. Li/Li$^+$).[4c,6] Consistent with numerous studies, O$_2$ was not detected throughout charging.[4c,g,h,5b] H$_2$ and CO evolution is observed above 4.2 V during the anodic scan of the Li$_2$CO$_3$-packed electrodes, but no gas evolution is observed below 4.5 V from blank carbon black electrodes (Figure S3). Absence of CO$_2$ when a blank

electrode is charged proves Li$_2$CO$_3$ oxidation to be the CO$_2$ source in Figure 1. The comparison of the blank and Li$_2$CO$_3$-packed electrode also indicates that the H$_2$ evolution observed (Figure 1) has to originate from a parasitic electrolyte degradation reaction induced by Li$_2$CO$_3$ oxidation, since the electrolyte otherwise appears stable at Li$_2$CO$_3$-free electrodes until at least 4.5 V.

To examine whether the highly reactive $^1O_2$ forms and could thus explain the absence of O$_2$ release, we constructed cells with the same Li$_2$CO$_3$ working electrodes and 0.1 M LiTFSI in dimethoxyethane (DME) containing 30 mM DMA as the electrolyte. Cells were held at various charging potentials until a capacity of 0.064 mAh was reached. The electrolyte was then extracted and subjected to HPLC and ^{1}H NMR analysis (Figure 2).

HPLC analysis showed that DMA-O$_2$ formed at all charging voltages from 3.8 V onwards (Figure 2a). Blank measurements, where electrodes without Li$_2$CO$_3$ were polarized analogously, did not yield DMA-O$_2$ (Figure S4).
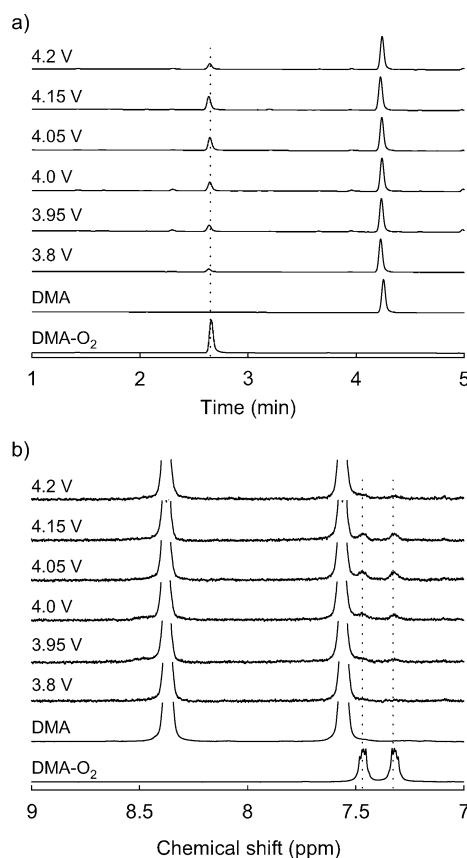

Figure 2. a) HPLC analysis of the electrolyte after polarizing carbon black/Li$_2$CO$_3$/PTFE (9:1:1 m:m) composite electrodes at the indicated potential to reach a capacity of 0.064 mAh in 0.1 M LiTFSI in DME that contained 30 mM DMA. ^{1}H NMR confirms DMA-O$_2$ to elute at 2.6 min (Figures S2, S5). b) ^{1}H NMR spectra of the same electrolyte samples. Reference measurements are shown with the starting electrolyte (labeled as DMA) and electrolyte where the DMA was fully converted into DMA-O$_2$ by in situ photogenerated $^1O_2$ (labeled as DMA-O$_2$) as described in the Supporting Information.

^{1}H NMR analysis of the samples confirmed the presence of DMA-O$_2$ at these voltages (Figure 2b, S6). The HPLC and NMR results confirm that electrochemical oxidation of Li$_2$CO$_3$ forms ^{1}O$_2$ from the onset of oxidation at 3.8 V.
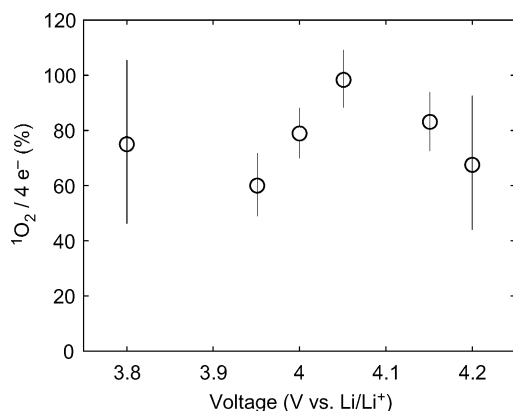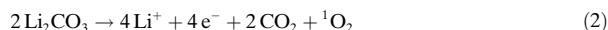

Figure 3. Amount of ^{1}O$_2$ (as quantified by HPLC as DMA-O$_2$) relative to the charge passed in Equation (2) at different charging potentials. Values represent lower bounds since not all ^{1}O$_2$ may react to DMA-O$_2$ or the electrolyte may be incompletely extracted.

Figure 3 relates the amount of ^{1}O$_2$ formed to the charge passed in the reaction:

$$2\,Li_2CO_3 \rightarrow 4\,Li^+ + 4\,e^- + 2\,CO_2 + {}^1O_2 \tag{2}$$

A maximum of one ^{1}O$_2$ could be produced per four electrons. ^{1}O$_2$ formed at all probed voltages to an extent well above 50% of the $4\,e^-/^1$O$_2$ maximum limit. The amount of ^{1}O$_2$ must, however, be inferred with caution from the measured amount of DMA-O$_2$ and represents a lower bound of the true value. This is because not all ^{1}O$_2$ will react with DMA, but may decay along other routes. Furthermore, the electrolyte may be incompletely extracted and thus result in an artificially low ^{1}O$_2$ value. At higher voltages (e.g., 4.2 V), DMA-O$_2$ could degrade to a minor extent, as shown in Figure S1 in the Supporting Information, which may explain the observed lower yield of DMA-O$_2$ at 4.2 V compared to 4.05 V in Figure 3. Overall, the values in Figure 3 suggest that the majority, if not all, of the "missing O$_2$" from the electrochemical oxidation of Li$_2$CO$_3$ forms ^{1}O$_2$ and is thus not detected in the gas phase.

The complete lack of O$_2$ evolution during oxidation of Li$_2$CO$_3$ (Figure 1) implies that the formed ^{1}O$_2$ reacts with cell components rather than being, even in part, deactivated to ^{3}O$_2$. We therefore investigated the use of a ^{1}O$_2$ quencher, which deactivates ^{1}O$_2$ to ^{3}O$_2$,[10] to possibly promote ^{3}O$_2$ evolution. A variety of quenchers have been reported, including azides and aliphatic amines.[10,11] We have previously shown that 1,4-diazabicyclo[2.2.2]octane (DABCO) is effective in non-aqueous environments.[8a] For use during electrochemical oxidation of Li$_2$CO$_3$, however, the electrochemical stability of the quenchers is problematic, since

DABCO and other quenchers (e.g., LiN$_3$) are electrochemically oxidized at approximately 3.5–3.6 V (Figure S7).[12] Nevertheless, diffusion of fresh quencher from the separator may counterbalance quencher oxidation at the working electrode and thus may show some quenching efficiency. Figure 4 shows CO$_2$ and O$_2$ evolution during an OEMS
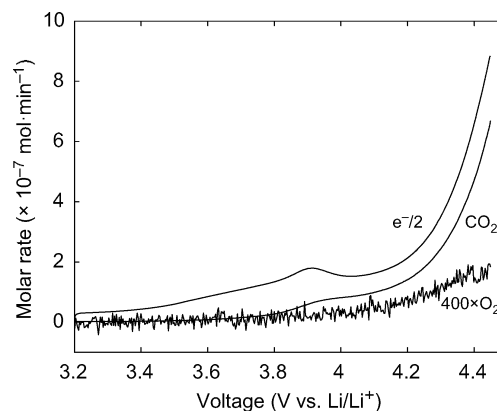

Figure 4. CO$_2$ and O$_2$ evolution from Super P/Li$_2$CO$_3$/PTFE (9:1:1 m:m:m) composite electrodes during a linear potential scan at 0.14 mVs^{-1} in 0.1 M LiTFSI in TEGDME that contained 30 mM DABCO.

measurement similar to Figure 1, but with an electrolyte that contained 30 mM DABCO. DABCO oxidation accounts for the anodic process that onsets at around 3.6 V and peaks at 3.9 V. As before, CO$_2$ evolution starts at around 3.8 V and reaches a rate close to $2\,e^-$/CO$_2$. Intriguingly, O$_2$ evolution does start together with CO$_2$ evolution at around 3.8 V with a similarly growing rate as the voltage rises. This result further corroborates ^{1}O$_2$ formation and also shows that if a suitable quencher can be found, then Li$_2$CO$_3$ could be oxidized without the detrimental effects of ^{1}O$_2$.

Detection of ^{1}O$_2$, and ^{3}O$_2$ when a quencher is present, implies that a mechanism of Li$_2$CO$_3$ oxidation involves the formation of O—O bonds. In analogy to carbonate oxidation in aqueous media,[13] it has been suggested that Li peroxodicarbonate (LiO$_2$COOCO$_2$Li) forms as an intermediate.[4h] Such an intermediate has been questioned on the basis that 1) CO$_3^{2-}$ is poorly soluble and would thus lack mobility to combine to peroxodicarbonate and 2) the high charge density of the peroxodicarbonate anion ($^-$O$_2$COOCO$_2^-$) would not allow O—O bond formation or would lead to immediate bond cleavage.[4c,14] However, neither large carbonate mobility nor dissociation are required and a mechanism via a peroxodicarbonate intermediate can be proposed (Figure S8a) and rationalized based on previous reports.[4i,15] Formally, peroxodicarbonate can form through a $1\,e^-$ oxidation/Li$^+$ extraction of two Li$_2$CO$_3$ to form two LiO$_2$CO$^{\bullet}$ moieties (**2**), which combine to LiO$_2$COOCO$_2$Li (**3**). Within the Li$_2$CO$_3$ crystal structure (Figure S8b), adjacent carbonate moieties appear to be sufficiently close to form O—O bonds once an e$^-$ and a Li$^+$ is extracted in each. Mobility of the intermediates or even dissociation from the crystal lattice is thus not required. A DFT study on the oxidation of Li$_2$CO$_3$ surfaces has shown that

after first oxidation/Li$^+$ extraction, further Li$^+$ extractions are energetically most favorable at adjacent carbonate moieties, which makes their recombination likely.[15] Such recombination within the crystal lattice is also supported by DFT work on the formation of Li$_2$CO$_3$ via peroxodicarbonate, which yields adjacent carbonate moieties within the Li$_2$CO$_3$ lattice.[4i] According to the same work, the O−O bond in LiO$_2$COOCO$_2$Li is strongly stabilized by coordination with Li$^+$ ions in comparison to $^-$O$_2$COOCO$_2$$^-$, which is unlikely to form in a nonaqueous environment. A possible ongoing pathway to form ^{1}O$_2$ is shown in Figure S8a. Further oxidation and decarboxylation could yield LiCO$_4$ (**4**; Figure S8a), which then in turn could yield ^{1}O$_2$. Clarification of the exact mechanism, however, will need further computational or/and experimental work.

In conclusion, by using a selective ^{1}O$_2$ trap and online mass spectrometry, we have shown that electrochemical oxidation of Li$_2$CO$_3$ in a nonaqueous environment yields up to stoichiometric amounts of ^{1}O$_2$ according to the reaction $2\,Li_2CO_3 \rightarrow 4\,Li^+ + 4\,e^- + 2\,CO_2 + {}^1O_2$. This explains the absence of O$_2$ evolution, which has been a long-standing conundrum and a cause for much speculation regarding potential reactive oxygen species. The reaction proceeds from an onset potential of approximately 3.8 V, which is close to its thermodynamic value of 3.82 V. When a ^{1}O$_2$ quencher is present, part of the formed ^{1}O$_2$ could be evolved as ^{3}O$_2$. Li$_2$CO$_3$ is a universal passivating agent in Li-ion battery cathodes and decisive in interfacial reactivity. Li$_2$CO$_3$ is also a common side product in Li-O$_2$ cathodes, as well as the targeted discharge product in Li-O$_2$/CO$_2$ batteries, where it then needs to be oxidized on charge to form a reversible system. Our results thus strongly suggest that Li$_2$CO$_3$ formation, even at impurity levels, will have a deleterious affect on the stability of all Li batteries where electrodes operate beyond 3.8 V vs. Li/Li$^+$, which includes most currently studied cathodes. Strategies to avoid ^{1}O$_2$ formation or the presence of Li$_2$CO$_3$ during battery operation are therefore warranted.

Conflict of interest

The authors declare no conflict of interest.

[1] J. W. Choi, D. Aurbach, *Nat. Rev. Mater.* **2016**, *1*, 16013.

[2] a) C. Sigala, D. Guyomard, A. Verbaere, Y. Piffard, M. Tournoux, *Solid State Ionics* **1995**, *81*, 167–170; b) N.-S. Choi, Z. Chen, S. A. Freunberger, X. Ji, Y.-K. Sun, K. Amine, G. Yushin, L. F. Nazar, J. Cho, P. G. Bruce, *Angew. Chem. Int. Ed.* **2012**, *51*, 9994–10024; *Angew. Chem.* **2012**, *124*, 10134–10166; c) Q. Zhong, A. Bonakdarpour, M. Zhang, Y. Gao, J. R. Dahn, *J. Electrochem. Soc.* **1997**, *144*, 205–213; d) A. Jarry, S. Gottis, Y.-S. Yu, J. Roque-Rosell, C. Kim, J. Cabana, J. Kerr, R. Kostecki, *J. Am. Chem. Soc.* **2015**, *137*, 3533–3539.

[3] a) M. M. Thackeray, S.-H. Kang, C. S. Johnson, J. T. Vaughey, R. Benedek, S. A. Hackney, *J. Mater. Chem.* **2007**, *17*, 3112–3125; b) Z. Lu, L. Y. Beaulieu, R. A. Donaberger, C. L. Thomas, J. R. Dahn, *J. Electrochem. Soc.* **2002**, *149*, A778–A791; c) M. Sathiya, G. Rousse, K. Ramesha, C. P. Laisa, H. Vezin, M. T. Sougrati, M. L. Doublet, D. Foix, D. Gonbeau, W. Walker, A. S. Prakash, M. Ben Hassine, L. Dupont, J. M. Tarascon, *Nat. Mater.* **2013**, *12*, 827–835; d) K. Luo, M. R. Roberts, R. Hao, N. Guerrini, D. M. Pickup, Y.-S. Liu, K. Edström, J. Guo, A. V. Chadwick, L. C. Duda, P. G. Bruce, *Nat. Chem.* **2016**, *8*, 684–691; e) N. Yabuuchi, K. Yoshii, S.-T. Myung, I. Nakai, S. Komaba, *J. Am. Chem. Soc.* **2011**, *133*, 4404–4419.

[4] a) Y.-C. Lu, B. M. Gallant, D. G. Kwabi, J. R. Harding, R. R. Mitchell, M. S. Whittingham, Y. Shao-Horn, *Energy Environ. Sci.* **2013**, *6*, 750–768; b) D. Aurbach, B. D. McCloskey, L. F. Nazar, P. G. Bruce, *Nat. Energy* **2016**, *1*, 16128; c) S. Meini, N. Tsiouvaras, K. U. Schwenke, M. Piana, H. Beyer, L. Lange, H. A. Gasteiger, *Phys. Chem. Chem. Phys.* **2013**, *15*, 11478–11493; d) Y. Wang, Z. Liang, Q. Zou, G. Cong, Y.-C. Lu, *J. Phys. Chem. C* **2016**, *120*, 6459–6466; e) V. Giordani, D. Tozier, H. Tan, C. M. Burke, B. M. Gallant, J. Uddin, J. R. Greer, B. D. McCloskey, G. V. Chase, D. Addison, *J. Am. Chem. Soc.* **2016**, *138*, 2656–2663; f) Z. Zhao, J. Huang, Z. Peng, *Angew. Chem. Int. Ed.* **2018**, *57*, 3874–3886; *Angew. Chem.* **2018**, *130*, 3936–3949; g) S. R. Gowda, A. Brunet, G. M. Wallraff, B. D. McCloskey, *J. Phys. Chem. Lett.* **2013**, *4*, 276–279; h) S. A. Freunberger, Y. Chen, Z. Peng, J. M. Griffin, L. J. Hardwick, F. Bardé, P. Novák, P. G. Bruce, *J. Am. Chem. Soc.* **2011**, *133*, 8040–8047; i) H.-K. Lim, H.-D. Lim, K.-Y. Park, D.-H. Seo, H. Gwon, J. Hong, W. A. Goddard, H. Kim, K. Kang, *J. Am. Chem. Soc.* **2013**, *135*, 9733–9742; j) L. Wang, L. Dai, L. Ma, L. Gong, Z. Lyu, Y. Zhou, J. Liu, M. Lin, M. Lai, Z. Peng, W. Chen, *ACS Omega* **2017**, *2*, 9280–9286.

[5] a) F. Lin, I. M. Markus, D. Nordlund, T.-C. Weng, M. D. Asta, H. L. Xin, M. M. Doeff, *Nat. Commun.* **2014**, *5*, 3529; b) S. E. Renfrew, B. D. McCloskey, *J. Am. Chem. Soc.* **2017**, *139*, 17853–17860; c) H. Zheng, Q. Sun, G. Liu, X. Song, V. S. Battaglia, *J. Power Sources* **2012**, *207*, 134–140; d) A. R. Armstrong, M. Holzapfel, P. Novák, C. S. Johnson, S.-H. Kang, M. M. Thackeray, P. G. Bruce, *J. Am. Chem. Soc.* **2006**, *128*, 8694–8698.

[6] S. Yang, P. He, H. Zhou, *Energy Environ. Sci.* **2016**, *9*, 1650–1654.

[7] a) P. R. Ogilby, *Chem. Soc. Rev.* **2010**, *39*, 3181–3209; b) J. Wandt, P. Jakes, J. Granwehr, H. A. Gasteiger, R.-A. Eichel, *Angew. Chem. Int. Ed.* **2016**, *55*, 6892–6895; *Angew. Chem.* **2016**, *128*, 7006–7009.

Supporting Information: Singlet Oxygen Generation during Electrochemical Oxidation of Li_2CO_3

Nika Mahne[†], Sara E. Renfrew[‡,§], Bryan D. McCloskey[‡,§] and Stefan A. Freunberger[†]*

[†] Institute for Chemistry and Technology of Materials, Graz University of Technology, Stremayrgasse 9, 8010 Graz, Austria

[‡] Energy Storage and Distributed Resources Division, Lawrence Berkeley National Laboratory, Berkeley, California 94720, United States

[§] Department of Chemical and Biomolecular Engineering, University of California Berkeley, Berkeley, California 94720, United States

Materials and Methods

Chemicals and Purification

Lithium bis(trifluoromethane)sulfonimide (LiTFSI, CAS-Nr. 90076-65-6) was purchased from SOLVIONIC and dried under reduced pressure for 24 h at 140 °C. Dimethoxyethane (DME, CAS-Nr. 115-10-6) and tetraethylene glycol dimethyl ether (TEGDME, CAS-Nr. 143-24-8) were purchased from TCI Chemicals. The ethers were dried over lithium and purified *via* distillation and further dried and stored over activated molecular sieves. The water content was determined by Karl-Fisher titration using a Methrom 851 Titrando. 9,10-Dimethylanthracene (DMA, CAS-Nr. 781-43-1, >98%) was purchased from TCI Chemicals. DMA was recrystallized in ethanol and its purity was confirmed by ^{1}H NMR spectroscopy and HPLC analysis. Photo-chemical generation of $^1O_2$ was done by an *in-situ* photo-chemical process with a sensitizer. The sensitizer in the $^3O_2$ saturated solution was irradiated with a red light-emitting diode (OSRAM). This procedure was used to synthesize DMA-O_2, which was further used as a reference. 1,4-Diazabicyclo[2.2.2]octane (DABCO, CAS-Nr. 280-57-9, ReagentPlus®, 99%) was purchased from Sigma Aldrich. DABCO was purified *via* recrystallization from absolute diethyl ether. Lithium peroxide (Li_2O_2) was synthesized as described previously and further ground in a ball mill (Pulverisette 7, Fritsch) with ZrO_2 grinding balls under inert conditions.[1] Its purity and diminished crystallite size were confirmed by ATR-IR and XRD and spectroscopy. Formic acid (CAS-Nr. 64-18-6, puriss. p.a. ∼98%) was purchased from Fluka® Analytical. Water (CAS-Nr. 7732-18-5, CHROMASOLV® for HPLC) was purchased from Sigma-Aldrich. Acetonitrile (CAS-Nr. 78-05-8, HiPerSolv CHROMANORM Prolabo®) was purchased from VWR Chemicals. High purity oxygen (O_2 3.5, 99.95vol%), high purity Ar (Ar 5.0, 99.999vol%) and a mixture of argon and oxygen (Ar 6.0 and O_2 5.5; Ar 5.01 vol%) were purchased from Messer Austria GmbH.

Polytetrafluoroethylene (PTFE, CAS-Nr. 9002-84-0, 60wt% dispersion in H_2O) was purchased from Sigma Aldrich. Carbon (Carbon black, C-NERGYTM Graphite and Carbon Black, SUPER C65 conductive carbon) was provided from IMERYL Graphite and Carbon. Lithium iron phosphate (LFP, CAS-Nr. 15365-1-7) was purchased from MTI Corporation. Delithiation of LFP was done according to a previously reported procedure.[2] Di(cyclopentadienyl)iron (Fc, CAS-Nr. 102-54-5, for synthesis) was purchased from Sigma Aldrich. Lithium carbonate (Li_2CO_3, CAS-Nr. 554-13-2, Puratronic®, 99.998% metal basis excluding Ca LT 20 ppm) was purchased from Alfa Aesar®, Thermo Fisher Scientific Chemicals. Li_2CO_3 was ground with carbon (1/9, m/m) for 1.5 h in a planetary mill (200 rpm). ATR-IR spectroscopy and XRD confirmed that no mechanochemically induced reaction occurred. The broadening of the significant Bragg reflections of Li_2CO_3 before and after grinding indicate that the crystallite size diminished through the grinding process.

Electrode Fabrication and Cell Design

Free standing Li_2CO_3/C black/PTFE electrodes (12 mm) were made from a slurry of lithium carbonate and Carbon black (1/9, w/w) with PTFE binder (9/1, w/w) using isopropyl alcohol. The LFP/C black/PTFE counter electrodes were prepared by mixing partially delithiated LFP with carbon and PTFE (8/1/1, w/w/w). Celgard separators (2400) and the electrodes were first washed with isopropyl alcohol and water (1/1, v/v) and subsequently with acetone. Electrodes and separators were dried under reduced pressure at 120 °C for 24 h and then transferred to an Ar-filled glove box. The counter electrode had three-fold the expected capacity of the working electrode. The test cells were assembled in a custom-built three-electrode cell configuration based on a Swagelok® design. Typical working electrodes had a carbon mass loading of 1 mg and the cells were assembled with 100 μL electrolyte. The electrolytes contained less than 15 ppm water.

Electrochemical and Spectroscopic Methods

Electrochemical tests were run on a potentiostat/galvanostat (either a SP-300 from Bio-Logic, France, or BT-2000 from Arbin). Cyclic voltammograms were recorded in a three-electrode arrangement with a glassy carbon or a Au-disc working electrode (BAS Inc.), a Ag wire pseudo-reference and a Pt wire counter electrode inside a glass cell with PTFE lid. The cells were run inside an Ar-filled glovebox and purged with high-purity Ar or O_2. The redox system Fc/Fc$^+$ was used to reference the measured data vs. Li/Li$^+$. The $Li_{1-x}FePO_4$ potential vs. Li/Li$^+$ was used to express all potentials on the lithium scale. DMA-O_2 as a reference compound (Figure 2, Figure S1, S2, S4-S6) was made by photooxygenation of DMA in O_2 saturated electrolyte with the sensitizer palladium(II) meso-tetra(4-

fluorophenyl)-tetrabenzoporphyrin (Pd_4F). The sensitizer Pd_4F was synthesized according a previously reported procedure and provided by S.M. Borisov from the Institute of Analytical Chemistry and Food Chemistry at Graz University of Technology.[3] Photosensitization is a process of transferring energy of absorbed light.[4] The photosensitization process is initiated by the excitation of the photo-sensitizer from its ground state, S_0, *via* radiation to its singlet excited state, S_n. Relaxation of Sn yields the lowest excited singlet state of the sensitizer S_1. Intersystem crossing (ISC) from S_1 generates the photo-sensitizers triplet state, T_1, which reacts further *via* an energy transfer process with the triplet state of molecular oxygen, generating singlet oxygen. DMA reacts with the *in-situ* generated singlet oxygen to the adduct $DMA-O_2$.[5] The sensitizer was excited in the red region (634 nm) of the spectrum.

Electrochemical Mass Spectrometry

The MS setup was built in-house and is similar to the one described previously.[6] It consists of a commercial quadrupole mass spectrometer (Balzers) with a turbomolecular pump (Pfeiffer), which is backed by a membrane pump and leak inlet, which samples from the purge gas stream. The electrochemical cell was a three-electrode cell of the type El-Cell DEMS (El-Cell GmbH, Hamburg, Germany). The setup was calibrated for different gases (Ar, O_2, CO_2, H_2, N_2 and H_2O) using calibration mixtures in steps over the anticipated concentration ranges to capture nonlinearity and cross-sensitivity. All calibrations and quantifications were performed using in-house software. The purge gas system consisted of a digital mass flow controller (Bronkhorst) and stainless steel tubing. The gas flow was fixed to 0.1 mL/min.

NMR Spectrometry

^1H NMR spectra of DMA, $DMA-O_2$ and the extracted electrolytes after polarization were recorded on a Bruker Avance III 300 MHz FT NMR spectrometer with autosampler (300.36 MHz, DMSO-d_6). Chemical shifts (δ) are referenced to the residual protonated solvent signals as internal standard.

High-Performance Liquid Chromatography

The high-performance liquid chromatography (HPLC) was used to determine the degree of the DMA to $DMA-O_2$ conversion. The electrolyte was extracted from all cell components using 400 μL DME, further sonicated in an ultrasonic bath for 10 min under exclusion of light and heat, centrifuged and the supernatant was transferred and removed by evaporation with N_2 stream at room temperature. The residue was dissolved in 500 μL DME and a volume of 2 μL was injected into the HPLC. The HPLC instrument was a 1200 Series (Agilent Technology). The eluent was monitored *via* an UV-

Vis detector (Agilent Technology G1365C MWD SL) at 210 nm. The samples were analyzed by a reversed-phase Poroshell column (120 EC-C8, 3.0 mm × 100 mm, Ø 2.7 μm, Agilent Technology) using a gradient system of acetonitrile (solvent B) and water containing 0.01% formic acid (solvent A). A pre-column (UHPLC 3PK, Poroshell 120 EC-C8 3.0 mm x 5 mm, Ø 2.7 μm, Agilent Technology) was connected before the reversed-phase column. The elution at a flow rate of 0.7 mL/min started with 50% solvent B and was then increased to 100% solvent B. The column was held at 20 °C throughout the measurements.

Supplementary References

[1] M. M. Ottakam Thotiyl, S. A. Freunberger, Z. Peng, P. G. Bruce, J. Am. Chem. Soc. 135, 494 - 500 (2013).

[2] D. Lepage, C. Michot, G. Liang, M. Gauthier, S. B. Schougaard, Angew. Chem. Int. Ed. 50, 6884 - 6887 (2011).

[3] S. M. Borisov, G. Nuss, W. Haas, R. Saf, M. Schmuck, I. Klimant, J. Photochem. Photobiol. A 201, 128 - 135 (2009).

[4] M. C. DeRosa, R. J. Crutchley, Coordin. Chem. Rev. 233-234, 351 - 371 (2002).

[5] A. G. Griesbeck, J. Mattey, Synthetic Organic Photochemistry, Marcel Dekker, (2004).

[6] Y. Chen, S. A. Freunberger, Z. Peng, F. Bard, P. G. Bruce, J. Am. Chem. Soc. 134, 7952 - 7957 (2012).
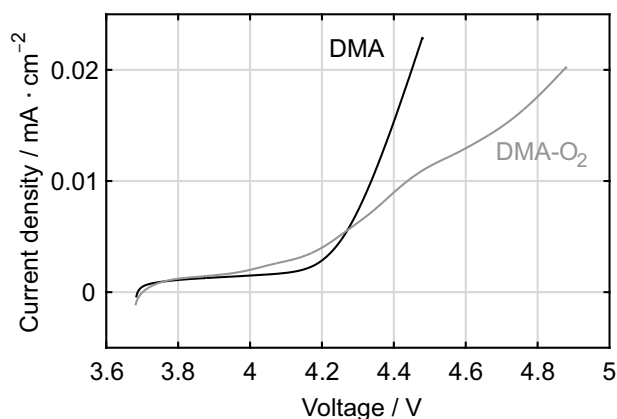
Supplementary Figures

Figure 7.1: Figure S1. Electrochemical stability of 9,10-dimethylanthracene (DMA) and 9,10-dimethylanthracene endoperoxide (DMA-O$_2$). Cyclic voltammetry was performed at a 3 mm glassy carbon disc electrode at a sweep rate of 50 mV·s^{-1}. First 2 mM DMA and 0.1 M LiClO$_4$ in DEGDME were measured under Ar atmosphere. ^{1}O$_2$ was then generated photochemically with the sensitizer Pd$_4$F under O$_2$ atmosphere, and the formed DMA-O$_2$ was subsequently measured under Ar atmosphere. Pd$_4$F was used in a concentration of 1 μM throughout the experiment.

Figure 7.2: Figure S2. HPLC UV analysis of electrolytes containing DMA after exposure to several possible reactants. DMA elutes at a retention time of 4.2 min and DMA-O_2 elutes at 2.6 min. HPLC UV chromatogramms ($\lambda_{210\,nm}$) of samples containing 30 μM DMA in 0.1 M LiTFSI DME in Ar after exposure to $^3O_2$, CO_2, Li_2O_2, Li_2CO_3, Li_2O_2/CO_2 for 24 h showing the stability of DMA in the course of this time frame. DMA-O_2 was produced by photooxygenation of DMA with Pd_4F.

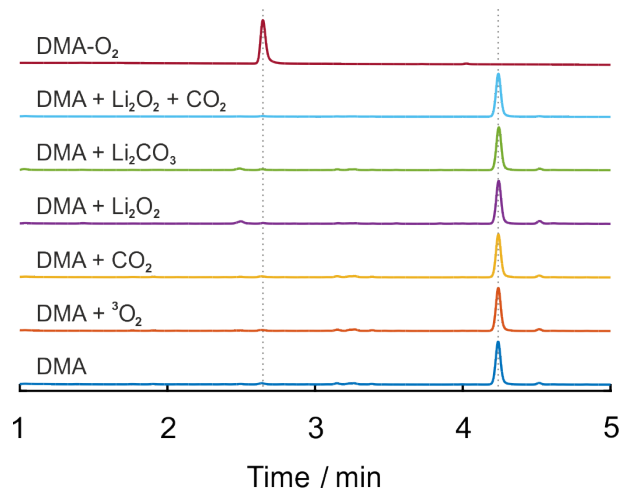**Figure 7.3:** Figure S3. CO_2, H_2, CO, and O_2 evolution from carbon black/PTFE (9/1, m/m) composite electrodes during a linear potential scan at 0.14 mV·s^{-1} in 0.1 M LiTFSI in TEGDME under an Ar atmosphere. For clarity values for CO_2, H_2, and CO are offset.
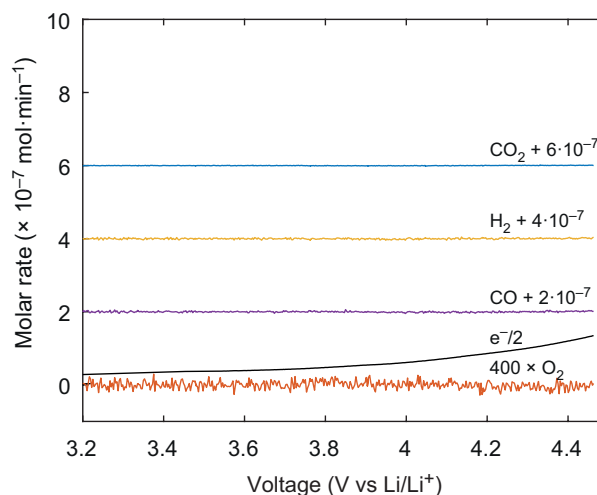

Figure 7.4: Figure S4. HPLC UV analysis of electrolyte containing DMA after polarization at a carbon black electrode in Ar atmosphere. The electrode was polarized stepwise at potentials starting from 3.8 V to 4.2 V. HPLC UV chromatogramms ($\lambda = 210$ nm) of the extracted electrolytes containing 30 μM DMA in 0.1 M LiTFSI DME after polarizing the electrode in Ar atmosphere show that no DMA-O_2 is formed without $^1O_2$ in this potential range.
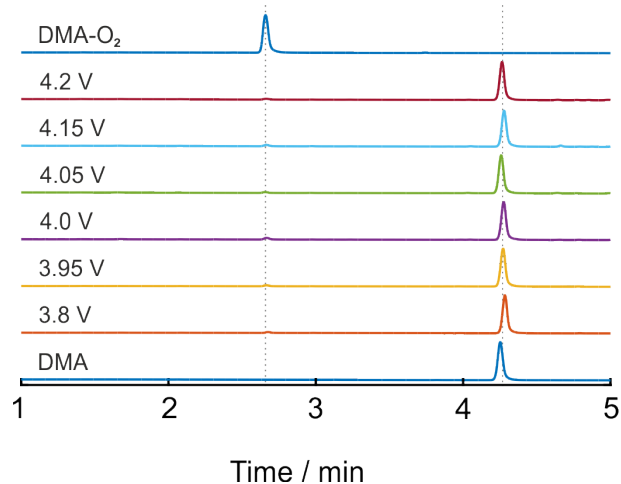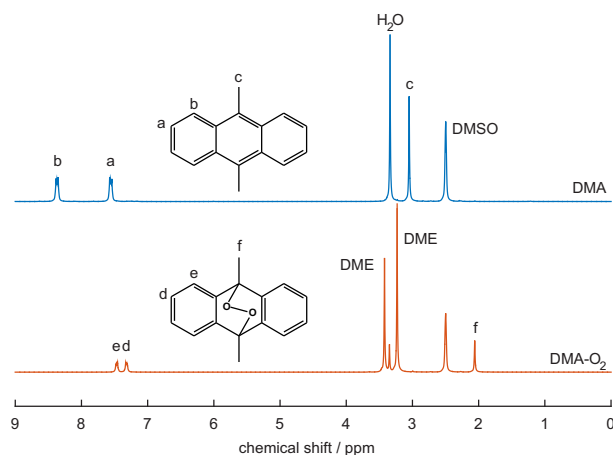
Figure 7.5: Figure S5. ^{1}H NMR spectra of 9,10 dimethylanthracene (DMA) and 9,10 dimethylanthracene endoperoxide (DMA-O$_2$) in DMSO-d$_6$. Residual solvent signals of DME (3.2 ppm and 3.5 ppm), H$_2$O (3.3 ppm) and DMSO-d$_6$ (2.5 ppm) are present in the aliphatic region of the ^{1}H NMR spectra due to sample preparation. DMA-O$_2$ was produced by photooxygenation of DMA with Pd$_4$F.
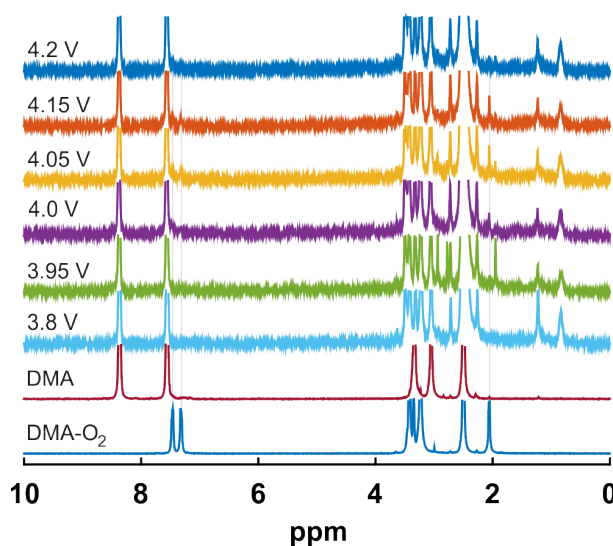

Figure 7.6: Figure S6. ^{1}H-NMR spectra of the extracted DMA containing electrolytes after oxidation of lithium carbonate. The spectra show the extracted electrolytes after oxidation of lithium carbonate in presence of DMA as electrolyte additive in Ar atmosphere. Residual solvent signals of DME (3.2 ppm, 3.5 ppm), H$_2$O (3.3 ppm) and DMSO d$_6$ (2.5 ppm) are present in the aliphatic region of the ^{1}H NMR spectra due to sample preparation. Reference signals of DMA and DMA-O$_2$ are highlighted in grey dashed lines.
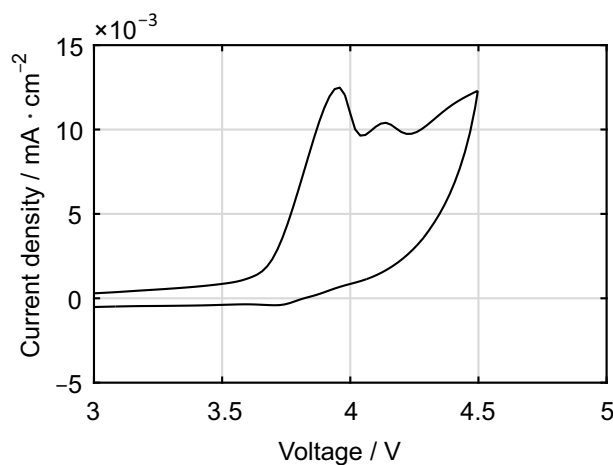
Figure 7.7: Figure S7. Electrochemical stability of DABCO. Cyclic voltammogram of 2 mM DABCO and 100 mM LiClO$_4$ in TEGDME at an Au-disc electrode with a scan rate of 100 mV·s^{-1}.

a)
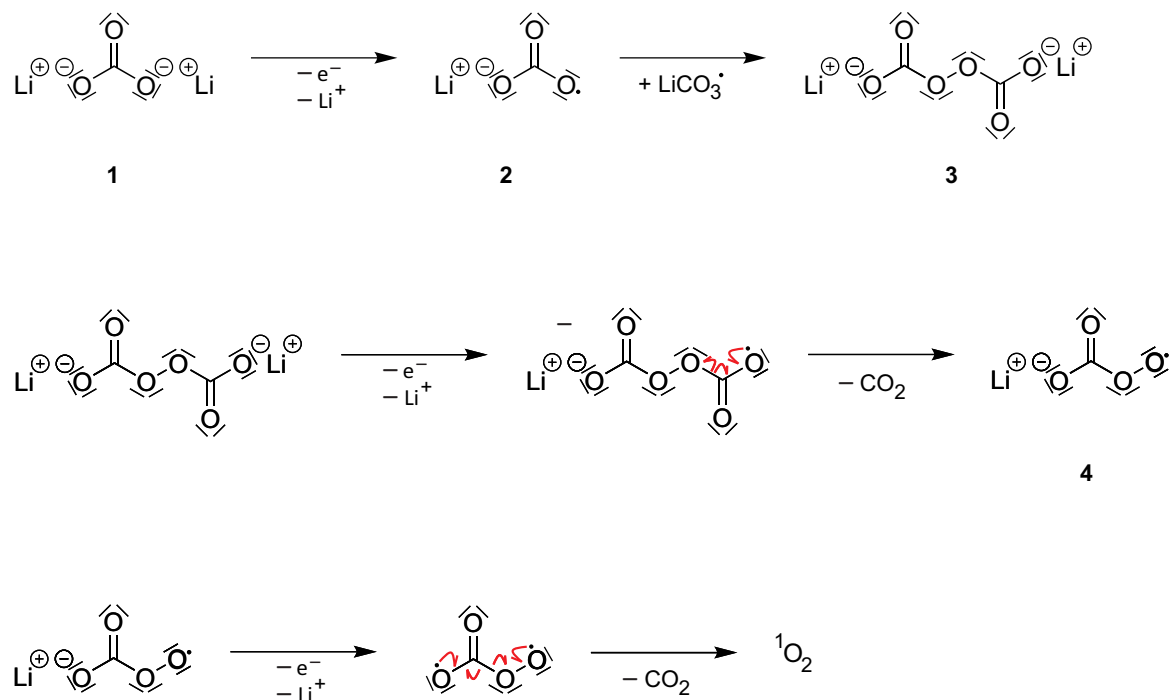
b)
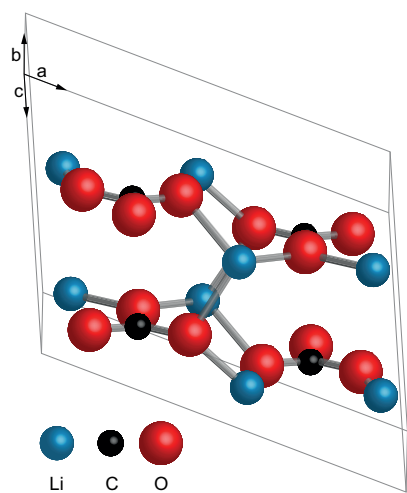
Figure 7.8: Figure S8. a) Proposed reaction mechanism of the electrochemical oxidation of lithium carbonate. Homolytic cleavage of the CO bond in the LiO_2COOCO_2 species leads to stepwise elimination of 2 CO_2 and $^1O_2$. Once released, $^1O_2$ can be deactivated through different deactivation pathways in its triplet ground state *inter alia via* a quencher. b) Unit cell of lithium carbonate.

Chapter 8

Novel Singlet Oxygen Quenchers

True reversibility of the cathode reaction in the Li-O_2 battery requires a set of qualities to obey the stoichiometry and to match each other during discharge and subsequent charge. One of these qualities is that the O_2 consumed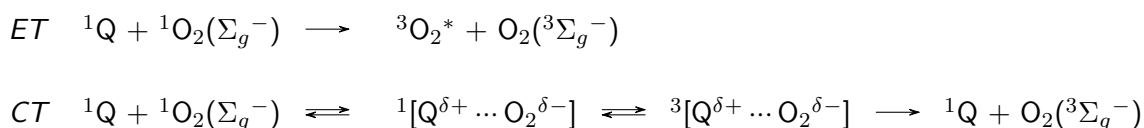 during discharge matches the amount released on subsequent charge.[60] Typically these measures deviate more or less significantly from the ideal due to parasitic reactions. Superoxide, peroxide and to a much greater extent singlet oxygen, have been identified to be the source for these irreversible parasitic reactions during cycling.[80, 51, 15] Therefore, one has to get down to the root of the issue of $^1O_2$ in metal-oxygen batteries in order for them to prevail as a future battery system.[76] We have shown that the addition of chemical traps and physical quenchers of $^1O_2$ as electrolyte additives significantly reduces the formation of carbonaceous side products during cycling (see *Chapter 4*). Despite the fact that chemical traps serve their purpose, they are inefficient as they cannot be reversibly regenerated as their formed product with singlet oxygen accumulates during cycling. In addition the trapped oxygen is not reversibly released to the system during oxygen evolution reaction (OER) and hence not available in the subsequent oxygen reduction reaction (ORR). For those reasons chemical trapping is not the desired mechanism to remove generated singlet oxygen during cycling. Physical quenchers, in contrast, are able to undergo a bimolecular process with singlet oxygen, which leads to $^3O_2$ and leaves the quencher unchanged. Therefore, it represents the process of choice as ground state oxygen and the quencher are reversibly recovered. Hence, the physical quencher DABCO has been identified as more efficient, compared to the trap DMA in Li-O_2 batteries.[51] DABCO's electrochemical stability ranges from 2.3 V to 3.6 V, which unfortunately is too low compared to the typically required potential range to recharge the Li-O_2 battery. With this significant detriment in mind we aimed to synthesise new singlet oxygen quenchers, which are possibly even stronger quenchers, are electrochemically stable to higher charging

potential, show chemical stability towards superoxide and peroxide. Ideally they should have higher quenching efficiency by *e.g.*, higher possible concentration in the electrolyte, and higher solubility compared to DABCO in glyme-based electrolytes.

8.1   Rational Design of Novel Amine-based $^1O_2$ Quenchers

Amines of various structural types have shown the ability to quench singlet oxygen *via* reversible charge transfer.[92] This process can be explained in terms of intermediate exciplex formation of singlet oxygen with the quencher. Subsequently, two competing ongoing processes can occur: energy transfer (ET) or charge transfer (CT), as illustrated in the reaction scemes below.[98] The essential difference between these processes is that in the first process energy transfer after exciplex formation yields an excited triplet state of the quencher from where it may decay to its ground state *via* non-radiative energy transfer or radiative energy transfer *via* phosphorescence.[86]

$$ET \quad ^1Q + {}^1O_2(\Sigma_g{}^-) \quad \longrightarrow \quad {}^3O_2{}^* + O_2({}^3\Sigma_g{}^-)$$

$$CT \quad ^1Q + {}^1O_2(\Sigma_g{}^-) \quad \rightleftharpoons \quad {}^1[Q^{\delta+}\cdots O_2{}^{\delta-}] \quad \rightleftharpoons \quad {}^3[Q^{\delta+}\cdots O_2{}^{\delta-}] \quad \longrightarrow \quad {}^1Q + O_2({}^3\Sigma_g{}^-)$$

The kinetics of these pathways is described by the kinetic constant k_Q.[98] At the same time there is always some likelihood for decay in the solvent with the kinetics k_d. Thus, the reactivity of a quencher in a certain solvent is described as the ratio of the decay of singlet oxygen and the quenching of singlet oxygen β_Q. For example, with a β_Q of 1.23×10^2 the reactivity of the cyclic amine DABCO is 1.5-fold the value of triethylamine ($\beta_Q = 0.76\times10^2$).[96] This demonstrates that there is considerable influence of the structure of aliphatic tertiary amines on their quenching ability. Our strategy derived therefrom is thus twofold: First, we want to investigate different tertiary amines, including branched ones, for their quenching ability to possibly find candidates with higher k_Q than DABCO. Nevertheless, no major effect is to be expected on oxidative stability. 3.6 V may even be enough if oxidation mediators are used to recharge the cell.[130] We designed a set of branched amines based on an unfolded DABCO-like structure with multiple nitrogens. Second, we want to investigate whether the amine can be modified for higher electrochemical stability whilst still showing high k_Q. The direction here is inspired by quaternised DABCOs as reported by Forsyth *et al.*[131,132] They have shown that quaternisation of DABCO with alkylhalides yields ionic liquids (IL) with an electrochemical stability in excess of 5 V *vs.* Li/Li$^+$. Their quenching ability is, however, unknown. Advantages may include higher solubility than molecular quenchers and potentially their use in pure substance as electrolyte.

IL are a promising alternative to state-of-the-art electrolyte mixtures in, *e.g.*, lithium-ion batteries as they overcome major safety issues of LIB's and comply some of the principles of *Green Chemistry*.[133] Essential properties of IL are their non-volatility, non-flammability, melting point below $100\,^\circ$C and high ionic conductivity. We thus synthesised a series of N-alkyl quaternised DABCOs with alkyl chain length of 1, 5 and 6 ($[C_nDABCO]^+$). As anion we either used the native I^-, which may at the same time act as oxidation mediator,[134] or $TFSI^-$.

8.1.1   Synthesis of novel singlet oxygen quenchers

Synthesis and purification of the following compounds illustrated in Figure 8.1 was performed by C. Leypold from the Institute for Chemistry and Technology of Materials from Graz University of Technology: 1-methyl-1,4-diazabicyclo[2.2.2]octan-1-ium bis(trifluoromethane)sulfonimide (DABCO-MeTFSI),   1-pentyl-1,4-diazabicyclo[2.2.2]octan-1-ium   bis(trifluoromethane)sulfonimide (DABCO-PeTFSI),   1-Hexyl-1,4-diazabicyclo[2.2.2]octan-1-ium   bis(trifluoromethane)sulfonimide (DABCO-HexTFSI) $N^1,N^{1'}$-(butane-1,4-diyl)bis(N^1-(2-(diethylamino)ethyl)-N^2,N^2-diethylethane-1,2-diamine)   (BuDiBiDi)   and $N^1,N^{1'}$-(hexane-1,6-diyl)bis(N^1-(2-(diethylamino)ethyl)-N^2,N^2-diethylethane-1,2-diamine) (HexDiBiDi).
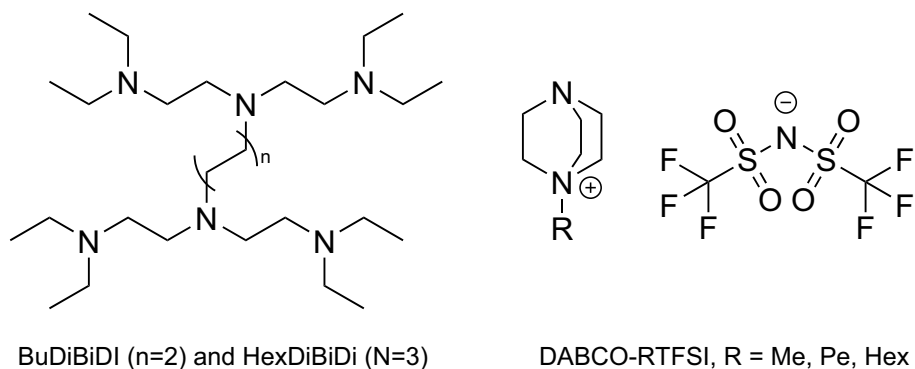

BuDiBiDI (n=2) and HexDiBiDi (N=3)   DABCO-RTFSI, R = Me, Pe, Hex

Figure 8.1: Synthesised novel amino-based singlet oxygen quenchers: BuDiBiDi (n = 2) and HexDiBiDi (left, n = 3) and DABCO-MeTFSI, DABCO-PeTFSI and DABCO-HexTFSI (right).

8.1.2   Electrochemical stability of singlet oxygen quenchers

The electrochemical stability of a set of widely known and novel singlet oxygen quenchers was determined *via* cyclic voltammetry. Subject to further analysis were the naturally occurring quenchers bilirubin and β-carotene (see Figure 8.2), the aliphatic amines DIPEA, DABCO, TMEDA and urotropin, aromatic amines DMPPDA and 1,4-benzenediamine, the novel aliphatic triamines BuDiBiDi and

HexDiBiDi, and the novel IL's DABCO-MeI, DABCO-MeTFSI, DABCO-PenTFSI, DABCO-HexTFSI (see Figure 8.3). The cyclic voltammogramms of 5 mM of analyte in 0.1 M LiClO$_4$ in TEGDME are grouped by their structure and shown in Figure 8.4, Figure 8.5 and in *Appendix B.1* Page 125.
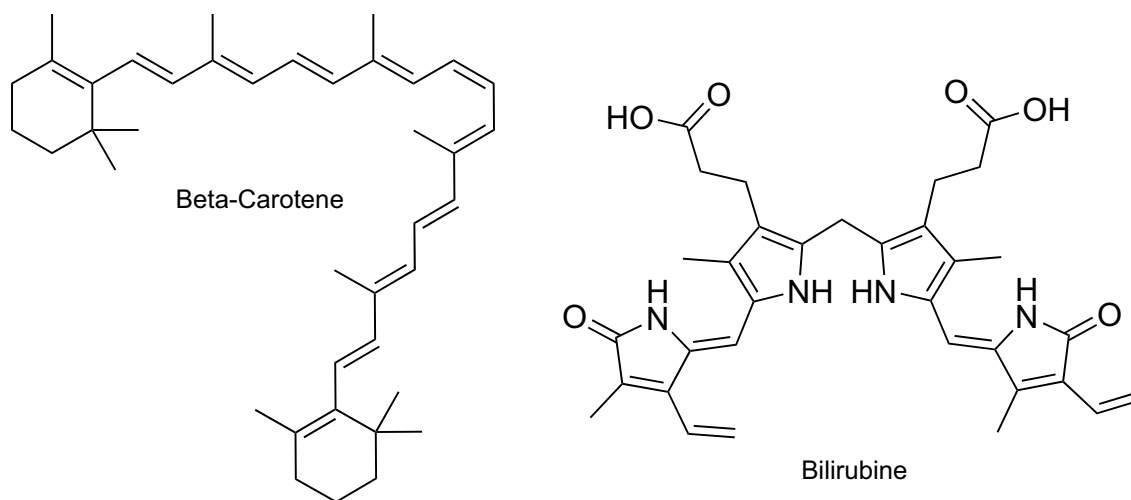

Figure 8.2: Two naturally occurring singlet oxygen quenchers: β-carotene (left) and bilirubine (right).
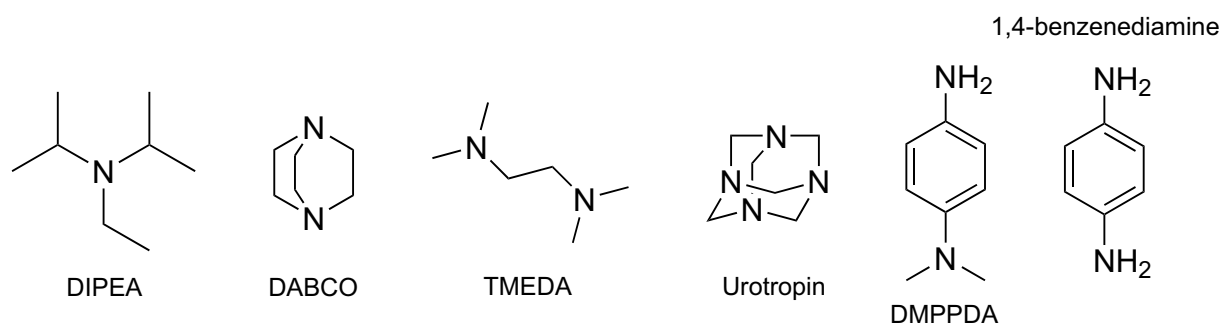

Figure 8.3: Widely known in literature and commercially available selected amino-based singlet oxygen quenchers. Chemical structures of singlet oxygen quenchers, from left to right: DIPEA, DABCO, TMEDA, urotropin, DMPPDA, 1,4-benzenediamine.

β-Carotene and bilirubine, DMPPDA, 1,4-benzenediamineare, DIPEA, TMEDA, urotropin, BuDiBiDi, HexDiBiDi, and DABCO-MeI show either poorer or equal electrochemical stability compared to DABCO, which is electrochemically inert between 2.3 to 3.6 V *vs.* Li/Li$^+$ (compare Table 8.1). BuDiBiDi and HexDiBiDi show similar electrochemical behaviour as DABCO, as can be expected from their structural similarity as aliphatic amines. The ILs differ in their counter ion and in the length of their alkyl chain. It was, however, reported that the efficiency of quenching increases when the ionization potential of the amine decreases.[92] These characteristics are observed in the cyclic voltammograms of the ILs: With increasing number of C-atoms at the *N*-alkylated chain of DABCO respectively the oxidation onset shifts to higher potentials. All determined oxidation onsets

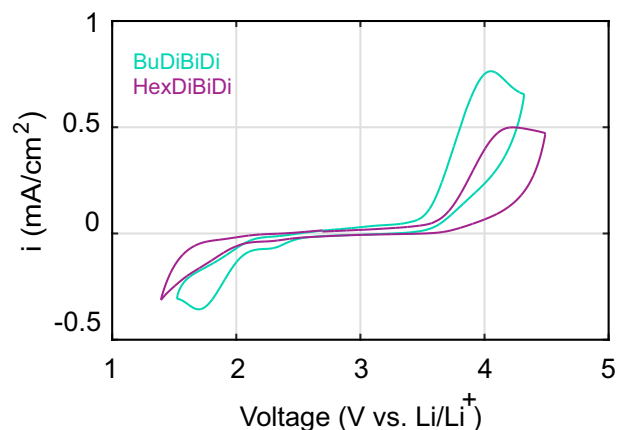and addition information regarding their physical state is summarised in Table 8.1.

Figure 8.4: Electrochemical stability of the novel triamines BuDiBiDi and HexDiBuDi. Cyclic voltammetry of 5 mM analyte and 0.1 M LiClO$_4$ in TEGDME was performed in Ar-atmosphere at a 3 mm Au pseudo disc electrode at a sweep rate of 100 mV·s^{-1}.
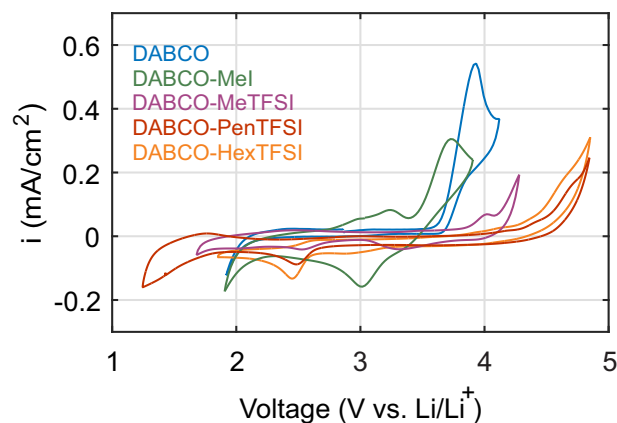

Figure 8.5: Electrochemical stability of a set of DABCO and novel IL DABCO-MeI, DABCO-MeTFSI, DABCO-PenTFSI and DABCO-HexTFSI. Cyclic voltammetry of 5 mM analyte and 0.1 M LiClO$_4$ in TEGDME was performed in Ar-atmosphere at a 3 mm Au pseudo disc electrode at a sweep rate of 100 mV·s^{-1}.

The screening leads to the conclusion that, in regard of the electrochemical stability of a set of quenchers, the novel triamines show similar redox behaviour like DABCO, but are more stable upon reduction. The novel IL with TFSI$^-$ as counter ion are significantly more stable than DABCO. Our aims and objectives to synthesise an additive with improved properties compared to DABCO including a broader electrochemical stability window, higher boiling point and higher solubility were successfully realised. Both classes of novel amines will be further analyzed in terms of their ability to quench singlet oxygen.

8.1.3   Determination of k_Q of singlet oxygen quenchers *via* monitoring trap degradation by photosensitized singlet oxygen

To determine the quenching efficiency the rate constant k_Q for physical quenching of ^{1}O$_2$ by the quencher has to be measured. This can be done by sensitized photooxygenation of a reactive substrate A (*e.g.*, DMA) in the presence of the quencher Q. The decay of the amount of substrate A with

Table 8.1: Oxidation onset and physical state of various amine-based ^{1}O$_2$ quenchers.

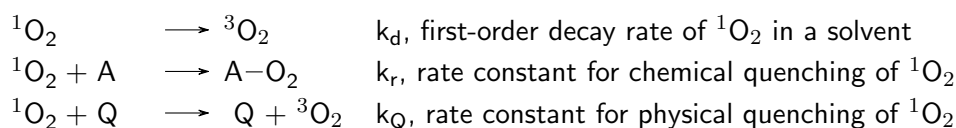| Class of Amine	Physical State	Amine / Quencher	Onset of Oxidation / V $vs.$ Li/Li$^+$
Natural	s	β-carotene	3.6
	s	bilirubine	3.4
Aromatic	s	DMPPDA	3.1
	s	1,4-benzenediamine	3.1
Aliphatic	l	DIPEA	3.6
	s	DABCO	3.6
	l	TMEDA	3.2
	s	urotropin	3.7
Novel branched	l(IL)	BuDiBiDi	3.5
	l(IL)	HexDiBuDi	3.6
Novel IL	l(IL)	DABCO-MeI	3.1
	l(IL)	DABCO-MeTFSI	3.9
	l(IL)	DABCO-PenTFSI	4.5
	l(IL)	DABCO-HexTFSI	4.4

quencher is compared to the decay without it,[98] as described below. At the stationary state continuous irradiation of a photo-sensitizer produces ^{1}O$_2$ at a production rate $I_A \cdot \phi_\Delta$ equals the rate of decay $k_d \cdot [^1$O$_2]_{ss}$ and thus the steady-state singlet oxygen concentration is

$$[^1\text{O}_2]_{ss} = \phi_\Delta \cdot \frac{I_A}{k_d} \tag{8.1}$$

I_a describes the absorbed photon flux (mol·L^{-1}·s^{-1}) in the sample. It is given by

$$I_A = f_{\text{abs}} \cdot F_{hv} \cdot \frac{\text{area}_{\text{beam}}}{\text{volume}_{\text{sample}}} \tag{8.2}$$

where f_{abs} is the fraction of the absorbed light ($f_{\text{abs, 634\,nm}} = 1 - 10^{-Abs\,634\,\text{nm}}$) and F_{hv} the incident photon flux[1]. The photonflux F$_{hv}$ illuminating the sample had a value of 2500 µmol·s^{-1}·m^{-2} when operated with the power of 1 W. The photo-sensitizer's quantum yield ϕ_Δ of singlet oxygen production is $\sim$1. There are three different rate constants for ^{1}O$_2$ according to the following deactivation processes:

$$
\begin{array}{lll}
^1\text{O}_2 & \longrightarrow\; ^3\text{O}_2 & k_{\text{d}}, \text{ first-order decay rate of } ^1\text{O}_2 \text{ in a solvent} \\
^1\text{O}_2 + \text{A} & \longrightarrow\; \text{A}-\text{O}_2 & k_{\text{r}}, \text{ rate constant for chemical quenching of } ^1\text{O}_2 \\
^1\text{O}_2 + \text{Q} & \longrightarrow\; \text{Q} + ^3\text{O}_2 & k_{\text{Q}}, \text{ rate constant for physical quenching of } ^1\text{O}_2
\end{array}
$$

---

[1]The photonflux of the red-LED ($\lambda_{\max}$ at 634 nm, OSLON SLL 80, OSRAM), used for excitation of the photo-sensitizer, was quantified via a light meter (Li-250A, LI-COR$^\circledR$, LI-COR inc., USA), whos light sensor (quantum type) was calibrated previously according to the supplied manual.

The first-order decay rate k_d of $^1O_2$ in a glyme solvent was estimated with $3\times10^4\,\mathrm{s}^{-1}$ on the basis of various k_d values of several solvents (acetonitrile $1.6\times10^4\,\mathrm{s}^{-1}$, diethylether $3.0\times10^4\,\mathrm{s}^{-1}$ and DMSO $5.2\times10^4\,\mathrm{s}^{-1}$)[98] and therefore not experimentally determined. First, the decay of the substrate A without a quencher is measured to determine the rate constant k_r. It will in the following be named k_A. The decay of the substrate concentration [A] is given by

$$-\frac{d[A]}{dt} = k_A \cdot [^1O_2]_{ss} \cdot [A] = r_{ox} \tag{8.3}$$

with r_{ox} being the rate of photooxygenation. This is a first order, homogeneous differential equation, which has the specific solution

$$[A] = [A]_0 \cdot e^{-t \cdot k_A \cdot [^1O_2]_{ss}} \tag{8.4}$$

when the starting condition is $[A]|_{t=0} = [A]_0$. k_A is then determined by fitting the experimental decay equation to 8.4. The solid line represents the fit of k_A, whereas the dotted line depicts the decay k_A of the substrate, illustrated in Figure 8.6. The calculations revealed a rate constant k_A of $9.91\times10^7\,\mathrm{L\cdot mol^{-1}\cdot s^{-1}}$ for the substrate A, here DMA.
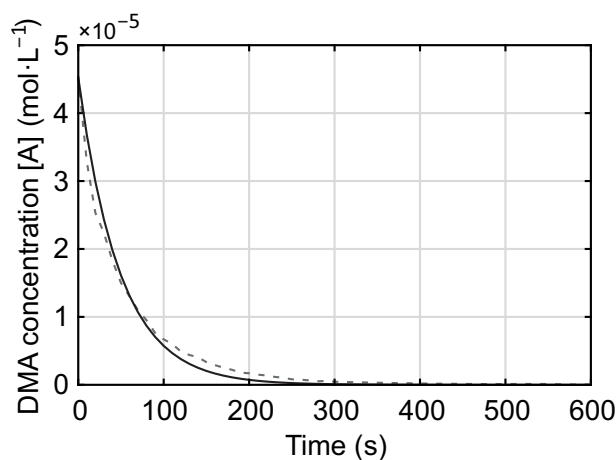

Figure 8.6: Exponential decay of DMA concentration [A] over the course of photooxygenation in absence of a quencher. The solid line represents the fit with Eq. 8.4 to obtain k_A. The dotted line shows the measured values of the DMA-concentration [A].

If additionally to the reactive substrate A a quencher Q is present in the system, the rate of photooxygenation r_{ox} is given by

$$\frac{1}{r_{ox}} = \frac{1}{I_A \cdot \phi_\Delta \cdot f_r^A} \cdot \left[1 + \frac{1}{[A]}\left(\beta_A + \frac{k_Q \cdot [Q]}{k_A}\right)\right] \tag{8.5}$$

β_A represents the concentration at which the decay of singlet oxygen in the solvent alone equals the decay due to quenching by A ($\beta_A = \frac{k_d}{k_A}$). k_Q is then expressed as

$$k_Q = \frac{k_A}{[Q]} \cdot \left(\frac{I_A \cdot \phi_\Delta \cdot [A]}{r_{ox}} - [A] - \beta_A \right) \tag{8.6}$$

herein r_{ox} is given by

$$r_{\text{ox}} = -\frac{d[A]}{dt} = k_Q \cdot [A] \tag{8.7}$$

where k is obtained by fitting $[A]$ with the solution of Eq. 8.7

$$[A] = [A]_0 \cdot e^{-t \cdot k} \tag{8.8}$$

Figure 8.7 illustrates the determinantion of k (including both k_Q and k_Q) and k_A for the photooxygenation reactions of a substrate in absence and presence of a quencher. The k_Q values, obtained in TEGDME from this screening are summarised in the Table 8.2. BuDiBiDi and HexDiBiDi possess a higher k_Q, DABCO-MeTFSI and DABCO-PenTFSI a lower k_Q than DABCO. Due to its low electrochemical stability BuDiBiDi and HexDiBiDi cannot be used as a quencher in Li-O_2 batteries, but could be applicable in other systems. DABCO-MeTFSI and DABCO-PenTFSI show lower k_Q rates than DABCO, but exhibit a broad electrochemical stability window and excellent solubility in glyme-based electrolytes. Therefore further tests regarding their chemical stability towards ROS ($^1O_2$, O_2^- and O_2^{2-}) have to be performed in order to incorporate permanently into a Li-O_2 battery. The ability of quenching singlet oxygen by various quenchers including the novel IL was tried to be determined *via* the use of an optical oxygen meter in oxygen-sensing planar foils containing photo-sensitizer and quencher embedded in a polymer matrix. The experiments had major drawbacks and did not reveal useful results. Further information about the sample preparation and drawbacks can be found in *Appendix A.2* on Page 121.
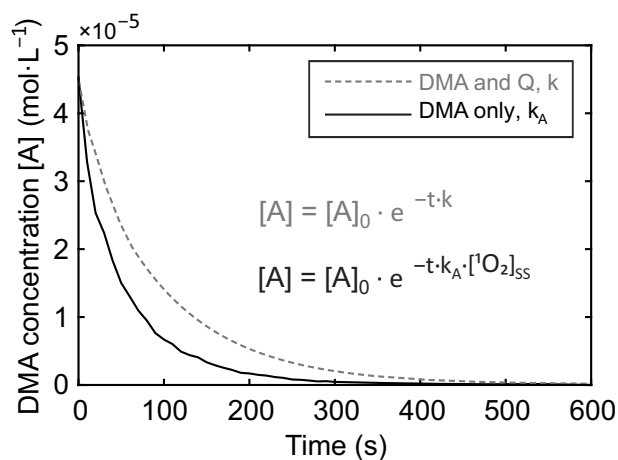
Figure 8.7: Exponential decay of the concentration of DMA [A] over the course of photooxygenation in absence of a quencher, and determinantion of k (including both k_Q and k_A) and k_A for the photooxygenation reactions of a substrate in absence (——) and presence of a quencher (- - -).

Following the experimental procedure of k_Q determination is elaborated. A UV-Vis spectrometer was equipped with a red-LED and fixed at a right angle to the spectrometer's beam to ensure reproducible conditions during the measurements and thus throughout the quencher screening.

Table 8.2: Determined k_Q of various quenchers.

Amine	k_Q / L·mol^{-1} s^{-1}
DABCO-PenTFSI	4.69×10^7
DABCO-MeTFSI	1.06×10^8
DIPEA	2.53×10^8
TMEDA	4.84×10^8
DABCO	5.49×10^8
BuDiBiDi	6.22×10^8
HexDiBiDi	6.48×10^8
DMPPDA	1.53×10^9

A hermetically sealed quartz cuvette with ~1 mL head space (QS, 10 mm, Hellma Analytics), was equipped with a solution of photo-sensitizer Pd$_4$F (1.2 μmol) and the trap DMA (45 μmol) in TEGDME, equipped with a stirring bar and assembled in an Ar filled glovebox. TEGDME was used as a solvent as it exhibits a lower volatility compared to DME. The solution was perfused with high purity oxygen with a constant flow rate of 1 mL·min^{-1} for 20 min. As the solvent was saturated with oxygen and the headspace acts as oxygen reservoir, we assume that the concentration of O$_2$ is constant over the course of the photooxygenation experiments. The cuvette was then placed in a sample holder kept at constant temperature (22 °C), comprising a magnetic stirrer to ensure continous mixing of the sample. Prior to photooxygenation reactions, a spectrum of the sample was recorded in the range between 200 nm - 800 nm, in order to calculate the initial concentration of the substrate [A]$_0$ (DMA, λ_{max} at 382 nm) in solution according to Beer-Lambert law[104]

$$A = \epsilon \cdot c \cdot d \tag{8.9}$$

Each photooxygenation reaction was performed first, for 10 s (0 - 300 min), and second, for 60 s (300 - 600 min), followed by 60 s period without illumination and accompanying stirring to ensure a continuous and homogeneous distribution of the components in solution. After each photooxidation step an absorbance spectrum was recorded (see Figure 8.8, left). Photooxydation of DMA was performed until all DMA was consumed *via* its specific reaction with $^1O_2$, visible due to the decrease in absorbance at 382 nm. In consideration of the photo-sensitizer self-absorbance, all recorded spectra were subject to solvent background correction and baseline correction, illustrated in Figure 8.8 (right). Photo-bleaching and reactions with singlet oxygen of the photo-sensitizer were not observed, as the absorbance values of the Q- and *Soret*-band of the photo-

sensitizer Pd_4F stayed constant over the whole time frame of the experiment (see Figure 8.9 - 8.16). The maximum of DMA absorbance over the course of the photo-oxygenation reactions was determined in the wavelength range between 375 nm and 385 nm and converted to its concentration [A].
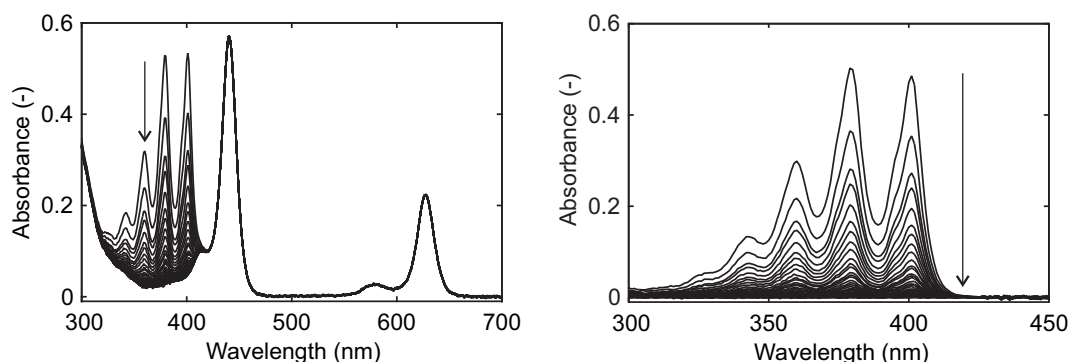

Figure 8.8: Absorption spectra of the photooxygenation reaction of DMA with $^1O_2$ using the photo-sensitizer Pd_4F in the wavelength range of 200 nm - 700 nm before (left) and after background correction and substraction of the dye absorbance (right).

Figure 8.9: Absorption spectra of the photooxygenation reaction of DMA with singlet oxygen in presence of DABCO (DMA:Q, n:n, 1:1) using the photo-sensitizer Pd_4F in the wavelength range of 200 nm - 800 nm (left) and the exponential decay of the traps concentration [A] over time (right).

Figure 8.10: Absorption spectra of the photooxygenation reaction of DMA with singlet oxygen in presence of DABCO-MeTFSI (DMA:Q, n:n, 1:1) using the photo-sensitizer Pd_4F in the wavelength range of 200 nm - 800 nm (left) and the exponential decay of the traps concentration [A] over time (right).
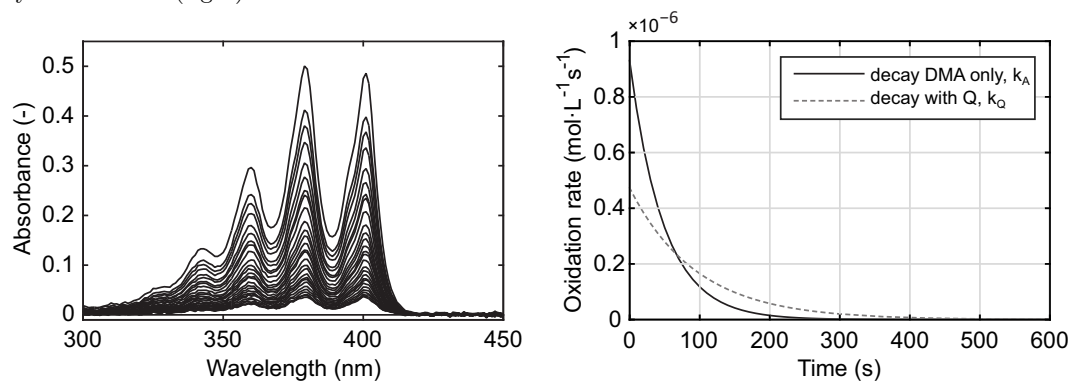
Figure 8.11: Absorption spectra of the photooxygenation reaction of DMA with singlet oxygen in presence of DABCO-PenTFSI (DMA:Q, n:n, 1:1) using the photo-sensitizer Pd_4F in the wavelength range of 200 nm - 800 nm (left) and the exponential decay of the traps concentration [A] over time (right).

Figure 8.12: Absorption spectra of the photooxygenation reaction of DMA with singlet oxygen in presence of BuDiBiDi (DMA:Q, n:n, 1:1) using the photo-sensitizer Pd_4F in the wavelength range of 200 nm - 800 nm (left) and the oxidation rate $[r_{ox}]$ over time (right).

Figure 8.13: Absorption spectra of the photooxygenation reaction of DMA with singlet oxygen in presence of HexDiBiDi (DMA:Q, n:n, 1:1) using the photo-sensitizer Pd_4F in the wavelength range of 200 nm - 800 nm (left) and the exponential decay of the traps concentration [A] over time (right).
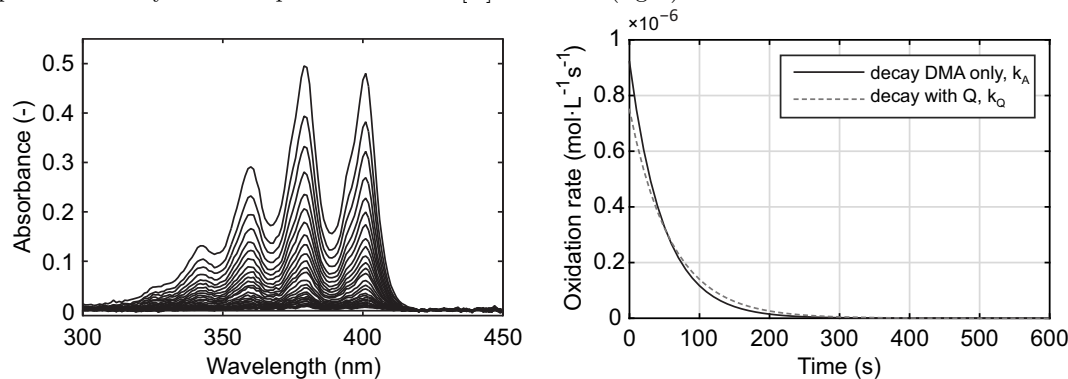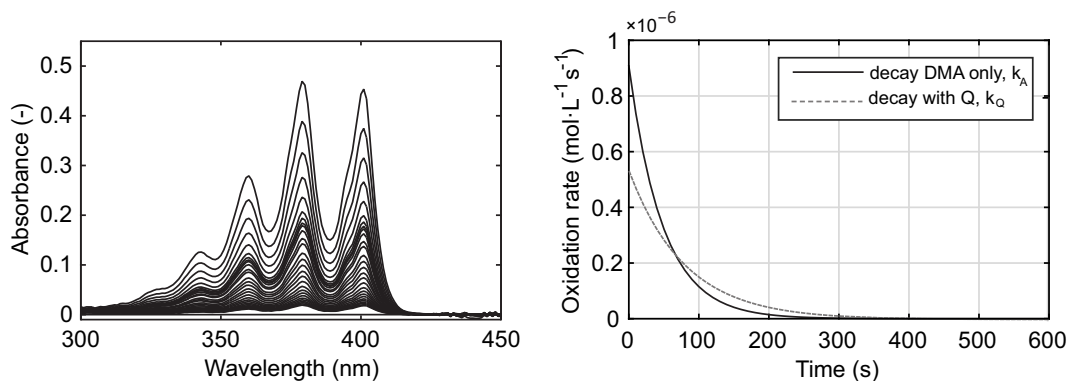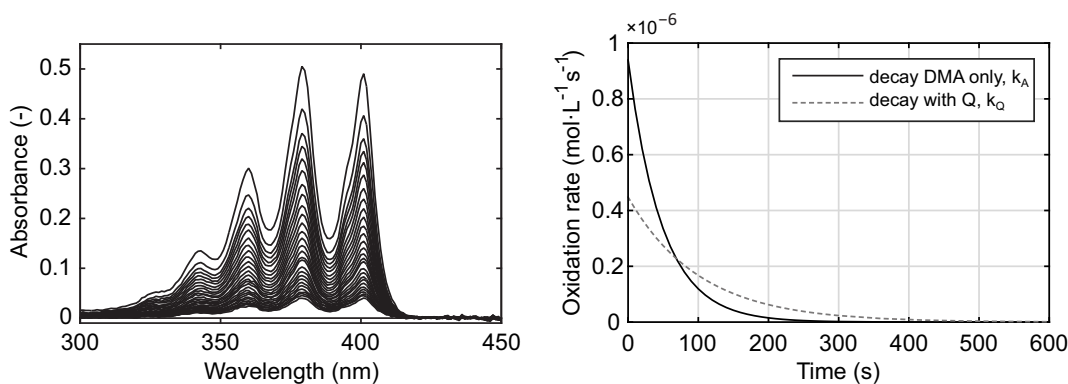
Figure 8.14: Absorption spectra of the photooxygenation reaction of DMA with singlet oxygen in presence of DIPEA (DMA:Q, n:n, 1:1) using the photo-sensitizer Pd_4F in the wavelength range of $200\,\text{nm} - 800\,\text{nm}$ (left) and the exponential decay of the traps concentration [A] over time (right).

Figure 8.15: Absorption spectra of the photooxygenation reaction of DMA with singlet oxygen in presence of DMPPDA (DMA:Q, n:n, 1:1) using the photo-sensitizer Pd_4F in the wavelength range of $200\,\text{nm} - 800\,\text{nm}$ (left) and the exponential decay of the traps concentration [A] over time (right).
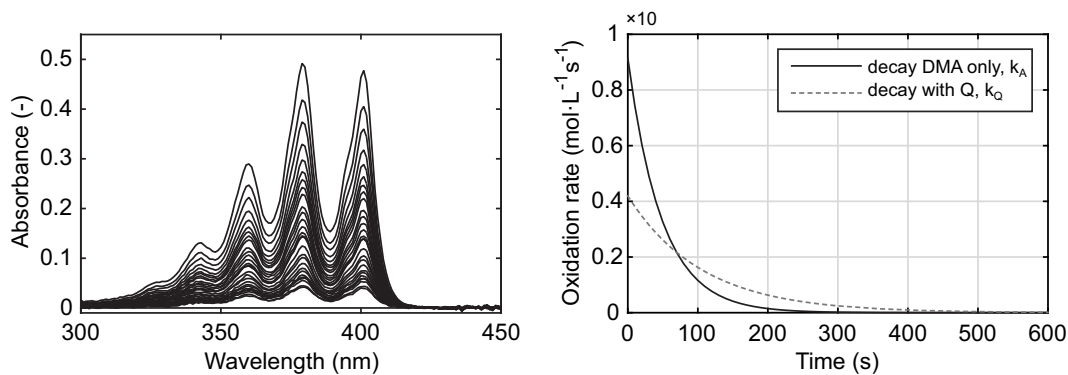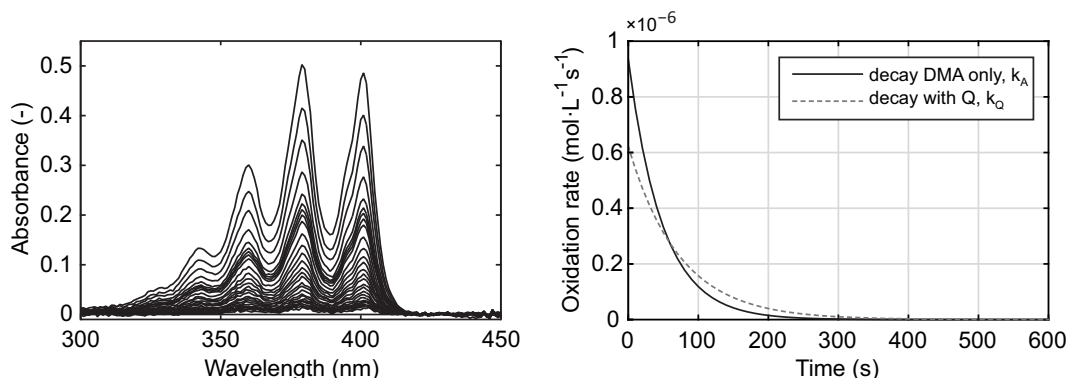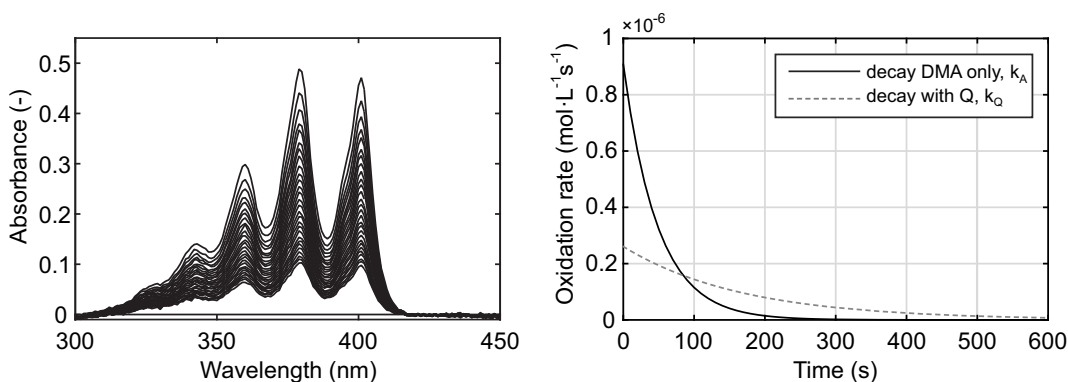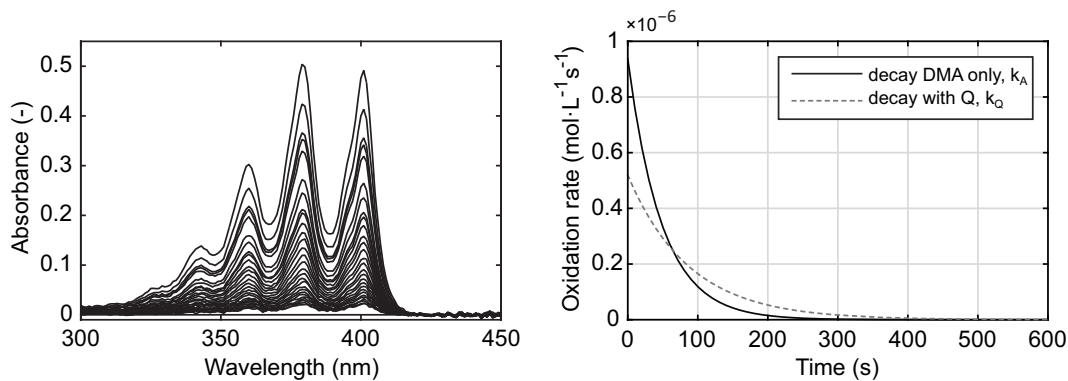

Figure 8.16: Absorption spectra of the photooxygenation reaction of DMA with singlet oxygen in presence of TMEDA (DMA:Q, n:n, 1:1) using the photo-sensitizer Pd_4F in the wavelength range of $200\,\text{nm} - 800\,\text{nm}$ (left) and the exponential decay of the traps concentration [A] over time (right).

8.1.4 Chemical stability of novel singlet oxygen quenchers towards ROS and RROS

DABCO, DABCO-MeTFSI, DABCO-PenTFSI and DABCO-HexTFSI were dissolved in 0.1 M LiClO$_4$ in d-DMSO, and exposed to *in-situ* generated $^1O_2$ for 10 min. Chemical stability towards singlet oxygen was confirmed by ^{1}H NMR spectroscopy (see *Appendix* Page 126), therefore cross-reactivity of the quencher with the IL's can be excluded therefore. The quenchers stability towards the RROS O$_2^{\bullet-}$ and O$_2^{2-}$ was examined by exposing an electrolyte containing 0.1 M LiClO$_4$ in TEGDME and quencher to Li$_2$O$_2$, and KO$_2$ with 18-crown-6 ether for a certain time, while stirring the solution mixture. After filtration, the electrolytes were subject to further characterisation *via* ^{1}H NMR spectroscopy in d-DMSO. Unfortunately DABCO-MeTFSI, DABCO-PenTFSI and DABCO-HexTFSI are not stable towards O$_2^{\bullet-}$ and O$_2^{2-}$ in this very time frame as confirmed by ^{1}H NMR spectroscopy.

8.1.5 Determination of Li$_2$O$_2$ yield of Li-O$_2$ batteries operated with novel quenchers as electrolyte

Electrolyte mixtures of DABCO-RTFSI (R = Pen, Hex) in LiTFSI (n:n, 1:1) were prepared according to the following procedure. DABCO-RTFSI was dissolved in 10 mL DCM and stored over molecular sieves for 24 h. The liquid mixture was transfered into a Schlenk flask and dried under reduced pressure at room temperature. LiTFSI was added to the viscous liquid in the ratio (n:n, 1:1) and stirred until a highly viscous liquid ionic liquid was obtained. Li-O$_2$ batteries in Swagelok$^®$ design were assembled with 70 μL DABCO-PenTFSI or DABCO-HexTFSI in LiTFSI electrolyte in order to galvanostatically discharge the cells and to quantify Li$_2$O$_2$ and generated side products at the cathode. The cells failed due to poor ionic conductivity in consequence of the high viscosity of the IL electrolyte. To decrease the viscosity of the electrolyte, cells could be operated in an incubator at elevated temperature, *e.g.*, 50 °C. The discharge product Li$_2$O$_2$ and carbonaceous side products can be further quantified according to Schafzahl *et al.*:[63] the Li$_2$O$_2$ yield of each discharged cell operated with a physical $^1O_2$ quencher is expected to be higher than in a cell without a quencher *e.g.*, 1 M LiTFSI in TEGDME. In addition the amount of generated side products should be decreased due to suppressed parasitic reactions. The obtained values for Li$_2$O$_2$ and side products such as Li$_2$CO$_3$ can further give indirect proof of their singlet oxygen quenching ability during discharge and charge. Experiments concerning this work are beyond the scope of this thesis, and is currently an ongoing topic in my working group.

Ongoing Topics

Within the course of this thesis we only could open the topic of singlet oxygen in non-aqueous battery chemistries. It turns out that singlet oxygen is of relevance to any battery chemistry where oxygen redox is involved. This includes further reaching topics within the realm of metal-O_2 batteries, such as the exact mechanism of singlet oxygen formation, reaction mechanism of singlet oxygen with organic substrates or the carbon electrode, the effect of surfaces and solid catalysts, the effect of oxidation and reduction mediators, and better quenchers (see *Chapter 8*). With singlet oxygen from lithium carbonate we have already shown that it is also of relevance beyond metal-O_2 batteries and other logical candidates are the highly topical intercalation materials with oxygen redox. All these topics are currently under investigation in our group. The question of reactivity of singlet oxygen with organic electrolytes arised already during the work on our first paper[51] and is further investigated in collaboration with Sergio Brutti from University of Basilicata. The current state is briefly summarized in the following.

Reaction Mechanism of Singlet Oxygen with Electrolyte

We have shown that exposure of glyme based electrolyte containing a Li^+ salt to $^1O_2$ yields the typically found parasitic products of the Li-O_2 cathode, respectively Li_2CO_3, Li acetate and Li formate.[51] Following mechanism was proposed by C. Leypold from the Institute for Chemistry and Technology of Materials and the corresponding calculations were performed by M. Leypold from the Institute of Organic Chemistry at Graz University of Technology. A possible reaction mechanism for the attack of $^1O_2$ on glyme is shown in Figure 8.17.a. A group transfer reaction with a pericyclic transition state for the direct access of H_2O_2 and the unsaturated ROCH=CHOR species 1 is proposed. Mechanistic calculations at the MP2/6-311++G** level of theory provided activation energies within the range of 84 - 98 kJ·mol^{-1}, depending on the conformation of the glyme during this rearrangement (Figure 8.17.b). Herein, the energetically preferred staggered-conformation of glyme leads to stereoisomer (E)-**1**, whereas gauche-glyme results in the formation of (Z)-**1**, respectively. This ongoing reaction

would be additionally favoured by a strong driving force towards the products. Notably, these calculated activation energies are much lower than the values of $\sim$132 to 180 kJ·mol^{-1} and $\sim$162 kJ·mol^{-1} for the attack of superoxide or for the autooxidation reaction that were calculated by Bryantsev *et al.*[70,73] or Brutti *et al.*[135] Intermediate 1 may undergo a variety of further reactions including a radical propagation step with $^3O_2$ to form the peroxoradical and C-centred radical species 2 (reaction I). Or it may undergo [2+2] and [2+1] cycloadditions with $^1O_2$ (Reactions II and III in Figure 8.17.a). All resulting species are instable and will decompose further. For example, intermediates such as 2 are known, in the presence of O_2, to easily undergo oxidative decomposition reactions.[136,137,138] There are many possible reaction pathways, which makes it virtually impossible to formulate a unique reaction path.[136] Incomplete decomposition leads to the formation of formic and acetic acids.
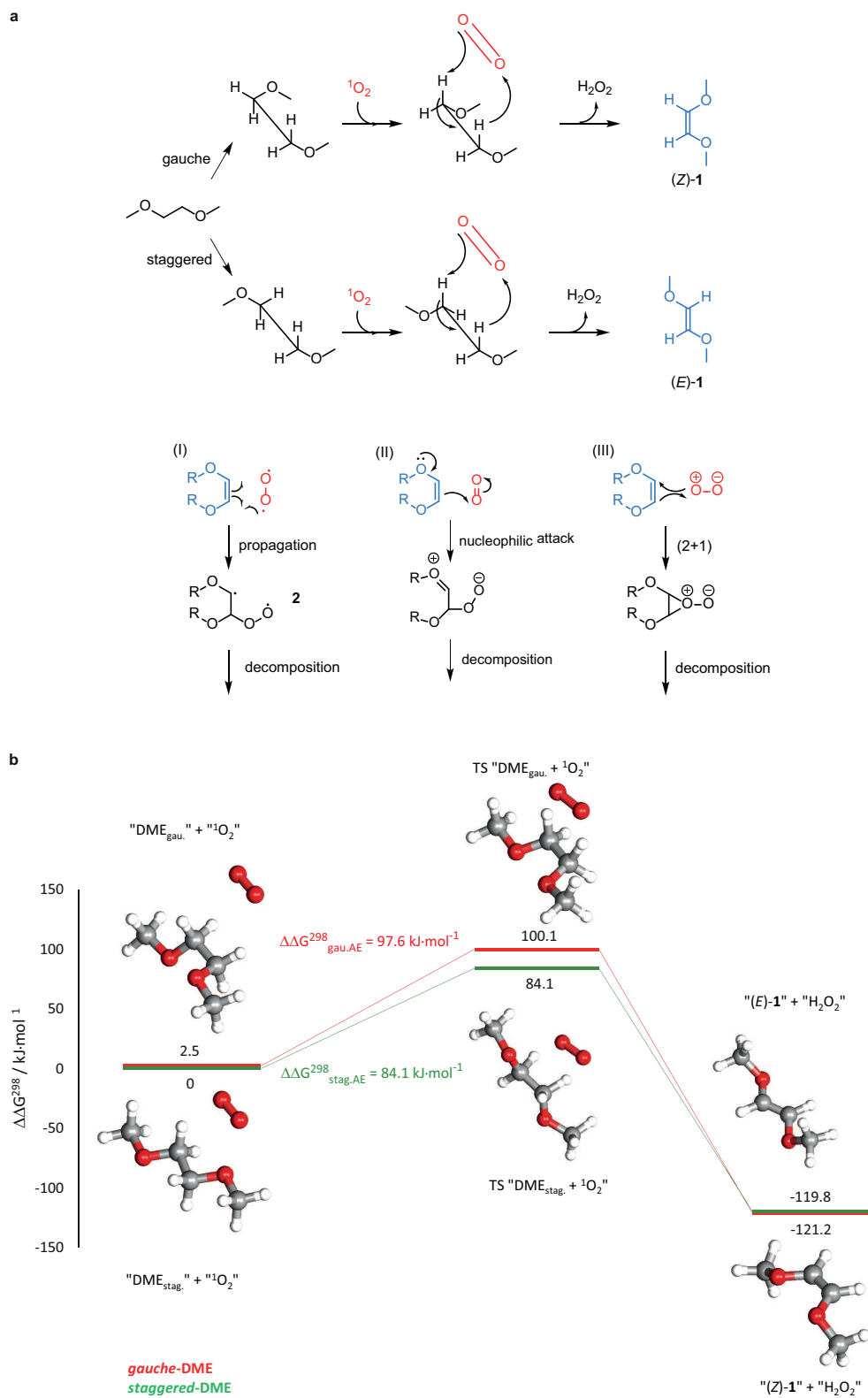
Figure 8.17: Possible first steps of the reaction mechanism of $^1O_2$ with DME (a) and reaction free energy profiles of the initial group transfer reaction and optimized geometries (b).

In the environment of the Li^+ containing electrolyte the equivalents are Li formate and Li acetate, which were observed as decomposition products.[51] These decomposition reactions release further CO_2 and H_2O. Finally, formation of Li_2CO_3 can occur by reaction between O_2 and CO_2 *via* Reactions 1 and 2.[139, 140]

$$2\,O_2^- + 2\,CO_2^- \longrightarrow O_2 + C_2O_2^{2-} \quad (1)$$
$$C_2O_2^{2-} + O_2^- + 4\,Li^+ \longrightarrow 2\,Li_2CO_3 + 2\,O_2 \quad (2)$$
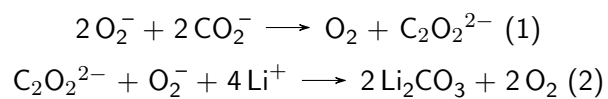
Overall Conclusions and Outlook

Through intense efforts and experimental studies, we have accomplished to developed a new set of *in-situ* and *ex-situ* methods based on NIR, Fluorescence, UV-Vis and ^{1}H NMR spectroscopy, HPLC-MS, and online electrochemical mass spectrometry to identify a mostly overlooked reactive oxygen species in non-aqueous battery chemistries. Parasitic chemistry in non-aqueous Li-O$_2$ and Na-O$_2$ batteries was identified to be triggered, not only by reduced reactive oxygen species superoxide and peroxide which has been presumed for years, but predominantly by singlet oxygen, an excited reactive oxygen species. We have shown that singlet oxygens forms from alkaline (M $=$ Li, Na) superoxides and peroxides, and upon electrochemical oxidation of lithium carbonate in non-aqueous ether-based electrolytes. Thus, so far unidentifiable parasitic reactions and concomitant side product formation on discharge and charge could be ascribed to singlet oxygen's nature, as hypothesized previously for high charging voltages only. Parasitic side products can be diminished by the use of singlet oxygen traps or quenchers. Effective physical quenchers, exhibiting attributes like chemical and electrochemical stability in the cell environment, and selective and fast reaction with singlet oxygen, could be additives as part of electrolytes, or part of ionic liquids in solvent free electrolytes, as we proposed in *Chapter 8*. By all means, singlet oxygen formation has to be circumvented due to its exceptional reactivity, in particular towards organic matter.

Singlet oxygen from electrochemical oxidation of lithium carbonate has far reaching implications for all cathode chemistry which operate beyond 3.8 V vs. Li/Li$^+$ will inevitable affect the stability of all lithium batteries, which includes most currently studied cathode chemistries. Awareness of the highly reactive singlet oxygen in non-aqueous metal-oxygen batteries gives a rationale for future research to mitigate its formation and paves the way towards achieving highly reversible batteries.

Appendix A

Experiments with Unexpected Outcomes

A.1 Singlet Oxygen Quenching in Oxygen-sensing Planar Foils in Presence of Singlet Oxygen Quenchers

Novel optical singlet oxygen quenchers have been synthesized and characterized as described in *Chapter 8*. Oxygen-sensing planar foils containing quenchers were prepared in order to investigate polymer consumption through $^1O_2$ in polymer-films. Modified oxygen-sensing planar foils were prepared according to Borisov *et al.*: PET-foils were washed with acetone, coated with a solution of photo-sensitizer, quencher and polymer in chloroform in a polymer matrix (10wt% polystyrene/PS or poly(methyl methacrylate)/PMMA in chloroform; 1.5mol% photo-sensitizer, 3.0mol% quencher, referred to the polymer), dried and sealed with a layer of PVOH (10wt% PVOH in H_2O) to obtain oxygen impermeable foils (see Figure A.1).[141] Each layer was knife-coated with a wet film thickness of 3MIL (BYK gardner). Reference foils contained either no photo-sensitizer and/or no quencher. Fol-

Figure A.1: Cross section of an oxygen-sensing foil consisting of a PET substrate, a layer of photo-sensitizer (Sens), quencher (Q) and chemical trap (T) in a polymer matrix, covered with an oxygen impermeable PVOH layer.
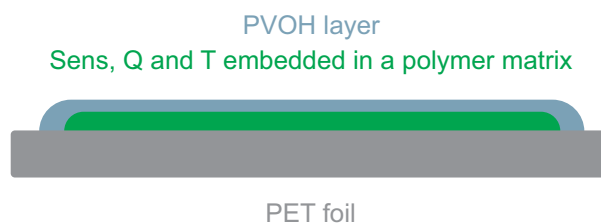
lowing commercially available and novel synthesised amines were tested towards their singlet oxygen quenching ability: DABCO, TMEDA, DIPEA, urotropine, DMPPDA, DABCO-MeTFSI, BuDiBiDi and HexDiBiDi (see Page 103 Figure 8.1 and 8.3). A high precision optical oxygen meter (OOM,

FireStingO$_2$-Mini, PyroScience GmbH, Germany) was operated at room temperature (20 °C) in order to monitor the response. The OOM was operated using PyroScience Oxygen logger software. The optical fiber was attached to a custom made vial-holder which was placed directly in front of the oxygen-sensing foils. The change in the $\Delta\phi(O_2)$ signal was recorded in the course of the measurement. A decrease of O$_2$ in the sample was expected as singlet oxygen was formed *via* photosensitization reaction during the measurement, due to consumption of the polymer. No O$_2$ consumption was observed in the samples with a PS matrix. Therefore we prepared new oxygen sensing foils, consisting of a more likely to be fragile PMMA matrix. Again no consumption of O$_2$ was observed. Therefore another set of oxygen sensing foils was prepared in which we incorporated additional possible chemical traps (1.5mol% referred to the polymer) by adding oleic acid to the slurry as singlet oxygen is known to react with substrates containing double bonds. Unfortunately no decrease in O$_2$ was detected. If there would be a reaction with an impurity as for example oleic acid, which contains a single double-bond, this would be observed by an increase in O$_2$ consumption. Unfortunately this impurity is not suitable for all amines: the primary amin functionality of the aromatic amine is known to react with the carboxy group of the oleic acid, where the amine gets protonated by the acid through an acid-base-reaction. Due to this ethyl linoleate was added as impurity to the slurry. None of our prepared oxygen sensing foils exhibited the expected O$_2$ consumption. Foils with DABCO yielded in a bigger O$_2$ consumption as without DABCO. There are several possible reasons such as *e.g.*, the photo-sensitizer was not suitable for this specific set-up, maybe the fiber diameter is too small and oxygen diffuses from the sides so there is no deoxygenation. Potentially the PVOH layer was not entirely dry due to high humidity and is therefore not completely oxygen-impermeable. As the expected outcome was not fulfilled all further tests were stopped.
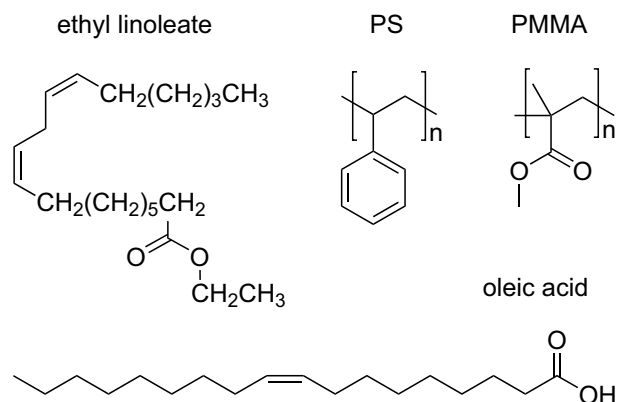

Figure A.2: Structures of possible chemical singlet oxygen sinks: polymers PS and PMMA, fatty acid oleic acid and fatty acid ester ethyl linoleate.

A.2 Quantification of $^3O_2$ during Electrochemical Oxidation of Li_2CO_3 using an Optical Trace Sensor

Given the strong indication for $^1O_2$ generation by DMA-O_2 formation identified through HPLC and ^1H NMR as described in *Chapter 7*, it could be expected that some of the $^1O_2$ decays to $^3O_2$ which would make it detectable in the gas phase. It may well be very little and may thus not have been detected in previous MS measurements.[142, 64] The strategy was to employ an exceptionally sensitive detection method for $^3O_2$ concentrations in the low ppb range. The experiment was performed without and in presence of an $^1O_2$ quencher. If the experiment with quencher gave significantly more $^3O_2$ gas than the experiment without quencher, it would very strongly corroborate the formation of $^1O_2$. The complication with this experiment is to find a quencher with oxidation stability beyond the onset of Li_2CO_3 oxidation at 3.8 V *vs.* Li/Li$^+$. DABCO works with a stability to 3.6 V. Alternatively NaN$_3$ and LiN$_3$ were used as potential singlet oxygen quenchers which exhibit a slightly higher oxidation onset at 3.7 V.[143, 144] Figure A.3 shows sketches of two different test cells which were used for the *in-situ* quantification of $^3O_2$ using an optical trace sensor. First our MS-test cell setup (see Figure C.2) as illustrated in Figure A.3 (left) was modified. It was equipped with an aluminum foil strip and a stainless steel mesh in contact with a stainless steel prestressed spring (WE), which functioned as current collectors. The test-cell was sealed with a solvent resistant lid (PEEK polymer) and clamped with a custom made clamping fixture. A high precision optical oxygen meter (OOM, FireStingO$_2$-Mini, PyroScience GmbH, Germany) was operated in an Ar (<0.1 ppm H$_2$O and <0.1 ppm O$_2$) filled glove box at constant temperature. The OOM contains an integrated humidity- and pressure-sensor for automatic temperature compensation of the oxygen measurements. It was operated using PyroScience Oxygen logger software. The optical fiber was attached to a custom made vial-holder, which was placed directly in front of an oxygen indicator. However, the measurement within the glass cell failed due to several reasons: It was not possible to record a stable $\Delta\phi(O_2)$ baseline as the used rubber seal was presumably still outgassing O_2, which caused a baseline drift. To avoid this, the rubber seal should be stored under vacuum for 24 h in order to eliminate oxygen contamination. Another experiment was performed in compliance of the just listed sources of possible errors. Unfortunately the improved set-up did not lead to the expected results. Therefore a new set-up in a modified Swagelok® cell design (Figure A.3, right) was designed. The indicator, a red light excitable oxygen sensing material (PtF3diperfluoroalkyl) and PTFE (AF 1600) was dissolved in chloroform and doctor-bladed onto a modified glass surface facing the electrode (see details in Figure A.3). The solvent was evaporated

in ambient air to result in a $3\,\mu$m-thick sensing film. The glass surface in the cell was modified *via* a silanization step in order to obtain sufficient bonding across the glass/indicator/PTFE matrix interface. Sensor calibration was performed outside the glove box, first in the gas phase using different gas mixtures (20 ppm O_2, 0.1% O_2 and 1.95% O_2 in N_2) and second in a 5wt% aqueous Na_2SO_3-solution to achieve anoxic conditions. The test cell in Swagelok$^{\circledR}$ design illustrated in Figure A.3 (right) was modified on the side of the working electrode: A steel tube was used as current collector, and was capped single sided with a glass window equipped with the O_2 sensing material. The test-cell was assembled in an Ar filled glovebox and was equiped with a partly delithiated LFP counter electrode, a separator soaked with $80\,\mu$L of $1\,$M LiTFSI in DME and a Li_2CO_3 packed C working electrode on a stainless steel mesh with a typical loading of $2\,$mg Li_2CO_3. The cell was rested at their OCV until a sufficient baseline was observed. In order to detect $^3O_2$ *in-situ via* an oxygen trace sensor during oxidation of Li_2CO_3, cyclic voltammetry was performed with a scan rate of $0.14\,$mV$\cdot$sec^{-1}, starting from OCV to a cut off potential of $4.5\,$V, which is within the stability of the electrolyte. Although a stable baseline was recorded, no change in $\Delta\phi(O_2)$ was detected upon chemical oxidation of Li_2CO_3. As the expected outcome was not fulfilled all further tests were stopped.
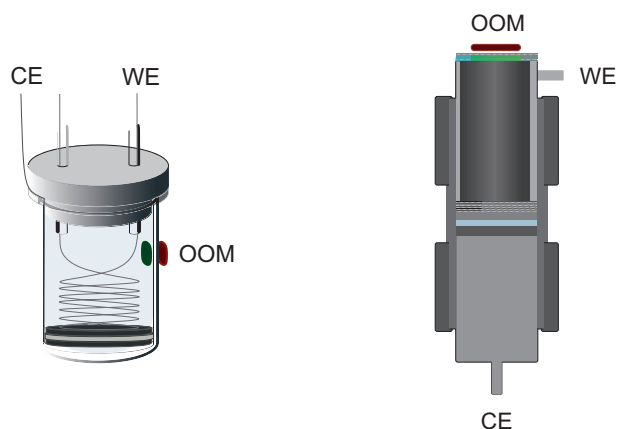
Figure A.3: Glas test cell (left) and Swagelok$^{\circledR}$ test-cell (right).

Appendix B

Quencher Stability

B.1 Electrochemical Stability of Singlet Oxygen Quenchers

The cyclic voltammogramms of 5 mM of analyte naturally occurring quenchers bilirubin and β-carotene (see Figure 8.2), aliphatic amines DIPEA, DABCO, TMEDA and Urotropin and aromatic amines DMPPDA and 1,4-Benzenediamine in 0.1 M LiClO$_4$ in TEGDME, are illustrated below.

Figure B.1: Electrochemical stability of two naturally occurring singlet oxygen quenchers β-carotene and bilirubine. Cyclic voltammetry of 5 mM analyte and 0.1 M LiClO$_4$ in TEGDME was performed in Ar-atmosphere at a 3 mm Au pseudo disc electrode at a sweep rate of 100 mV·s^{-1}.
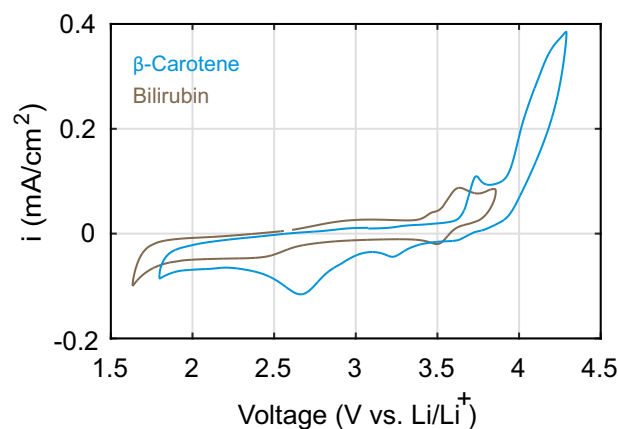
Figure B.2: Electrochemical stability of a set of alyphatic and aromatic quenchers DIPEA, DABCO, TMEDA, Urotropin, DMPPDA, 1,4-Benzenediamine. Cyclic voltammetry of 5 mM analyte and 0.1 M LiClO$_4$ in TEGDME was performed in Ar-atmosphere at a 3 mm Au pseudo disc electrode at a sweep rate of 100 mV·s^{-1}.
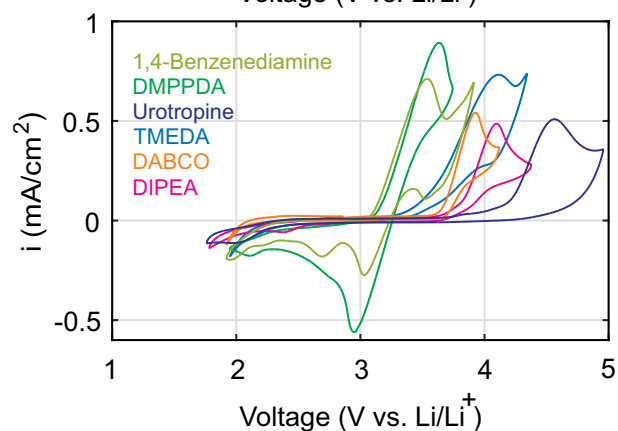
B.2   Stability of Quenchers towards ROS and RROS

^{1}H NMR spectra of DABCO and DABCO-RTFSI (R = Me, Pen, Hex) exposed to *in-situ* generated
[1]O_2 over the course of 10 min, to KO_2 (1 h exposure) and Li_2O_2 (24 h exposure) are illustrated in
Figure B.3 - B.6.
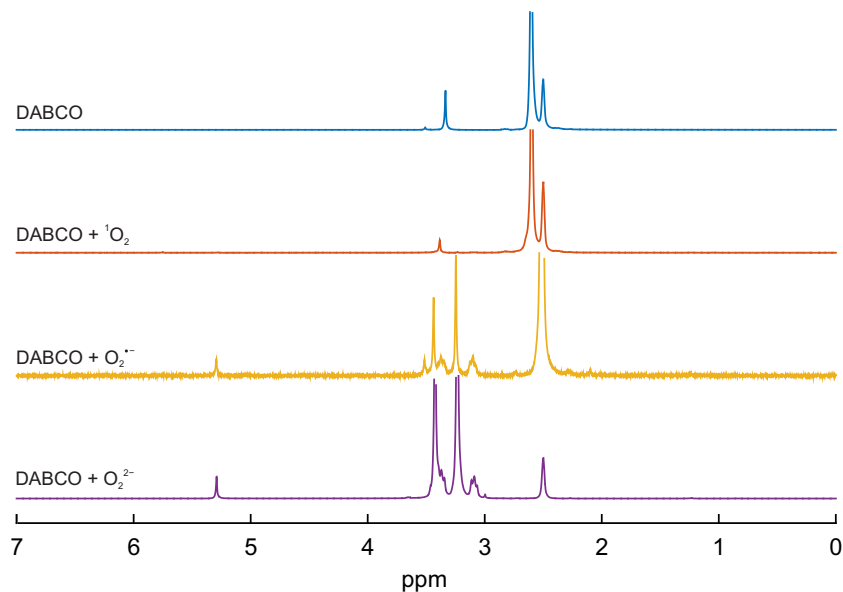
Figure B.3: ^{1}H NMR spectra of DABCO exposed to *in-situ* generated [1]O_2 over the course of 10 min and to RROS O_2^- and O_2^{2-}.
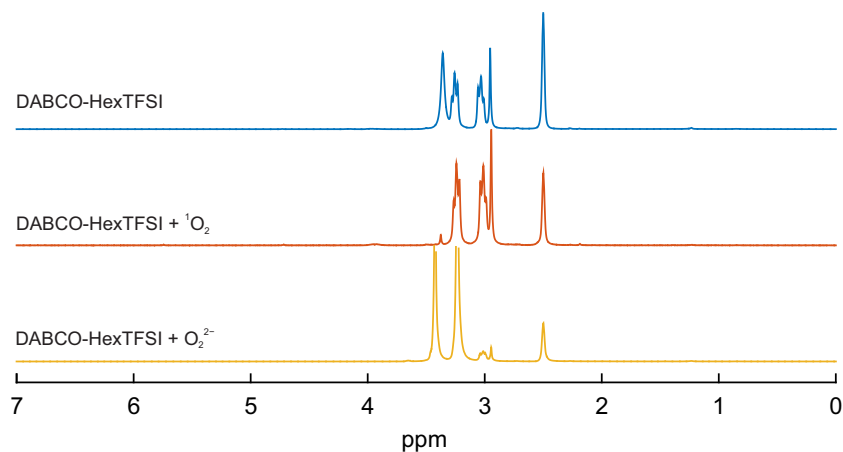
Figure B.4: ^{1}H NMR spectra of DABCO-MeTFSI exposed to *in-situ* generated [1]O_2 over the course of 10 min and to RROS O_2^- and O_2^{2-}.
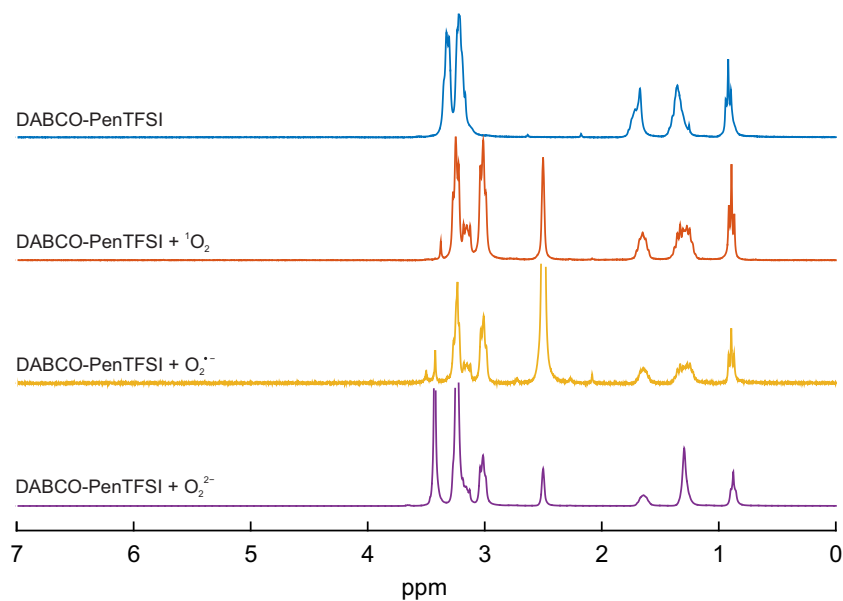
Figure B.5: ^{1}H NMR spectra of DABCO-PenTFSI exposed to *in-situ* generated $^1O_2$ over the course of 10 min and to RROS O_2^- and O_2^{2-}.
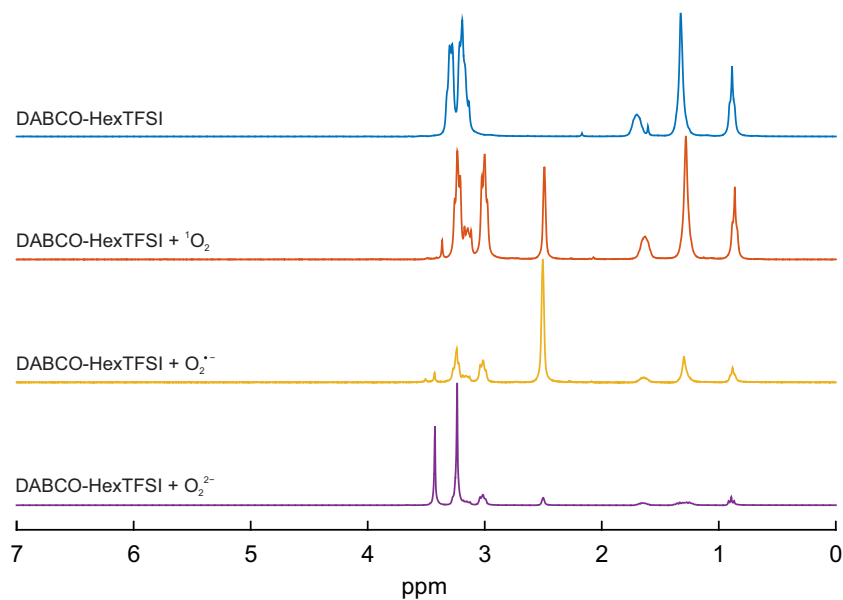
Figure B.6: ^{1}H NMR spectra of DABCO-HexTFSI exposed to *in-situ* generated $^1O_2$ over the course of 10 min and to RROS O_2^- and O_2^{2-}.

Appendix C

Methods

C.1 Materials for Electrochemical Experiments

The choice of suitable reference electrodes, careful exclusion of oxygen and water from the electrochemical cell operated in a Ar-filled glovebox, and thorough cleaning and drying of all substances and equipment are the most obvious aspects. These modes of operation were adhered throughout all experiments.

Carbon (C, C-NERGY[TM] Graphite and Carbon Black, SUPER C65 conductive carbon) was purchased from IMERYL Graphyte and Carbon. **Super P**[®] (conductive carbon black, Batch-Nr.0011412) was purchased from TIMCAL. **Lithium ironphosphate** ($LiFePO_4$, LFP, CAS-Nr.15365-1-7, powder for Li-ion Battery Cathode, Model: P198-S21) was purchased from MTI Corporation. The delithiation of $LiFePO_4$ was done either electrochemical or chemical.[145] The $Li_{1-x}FePO_4$ potential versus Li^0/Li^+ was used to express all potentials in this work on the lithium scale. **Lithium peroxide** (Li_2O_2) was synthesized as described following. The precursor for the synthesis of Lithium peroxide , LiOH anhydride was synthesized according to a previously reported procedure.[62] Lithium peroxide (Li_2O_2) was synthesized under inert conditions according to a previously reported procedure.[146] The synthesized Li_2O_2 particles were further ground in a ball mill (Pulverisette 7, Fritsch) with ZrO_2 grinding balls under inert conditions. To control the heat development during the grinding process, a program with alternating intervals of 5 min grinding and 20 min rest was applied and repeated 48 times. The XRD diffractogram of Li_2O_2 after baseline correction and Rietveld refinement is shown in Figure C.1. The pristine (hexagonal crystal system with a=3.1434(5) and c=7.6496(8)) and the grinded sampled contain pure and crystalline Li_2O_2 besides impurities in negligible concentrations lower than 1% (see

Figure C.1: XRD diffractogramm of Li_2O_2 and XRD pattern of ICSD standards of LiOH and Li_2CO_3). The broadening of the reflexion peaks indicate that the grinding process diminished the crystallite size of Li_2O_2, which was further determined *via* the formula: $n \cdot \lambda = 2d \cdot \sin\theta$ known as Bragg's Law. The evaluation of the obtained data from XRD analysis was performed using the provided program XPert High Score Plus. The calculated crystallite size before and after the grinding process decreased from by factor of $\sim$6. The crystallite size of the grounded Li_2O_2 is distributed over the average values of 80-200 Å. **Lithium carbonate** (Li_2CO_3, CAS-Nr.554-13-2, Puratronic®, 99.998% metal basis excluding Ca LT 20 ppm) was purchased from Alfa Aesar, Thermo Fisher Scientific Chemicals. The Li_2CO_3 powder was ground in a porcelain mortar and pistil. The grinded particles were homogenized in isopropyl alcohol. Only the fine particles from the supernatant were dried at room temperature and further dried under reduced pressure at 150 °C. Li_2CO_3 and carbon was ground for 1.5 h with 200 rpm in a planetary mill in the ratio 1:9 and 9:1 (w:w).
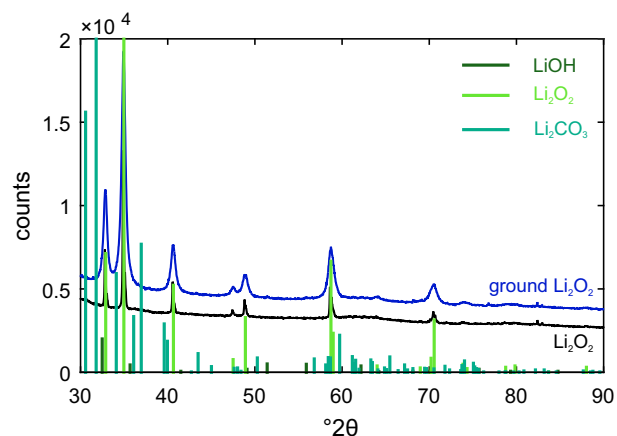
Figure C.1: The XRD diffractogramm of the sample before and after grinding indicates that Li_2O_2 is the predominant phase in both samples indicatined by the reference bragg reflexes of the ICSD standards of LiOH and Li_2CO_3. The broadening of the significant bragg reflexes of Li_2O_2 before and after grinding indicate that the crystallite size diminished through the grinding process.

Lithium bis(trifluoromethane)sulfonimide (LiTFSI, CAS-Nr.90076-65-6), **lithium perchlorate** ($LiClO_4$, CAS-Nr.7791-03-9, battery grade, dry, 99.99% trace metals basis) and **tetrabutylammoniumperchlorate** (TBA, CAS-Nr.1923-70-2, for electrochemical analysis, >99.0%) were purchased from Sigma Aldrich. LiTFSI, $LiClO_4$ and TBA were dried under reduced pressure for 24 h at 140 °C. **Dimethoxy ethane** (DME, CAS-Nr.115-10-6), **diethylene glycol dimethyl ether** (DEGDME, CAS-Nr.111-96-6), **tetraethylene glycol dimethyl ether** (TEGDME, CAS-Nr.143-24-8), were purchased from TCI Chemicals. The ethers were dried over lithium and purified *via* distillation and further dried and stored over activated molecular sieves. The water content was determined by Karl-Fisher titration (Methrom 851 Titrando). **Dimethoxy ethane** (DME, CAS-Nr.115-10-6, dry), propylene carbonate (PC, CAS-Nr.108-32-7), dimethyl carbonate (DMC, CAS-Nr.616-38-6, selectilyte), ethylene carbonate (EC, CAS-Nr.96-49-1, selectilyte) and bis(trifluoromethane)sulfonimide lithium (LiTFSI, CAS-

Nr.90076-65-6) were purchased from BASF.

C.2   Materials for Chemical Experiments

Solvents for use in synthesis and for electrolyte mixtures were distilled and stored in the glovebox over molecular sieves. **H$_2$O$_2$** (35wt%, for synthesis), **Sodium hypochlorite** (NaClO, CAS-Nr. 7681-52-9, 10-14% solution) and **acetonitrile** (MeCN-d$_3$, CAS-Nr. 2206-26-0, 99.8atom%) was purchased from Sigma Aldrich. **Potassium superoxide** (KO$_2$, CAS-Nr. 12030-88-5) was purchased from Strem Chemicals, Inc. The photo-sensitizer palladium(II) meso-tetra(4-fluorophenyl)tetrabenzoporphyrin (Pd$_4$F) was synthesized according a previously reported procedure[114] and provided by the Institute of Analytical Chemistry and Food Chemistry at Graz University of Technology. Singlet oxygen was generated photochemically by illuminating a O$_2$-saturated electrolyte containing a small concentration of the photo-sensitizer Pd4F inside a closed vessel. The photo-sensitizer was irradiated with a red LED light source (632 nm). Photo-oxygenation experiments were performed in oxygen saturated solutions of Pd$_4$F in solutions containing DMA or DPA in a 10 mm cuvette with screw cap. The reaction process was controlled *via* absorption spectroscopy every 60 sec. The cuvette was shaken to every 60 sec to provide suffiecient oxygen supply. **1,4,7,10,13,16-Hexaoxacyclooctadecane** (18-crown-6, CAS-Nr. 17455-13-9, >99.0%) was purchased from Sigma Aldrich. 2,5-bis(4-bromobenzyl)-3,6-bis(4-(tert-butyl)phenyl)-2,5-dihydropyrrolo[3,4-c]pyrrole-1,4-dione was synthesized and provided by S. Borisov from the Institute of Analytical Chemistry and Food Chemistry from Graz University of Technology. **M™ NOVOTEC™ 7200** was purchased from 3M. **9-(Chloromethyl)anthracene** (CAS-Nr. 24463-19-2, 98+%) was purchased from Alfa Aesar GmbH & Co KG. **Isopropyl alcohol** (IPA, CAS-Nr. 67-63-0), **acetone** (CAS-Nr.76-64-1) and **H$_2$O** (Millipore) were obtained by in-house supply. **Ethanol** (CAS-Nr. 64-17-5, 100% HPLC grade, absolut) was purchased from CHEM LAB NV. **Diketo-pyrrolo-pyrrol** (Irgazin Orange DPP®, pigment orange 73, Nr.23178) was purchased from Kremer Pigmente GmbH & Co KG. **Potassium tert-butoxide** (CAS-Nr.856-47-4, reagent grade >98%) was purchased from Aldrich. **Methanol** (CAS-Nr. 67-56-1, Analar NOMRAPUR) was purchased from VWR Chemicals. **Dichlormethane** (CAS-Nr. 75-09-2, laboratory reagent grade) and cyclohexane (CAS-Nr. 110-82-7) were purchased from Fisher Chemicals. **Tetrahydrofurane** (CAS-Nr.109-99-9), **N,N-Dimethylformamide** (CAS-Nr. 68-12-2, 99.5% for synthesis), **Sodium sulfite** (Na$_2$SO$_3$, CAS-Nr. 7757-86-7, >98%, anhydrous) and **Silica gel** (CAS-Nr. 7631-86-9, Nr.60 for preparative TLC, 0.04-0.063nm) were purchased from Carl Roth GmbH+Co.KG. Ethanol ROTIPURAN®,

99,8%). **0-Phenyl-9-anthraceneboronic acid** (CAS-Nr. 334658-75-2, >98.0%, contains varying amounts of anhydride) was purchased from TCI Europe. **1,1'-Bis(diphenylphosphino)ferrocenedi chlorpalladium (II)** was purchased from ABCR (Pd(dppf)Cl$_2$, 99.9%, CAS-Nr.: 72287-26-4). **Toluene**(CAS-Nr. 108-88-3, laboratory reagent grade) and **dichlormethane**(CAS-Nr. 75-09-2, laboratory reagent grade) was purchased from Fisher Chemicals. **2,5-bis(4-bromobenzyl)-3,6-bis(4-(tert-butyl)phenyl)-2,5-dihydropyrrolo[3,4-c]pyrrole-1,4-dione** was synthesized by by S. Borisov from the Institute of Analytical Chemistry and Food Chemistry from Graz University of Technology. **1,4-Benzenediamine** (CAS-Nr. 106-50-3, >99%), **Hexamethylenetetramine** (CAS-Nr. 100-97-0, >99%) and **N,N,N',N'-Tetramethylethylendiamin** (TMEDA, CAS-Nr. 110-18-9, >99%) were purchased from Carl Roth GmbH + Co. KG. **N,N-Dimethyl-p-phenylenediamine** (DMPPDA, CAS-Nr. 99-98-9, >97%) was purchased from Fluka. **N,N-Diisopropylethylamine** (DIPEA, CAS-Nr. 7087-68-5, >99%) and **N,N,N,N-Tetraethylethylenediamine** (TEEDA, CAS-Nr. 150-77-6, >99%) were purchased from Sigma Aldrich. 1,3,3-Trimethyl-2-[3,7,12,16-tetramethyl-18-(2,6,6-trimethylcyclohex-1-en-1-yl)octadeca-1,3,5,7,9,11,13,15,17-nonaen-1-yl]cyclohex-1-ene (beta-carotene, CAS.Nr. 7235-40-7,>97%) and bilirubin (CAS-Nr. 635-65-4, >98%) were purchased from TCI Chemicals Europe. **Pd(II) meso-tetra-(pentafluorophenyl)porphyrin** (PdT975, CAS-Nr. 72076-09-6, >99%) was purchased from Frontier Scientific®. **Polystyrole** (PS, CAS-Nr. 9003-53-6, avarage MW 260.000, density 1.050) and **Polyvinylalcohole** (PVOH, CAS-Nr. 9002-89-5, 99%, hydrolyzed, avarage MW 86.000, sp^2 Scientific Polymer) was purchased from ACROS Organics USA. **Oleic acid** (CAS-Nr. 112-80-1, >99%) and **linoleic acid ethyl ester** (Ethyl linoleate, CAS-Nr. 544-35-4,>99%) were purchased from Sigma Aldrich. **Deuterium oxide** (CAS-Nr. 7789-20-0), **deuterated dimethylsulfoxide** (DMSO-d$_6$, CAS-Nr. 2206-27-1) and **deuterated chloroform** (CHCl$_3$, CAS-Nr. 865-49-6) were purchased from euriso-top®. **Formic acid** (CAS-Nr. 64-18-6, puriss. p.a. ∼98%) was purchased from Fluka® Analytical. **Water** (H$_2$O, CHROMASOLV® for HPLC) was purchased from Sigma-Aldrich. Acetonitrile (MeCN, CAS-Nr. 78-05-8, HiPerSolv CHROMANORM Prolabo®) was purchased from VWR Chemicals. APCI/APPI tuning mix was purchased from Agilent Technologies. **Lithium azide** (LiN$_3$, CAS-Nr. 19597-69-4, 20 wt.% in H$_2$O) and **sodium acide** (NaN$_3$, CAS-Nr. 247-852-1, ReagentPlus®, ≥99.5%) was purchased from Sigma Aldrich. The LiN$_3$ was mixed with methanol and dried under reduced pressure. NaN$_3$ was dried under reduced pressure and used without further purification. **Cobald(II) chloride** (CoCl$_2$, CAS-Nr. 7646-79-9, anhydrous) was purchased from Merck-Schuchardt. **Gas mixtures of O$_2$ in N$_2$** (20 ppm O$_2$, 0.1% O$_2$ and 1.95% O$_2$, validation class 1) were purchased from Linde Gas GmbH. High purity **oxygen** (O$_2$ 3.5, >99.95vol%), high

purity **Ar** (Ar 5.0, ⟩99.999vol%) and a **mixture of Ar 6.0 and O$_2$ 5.5** (Ar 5.01vol%) were purchased from Messer Austria GmbH. **1H,1H,2H,2H-Perfluorooctyldimethylchlorosilane** ($C_{10}H_{10}ClF_{13}Si$, CAS-Nr. 102488-47-1, 97%) was purchased from abcr GmbH. **Microscope slides** were purchased from Gerhard Menzel B.V. & Co. KG. **Silica gel** disks (Nr.60F254) were purchased from Merck KGaA. Electrochemical tests were run on either a SP-300 (BioLogic SA, France) or BT-2000 (Arbin Instruments) potentiostat/galvanostat. Cyclic voltammograms were recorded in a three-electrode arrangement with glassy carbon disc working electrode (BAS Inc.), a Ag wire pseudo-reference and a Pt wire counter electrode inside a glass cell with PTFE lid. The cells were run inside an Ar filled glovebox and purged with high-purity Ar or O$_2$. The redox system Fc/Fc$^+$ was used to reference the measured data *vs.* the Li/Li$^+$ scale. Test cells were assembled in a custom-built cell configuration based on a Swagelok$^®$ design. The Li$_{1-x}$FePO$_4$ potential *vs.* Li^0/Li$^+$ was used to express all potentials in this work on the lithium scale.

C.3   Methods

XRD measurements were performed on a Bruker Advance D8 diffractometer with a LynxEye Detektor using Cu Kα radiation over the range 20 - 110 °2θ (3s/step, RBragg = 6.4). Rietveld refinement was performed with the program XPert High Score Plus. Moisture and air-sensitive samples were prepared in an N$_2$ glove box and covered with a hermetical film (SpectroCertified polyimide Kapton$^®$ thin-film, Chemplex Industries, Inc.) in order to ensure that the sample is measured under inert gas condition. **ATR-IR** measurements were performed in an Ar-filled glovebox on a Bruker ALPHA-P spectrometer. ATR-IR spectra were recorded in a wavelength range between 4000 - 400 cm^{-1}, a baselinecorrecion done after the measurement with help of the accompanied software OPUS 6.5. ^{1}**H NMR** spectra of DMA, DMA-O$_2$ and of the extracted electrolytes after oxidation of C or Li$_2$CO$_3$ packed electrodes were recorded on a Bruker Avance III 300 MHz FT NMR spectrometer with autosampler (300.36 MHz). Chemical shifts (δ) are referenced to the residual protonated solvent signals as internal standard.

C.4 Test Cells

Following custom made cells were used to perform *in-situ* and *ex-situ* experiments which are described in this thesis. The cells were designed by S.A. Freunberger and manufactured by J. Schlegl from the Institute for Chemistry and Technology of Materials from Graz University of Technology.
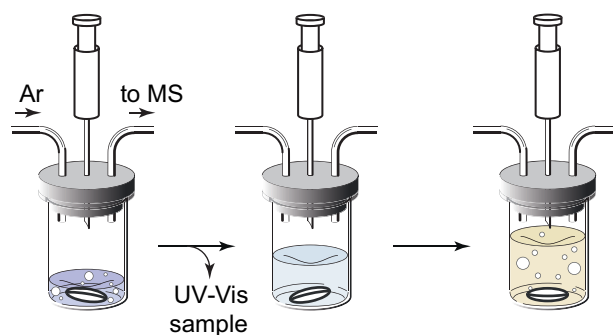
Figure C.2: Cell design for Mass spectrometry measurements. Schematic of the test setup to quantify total superoxide/peroxide and carbonaceous products in battery electrodes. Adapted from Schafzahl *et al.*[63]
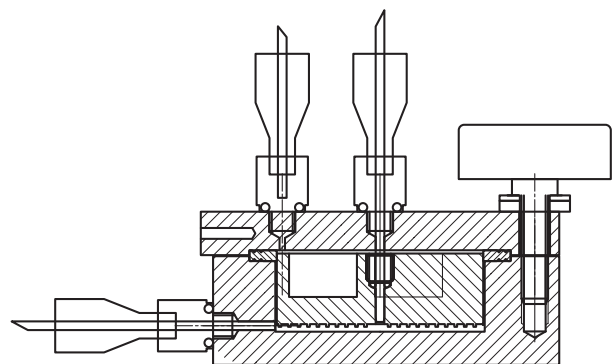
Figure C.3: Cell design for online electrochemical measurements (OEMS).
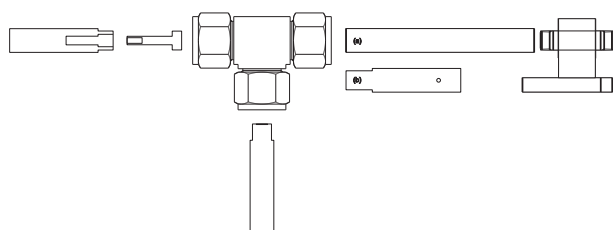
Figure C.4: Swagelok® cell design for metal-O$_2$ batteries.
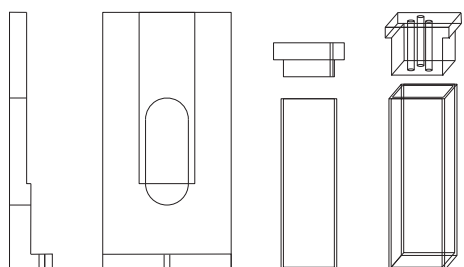
Figure C.5: A set of custom made cells for *in-situ* Fluorescence, NIR- and UV-VIS spectroscopy measurements, including a cell holder. The cell holder was made for cuvettes with a lightpath of 1 mm, 2 mm and 10 mm.

Bibliography

[1] Dunn, B., Kamath, H. & Tarascon, J.-M. Electrical energy storage for the grid: A battery of choices. *Science* **334**, 928–935 (2011).

[2] Larcher, D. & Tarascon, J. M. Towards greener and more sustainable batteries for electrical energy storage. *Nature Chemistry* **7**, 1929 (2014).

[3] Wagner, F. T., Lakshmanan, B. & Mathias, M. F. Electrochemistry and the future of the automobile. *The Journal of Physical Chemistry Letters* **1**, 2204–2219 (2010).

[4] Whittingham, M. S. Ultimate limits to intercalation reactions for lithium batteries. *Chemical Reviews* **114**, 11414–11443 (2014).

[5] Noorden, R. V. The rechargeable revolution: A better battery. *Nature* **507**, 2628 (2014).

[6] Aurbach, D., McCloskey, B. D., Nazar, L. F. & Bruce, P. G. Advances in understanding mechanisms underpinning lithiumair batteries. *Nature Energy* **1**, 16128 (2016).

[7] Hartmann, P. *et al.* A rechargeable room-temperature sodium superoxide (nao2) battery. *Nature Materials* **12**, 228232 (2012).

[8] Choi, J. W. & Aurbach, D. Promise and reality of post-lithium-ion batteries with high energy densities. *Nature Reviews Materials* **1**, 16013 (2016).

[9] Luntz, A. C. & McCloskey, B. D. Nonaqueous liair batteries: A status report. *Chemical Reviews* **114**, 11721–11750 (2014).

[10] Obrovac, M. N. & Chevrier, V. L. Alloy negative electrodes for li-ion batteries. *Chemical Reviews* **114**, 11444–11502 (2014).

[11] Chevrier, V. L. & Ceder, G. Challenges for na-ion negative electrodes. *Journal of The Electrochemical Society* **158**, A1011–A1014 (2011).

[12] Sun, Y., Liu, N. & Cui, Y. Promises and challenges of nanomaterials for lithium-based rechargeable batteries. *Nature Energy* **1**, 16071 (2016).

[13] Bruce, P. G., Freunberger, S. A., Hardwick, L. J. & Tarascon, J.-M. Li-o2 and li-s batteries with high energy storage. *Nature Materials* **11**, 19–29 (2012). 10.1038/nmat3191.

[14] Pang, Q., Liang, X., Kwok, C. Y. & Nazar, L. F. Advances in lithiumsulfur batteries based on multifunctional cathodes and electrolytes. *Nature Energy* **1**, 16132 (2016).

[15] Mahne, N., Renfrew, S. E., McCloskey, B. D. & Freunberger, S. A. Electrochemical oxidation of lithium carbonate generates singlet oxygen. *Angew. Chem. Int. Ed.* (2018).

[16] Choi, N.-S. *et al.* Challenges facing lithium batteries and electrical double-layer capacitors. *Angewandte Chemie International Edition* **51**, 9994–10024 (2012). CAPLUS AN 2012:1325861(Journal).

[17] Christensen, J. *et al.* A critical review of li/air batteries. *Journal of The Electrochemical Society* **159**, R1–R30 (2012).

[18] Girishkumar, G., McCloskey, B., Luntz, A. C., Swanson, S. & Wilcke, W. Lithiumair battery: Promise and challenges. *The Journal of Physical Chemistry Letters* **1**, 2193–2203 (2010).

[19] Laoire, C. O., Mukerjee, S., Plichta, E. J., Hendrickson, M. A. & Abraham, K. M. Rechargeable lithium/tegdme-lipf6/o2 battery. *Journal of The Electrochemical Society* **158**, A302–A308 (2011).

[20] Hassoun, J., Croce, F., Armand, M. & Scrosati, B. Investigation of the o2 electrochemistry in a polymer electrolyte solid-state cell. *Angewandte Chemie International Edition* **50**, 2999–3002 (2011).

[21] McCloskey, B. D., Garcia, J. M. & Luntz, A. C. Chemical and electrochemical differences in non-aqueous li-o2 and na-o2 batteries. *The Journal of Physical Chemistry Letters* (2014).

[22] Landa-Medrano, I. *et al.* Sodiumoxygen battery: Steps toward reality. *The Journal of Physical Chemistry Letters* **7**, 1161–1166 (2016).

[23] McCloskey, B. D. *et al.* Limitations in rechargeability of li-o2 batteries and possible origins. *Journal of Physical Chemistry Letters* **3**, 3043–3047 (2012). Times Cited: 0.

[24] Liu, T., Kim, G., Casford, M. T. L. & Grey, C. P. Mechanistic insights into the challenges of cycling a nonaqueous nao2 battery. *The Journal of Physical Chemistry Letters* 4841–4846 (2016).

[25] Landa-Medrano, I. *et al.* New insights into the instability of discharge products in nao2 batteries. *ACS Applied Materials Interfaces* **8**, 20120–20127 (2016).

[26] Mizuno, F., Nakanishi, S., Kotani, Y., Yokoishi, S. & Iba, H. Rechargeable li-air batteries with carbonate-based liquid electrolytes. *Electrochemistry* **78**, 403–405 (2010).

[27] Xu, W. *et al.* Investigation on the charging process of li2o2-based air electrodes in li-o2 batteries with organic carbonate electrolytes. *Journal of Power Sources* **196**, 3894–3899 (2011).

[28] Abraham, K. M. & Jiang, Z. A polymer electrolyte-based rechargeable lithium/oxygen battery. *Journal of The Electrochemical Society* **143**, 1–5 (1996).

[29] Laoire, C. O., Mukerjee, S., Abraham, K. M., Plichta, E. J. & Hendrickson, M. A. Influence of nonaqueous solvents on the electrochemistry of oxygen in the rechargeable lithiumair battery. *The Journal of Physical Chemistry C* **114**, 9178–9186 (2010).

[30] Laoire, C. O., Mukerjee, S., Abraham, K. M., Plichta, E. J. & Hendrickson, M. A. Elucidating the mechanism of oxygen reduction for lithium-air battery applications. *The Journal of Physical Chemistry C* **113**, 20127–20134 (2009).

[31] Lu, Y.-C. *et al.* Lithium-oxygen batteries: bridging mechanistic understanding and battery performance. *Energy Environmental Science* **6**, 750–768 (2013).

[32] Lim, H.-D. *et al.* Rational design of redox mediators for advanced lio2 batteries. *Nature Energy* **1**, 16066 (2016).

[33] Younesi, R. *et al.* Ether based electrolyte, lib(cn)4 salt and binder degradation in the lio2 battery studied by hard x-ray photoelectron spectroscopy (haxpes). *The Journal of Physical Chemistry C* **116**, 18597–18604 (2012).

[34] Bryantsev, V. S. *et al.* The identification of stable solvents for nonaqueous rechargeable li-air batteries. *Journal of The Electrochemical Society* **160**, A160–A171 (2013).

[35] Freunberger, S. A. *et al.* The lithiumoxygen battery with ether-based electrolytes. *Angewandte Chemie International Edition* **50**, 8609–8613 (2011).

[36] Younesi, R., Hahlin, M., Bjrefors, F., Johansson, P. & Edstrm, K. Li-o2 battery degradation by lithium peroxide (li2o2): a model study. *Chemistry of Materials* **25**, 7784 (2012).

[37] McCloskey, B. D., Burke, C. M., Nichols, J. E. & Renfrew, S. E. Mechanistic insights for the development of li-o2 battery materials: addressing li2o2 conductivity limitations and electrolyte and cathode instabilities. *Chemical Communications* **51**, 12701–12715 (2015).

[38] Mahne, N., Fontaine, O., Thotiyl, M. O., Wilkening, M. & Freunberger, S. A. Mechanism and performance of lithium-oxygen batteries - a perspective. *Chemical Science* doi: 10.1039/C7SC02519J (2017).

[39] McCloskey, B. D., Scheffler, R., Speidel, A., Girishkumar, G. & Luntz, A. C. On the mechanism of nonaqueous lio2 electrochemistry on c and its kinetic overpotentials: Some implications for liair batteries. *The Journal of Physical Chemistry C* **116**, 23897–23905 (2012).

[40] Viswanathan, V. *et al.* Electrical conductivity in li2o2 and its role in determining capacity limitations in non-aqueous li-o2 batteries. *The Journal of Chemical Physics* **135**, 214704 (2011).

[41] Gutmann, V. Solvent effects on the reactivities of organometallic compounds. *Coordination Chemistry Reviews* **18**, 225–255 (1976).

[42] Johnson, L. *et al.* The role of lio2 solubility in o2 reduction in aprotic solvents and its consequences for lio2 batteries. *Nature Chemistry* **6**, 1091 – 1099 (2014).

[43] Kwabi, D. G. *et al.* Experimental and computational analysis of the solvent-dependent o2/li+-o2 redox couple: Standard potentials, coupling strength, and implications for lithiumoxygen batteries. *Angewandte Chemie International Edition* **55**, 3129–3134 (2016).

[44] Burke, C. M., Pande, V., Khetan, A., Viswanathan, V. & McCloskey, B. D. Enhancing electrochemical intermediate solvation through electrolyte anion selection to increase nonaqueous lio2 battery capacity. *Proceedings of the National Academy of Sciences* **112**, 9293–9298 (2015).

[45] Sharon, D. *et al.* Mechanistic role of li+ dissociation level in aprotic lio2 battery. *ACS Applied Materials Interfaces* (2016).

[46] Gunasekara, I., Mukerjee, S., Plichta, E. J., Hendrickson, M. A. & Abraham, K. M. A study of the influence of lithium salt anions on oxygen reduction reactions in li-air batteries. *Journal of The Electrochemical Society* **162**, A1055–A1066 (2015).

[47] Kwabi, D. G. *et al.* The effect of water on discharge product growth and chemistry in li-o2 batteries. *Physical Chemistry Chemical Physics* **18**, 24944–24953 (2016).

[48] Schwenke, K. U., Metzger, M., Restle, T., Piana, M. & Gasteiger, H. A. The influence of water and protons on li2o2 crystal growth in aprotic li-o2 cells. *Journal of The Electrochemical Society* **162**, A573–A584 (2015).

[49] Aetukuri, N. B. *et al.* Solvating additives drive solution-mediated electrochemistry and enhance toroid growth in non-aqueous lio2 batteries. *Nature Chemistry* **7**, 50–56 (2014).

[50] Khetan, A., Luntz, A. & Viswanathan, V. Trade-offs in capacity and rechargeability in nonaqueous lio2 batteries: Solution-driven growth versus nucleophilic stability. *The Journal of Physical Chemistry Letters* **6**, 1254–1259 (2015).

[51] Mahne, N. *et al.* Singlet oxygen generation as a major cause for parasitic reactions during cycling of aprotic lithiumoxygen batteries. *Nature Energy* **2**, 17036 (2017).

[52] Adams, B. D. *et al.* Current density dependence of peroxide formation in the li-o2 battery and its effect on charge. *Energy Environmental Science* **6**, 1772–1778 (2013).

[53] Black, R. *et al.* Screening for superoxide reactivity in li-o2 batteries: Effect on li2o2/lioh crystallization. *Journal of the American Chemical Society* **134**, 2902–2905 (2012).

[54] Liu, T. *et al.* Cycling li-o2 batteries via lioh formation and decomposition. *Science* **350**, 530–533 (2015).

[55] Lu, J. *et al.* A lithiumoxygen battery based on lithium superoxide. *Nature* **529**, 377–382 (2016).

[56] Yang, J. *et al.* Evidence for lithium superoxide-like species in the discharge product of a li-o2 battery. *Physical Chemistry Chemical Physics* **15**, 3764–3771 (2013).

[57] Chen, Y., Freunberger, S. A., Peng, Z., Bard, F. & Bruce, P. G. Lio2 battery with a dimethylformamide electrolyte. *Journal of the American Chemical Society* **134**, 7952–7957 (2012).

[58] McCloskey, B. D., Bethune, D. S., Shelby, R. M., Girishkumar, G. & Luntz, A. C. Solvents critical role in nonaqueous lithiumoxygen battery electrochemistry. *The Journal of Physical Chemistry Letters* **2**, 1161–1166 (2011).

[59] Peng, Z., Freunberger, S. A., Chen, Y. & Bruce, P. G. A reversible and higher-rate li-o2 battery. *Science* **337**, 563–566 (2012).

[60] McCloskey, B. D. *et al.* Combining accurate o2 and li2o2 assays to separate discharge and charge stability limitations in nonaqueous lio2 batteries. *The Journal of Physical Chemistry Letters* 2989–2993 (2013).

[61] Hartmann, P. *et al.* A comprehensive study on the cell chemistry of the sodium superoxide (nao2) battery. *Physical Chemistry Chemical Physics* **15**, 11661–11672 (2013).

[62] Ottakam Thotiyl, M. M., Freunberger, S. A., Peng, Z. & Bruce, P. G. The carbon electrode in nonaqueous lio2 cells. *Journal of the American Chemical Society* **135**, 494–500 (2013).

[63] Schafzahl, B. *et al.* Quantifying total superoxide, peroxide, and carbonaceous compounds in metalo2 batteries and the solid electrolyte interphase. *ACS Energy Letters* 170–176 (2017).

[64] Freunberger, S. A. *et al.* Reactions in the rechargeable lithiumo2 battery with alkyl carbonate electrolytes. *Journal of the American Chemical Society* **133**, 8040–8047 (2011).

[65] Ingraham, L. & Meyer, D. *Biochemistry of Dioxygen* (Plenum Press, New York, 1985).

[66] Hayyan, M., Hashim, M. A. & AlNashef, I. M. Superoxide ion: Generation and chemical implications. *Chemical Reviews* (2016).

[67] Panieri, E. & Santoro, M. M. Ros homeostasis and metabolism: a dangerous liason in cancer cells. *Cell Death Amp; Disease* **7**, e2253 (2016).

[68] Sawyer, D. T. & Valentine, J. S. How super is superoxide? *Accounts of Chemical Research* **14**, 393–400 (1981).

[69] Aurbach, D., Daroux, M., Faguy, P. & Yeager, E. The electrochemistry of noble metal electrodes in aprotic organic solvents containing lithium salts. *Journal of Electroanalytical Chemistry* **297**, 225–244 (1991). Doi: DOI: 10.1016/0022-0728(91)85370-5.

[70] Bryantsev, V. S. *et al.* Predicting solvent stability in aprotic electrolyte liair batteries: Nucleophilic substitution by the superoxide anion radical (o2). *The Journal of Physical Chemistry A* **115**, 12399–12409 (2011).

[71] Bryantsev, V. S. Predicting the stability of aprotic solvents in li-air batteries: pka calculations of aliphatic c-h acids in dimethyl sulfoxide. *Chemical Physics Letters* **558**, 42–47 (2013).

[72] Bryantsev, V. S., Blanco, M. & Faglioni, F. Stability of lithium superoxide lio2 in the gas phase: Computational study of dimerization and disproportionation reactions. *The Journal of Physical Chemistry A* **114**, 8165–8169 (2010).

[73] Bryantsev, V. S. & Faglioni, F. Predicting autoxidation stability of ether- and amide-based electrolyte solvents for liair batteries. *The Journal of Physical Chemistry A* **116**, 7128–7138 (2012).

[74] Assary, R. S., Lau, K. C., Amine, K., Sun, Y.-K. & Curtiss, L. A. Interactions of dimethoxy ethane with li2o2 clusters and likely decomposition mechanisms for lio2 batteries. *The Journal of Physical Chemistry C* **117**, 8041–8049 (2013).

[75] Andrieux, C. P., Hapiot, P. & Saveant, J. M. Mechanism of superoxide ion disproportionation in aprotic solvents. *Journal of the American Chemical Society* **109**, 3768–3775 (1987).

[76] Luntz, A. C. & McCloskey, B. D. Liair batteries: Importance of singlet oxygen **2**, 17056 (2017).

[77] Alfano, A. J. & Christe, K. O. Singlet delta oxygen production from a gassolid reaction. *Angewandte Chemie International Edition* **41**, 3252–3254 (2002).

[78] Li, Q. *et al.* A spectroscopic study on singlet oxygen production from different reaction paths using solid inorganic peroxides as starting materials. *Bulletin of the Korean Chemical Society* **28**, 1656–1660 (2007).

[79] Ogilby, P. R. Singlet oxygen: there is indeed something new under the sun. *Chemical Society Reviews* **39**, 3181–3209 (2010).

[80] Wandt, J., Jakes, P., Granwehr, J., Gasteiger, H. A. & Eichel, R.-A. Singlet oxygen formation during the charging process of an aprotic lithiumoxygen battery. *Angewandte Chemie International Edition* **55**, 6892–6895 (2016).

[81] Schafzahl, L. *et al.* Singlet oxygen during cycling of the aprotic sodiumo2 battery. *Angewandte Chemie International Edition* **56**, 15728–15732 (2017).

[82] Holleman, A. & Wiberg, N. *Lehrbuch der Anorganischen Chemie*, vol. 102 (Walter de gruyter Co., Berlin, New York, 2007).

[83] Coulson, C. A. Representation of simple molecules by molecular orbitals. *Quarterly Reviews, Chemical Society* **1**, 144–178 (1947).

[84] DeRosa, M. C. & Crutchley, R. J. Photosensitized singlet oxygen and its applications. *Coordination Chemistry Reviews* **233-234**, 351–371 (2002).

[85] Wilkinson, F., Helman, W. P. & Ross, A. B. Rate constants for the decay and reactions of the lowest electronically excited singlet state of molecular oxygen in solution. an expanded and revised compilation. *Journal of Physical and Chemical Reference Data* **24**, 663–677 (1995).

[86] Schweitzer, C. & Schmidt, R. Physical mechanisms of generation and deactivation of singlet oxygen. *Chem. Rev.* **103**, 16851758 (2003).

[87] Khan, A. U. Direct spectral evidence of the generation of singlet molecular oxygen (1.delta.g) in the reaction of potassium superoxide with water. *Journal of the American Chemical Society* **103**, 6516–6517 (1981).

[88] McKeown, E. & Waters, W. A. The oxidation of organic compounds by singlet oxygen. *J. Chem. Soc. B,* (1966).

[89] Foote, C. S. Photosensitized oxygenations and the role of singlet oxygen. *Acc. Chem. Res.* (1968).

[90] Foner, S. N. & Hudson, R. L. Oh, ho2, and h2o2 production in the reaction of atomic hydrogen with molecular oxygen. *The Journal of Chemical Physics* **23**, 1974 (1955).

[91] Griesbeck, A. G. & Mattey, J. *Synthetic Organic Photochemistry* (Marcel Dekker, 2004). URL

[92] Darmanyan, A. P. & Jenks, W. S. Charge-transfer quenching of singlet oxygen o2(1g) by amines and aromatic hydrocarbons. *J. Phys. Chem. A* **102**, 7420–7426 (1998).

[93] Lengfelder, E., Cadenas, E. & Sies, H. Effect of dabco (1,4-diazabicyclo[2,2,2]-octane) on singlet oxygen monomol (1270 nm) and dimol (634 and 703 nm) emission **164**, 366–370 (1983).

[94] Corey, E., Mehrotra, M. M. & Khan, A. Antiarthritic gold compounds effectively quench electronically excited singlet oxygen. *Science.* **236**, 68–69 (1987).

[95] Monroe, B. M. & Mrowca, J. J. Quenching of singlet oxygen by nickel complexes. *J. Phys. Chem.* **83**, 591595 (1979).

[96] Young, R. H. & Martin, R. L. On the mechanism of quenching of singlet oxygen by amines. *Journal of the American Chemical Society* **94**, 5183–5185 (1972).

[97] Baltschun, D. *et al.* Singlet oxygen quenching abilities of carotenoids. *Liebigs Annalen* **1997**, 1887–1893 (1997).

[98] Wilkinson, F., Helman, W. P. & Ross, A. B. Rate constants for the decay and reactions of the lowest electronically excited singlet state of molecular oxygen in solution. an expanded and revised compilation. *Journal of Physical and Chemical Reference Data* **24** (1995).

[99] Bagrov, I. V., Belousova, I. M., Kiselev, V. M., Kislyakov, I. M. & Sosnov, E. N. Observation of the luminescence of singlet oxygen at = 1270 nm under led irradiation of ccl4. *Optics and Spectroscopy* **113**, 57–62 (2012).

[100] Regensburger, J., Maisch, T., Felgentrger, A., Santarelli, F. & Bumler, W. A helpful technology the luminescence detection of singlet oxygen to investigate photodynamic inactivation of bacteria (pdib). *Journal of Biophotonics* **3**, 319–327 (2010).

[101] Gomes, A., Fernandes, E. & Lima, J. L. F. C. Fluorescence probes used for detection of reactive oxygen species. *Journal of Biochemical and Biophysical Methods* **65**, 45–80 (2005).

[102] Ouannes, C. & Wilson, T. Quenching of singlet oxygen by tertiary aliphatic amines. effect of dabco (1,4-diazabicyclo[2.2.2]octane). *Journal of the American Chemical Society* **90**, 6527–6528 (1968).

[103] Umezawa, N. *et al.* Novel fluorescent probes for singlet oxygen. *Angew. Chem. Int. Ed.* **38** (1999).

[104] Valeur, B. *Molecular Fluorescence: Principles and Applications* (Wiley-VCH Verlag GmbH).

[105] Lakowicz, J. R. *Principles of Fluorescence Spectroscopy* (Springer Science+Business Media, LLC), third edition edn.

[106] Tanaka, K. *et al.* Rational design of fluorescein-based fluorescence probes. mechanism-based design of a maximum fluorescence probe for singlet oxygen. *J. Am. Chem. Soc.* **123**, 2530–2536 (2001).

[107] Li, X. *et al.* 4,5-dimethylthio-4-[2-(9-anthryloxy)ethylthio]tetrathiafulvalene, a highly selective and sensitive chemiluminescence probe for singlet oxygen. *J. AM. CHEM. SOC.* **126**, 1154311548 (2004).

[108] Miyamoto, S., Martinez, G. R., Medeiros, M. H. G. & Mascio, P. D. Singlet molecular oxygen generated from lipid hydroperoxides by the russell mechanism: Studies using 18o-labeled linoleic acid hydroperoxide and monomol light emission measurements. *J. AM. CHEM. SOC.* **125**, 6172–6179 (2003).

[109] Cao, Y., Koo, Y.-E. L., Koo, S. M. & Kopelman, R. Ratiometric singlet oxygen nano-optodes and their use for monitoring photodynamic therapy nanoplatforms. *Photochemistry and Photobiology* **81**, 1489–1498 (2005).

[110] Albiter, E., Alfaro, S. & Valenzuela, M. A. Photosensitized oxidation of 9,10-dimethylanthracene with singlet oxygen by using a safranin o/silica composite under visible light. *Photochem. Photobiol. Sci.* **14**, 597–602 (2015).

[111] Wasserman, H. H., Scheffer, J. R. & Cooper, J. L. Singlet oxygen reactions with 9,10-diphenylanthracene peroxide. *Journal of the American Chemical Society* **94**, 4991–4996 (1972).

[112] Griesbeck, A. & Mattay, J. vol. 12 (CRC Press, Boca Raton, Florida, USA, 2004).

[113] Borisov, S. M., Zenkl, G. & Klimant, I. Phosphorescent platinum(ii) and palladium(ii) complexes with azatetrabenzoporphyrins. *ACS Appl. Mater. Interfaces* **2**, 366374 (2010).

[114] Borisov, S. M., Nuss, G. & Klimant, I. Red light-excitable oxygen sensing materials based on platinum(ii) and palladium(ii) benzoporphyrins. *Anal. Chem.* **80**, 94359442 (2008).

[115] Jones, R. N. The ultraviolet absorption spectra of anthracene derivatives. *Chemical reviews* (1947).

[116] Clayden, J., Greeves, N., Warren, S. & Wothers, P. *Organic Chemistry* (Oxford University Press, 2001).

[117] Hesse-Meier-Zeeh, Bienz, S., Bigler, L., Fox, T. & Meier, H. *Spektroskopische Methoden in der organischen Chemie*, vol. 9 (Georg Thieme Verlag, Stuttgart, 2016).

[118] Lemp, E. & Zanocco, A. *Singlet Oxygen: Applications in Biosciences and Nanosciences: Singlet Oxygen Chemical Acceptors*, vol. 2 of *Comprehensive Series in Photochemical Photobiological Sciences*.

[119] Gray, V. *et al.* Photophysical characterization of the 9,10-disubstituted anthracene chromophore and its applications in triplet-triplet annihilation photon upconversion. *Journal of Materials Chemistry C* **3**, 11111–11121 (2015).

[120] Ye, C., Zhou, L., Wang, X. & Liang, Z. Photon upconversion: from two-photon absorption (tpa) to triplet-triplet annihilation (tta). *Physical Chemistry Chemical Physics* **18**, 10818–10835 (2016).

[121] Singh-Rachford, T. N., Islangulov, R. R. & Castellano, F. N. Photochemical upconversion approach to broad-band visible light generation. *J. Phys. Chem. A* **112**, 39063910 (2008).

[122] Simon, Y. C. & Weder, C. Low-power photon upconversion through triplet-triplet annihilation in polymers. *Journal of Materials Chemistry* **22**, 20817–20830 (2012).

[123] Liang, Z.-Q. *et al.* New anthracene derivatives as triplet acceptors for efficient green-to-blue low-power upconversion. *ChemPhysChem* **14**, 3517–3522 (2013).

[124] Brjesson, K., Rudquist, P., Gray, V. & Moth-Poulsen, K. Photon upconversion with directed emission. *Nature Communications* **7** (2016).

[125] Freunberger, S. A. True performance metrics in beyond-intercalation batteries. *Nature Energy* **2**, 17091 (2017).

[126] Nichols, J. E., Knudsen, K. B. & McCloskey, B. D. Oxygen pressure influences spatial nao2 deposition and the sudden death mechanism in nao2 batteries. *The Journal of Physical Chemistry C* (2018).

[127] Xiao, N., Rooney, R. T., Gewirth, A. A. & Wu, Y. The long-term stability of ko2 in k-o2 batteries. *Angewandte Chemie International Edition* **57**, 1227–1231 (2018).

[128] Meini, S. *et al.* Rechargeability of li-air cathodes pre-filled with discharge products using an ether-based electrolyte solution: implications for cycle-life of li-air cells. *Physical Chemistry Chemical Physics* **15**, 11478–11493 (2013).

[129] Renfrew, S. E. & McCloskey, B. D. Residual lithium carbonate predominantly accounts for first cycle co2 and co outgassing of li-stoichiometric and li-rich layered transition-metal oxides. *Journal of the American Chemical Society* **139**, 17853–17860 (2017).

[130] Chen, Y., Freunberger, S. A., Peng, Z., Fontaine, O. & Bruce, P. G. Charging a lio2 battery using a redox mediator. *Nature Chemistry* **5**, 489–494 (2013).

[131] Yoshizawa-Fujita, M., MacFarlane, D. R., Howlett, P. C. & Forsyth, M. A new lewis-base ionic liquid comprising a mono-charged diamine structure: A highly stable electrolyte for lithium electrochemistry. *Electrochemistry Communications* **8**, 445–449 (2006).

[132] Yoshizawa-Fujita, M., Johansson, K., Newman, P., MacFarlanea, D. R. & Forsyth, M. Novel lewis-base ionic liquids replacing typical anions. *Tetrahedron Letters* **47**, 27552758 (2006).

[133] Anastas, P. T. & Warner, J. C. *Green Chemistry: Theory and Practice* (Oxford University Press, New York, 1998).

[134] Lim, H.-D. *et al.* Superior rechargeability and efficiency of lithiumoxygen batteries: Hierarchical air electrode architecture combined with a soluble catalyst. *Angewandte Chemie International Edition* **53**, 3926–3931 (2014).

[135] Carboni, M., Marrani, A. G., Spezia, R. & Brutti, S. 1,2-dimethoxyethane degradation thermodynamics in lio2 redox environments. *Chemistry A European Journal* **22**, 1718817203 (2016).

[136] Curran, H. J., Gaffuri, P., Pitz, W. J. & Westbrook, C. K. *A Comprehensive Modeling Study of N-Heptane Oxidation*, vol. 114 (1998).

[137] Atkinson, R. Atmospheric reactions of alkoxy and -hydroxyalkoxy radicals. *International Journal of Chemical Kinetics* **29**, 99–111 (1997).

[138] Sinha, A. & Thomson, M. J. *The chemical structures of opposed flow diffusion flames of C3 oxygenated hydrocarbons (isopropanol, dimethoxy methane, and dimethyl carbonate) and their mixtures*, vol. 136 (2004).

[139] Roberts, J. L., Calderwood, T. S. & Sawyer, D. T. Nucleophilic oxygenation of carbon dioxide by superoxide ion in aprotic media to form the peroxydicarbonate(2-) ion species. *Journal of the American Chemical Society* **106**, 4667–4670 (1984).

[140] Wadhawan, J. D., Welford, P. J., McPeak, H. B., Hahn, C. E. W. & Compton, R. G. The simultaneous voltammetric determination and detection of oxygen and carbon dioxide: A study of the kinetics of the reaction between superoxide and carbon dioxide in non-aqueous media using membrane-free gold disc microelectrodes. *Sensors and Actuators B: Chemical* **88**, 40–52 (2003).

[141] Enko, B. *et al.* Singlet oxygen-induced photodegradation of the polymers and dyes in optical sensing materials and the effect of stabilizers on these processes. *J. Phys. Chem. A* **117**, 8873–8882 (2013).

[142] Gowda, S. R., Brunet, A., Wallraff, G. M. & McCloskey, B. D. Implications of co2 contamination in rechargeable nonaqueous lio2 batteries. *The Journal of Physical Chemistry Letters* **4**, 276–279 (2013).

[143] Eshetu, G. *et al.* Lithium azide as an electrolyte additive for all-solid-state lithium-sulfur batteries. *Angew Chem Int Ed Engl.* **56**, 15368–15372 (2017).

[144] Shanmukaraj, D. *et al.* Sacrificial salts: Compensating the initial charge irreversibility in lithium batteries. *Electrochemistry Communications* **12**, 1344–1347 (2010).

[145] Trinh, N. D., Saulnier, M., Lepage, D. & Schougaard, S. B. Conductive polymer film supporting lifepo4 as composite cathode for lithium ion batteries. *Journal of Power Sources* **221**, 284–289 (2013).

[146] Ferapontov, Y. A., Kokoreva, N. V., Kozlova, N. P. & Ulyanova, M. A. Thermal analysis of lithium peroxide prepared by various methods. *Russian Journal of General Chemistry* (2009).

Publications

Peer reviewed papers

[1] N. Mahne, B. Schafzahl, C. Leypold, M. Leypold, S. Grumm, A. Leitgeb, G.A. Strohmeier, M. Wilkening, O. Fontaine, D. Kramer, C. Slugovc, S.M. Borisov and S.A. Freunberger
Singlet oxygen generation as a major cause for parasitic reactions during cycling of aprotic lithiumoxygen batteries
Nature Energy **2017** 2, 17036; DOI: 10.1038/nenergy.2017.36

[2] N. Mahne, O. Fontaine, M.O. Thotiyl, M. Wilkening and S.A. Freunberger
Mechanism and performance of lithium-oxygen batteries - a perspective
Chem. Sci. **2017** 8, 6716; DOI: 10.1039/c7sc02519j

[3] L. Schafzahl†, N. Mahne†, B. Schafzahl, M. Wilkening, C. Slugovc, S.M. Borisov, and S.A. Freunberger
Singlet Oxygen during Cycling of the Aprotic SodiumO$_2$ Battery
Angew. Chem. Int. Ed. **2017** 56, 49, 15728 - 15732; DOI: 10.1002/anie.201709351

[4] L. Schafzahl†, N. Mahne†, B. Schafzahl, M. Wilkening, C. Slugovc, S.M. Borisov, and S.A. Freunberger
Singulett-Sauerstoff in der aprotischen Natrium-O$_2$-Batterie
Angew. Chem. **2017** 129, 49, 15934 - 15938; DOI: 10.1002/ange.201709351

[5] N. Mahne, S.E. Renfrew, B.D. McCloskey and S.A. Freunberger
Electrochemical Oxidation of Lithium Carbonate Generates Singlet Oxygen
Angew. Chem. Int. Ed. **2018** 57, 1 - 6; DOI: 10.1002/anie.201802277

[6] N. Mahne, S.E. Renfrew, B.D. McCloskey and S.A. Freunberger
Elektrochemische Oxidation von Lithiumcarbonat Generiert Singulett-Sauerstoff
Angew. Chem. **2018** 130, 1 - 6; DOI: 10.1002/ange.201802277

Selected Talks and Poster Presentations

[6] *New Insights into Parasitic Reactions in Non-Aqueous Alkaline-O$_2$ Batteries*,
231st ECS Meeting, New Orleans, USA, 06/2017

[7] *New Insights into Parasitic Reactions in Aprotic Li-O$_2$ Batteries*
2nd Graz Battery Days: Next Generation Materials and Systems - Truth and Consequences, Graz, Austria, 09/2016

Other Papers and Talks

[8] T.M. Smith, N. Mahne, A. Prosvirin, K.R. Dunbar, J. Zubieta
Inorganic Chemistry Communications **2013** 33, 1 - 5; DOI: 10.1016/j.inoche.2013.03.027
A tetranuclear oxofluorovanadium(IV) cluster encapsulating a Na(H$_2$O)$_n$$^+$ subunit.

Curriculum vitae

Personal

First name, family name	Nika Mahne
Date of birth	February 4th, 1989 in Ljubljana
Parents	Marina und Peter Mahne
Nationality	Austrian

Education

02/2015 – 04/2018	Doctoral programme in Technical Sciences Advisor and Principal Investigator: Dr. Stefan A. Freunberger Institute for Chemistry and Technology of Materials Doctoral Supervisor: Prof. Sergey M. Borisov Institute of Analytical Chemistry and Food Chemistry
11/2014	Dipl.-Ing. awarded from Graz University of Technology, Austria Master Thesis on *Oxide Coated Europium Activated Silicon Nitride Phosphors for Use in Chip-On-Board Technology* in cooperation with TRIDONIC GmbH, Advisor: Prof. Roland Fischer, Institute of Inorganic Chemistry
01/2012 – 11/2014	Master Programme Technical Chemistry Graz University of Technology, Austria Focus on Renewable Resources and Energy Storage
10/2007 – 01/2012	Bachelor Programme Chemistry, Graz University of Technology, Austria

Research Abroad

05/2017 – 08/2017	Short-Term Scholar at the University of California–Berkeley, California, USA, Department of Chemical and Biomolecular Engineering Advisor: Prof. Bryan D. McCloskey
10/2015	SWAXS measurements, Elettra Sincrotrone Trieste, Basovizza, Italy
03/2015	NIR spectroscopy measurements, Universitätsklinikum Regensburg, Regensburg, Germany
04/2013 – 09/2013	ERASMUS, Technische Universität Berlin, Germany, Faculty II - Mathematics and Natural Sciences, Institute of Chemistry
06/2012 – 08/2012	Summer School Chemistry, Syracuse University, New York, USA, Department of Chemistry
06/2010 – 08/2010	Summer School Chemistry, University of Novi Sad, Serbia Department of Chemistry